論文 / 著書情報
Article / Book Information

題目(和文)	薄膜分布反射型レーザの低消費電力動作構造および作製プロセスに関する研究
Title(English)	Study of Low-Power Consumption Structure and Fabrication Process of Membrane Distributed Reflector Lasers
著者(和文)	高橋 直樹
Author(English)	Naoki Takahashi
出典(和文)	学位:博士(工学), 学位授与機関:東京工業大学, 報告番号:甲第12699号, 授与年月日:2024年3月26日, 学位の種別:課程博士, 審査員:西山 伸彦,中川 茂,宮本 智之,庄司 雄哉,雨宮 智宏,松尾 慎治
Citation(English)	Degree:Doctor (Engineering), Conferring organization: Tokyo Institute of Technology, Report number:甲第12699号, Conferred date:2024/3/26, Degree Type:Course doctor, Examiner:,,,,,
学位種別(和文)	博士論文
Type(English)	Doctoral Thesis

Study of Low-Power Consumption Structure and Fabrication Process of Membrane Distributed Reflector Lasers

by

Naoki Takahashi

Department of Electrical and Electronic Engineering
Graduate School of Science and Engineering
Tokyo Institute of Technology

A DOCTORAL DISSERTATION

Directed by Professor Nobuhiko Nishiyama

S9-1 2-12-1 O-okayama, Meguro-ku, Tokyo, 152-8552, Japan
Tokyo Institute of Technology

Study of Low-Power Consumption Structure and Fabrication Process of Membrane Distributed Reflector Lasers

Contents

Chapter 1. Introduction

1.1 Introduction 1

1.2 Development of semiconductor lasers 2

1.3 Low power consumption lasers 5

1.3.1 Vertical cavity surface emitting lasers (VCSELs) 6

1.3.2 Photonic crystal lasers 7

1.3.3 Microdisk/microring lasers 9

1.3.4 Nanowire plasmonic lasers 10

1.3.5 Distributed feedback (DFB) and distributed reflector (DR) lasers 12

1.4 Membrane lasers 14

1.4.1 Concept of the membrane structure 14

1.4.2 History of membrane lasers in our lab 16

1.4.3 History of membrane lasers in other research groups 23

1.5 Application dependence of laser performance and design 25

1.6 Objective and outline of this thesis 27

Reference 29

Chapter 2. Theoretical analysis of membrane laser for low-power consumption operation

2.1 Introduction 44

2.2 Basic theory of semiconductor lasers 45

2.2.1 Threshold current and external differential quantum efficiency 45

2.2.2 Transfer matrix method (TMM) 48

2.2.3 Frequency response 53

2.3 Analysis of optical confinement structure for lateral direction 57

2.3.1 Internal loss and differential resistance 57

2.3.2 Design of buried-ridge-waveguide (BRW) structure 60

2.4 Analysis for optical confinement structure for cavity direction 66
2.4.1 Carrier density analysis 66
2.4.2 Design of asymmetric corrugation-pitch-modulation (ACPM) grating 67
2.5 Estimation of consumption power 74
2.6 Conclusion 82
Reference 84

Chapter 3. Fabrication technologies for membrane photonic devices

3.1 Introduction 88
3.2 Fabrication process and equipment 89
3.3 Selective area regrowth using organo-metallic vapor-phase epitaxy (OMVPE) 109
3.4 Surface grating formation using electron beam lithography 115
3.4.1 Grating design 115
3.4.2 Fabrication process 120
3.5 Conclusion 125
Reference 127

Chapter 4. Characteristics of membrane distributed-reflector lasers

4.1 Introduction 129
4.2 OMVPE growth conditions and initial epi-wafer 130
4.3 Membrane Fabry-Perot laser with BRW structure 138
4.4 Low threshold current membrane DR laser 142
4.4.1 Static characteristics 143
4.4.2 Dynamic characteristics 147
4.5 Discussion of consumption power of membrane DR laser 150
4.6 Conclusion 152
Reference 153

Chapter 5. Future prospects: extension of applications of membrane lasers

5.1 Introduction 154
5.2 Application for on-chip optical interconnect 155
5.2.1 Short distance optical communication 155
5.2.2 Requirements of on-chip optical interconnect 160
5.2.3 Optical link with InP waveguide 166
5.3 Application for optical neural network 173
5.3.1 Optical neural network using photonic integrated circuit 173
5.3.2 Concept of all optical neural network using membrane laser 178
5.3.3 Characterization and future prospect 180
5.4 Application for B5G/6G communication system 186
5.4.1 Radio-over-fiber (RoF) 186
5.4.2 Photon-photon resonance (PPR) for high-speed modulation 188
5.4.3 Characterization and future prospect 192
5.5 Conclusion 198
Reference 199

Chapter 6. Conclusion

Acknowledgements

Publication list

Chapter 1

Introduction

1.1 Introduction	1
1.2 Development of semiconductor lasers	2
1.3 Low power consumption lasers	5
1.3.1 Vertical cavity surface emitting lasers (VCSELs)	6
1.3.2 Photonic crystal lasers	7
1.3.3 Microdisk/microring lasers	9
1.3.4 Nanowire plasmonic lasers	10
1.3.5 Distributed feedback (DFB) and distributed reflector (DR) lasers	12
1.4 Membrane lasers	14
1.4.1 Concept of the membrane structure	14
1.4.2 History of membrane lasers in our lab	16
1.4.3 History of membrane lasers in other research groups	23
1.5 Application dependence of laser performance and design	25
1.6 Objective and outline of this thesis	27
Reference	29

1.1 Introduction

Semiconductor lasers have made remarkable progress since the first device was demonstrated in the early 1960s and are now widely used as a light source for various applications such as optical fiber communications and sensing. In addition to basic Fabry-Pérot lasers, the development of distributed feedback lasers and introduction of quantum well have realized advanced functions and performance, and the range of their applications is ever expanding. These lasers have resonators formed along an optical axis parallel to the active layer planes, but vertical cavity surface emitting lasers with resonators formed along a vertical axis and ring lasers with resonators formed in a ring shape have also been developed and are used in a variety of applications. While the performance required of semiconductor lasers varies depending on the application, in most cases, reducing power consumption is one of the most important challenges.

In this chapter, the history of semiconductor lasers is reviewed, and the evolution of expectations for semiconductor lasers and the development path to meet those expectations are introduced. Various types of semiconductor lasers that can operate with low power consumption are then introduced. In particular, our group has proposed and demonstrated a semiconductor membrane laser that uses a thin-film III/V layer capable of low-power consumption operation, and the history of this laser is discussed in detail. Finally, the objectives and an outline of this thesis will be described.

1.2 Development of semiconductor lasers

Light amplification by stimulated emission of radiation (LASER) is a generic term for oscillators and amplifiers of light waves using induced emission of photons from optical transitions of electrons. The idea, based on the principle of microwave amplification by stimulated emission of radiation (MASER) [1], was proposed as early as 1957. The basic theory of lasers was established by Schawlow-Townes in 1958 [2],

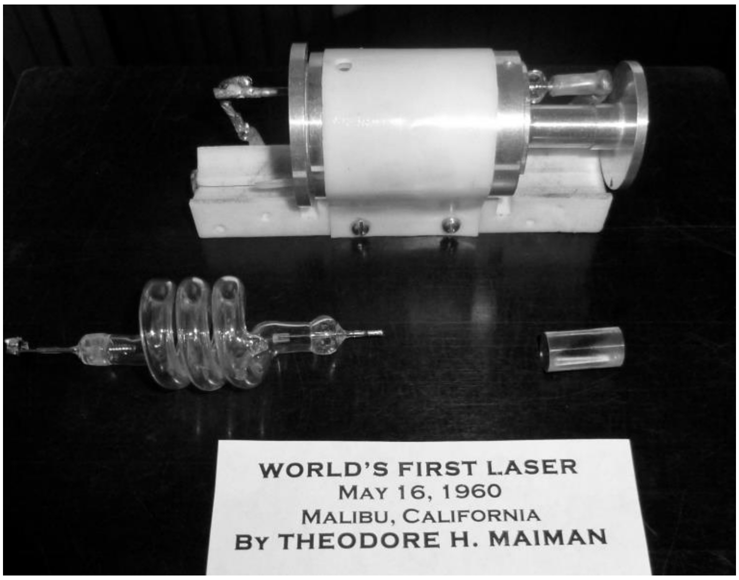

Fig. 1.1 World's first ruby laser designed by T. Mainman [1]

and the world's first laser oscillation was successfully achieved by T. H. Maiman at Hughes Research Laboratories in 1960, using a three-level medium ruby [3]. Fig. 1.1 shows the photography of the first ruby laser designed by T. Mainman. The first laser oscillation in a semiconductor was observed two years later, in 1962. In the U.S., semiconductor lasers were being developed competitively, and four groups succeeded in oscillation almost simultaneously. The earliest group, led by R. N. Hall at GE Laboratories, reported 77 K pulsed oscillation of a GaAs homojunction laser [4]. M. I. Nathan *et al*. at IBM and T. M. Quist *et al*. at MIT also used GaAs, and N. Holonyak *et al*. at GE Semiconductor Division succeeded in red laser oscillation using GaAsP mixed crystal [5]-[7].

The compound semiconductor GaAs attracted researchers' attention at the time as a new semiconductor material to replace silicon, but the extremely high oscillation threshold current density resulted in only pulse operations of microseconds or less, which was a fatal drawback for practical use. However, a breakthrough came in 1970 with the invention of the AlGaAs/GaAs double heterostructure laser [8]-[14]. In a double heterostructure laser, a thin (~ 0.1 μm) GaAs active layer is sandwiched from both sides by an AlGaAs cladding layer with a larger band gap. Electrons and holes injected into the active layer are confined to the active layer due to the potential barrier of the heterojunction. This allows the optical gain required for lasing to be achieved at a relatively low current density. It is also important to note that the refractive index of the active layer is larger than that of the cladding layer, and the double heterostructure acts as an efficient optical waveguide. Thanks to the confinement of carriers and photons, the threshold current density at room temperature was dramatically reduced to nearly 1 kA/cm^2, enabling continuous operation at room temperature with a laser mounted on an appropriate heat sink. Almost simultaneously, this feat was accomplished by the Alferov's group at Ioffe Physico-Technical Institute and M. Panish and I. Hayashi at Bell Labs [8][9].

The AlGaAs/GaAs double heterostructure laser was made possible by the special properties of this material and the development of epitaxial growth techniques [10]. Since the observation of GaAs injection emission, interest in light-emitting diodes based on compound semiconductor materials has increased and epitaxial growth techniques, especially vapor-phase and liquid-phase epitaxy, have been developed. Rupprecht *et al.* at IBM noticed that AlGaAs on GaAs is lattice-matched to the substrate regardless of its composition ratio [11]. This is extremely important, and heterojunctions with very few defects can be obtained in the wavelength range of 0.7~0.9 μm. Benefiting from these factors, Hayashi *et al.* and Alferov *et al.* both used liquid-phase growth techniques to fabricate AlGaAs/GaAs double heterostructures on GaAs substrates and successfully achieved room temperature continuous operation [12][13].

In the 1970s, silica optical fiber had the lowest loss in the wavelength range of AlGaAs/GaAs lasers [14], but as optical fiber technology advanced and the purity of silica improved, it was found that the loss was lowest at 1310 nm and 1550 nm [15][16]. This prompted the development of laser materials in this wavelength band for telecommunication applications, and the GaInAsP-based material on InP substrates attracted much attention. GaInAsP is a quaternary mixed crystal, and by choosing the composition appropriately, a wide wavelength range of 1.1 to 1.6 μm can be obtained while lattice matching with InP [17]-[20]. Fig. 1.2 shows room temperature CW operation of GaInAsP/InP DH lasers emitting at 1.51 μm. Initially, liquid-phase epitaxy (LPE)

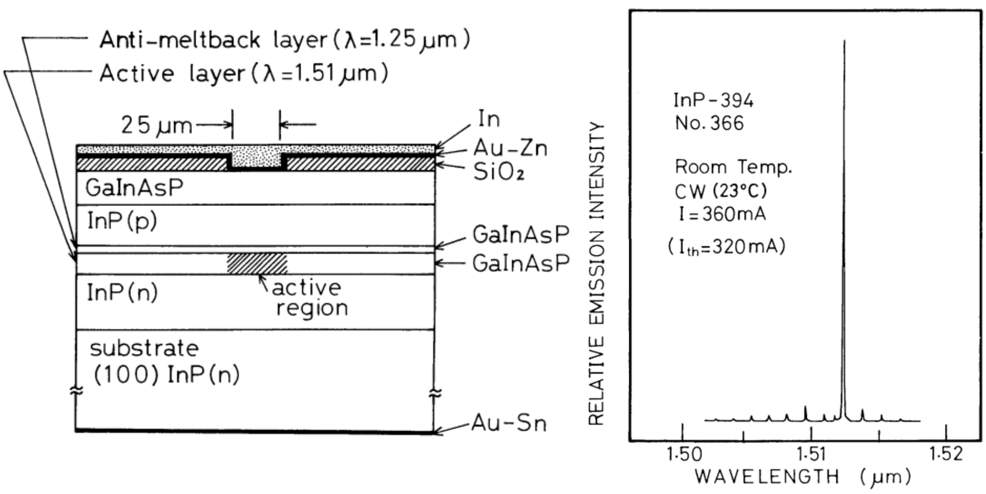

Fig. 1.2 Schematic diagram of stripe laser and lasing spectrum [19].

[21][22] was used, and it was difficult to grow thin crystals of less than 100 nm with good reproducibility, but new epitaxy techniques, such as organo-metallic vapor phase epitaxy (OMVPE) [23][24] and molecular beam epitaxy (MBE) [25][26], were developed in the United States to make this possible and are being used in semiconductor lasers. Theoretically and experimentally, it has become clear that when the thickness of the active layer of semiconductor lasers is reduced to 10 nm or less, the quantum characteristics of the carriers as waves become more prominent, and various laser characteristics are improved, such as reduction of the threshold current and expansion of the modulation bandwidth [27]. Furthermore, since ultra-thin layers have the advantage that crystal defects will not occur even in the presence of strain, it is possible to further improve the laser characteristics by actively introducing strain [28][29]. Strained quantum well structures are used in almost all semiconductor lasers currently commercialized.

Semiconductor lasers have thus reached their present form through the development of materials and epitaxial growth technology. So far, the history of the development of compound semiconductor lasers has been reviewed, focusing on the compound semiconductor materials of the light-emitting layer. In the next section, focusing on the laser structure, approaches to low power consumption, which is one of the most important issues, will be described.

1.3 Low power consumption lasers

Low-power lasers are particularly important in the field of optical communications, where optical signals are used to transmit information. For example, data centers, the backbone of modern telecommunications networks, handle enormous amounts of data and correspondingly consume enormous amounts of power and heat. Low-power lasers in optical communication systems are therefore an important factor in contributing to overall energy efficiency and reducing operating costs. This section describes semiconductor lasers capable of low-power operation for optical communications.

1.3.1 Vertical-cavity surface-emitting lasers (VCSELs)

In general edge-emitting lasers, light is emitted in a direction parallel to the substrate surface. On the other hand, vertical-cavity surface-emitting lasers (VCSELs) use a highly reflective distributed Bragg reflector (DBR) consisting of a semiconductor or dielectric layered structure as a reflector to resonate and emit light in a vertical direction to the substrate surface as shown in Fig. 1.3 [30]-[33]. VCSELs was proposed by K. Iga in 1977. The first device was realized in 1979 using GalnAsP/InP material in the active region [34]. In early attempts, the threshold was very high, 800 mA at 77 K pulsed operation. Later, room temperature continuous operation at a wavelength of 894 nm was demonstrated on a GaAs substrate by K. Iga and F. Koyama [35]. This accelerated the development of VCSELs worldwide, and in 1989, J. Jewell *et al*. at Bell Laboratories demonstrated 1.3 mA low threshold current with 958 nm output wavelength [36]. As the promising device with low cost and low power consumption light source for data transmission, VCSELs received much attention in recent years. Significant reduction of threshold current was accomplished by various current blocking methods such as oxidation, ion implantation, and tunnel junction structures [37]-[44]. The high-power conversion efficiency of 62% was achieved in 2008 by K. Takaki, (Furukawa electric) [45]. Low energy cost of 81 fJ/bit

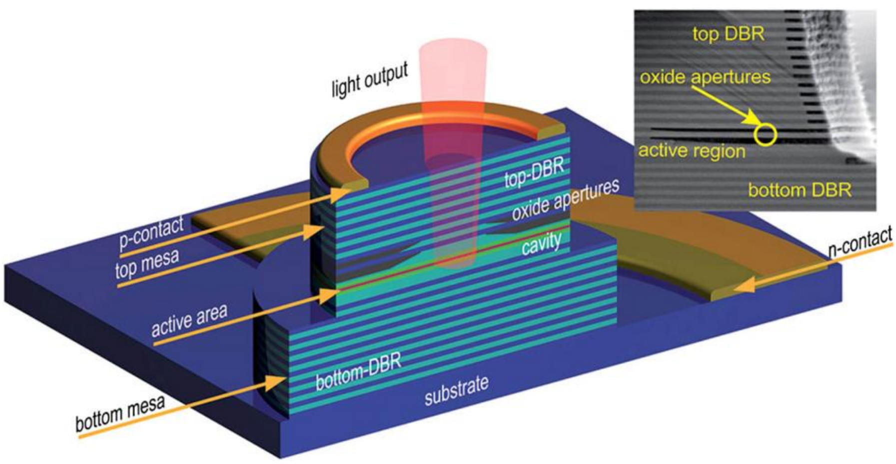

Fig. 1.3 Schematic diagram and SEM image of top-emitting vertical-cavity surface-emitting lasers (VCSELs) [30].

was demonstrated in 2011 [46] and 56 fJ/bit in 2012 [47] by P. Moser at TU Berlin. Further, the 50 fJ/bit for 40 Gbps non-return-to-zero (NRZ) [48] and 153.4 fJ/bit for 100 Gbps Pulse Amplitude Modulation 4 (PAM4) were recorded in 2022 [49]. Surface emitting lasers are playing a central role as a light source for current short-haul optical local area networks (LANs) and optical interconnects in data centers and supercomputers due to their advantages such as low threshold current, low power consumption, two-dimensional array capability, and the ability to test performance on a wafer-by-wafer basis. On the other hand, the vertical direction of emission makes it difficult to apply to silicon photonics and other applications that require light to be coupled in-plane.

1.3.2 Photonic crystal lasers

The photonic crystal structure is a concept proposed by E. Yablonovitch and S. John in 1987 [50][51]. This structure is inspired by the fact that each atom in a crystal lattice has its own potential energy, and by changing the dielectric constant in space, a photonic band gap (PBG) is formed in which light cannot propagate in a specific wavelength band [52]. In the periodic structure where the PBG is formed, introducing a defect in a part of the structure makes it possible to strongly confine light to the narrow part and obtain a high Q-value [53]-[56]. Distributed feedback (DFB) and DBR structures are one-dimensional photonic crystals, and after the realization of the first GaInAsP/InP-based laser using optical excitation of a two-dimensional photonic crystal in 1999 [57], photonic crystal lasers with current injection structures [58][59] were also reported. After that, room temperature continuous oscillation was achieved [60]-[64]. However, the photonic crystal lasers described above faced several problems. One is that they do not have a carrier confinement structure. Most photonic crystal lasers form a resonator by forming periodic air holes in the thin-film structure containing the gain medium, and although strong optical confinement can be obtained at the defects, there was a lot of carrier leakage. In addition, in order to increase optical confinement in the vertical direction, thin-film structures of low refractive index materials such as air are often used for the top and

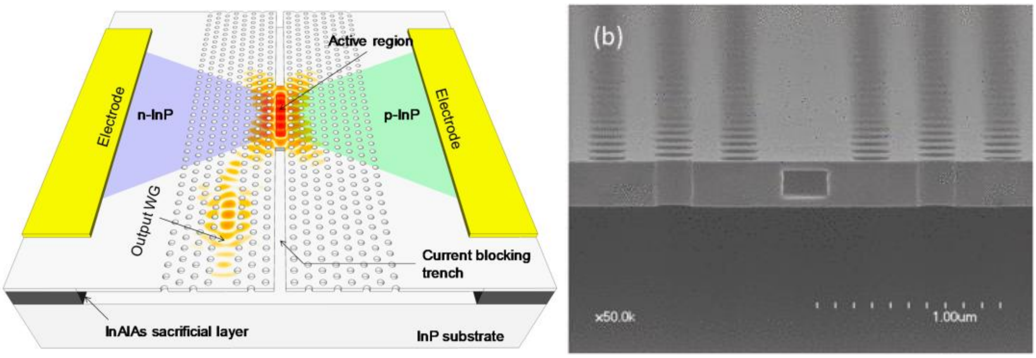

Fig. 1.4 Schematic diagram and SEM image of photonic crystal laser on Si [65].

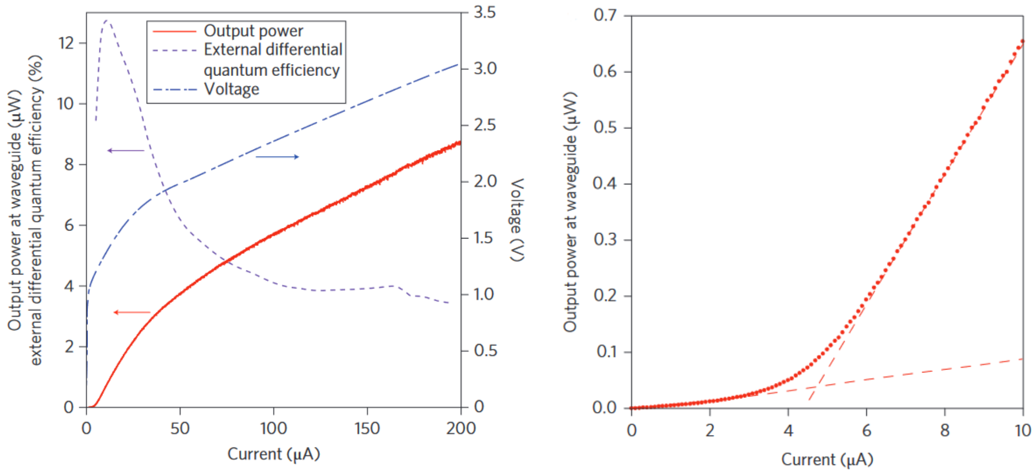

Fig. 1.5 Output power, applied voltage and external differential quantum efficiency of the LEAP laser versus injected current [69].

bottom cladding, which has the problem of poor heat dissipation. To solve these problems, the Buried Hetero (BH) structure was introduced by the NTT group as shown in Fig. 1.4 [65][66]. This laser is called LEAP (Lambda-scale embedded active region photonic-crystal) laser, and the BH structure makes it possible to confine the carriers in the resonator, and also to improve the thermal characteristics by embedding them in InP, which has relatively low thermal resistance. In this device, periodic air holes are formed on both sides of the embedded active region, and the thin-film structure is formed by removing the lower sacrificial layer. The optical output is extracted through an optical waveguide. A BH structure based PhC with optical pumping was first demonstrated, achieving a low threshold input power of 1.3 μW and low power consumption of 13 fJ/bit at a modulated output power of 5 GHz [66]. Subsequently, current-injected PhCs were obtained [67][68], and extremely low-energy operation with a threshold current of 4.8 μA and an operating energy of 4.4 fJ/bit was reported, but the optical output power of 2.17 μW is low due to the very small active region and is insufficient in terms of optical output power for error-free operation (Fig. 1.5) [69].

1.3.3 Microdisk/microring lasers

Semiconductor whispering gallery-mode (WGM) microcavities are promising compact and energy-efficient light sources because of their small size, high Q-factor, flat geometry, in-plane emission, and sensitivity to the environment. The development of electrically pumped whispering gallery-mode microdisk lasers, first demonstrated in 1992, was an important achievement: single-mode operation and sub-mA threshold [70]. Whispering Gallery mode which resonates inside the disk or sphere was studied many years ago [71]-[75]. and a record low threshold current of 40 μA was achieved in 2000 [76]. However, challenges related to low optical output and integration with waveguides remain. Recent efforts to integrate InP-based microdisk lasers on silicon-on-insulator (SOI) substrates have addressed the integration challenge [77]. This group achieved a low threshold current of 0.5 mA and coupling optical output power to the Si line waveguide,

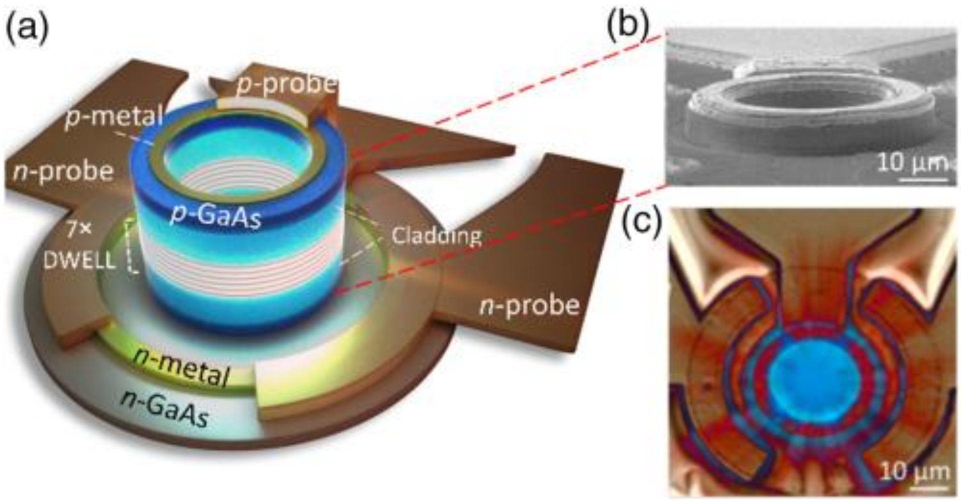

Fig. 1.6 Schematic illusuration and SEM image of microring laser [79].

while continuous wave output power was about 10 μW, which was insufficient for data transmission. The threshold current and optical output of a microdisk laser can be controlled by the radius of the cavity [78]. Recently, by properly designing the radius and increasing the optical output, fundamental properties such as modulation characteristics have become clear, and the variety of applications has expanded [79][80].

1.3.4 Nanowire plasmonic lasers

With the development of the various types of lasers described above, the size of semiconductor lasers is gradually decreasing. However, these lasers are still limited by the diffraction limit and cannot achieve sizes smaller than half the optical wavelength. This limit poses challenges for integration with modern transistors and leads to energy dissipation, limiting the practical application of micro/nano lasers [81]. Plasmonic lasers have emerged as a promising solution to overcome these size limitations [82]-[86].

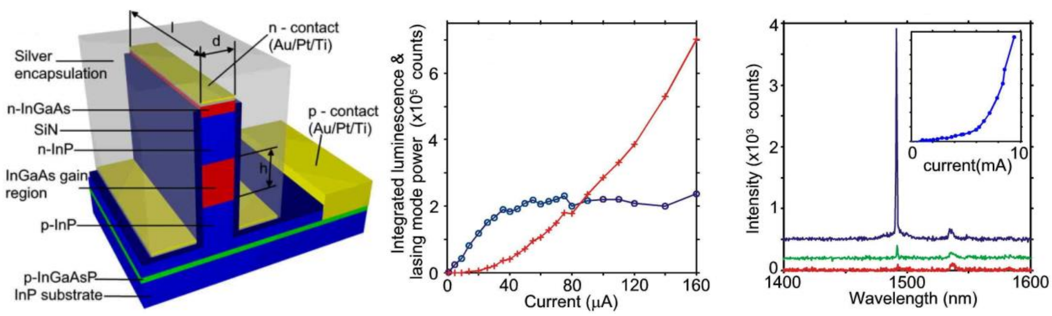

Fig. 1.7 Electrically injected plasmonic laser formed by a rectangular n-InP/GaInAs/ p-InP pillar [91].

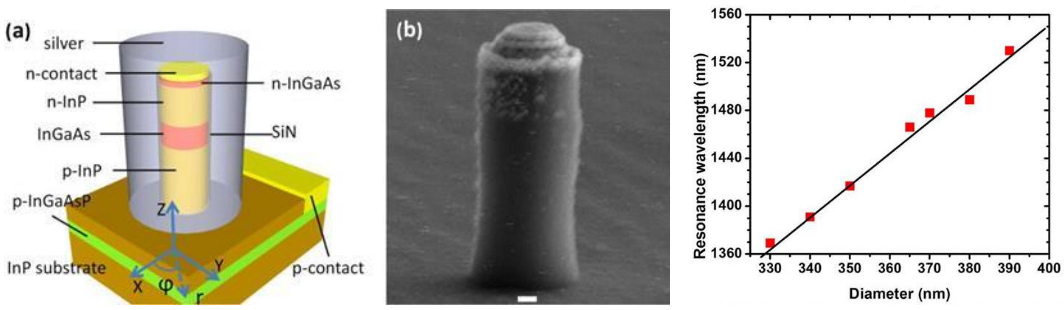

Fig. 1.8 Electrical injection metallic nanolaser with cylindrical core-shell structure [92].

Plasmonic lasers utilize surface plasmons at the metal-dielectric interface to realize deep subwavelength laser sources. The coupling of surface plasmons and light waves compresses the physical dimensions of the plasmonic cavity to the nanometer scale, allowing simultaneous amplification of photons and surface plasmons, similar to photonic lasing in pure dielectric materials. The strong interaction between photons and surface plasmons enhances the local field, providing plasmonic lasers with high power density, low theoretical consumption, and fast response [87]-[90]. Notably, plasmonic lasers achieve a minimum size (~10 nm) comparable to metal-oxide-semiconductor field-effect transistors. The coupling efficiency of silicon waveguides reaches 90%. However, although electrical injection operation is central to the application of plasmonic lasers, there are still significant challenges to its realization. The large ohmic losses and Joule heating of electrical injection significantly reduce the effective gain and increase the operating threshold. The typical amplitude of the electrical density of electrically driven plasmonic lasers is ~70 A /cm^2 or more, which is almost an order of magnitude larger than that of photonic micro lasers. In 2007, Hill *et al*. demonstrated an electrically driven metal clad nanowire (NW) laser that compressed laser dimensions into the subwavelength range In 2009, Hill *et al*. realized the first electrically driven plasmonic laser consisting of n-InP/GaInAs/p-InP pillars with rectangular cross sections (Fig. 1.7) [91]. By using direct current electric injection with forward bias above ~10^4 A/cm^2, super-linear emission with a line width of ~0.5 nm was observed from a device with the GaInAs pillar length of 6 μm and thickness of 310 nm at room temperature. Furthermore, Ding *et al*. presented a plasmonic laser with an orientationally polarized beam based on a cylindrical InP/GaInAs/InP pillar (Fig. 1.8) [92]. The radius of the semiconductor pillars ranged from 165 nm to 250 nm, and the thickness of the SiN layer was 120 nm. Measurements with DC current injection was made at 78 K and L-I curve shows a threshold current around 80 µA. The oscillation wavelength is tunable from 1.37 μm to 1.53 μm by changing the radius of the pillar, indicating the possibility of multicolor metal-clad lasers. However, CW operation is realized only at 78K, and further resistance reduction or heat dissipation improvement is required for room temperature operation.

1.3.5 Distributed feedback (DFB) and distributed reflector (DR) lasers

Distributed feedback (DFB) lasers, which have developed as an important light source for high-speed optical fiber communications [93][94], have made a significant contribution to overcoming the challenges faced by semiconductor lasers before the Fabry-Perot structure with cleaved mirrors was adopted. The initial semiconductor laser design faced difficulties related to multimode operation and long-distance transmission due to dispersion issues. Recognizing these limitations, the DFB laser emerged as a solution, with Kogelnik and Shank proposing the concept in 1972 [95][96]. Their idea involved introducing a periodic refractive index structure in the form of a grating, enabling wavelength selection and achieving strong optical confinement through robust reflection inside the cavity. DFB lasers are categorized into two main types: index-coupled (IC) and gain-coupled (GC) DFB lasers, with a combination of both in complex-coupled (CC) DFB lasers [97]. The IC-DFB laser's single-mode characteristics depend on the phase at the cavity facet during reflection [98]. However, controlling the facet phase is challenging due to the grating's small period, typically less than 300 nm, and the facet being formed by cleaving. Antireflection (AR) coatings are often employed to suppress reflections, and phase shift structures aid in achieving low threshold current and single-mode operation at the Bragg wavelength. Conversely, CC-DFB lasers offer advantages such as good single-mode characteristics and resistance to facet conditions [99][100]. In addition to property improvements with diffraction gratings, material improvements were explored, leading to the development of AlGaInAs/InP DFB lasers tuned for high-speed optical communications [101]-[103]. In 2009, a milestone of 40 Gbit/s operation with direct modulation was reached [104].

Our group has focused on the development of CC-DFB lasers and has proposed and developed CC-DFB lasers using low-damage etching techniques and organo-metallic vapor phase epitaxy (OMVPE) [105]-[107]. CC-DFB lasers with fully etched quantum wells forming a wire-like active region showed low threshold current operation due to

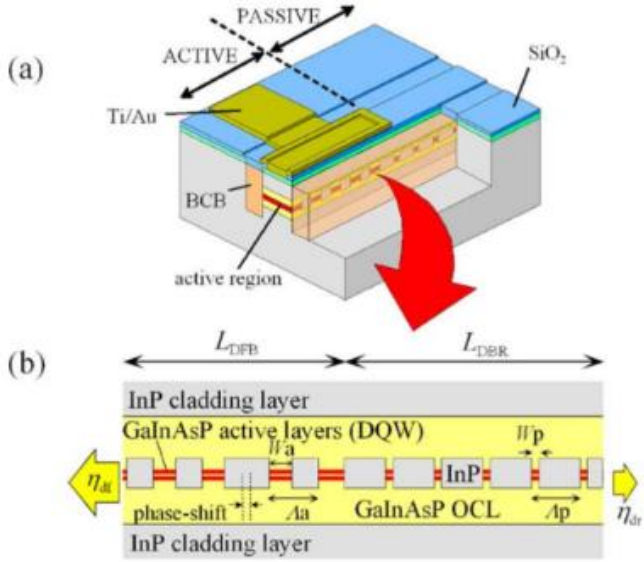

Fig. 1.9 Schematic diagram of DR laser and cross-sectional structure of wirelike active regions [111].

reduced active volume and strong exponential coupling. In particular, a sub-mA threshold current of 0.7 mA was achieved in 2000 [108], demonstrating the continued optimization of DFB laser performance. To further increase efficiency, distributed reflector (DR) lasers, which consist of an active DFB section and a passive distributed Bragg reflector (DBR) section, were introduced. The DR laser was proposed by Y. Suematsu *et al*. at Tokyo Institute of Technology in 1988 [109][110]. Typical in-plane lasers output light with equal intensity in the forward and backward directions. DR lasers have a DBR in the back, which allows the backward output to be returned to the active layer, resulting in high efficiency. Various DR lasers have been developed to achieve low threshold current operation with a wire-like active region and high efficiency without the need for faceted coatings. In 2009, a DR laser with a wire-like active region (Fig. 1.9) achieved a low threshold current of 0.9 mA and an impressive efficiency of 48%, demonstrating its potential for low power consumption operation [111]. High speed direct modulation using non-return-to zero 10 Gbit/s and 25 Gbit/s signals were demonstrated [112][113]. The energy cost for transmission was approximately 1.7 pJ/bit for 10 Gbit/s operation.

1.4 Membrane laser

1.4.1 Concept of the membrane structure

The design of active structures on InP membranes requires a careful balance between optical and electrical properties, particularly in relation to the thicknesses of the core and cladding layers. Thinner layers offer the advantages of higher optical confinement and lower diode resistance, but they also pose challenges in managing optical loss and sheet resistance in thin conductive layers. This trade-off is even more significant with InP membranes compared to conventional amplifiers.

The key feature of the membrane structure is strong optical confinement, as shown in Fig. 1.10. By optimizing the thickness of the membrane structure, the optical confinement factor of the semiconductor core layer can be three times higher than in a conventional structure with thick semiconductor cladding layers. To fully exploit this strong optical confinement, the core layer thickness of the membrane structure must be thin, which presents a challenge for electrical injection. In the conventional structure,

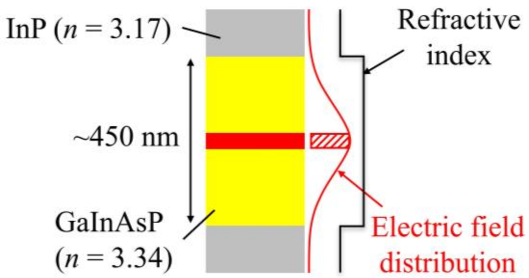

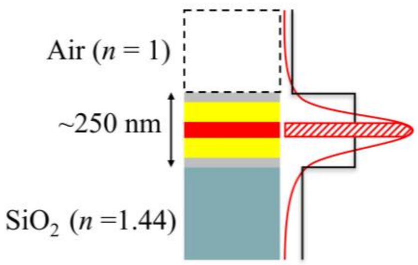

	Conventional structure	Membrane structure
Relative refractive index difference Δ	5%	40%
Optical confinement factor ζ_{act}	1.1%/well	3.0%/well

Fig. 1.10 Comparison of the optical confinement between the conventional semiconductor laser and membrane laser.

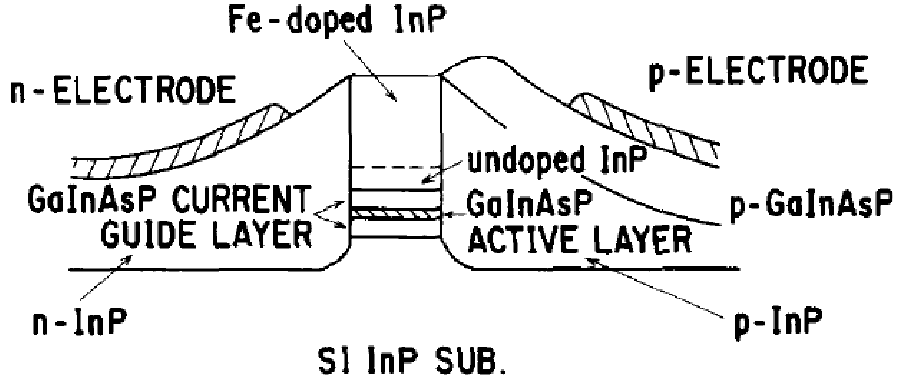

Fig. 1.11 Cross sectional view of the structure of LCI type GaInAsP/InP laser [114].

relatively thick cladding layers allow for the introduction of electrodes with high optical absorption at the top and bottom of the diodes, enabling current injection along the vertical direction. However, in the membrane structure, electrodes cannot be placed directly on the top or bottom since the cladding layers in the vertical direction are either air or insulator. Therefore, to inject current into the membrane structure, electrodes at the sides of the active region are required. Although current initially flows in the lateral direction, the p-i-n junction can be either in the lateral or vertical direction.

The lateral current injection (LCI) structure was originally proposed by Oe *et al.* (Fig. 1.11) [114] for photonics-electronics integration purposes prior to the development of the membrane structure. One side of the active region consists of p-type layers, while the other side has n-type layers. To achieve good current confinement and refractive index difference for lateral optical confinement, a buried hetero (BH) structure must be introduced using regrowth technology. Aihara *et al.* [115] reported the fabrication of a BH structure through direct wafer bonding of an active stack to silicon, followed by regrowth steps to form the passive and doped regions. To create the p- and n-type layers as side cladding layers, there are two methods. One is two times selective regrowth of *p*- and *n*-layers, once for each side [116][117]. The other way is to perform one uniform regrowth of undoped layers and then apply impurity diffusion or implantation to form the p- and n-doped regions [115][118]. The advantage of the LCI structure for the membrane structure is its relatively simple fabrication process, even though regrowth is necessary. After wafer bonding onto a host substrate, the fabrication process essentially continues as a planar process. One potential challenge of this LCI structure is ensuring the quality of the regrowth interfaces between the side cladding layers and active region. This interface may affect the electrical characteristics, such as excess voltage drops, and the optical characteristics induced by surface recombination. To avoid these issues, a carefully considered regrowth process, particularly with respect to the preparation process, is essential.

The total thickness of the InP membrane structure is only several hundred nanometers. Despite the small thickness, careful consideration of the layer structure is crucial to achieve high-performance characteristics. The optical confinement factor reaches a maximum at a core thickness of 150 nm. However, due to concerns regarding high-speed modulation characteristics and current injection efficiency, a thickness of 150 nm may not be sufficient for two reasons. Firstly, active layers such as quantum wells (QWs) and barriers, which are typically composed of GaInAsP/GaInAsP or AlGaInAs/AlGaInAs for 1.3 μm or 1.55 μm lasers, have a high surface recombination rate due to the presence of As atoms, leading to non-radiative carrier recombination [119][120]. To mitigate this, a sufficiently thick InP layer with low surface recombination rate should be used to sandwich the active layers. The internal quantum efficiencies of Fabry–Perot membrane lasers improve significantly with increasing InP cap layer thickness up to 50 nm. Secondly, multiple QWs must be employed to increase the differential gain for high-speed operation. Consequently, the total thickness of the structure becomes greater than 200 nm [121]. This careful balancing of optical and electrical properties in the membrane structure enables high modal gain and low power consumption operation.

1.4.2 History of membrane lasers in our lab

Towards realizing ultra-low power consumption, our group has proposed and investigated the membrane laser. Our group started researching membrane lasers around 1999. In this section, the history of membrane lasers is described.

Optically pumped membrane DFB lasers (2001~2008)

Initially, membrane lasers were operated by optical pumping, and in 2001, room-temperature continuous operation of a membrane DFB laser with a wire-like active region (Fig. 1.12) by optical pumping was demonstrated for the first time [122]. Figure shows the schematic structure of a membrane DFB laser. The threshold pump power was 38 mW. 4 μm thick BCBs were used to form the membrane structure on the InP host substrate. Four years later, single-mode operation with a side-mode suppression ratio (SMSR) of 36 dB and a low threshold pump power of 0.64 mW was achieved by employing a thin stripe structure and a narrow pump beam [123][124]. A multi-wavelength laser array with a maximum wavelength range of 75 nm was also realized by modulating the DFB grating period, grating duty ratio, and stripe width [125]-[127]. In 2007, a short-cavity membrane DFB laser device with a surface corrugated structure and a high refractive index coupling coefficient of 4200 cm^{-1} was fabricated [128]. A low threshold optical pump power of 0.34 mW was achieved under RT-CW conditions in a device 2.0 μm wide and 80 μm long. This LCI structure fabricated by two-step OMVPE regrowth.

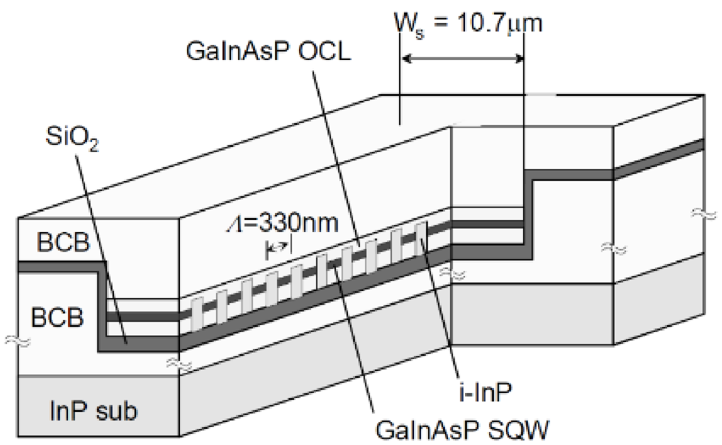

Fig. 1.12 Schematic structure of the first membrane DFB laser operated by optical pumping [122].

Lateral-current-injection (LCI) laser on SI-InP (2008~2011)

As described in the previous section, a LCI lasers have long history since 1970s. To realize the current injected membrane lasers, our group has been investigating LCI lasers since 2009. Fundamental properties of a LCI laser were investigated through evaluating the LCI lasers on semi-insulating InP substrate [129]. The first top-air-clad LCI Fabry-Perot laser with 400-nm-thick core layer was demonstrated with threshold current of 49 mA under RT-pulsed condition [130]. RT-CW operation at threshold current of 11 mA was obtained by modifying the structural design as shown in Fig. 1.13 [131]. In 2011, an LCI-DFB laser with an a-Si surface grating was demonstrated [132]. A device with a stripe width of 2.0 μm and a cavity length of 300 μm showed a threshold current of 7.0 mA and an external differential quantum efficiency as low as 43% from the front facet under RT-CW conditions. λ/4 shifted LCI-DFB laser with a-Si surface grating [133] and LCI-DFB laser with wire-like active region [134] were successfully operated. However, the internal quantum efficiency of these devices was as low as 40%, about half that of typical semiconductor lasers. Therefore, two approaches were considered to improve the internal quantum efficiency: one is a distributed quantum well structure (Fig. 1.14) [135] and the other is a thick InP cap (Fig. 1.15) [136]. The former approach was proposed to reduce leakage current through the optical confinement layer (OCL) by distributing quantum wells in the core layer to inject current uniformly into each quantum well. As a result, an internal quantum efficiency of 70% was achieved. The latter approach was

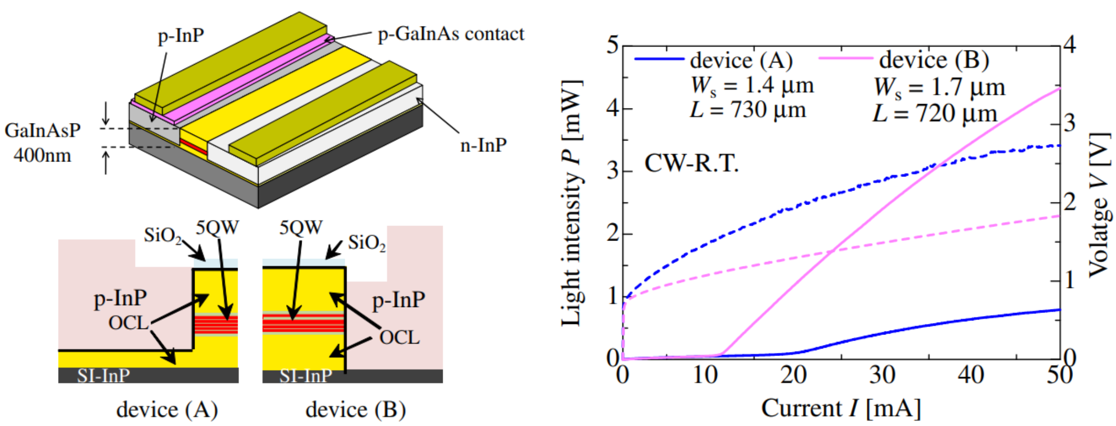

Fig. 1.13 Schematic of first LCI-FP laser on SI-InP with RT-CW operation [131].

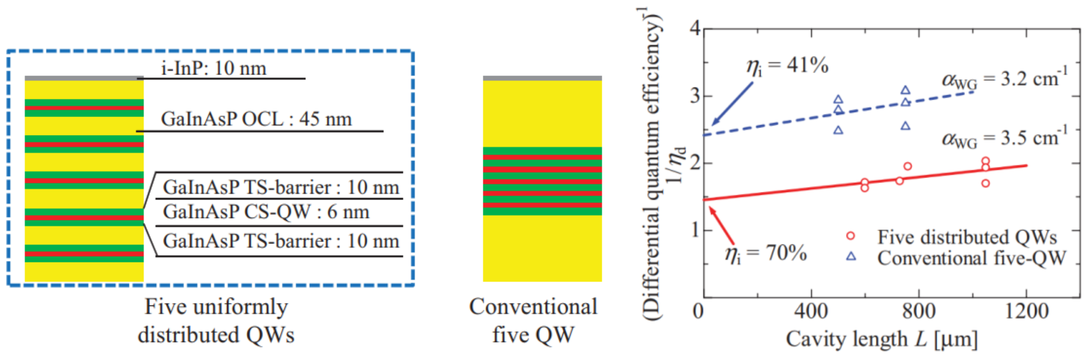

Fig. 1.14 Internal quantum efficiency improvement by introducing distributed quantum well structure [135].

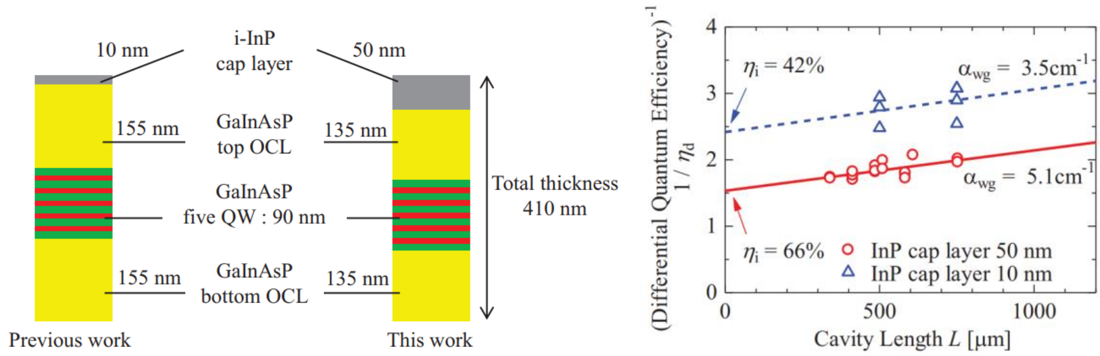

Fig. 1.15 Internal quantum efficiency improvement by introducing thick InP cap [136].

proposed to suppress surface recombination; InP has a wider band gap energy than the OCL layer. To suppress surface recombination, carriers must be kept away from the semiconductor surface. A thick InP cap layer (50 nm) increased the internal quantum efficiency to 66%. These results prove that the internal quantum efficiency of LCI lasers is comparable to that of conventional vertical current injection lasers.

LCI Membrane DFB/DR Laser on Si (2011~)

The first current injection operation of a membrane DFB laser with LCI structure was realized in 2011 by combining the LCI structure and wire-like active region described above (Fig. 1.16) [137]. The lateral p-n junctions of the LCI structure were formed by two-step OMVPE regrowth and bonded on a Si substrate by benzocyclobutene (BCB).

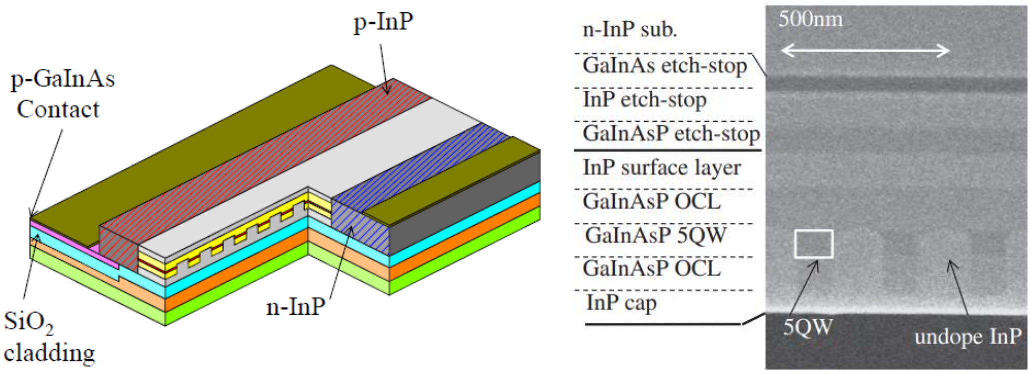

Fig. 1.16 First current injection operation of a membrane DFB laser with LCI structure and wire-like active region [137].

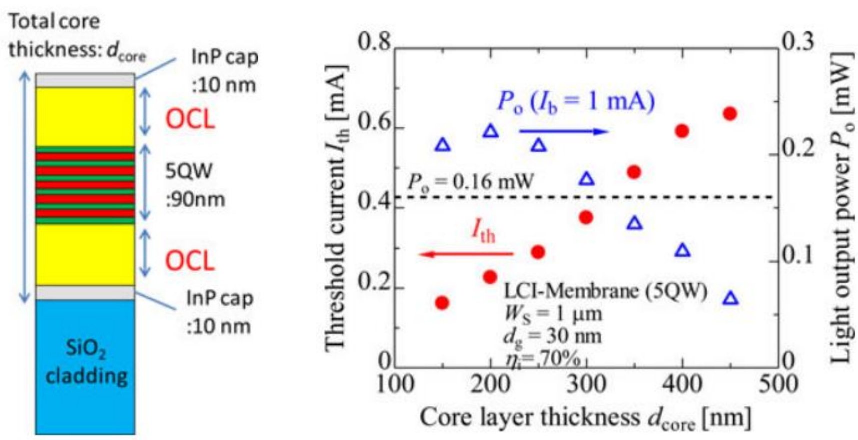

Fig. 1.17 Calculated threshold current and light output power dependence of core layer thickness of an LCI-membrane-DFB laser [141].

The threshold current was as high as 83 mA in RT pulse operation, indicating that low threshold current operation could not be achieved at this point. Subsequently, a membrane DFB laser with a surface etched grating was fabricated to lower the threshold current, and a threshold current of 11 mA was obtained under RT pulse conditions [138][139], which was still high value. One of the causes of the high threshold current operation is the degradation of optical properties due to the diffusion of Zn, which has a large diffusion coefficient. Therefore, the dopant in the GaInAs contact layer was replaced with Be instead of Zn, resulting in a low threshold current of 3.8 mA under RT-pulse conditions [140]. For low threshold current and high-speed operation, semiconductor core layer thickness dependences of the lasing properties of LCI-membrane-DFB lasers, such as the threshold current, output power, relaxation oscillation frequency, and a 3-dB bandwidth, were investigated theoretically [141]. Considering injection power and output power, the optimal core layer thickness was obtained to be 200 nm as shown in Fig. 1.17, and this analysis determined the vertical optical confinement structure of the membrane laser. Also, to achieve RT-CW operation, the thermal characteristics of a membrane DFB laser were analyzed [142]. By reducing the BCB thickness from 6 μm to 2 μm to reduce thermal resistance, the first RT-CW operation of a membrane Fabry-Perot laser bonded on an InP

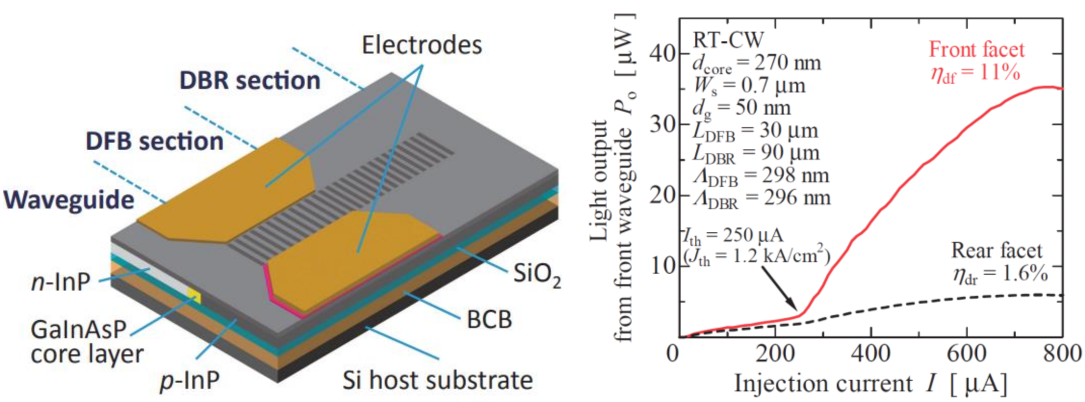

Fig. 1.18 Membrane DR laser on Si substrate with passive waveguide formed by a butt-joint built-in (BJB) regrowth process [145].

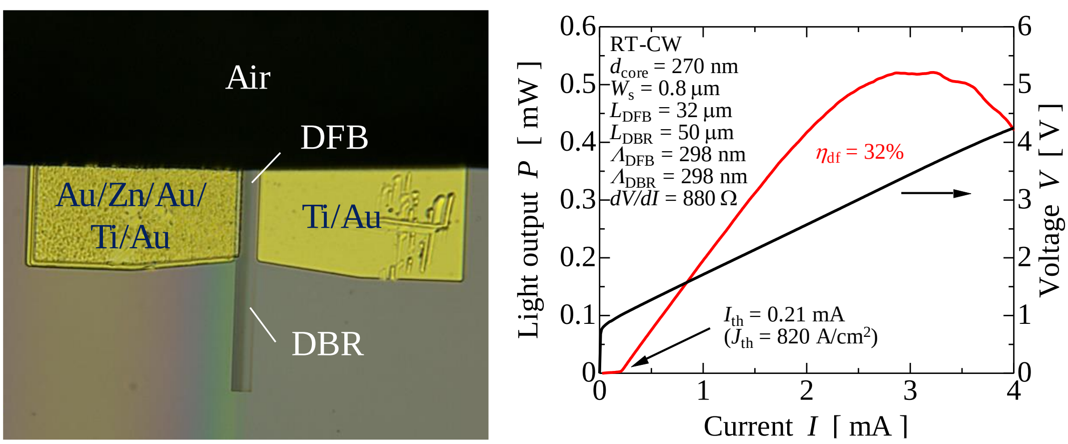

Fig. 1.19 Low threshold and high efficiency membrane DR laser by reducing the doping concentration of the *p*-InP side cladding layer [146].

substrate was demonstrated in 2013 with a threshold current of 3.5 mA [143]. This device also aimed to achieve a very strong optical confinement effect by reducing the core thickness to 220 nm, compared to about 400 nm for conventional membrane lasers. In the following year, RT-CW operation of LCI membrane Fabry-Perot bonded to a Si substrate was also achieved, and operation at a threshold current of 2.5 mA and an external differential quantum efficiency of 22%/facet was confirmed [144]. In 2015, a membrane DR laser on Si substrate consisting of a 30 μm active DFB section and a 90 μm passive DBR section was fabricated. The passive waveguide was formed by a butt-joint built-in (BJB) regrowth process (Fig. 1.18). As a result, a threshold current of 0.25 mA and a front external differential efficiency of 11% were obtained [145]. In 2017, to reduce internal losses, the doping concentration of the *p*-InP side cladding layer was lower than before. A threshold current of 0.21 mA and an external differential quantum efficiency of 32% from the front facet were obtained (Fig. 1.19) [146]. To further improve the differential quantum efficiency, a relatively low index coupling structure (index coupling factor of about 800 cm^{-1}) was adopted to suppress surface scattering losses, and a differential quantum efficiency of 36% and a power conversion efficiency of 14.6% were obtained [147].

1999~2008	**2008~2011**	**2011~2018**	**2018~2023**
Optically pump	**LCI laser on SI-InP**	**LCI laser on Si**	**This study**
First DFB laser (RT-CW) (Dr. Okamoto)	First LCI laser (RT-pulse) (Dr. Okumura)	First LCI laser on Si (Dr. Okumura)	High-temperature operation ★ T_{max} = 120 °C (Dr. Fang)
RT-CW ★ P_{th} = 0.64 mW (Dr. Okamoto)	LCI-FP laser (RT-CW) ★ I_{th} = 11 mA (Dr. Okumura)	High-efficiency membrane DR laser ★ η_d = 36% (Dr. Hiratani)	Ultra-low threshold current membrane DR laser
★ P_{th} = 0.34 mW (Dr. Sakamoto)	LCI-DFB laser (RT-CW) ★ I_{th} = 7.0 mA (Dr. Shindo)	Low threshold current membrane DR laser ★ I_{th} = 0.21 mA (Mr. Tomiyasu)	High-efficiency membrane integrated optical link

Fig. 1.20 The history of research for membrane laser in our lab.

Fig. 1.20 shows the development of research for membrane laser.

My research to be described in following chapter contributes to the low-threshold operation, high-speed direct modulation and integration of membrane optical devices. Since the beginning of my research, direct bonding technology has been established by co-worker Dr. Fang, who reported improved thermal resistance and maximum oscillation temperature. My research contributes to low-threshold operation and high-speed direct modulation integrated optical devices.

1.4.3 Research of membrane lasers in other groups

NTT Device Technology Laboratories has focused on combining low-power lasers and Si photonics to reduce power consumption in data center optical networks. They reported a membrane BH DFB laser on SiO_2/Si substrate in 2014 based on fabrication techniques developed for photonic crystal lasers [148]. Their process involves direct bonding of epitaxial substrates with active layer deposition, followed by laser structure formation [149]. The BH structure is formed by growing undoped InP followed by Zn thermal diffusion and Si ion implantation, respectively, for the p- and n-type doping as shown in Fig. 1.21[150][151]. In 2016, a monolithic integration of a 50 μm long resonator membrane DR laser and a spot size converter consisting of a tapered InP wire waveguide and a SiO_x waveguide on a SiO_2/Si substrate was demonstrated [152]. The device demonstrates direct modulation of 25.8 Gbit/s at a bias current of 2.5 mA and a low energy cost of 132 fJ/bit. Although high optical confinement is advantageous to higher relaxation oscillation frequency, it was limited to ~20 GHz owing to the self-heating effect under increasing bias current, which reduces differential gain. To overcome this heating problem, they proposed a silicon carbide (SiC) substrate for its high thermal conductivity (490 W m^{-1} K^{-1}) and moderate refractive index (~2.6) [153][154], which improve the thermal conductivity while maintaining a large optical confinement [155]. They fabricated a membrane DR laser with a 50-μm-long active region on the SiC substrate (Fig. 1.22) [156] and demonstrated a relaxation oscillation frequency of 42 GHz and 60

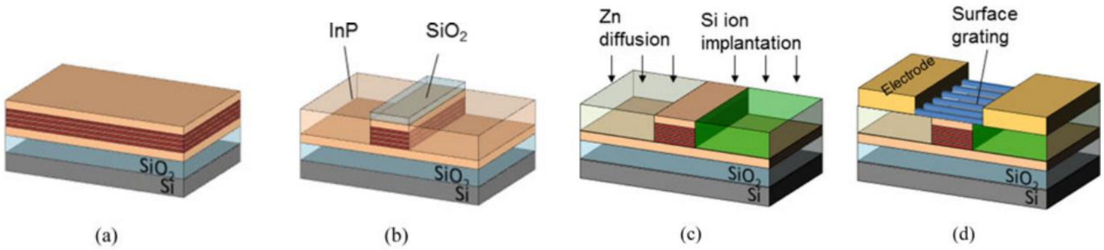

Fig. 1.21 Procedure for fabricating membrane BH DFB laser on SiO_2 /Si substrate [151].

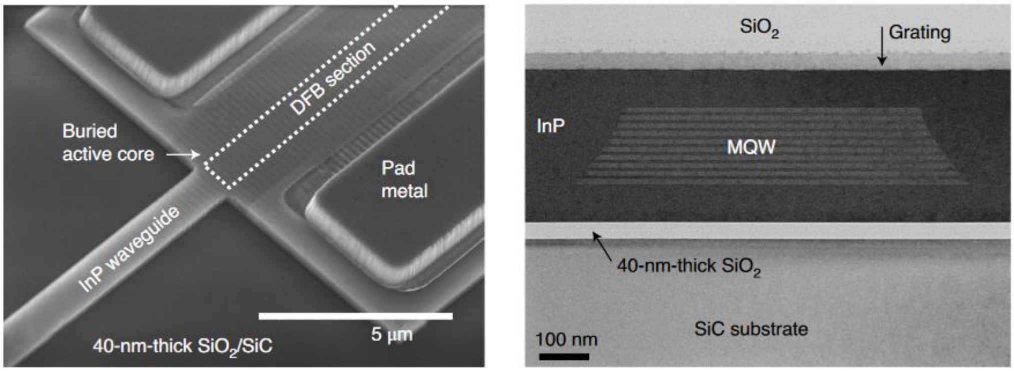

Fig. 1.22 SEM image of the device on SiC substrate [156].

GHz intrinsic 3 dB bandwidth (f_{3dB}). By employing the photon–photon resonance (PPR) at 95 GHz due to optical feedback from an integrated output waveguide, they achieved an f_{3dB} of 108 GHz and demonstrate 256 Gbps four-level pulse-amplitude modulations with energy cost of 475 fJ/bit. Recently, new attempts to combine Si photonics and membrane lasers using micro-transfer printing methods [157]-[161] have been reported. This method allows thin film components (such as lasers) fabricated on a native wafer to be transferred to another wafer by using a soft elastomer stamp. The membrane DR laser integrated with a 220-nm-thick Si waveguide exhibits a low threshold current of 1.2 mA and achieves an E-O bandwidth of over 25 GHz and 50 Gbit/non-return-to-zero (NRZ) signal modulation with a 2.5 dB extinction ratio [162].

1.5 Application dependence of laser performance and design

The performance required of semiconductor lasers varies depending on the application, so the optimum structure should be considered accordingly. The practical application of short-range optical communication requires a significant performance improvement that can cover the installation cost. Energy cost, which is the power required to transmit one bit, is an important indicator and is determined by optical output power and modulation speed. These laser characteristics are related to parameters such as cavity length and optical confinement.

VCSELs are widely used in fiber-based communications, such as data center-to-data center communications, because of their low threshold current and high differential efficiency as shown in Table 1.1. In the case of on-board or on-chip optical interconnection, which is an even shorter distance communication, light is transmitted using waveguides on the board instead of fibers. In such cases, VCSELs face the challenge of coupling to the waveguide with high efficiency. For in-plane emitting lasers, there is a trade-off between structural parameters and characteristics, such as Fig. 1.23.

Shorter cavity lengths improve threshold current and modulation efficiency, but too

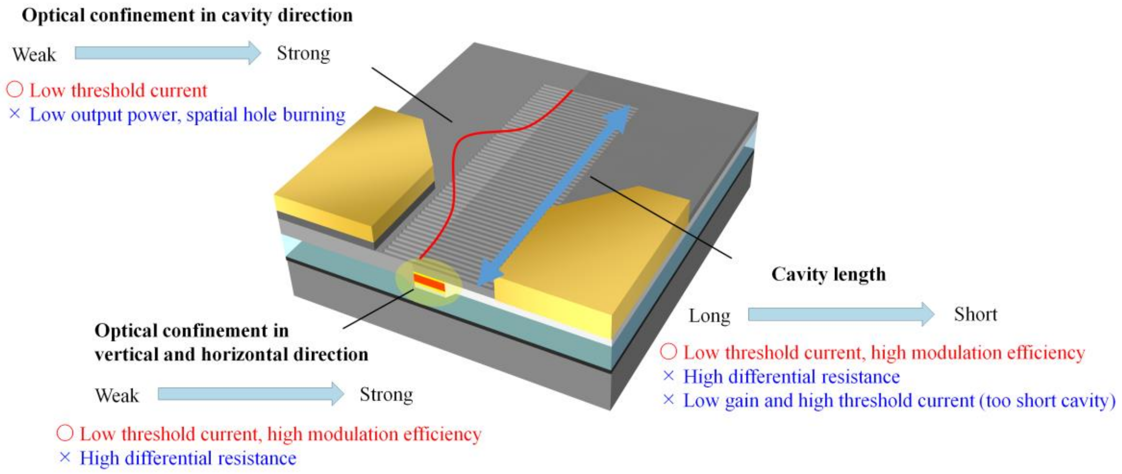

Fig. 1.23 Trade-off between structural parameters and laser characteristics.

Table 1.1 Low power consumption light sources.

Device	Threshold current	Output power	Temperature	Substrate	Ref.
VCSEL	0.15 mA	2.0 mW @6.4 mA	RT	GaAs	[31]
VCSEL	0.5 mA	2.5 mW @5 mA	RT	GaAs	[48]
VCSEL	1.5 mA	1.6 mW @8 mA	RT	InP	[33]
PhC	4.8 µA	8.75 µW @200 µA	RT	Si	[69]
PhC	181 nA	0.65 pW @1 µA	50K	GaAs	[64]
Microring	3.5 mA	0.18 mW @80 mA	RT	InP	[78]
Microring	3.0 mA	0.27 mW @38 mA	RT	GaAs	[79]
Microdisk	0.5 mA	25 µW @1.8 mA	RT	Si	[77]
Microdisk	4.5 mA	86 µW @40 mA	RT	InP	[80]
Plasmon	33.7 mA	0.03 mW @46 mA	78K	GaN	[86]
Plasmon	0.08 mA	-	RT	InP	[92]
Plasmon	0.04 mA	-	78K	InP	[91]
DR	1.0 mA	1.4 mW @10 mA	RT	InP	[113]
Membrane DR	0.9 mA	0.93 mW @14 mA	RT	Si	[151]
Membrane DR	2.8 mA	1.9 µW @30 mA	RT	SiC	[156]
Membrane DR (Previous study)	0.21 mA	0.52 mW @3.2 mA	RT	Si	[146]

short cavity length increases resistance and insufficient gain increases threshold. For optical confinement, higher confinement in the direction perpendicular to the direction of light propagation improves the threshold current and modulation efficiency. Membrane lasers have a structure that can confine light strongly in the vertical direction, while ridge lasers can confine light strongly in the horizontal direction. By increasing optical confinement in both directions, ultra-low threshold and high modulation efficiency are expected. One structure that achieves this is a photonic crystal laser, but its output power is low due to output saturation caused by high differential resistance as shown in Table

1.1. In the direction of light propagation, light can be strongly confined inside the cavity by increasing the refractive index coupling coefficient κ or by introducing phase-shifting gratings, but since this is the output direction of light, the output power is reduced, leading to a decrease in differential quantum efficiency. In addition, too strong confinement causes spatial hole-burning, leading to unstable operation and saturation of output. Thus, the characteristics of semiconductor lasers are intricately related to various structural parameters, and there is a trade-off relationship between them. By comprehensively considering these trade-offs, the relationship between structural parameters and laser characteristics can be clarified, and the ideal semiconductor laser can be determined.

1.6 Objective and outline of this thesis

As mentioned above, the basic characteristics, such as current injection, were already identified, and research on membrane lasers was approaching the stage of improving the threshold current and modulation speed when this study was started. Also, for the membrane optical link, data transmission had been demonstrated, and improving its characteristics was the next objective. According to the research history described above, the remaining challenges for membrane lasers are as follows. When considering data transmission, lowering the threshold current and increasing modulation efficiency are important to reduce overall power consumption, but laser design to achieve these objectives has been insufficient. In addition, when considering optical links, the conventional embedded waveguide lacks versatility in the application of the technology.

Hence, the objectives of this thesis are given as follows:

(1) Investigation of design of membrane laser with suitable optical confinement structure
   - (a) Calculation of membrane laser characteristics for suitable laser design
   - (b) Establishment of fabrication techniques

(2) Realization of low power consumption membrane laser
   - (a) Characterization of static and dynamic properties of membrane DR laser
   - (b) Demonstration of low power consumption membrane optical link

(3) Demonstration of membrane laser deployment in various applications

Fig. 1.24 shows the outline of this thesis. In Chapter 2, the analysis method of semiconductor lasers is explained, and the characteristics of membrane lasers are analytically discussed. The suitable structure for low power consumption and high efficiency operation is proposed. In Chapter 3, fabrication techniques for membrane lasers are discussed. The challenges in introducing the proposed structure are clarified, and an experimental approach to these challenges is presented. In Chapter 4, the membrane DR laser with low-power operation is demonstrated. Chapter 5 will discuss the deployment of membrane lasers in various applications. Demonstrations will be given of challenging approaches such as on-chip optical interconnects and artificial intelligence. Finally, the summary of this thesis will be given in chapter 6.

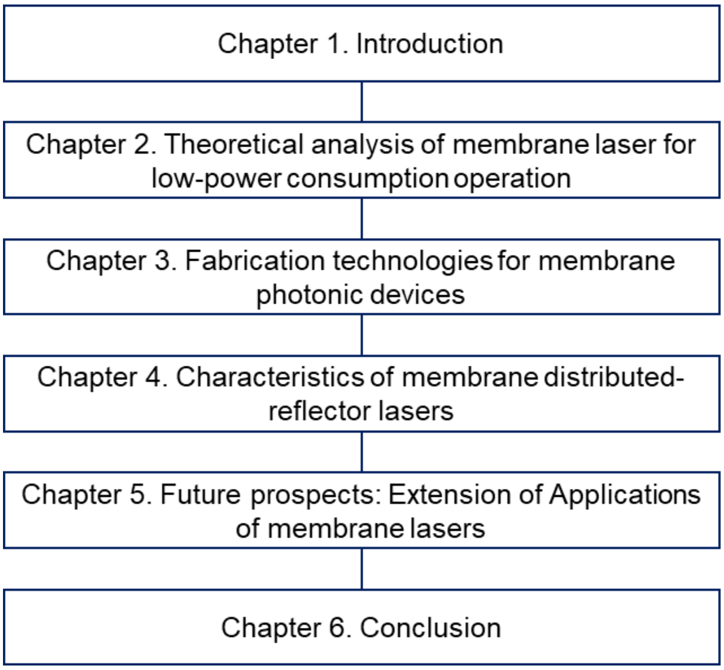

Fig. 1.24 Outline of this thesis.

Reference

[1] J. P. Gordon, H. J. Zeiger, and C. H. Townes, "The Maser—New Type of Microwave Amplifier, Frequency Standard, and Spectrometer," *Physical Review,* vol. 99, no. 4, pp. 1264-1274, 1955.

[2] A. L. Schawlow and C. H. Townes, "Infrared and optical Masers", *Physical Review*, vol. 112, no, 6, 1958.

[3] T. H. Maiman, "Stimulated Optical Radiation in Ruby," *Nature,* vol. 187, no. 4736, pp. 493-494, 1960.

[4] R. N. Hall, G. E. Fenner, J. D. Kingsley, T. J. Soltys, and R. O. Carlson, "Coherent Light Emission from GaAs Junctions," *Physical Review Letters,* vol. 9, no. 9, pp. 366-368, 1962.

[5] M. I. Nathan, W. P. Dumke, G. Burns, F. H. Dill, and G. Lasher, "Stimulated emission of radiation from GaAs p-n junctions," *Applied Physics Letters,* vol. 1, no. 3, pp. 62-64, 1962.

[6] T. M. Quist, R. H. Rediker, R. J. Keyes, W. E. Krag, B. Lax, A. L. McWhorter, and H. J. Zeigler, "Semiconductor maser of GaAs," *Applied Physics Letters,* vol. 1, no. 4, pp. 91-92, 1962.

[7] N. Holonyak and S. F. Bevacqua, "Coherent (visible) light emission from $Ga(As_{1-x}P_x)$ junctions," *Applied Physics Letters,* vol. 1, no. 4, pp. 82-83, 1962.

[8] I. Hayashi, M. Panish, P. Foy, and S. Sumski, "Junction lasers which operate continuously at room temperature," *Applied Physics Letters*, vol. 17, pp. 109-111, 1970.

[9] M. Panish, I. Hayashi, and S. Sumski, "Double-heterostructure injection lasers with room-temperature thresholds as low as 2300 A/cm," *Applied Physics Letters*, vol. 16, p. 326, 1970.

[10] H. Kroemer, "A Proposed Class of Heterojuncton Injection Lasers," *Proceedings of the IEEE*, vol. 51, pp. 1782-1783, 1963.

[11] H. Rupprecht, J. M. Woodall and G. D. Pettit, "Efficient visible electroluminescence at 300°C from $Ga_{1-x}Al_xAs$ p-n junctions grown by liquid-phase epitaxy", *Applied Physics Letters*, vol. 11, no. 3, pp. 81-83, 1967.

[12] I. Hayashi, M. B. Panish and F. K. Reinhart, "GaAs–$Al_xGa_{1-x}As$ Double Heterostructure Injection Lasers", *Journal of Applied Physics*, vol. 42, no. 5, pp. 1929-1941, 1971.

[13] Zh. I. Alferov, V. M. Andreyev, S. G. Konnikov, V. R. Larionov, and G. N. Shelovanova. "Liquid phase epitaxy of $Al_xGa_{1-x}As$-GaAs heterostructures."

Kristall und Technik, vol. 10, no. 2, pp. 103-110, 1975.

[14] F. Kapron, D. B. Keck, and R. D. Maurer, "Radiation losses in glass optical waveguides," *Applied Physics Letters*, vol. 17, pp. 423 425, 1970.

[15] M. Horiguchi and H. Osanai, "Spectral losses of low-OH-content optical fibres," *Electronics Letters*, vol. 12, pp. 310-312, 1976.

[16] T. Miya, Y. Terunuma, T. Hosaka, and T. Miyashita, "Ultimate low-loss single-mode fibre at 1.55 μm," *Electronics Letters*, vol. 15, pp. 106-108, 1979.

[17] K. Oe and K. Sugiyama, "GaInAsP-InP double heterostructure lasers prepared by a new LPE apparatus," *Japanese Journal of Applied Physics*, vol. 15, p. 2003, 1976.

[18] T. Yamamoto, K. Sakai, S. Akiba, and Y. Suematsu, "Fast pulse behaviour of InGaAsP/InP double-heterostructure lasers emitting at 1.27 μm," *Electronics Letters*, vol. 13, pp. 142-143, 1977.

[19] S. Arai, M. Asada, Y. Suematsu and Y. Itaya, "Room Temperature CW Operation of GaInAsP/InP DH Laser Emitting at 1.51 μm", *Japanese Journal of Applied Physics*, vol. 18, no. 12, pp. 2333–2334, 1979.

[20] S. Akiba, K. Sakai, Y. Matsushima, and T. Yamamoto, "Room temperature cw operation of InGaAsP/InP heterostructure lasers emitting at 1.56 μm," *Electronics Letters*, vol. 15, pp. 606-607, 1979.

[21] K. Iga and S. Kinoshita, "Liquid Phase Epitaxy and Growth Technology." *Process Technology for Semiconductor Lasers: Crystal Growth and Microprocesses*, pp. 51-81, 1996.

[22] E. Kuphal, "Liquid phase epitaxy", *Applied Physics A Solids and Surfaces*, vol. 52, no. 6, pp. 380–409, 1991.

[23] H. M. Manasevit and W. I. Simpson, "The Use of Metal-Organics in the Preparation of Semiconductor Materials", *Journal of The Electrochemical Society*, vol. 116, no. 12, p. 1725, 1969.

[24] J. P. Duchemin, M. Bonnet, F. Koelsch and D. Huyghe, "A New Method for Growing GaAs Epilayers by Low Pressure Organometallics", *Journal of The Electrochemical Society*, vol. 126, no. 7, pp. 1134–1142, 1979.

[25] A. Y. Cho and J. R. Arthur, Jr., "Molecular beam epitaxy," *Prog. Solid State Chem.*, vol. 10, pp. 157–192, 1975.

[26] C. T. Foxon and B. A. Joyce, "Interaction kinetics of As_2 and Ga on 100 GaAs surfaces," *Surf. Sci.*, vol. 64, pp. 293–307, 1977.

[27] M. B. Panish, "Heterostructure injection lasers," *Proceedings of the IEEE*, vol. 64, no. 10, pp. 1512-1540, 1976.

[28] M. D. Camras, "Stimulated emission in strained-layer quantum-well heterostructures", *Journal of Applied Physics*, vol. 54, no. 11, pp. 6183–6189, 1983.

[29] D. Ahn and C. S. Lien, "Optical gain in a strained-layer quantum-well laser," *IEEE Journal of Quantum Electronics*, vol. 24, no. 12, pp. 2400-2406, 1988.

[30] H. Li, P. Wolf, P. Moser, G. Larisch, J. A. Lott, D. Bimberg, "Vertical-cavity surface-emitting lasers for optical interconnects," *SPIE Newsroom*, 25, 2014.

[31] E. Simpanen, J. S. Gustavsson, E. Haglund, E. P. Haglund, A. Larsson, W. V. Sorin, S. Mathaiand M. R. Tan, "1060 nm single-mode vertical-cavity surface-emitting laser operating at 50 Gbit/s data rate", *Electronics Letters*, vol. 53, no. 13, pp. 869–871, 2017.

[32] S. Hu, X. Gu, H. R. Ibrahim, M. Nakahama, S. Shinada, F. Koyama, "1060-nm single-mode transverse coupled cavity VCSEL with intra-cavity surface relief for 58-Gbps modulation and 5-km single-mode fiber transmission," *Appl. Phys. Lett.*, vol. 120, no. 26, 27 June 2022.

[33] J. V. Kerrebrouck, X. D. Pang, O. Ozolins, R. Lin, A. Udalcovs, L. Zhang, H. Li, S. Spiga, M. C. Amann, L. Gan, M. Tang, S. Fu, R. Schatz, G. Jacobsen, S. Popov, D. Liu, W. Tong, G. Torfs, J. Bauwelinck, J. Chen, and X. Yin, "High-Speed PAM4-Based Optical SDM Interconnects With Directly Modulated Long-Wavelength VCSEL," *Journal of Lightwave Technology*, vol. 37, no. 2, pp. 356-362, 2019.

[34] H. Soda, K. Iga, C. Kitahara, and Y. Suematsu, "GaInAsP/InP surface emitting injection lasers," *Japanese Journal of Applied Physics,* vol. 18, p. 2329, 1979.

[35] F. Koyama, S. KINOSHITA, and I. Kenichi, "Room temperature cw operation of GaAs vertical cavity surface emitting laser," *IEICE TRANSACTIONS (1976-1990),* vol. 71, pp. 1089-1090, 1988.

[36] J. L. Jewell, Y. H. Lee, S. Walker, A. Scherer, J. P. Harbison, L.T. Florez, S. L. McCall, "Low-threshold electrically pumped vertical-cavity surface-emitting microlasers", *Electronics Letters*, vol. 25, pp. 1123-1124, 1989.

[37] F. Koyama, K. Tomomatsu, and K. Iga, "GaAs surface emitting lasers with circular buried heterostructure grown by metalorganic chemical vapor deposition and two-dimensional laser array," *Applied physics letters*, vol. 52, pp. 528-529, 1988.

[38] Y. Hayashi, T. Mukaihara, N. Hatori, N. Ohnoki, A. Matsutani, F. Koyama, and K. Iga, "Lasing characteristics of low-threshold oxide confinement InGaAs-GaAlAs vertical-cavity surface-emitting lasers," *IEEE Photonics Technology Letters*, vol.

7, pp. 1234-1236, 1995.

[39] K. D. Choquette, K. Lear, R. Schneider, K. Geib, J. Figiel, and R. Hull, "Fabrication and performance of selectively oxidized vertical-cavity lasers," *IEEE Photonics Technology Letters*, vol. 7, pp. 1237-1239, 1995.

[40] D. Huffaker, D. Deppe, C. Lei, and L. Hodge, "Sealing AlAs against oxidative decomposition and its use in device fabrication," *Applied physics letters*, vol. 68, pp. 1948-1950, 1996.

[41] B. Weigl, M. Grabherr, C. Jung, R. Jager, G. Reiner, R. Michalzik, *et al.*, "High-performance oxide-confined GaAs VCSELs," *IEEE Journal of Selected Topics in Quantum Electronics*, vol. 3, pp. 409-415, 1997.

[42] R. Shau, M. Ortsiefer, J. Rosskopf, G. Bohm, F. Kohler, and M. Amann, "Vertical-cavity surface-emitting laser diodes at 1.55 μm with large output power and high operation temperature," *Electronics Letters*, vol. 37, pp. 1295-1296, 2001.

[43] N. Nishiyama, C. Caneau, G. Guryanov, X. Liu, M. Hu, and C. Zah, "High efficiency long wavelength VCSEL on InP grown by MOCVD," *Electronics Letters*, vol. 39, pp. 437-439, 2003.

[44] N. Nishiyama, C. Caneau, B. Hall, G. Guryanov, M. Hu, X. Liu, *et al.*, "Long-wavelength vertical-cavity surface-emitting lasers on InP with lattice matched AlGaInAs–InP DBR grown by MOCVD," *IEEE Journal of Selected Topics in Quantum Electronics*, vol. 11, pp. 990-998, 2005.

[45] K. Takaki, N. Iwai, K. Hiraiwa, S. Imai, H. Shimizu, T. Kageyama, Y. Kawakita, N. Tsukiji and A. Kasukawa., "A recorded 62% PCE and low series and thermal resistance VCSEL with a double intra-cavity structure," *21st International Semiconductor Laser Conference*, PDP1, 2008.

[46] P. Moser, W. Hofmann, P. Wolf, J. Lott, G. Larisch, A. Payusov, *et al.*, "81 fJ/bit energy-to-data ratio of 850 nm vertical-cavity surface-emitting lasers for optical interconnects," *Applied Physics Letters*, vol. 98, p. 231106, 2011.

[47] P. Moser, J. Lott, P. Wolf, G. Larisch, H. Li, N. Ledentsov, *et al.*, "56 fJ dissipated energy per bit of oxide-confined 850 nm VCSELs operating at 25 Gbit/s," *Electronics letters*, vol. 48, pp. 1292-1294, 2012.

[48] Ibrahim, Hameeda R., *et al.* "1060nm Single-mode Metal-aperture VCSEL Array with Transverse Resonance and Low Power Consumption below 50 fJ/bit." *2021 European Conference on Optical Communication (ECOC). IEEE*, 2021.

[49] H. A. Wu, W. N. Fu, D. F. Wu, and M. L. Feng, "2.9 K VCSEL demonstrates 100 Gbps PAM-4 optical data transmission," *Applied Physics Letters,* vol. 121, no. 1, 2022.

[50] E. Yablonovitch “Inhibited Spontaneous Emission in Solid-State Physics and Electronics”, *Phys. Rev. Lett.*, vol. 58, p, 2059, 1987.

[51] S. John, “Strong Localization of Photons in Certain Disordered Dielectric Superlattices”, *Phys. Rev. Lett.* 58, p. 2486, 1987.

[52] E. Yablonovitch, T. Gmitter and K. Leung, “Photonic band structure: The face-centered-cubic case employing nonspherical atoms”, *Physical Review Letters*, vol. 67, no. 17, pp. 2295–2298, 1991.

[53] Y. Akahane, T. Asano, B.-S. Song, and S. Noda, “High-Q photonic nanocavity in a two-dimensional photonic crystal,” *Nature*, vol. 425, pp. 944-947, 2003.

[54] T. Tanabe, M. Notomi, E. Kuramochi, A. Shinya, and H. Taniyama, “Trapping and delaying photons for one nanosecond in an ultrasmall high-Q photonic-crystal nanocavity,” *Nature Photonics*, vol. 1, pp. 49-52, 2006.

[55] M. Notomi, E. Kuramochi, and H. Taniyama, “Ultrahigh-Q nanocavity with 1D photonic gap,” *Optics Express*, vol. 16, pp. 11095-11102, 2008.

[56] E. Kuramochi, H. Taniyama, T. Tanabe, K. Kawasaki, Y.-G. Roh, and M. Notomi, “Ultrahigh-Q one-dimensional photonic crystal nanocavities with modulated mode-gap barriers on SiO_2 claddings and on air claddings,” *Optics Express*, vol. 18, pp. 15859-15869, 2010.

[57] O. Painter, R. Lee, A. Scherer, A. Yariv, J. O'brien, P. Dapkus, *et al.*, “Two-dimensional photonic band-gap defect mode laser,” *Science*, vol. 284, pp. 1819-1821, 1999.

[58] W. Zhou, J. Sabarinathan, B. Kochman, E. Berg, O. Qasaimeh, S. Pang, *et al.*, “Electrically injected single-defect photonic bandgap surface-emitting laser at room temperature,” *Electronics Letters*, vol. 36, pp. 1541-1542, 2000.

[59] W. D. Zhou, J. Sabarinathan, P. Bhattacharya, B. Kochman, E. W. Berg, P.-C. Yu, *et al.*, “Characteristics of a photonic bandgap single defect microcavity electroluminescent device,” *IEEE Journal of Quantum Electronics*, vol. 37, pp. 1153-1160, 2001.

[60] D. Ohnishi, T. Okano, M. Imada, and S. Noda, “Room temperature continuous wave operation of a surface-emitting two-dimensional photonic crystal diode laser,” *Optics Express*, vol. 12, pp. 1562-1568, 2004.

[61] K. Nozaki, S. Kita, and T. Baba, “Room temperature continuous wave operation and controlled spontaneous emission in ultrasmall photonic crystal nanolaser,” *Optics Express*, vol. 15, pp. 7506-7514, 2007.

[62] M. Nomura, N. Kumagai, S. Iwamoto, Y. Ota, and Y. Arakawa, “Photonic crystal nanocavity laser with single quantum dot gain,” *Conference on Lasers and*

Electro-Optics 2009 and 2009 Conference on Quantum electronics and Laser Science Conference CLEO/QELS 2009, pp. 1-2, 2009.

[63] D. Englund, B. Ellis, E. Edwards, T. Sarmiento, J. S. Harris, D. A. Miller, *et al.*, "Electrically controlled modulation in a photonic crystal nanocavity," *Optics Express*, vol. 17, pp. 15409-15419, 2009.

[64] B. Ellis, M. A. Mayer, G. Shambat, T. Sarmiento, J. Harris, E. E. Haller, *et al.*, "Ultralow-threshold electrically pumped quantum-dot photonic-crystal nanocavity laser," *Nature Photonics*, vol. 5, pp. 297-300, 2011.

[65] K. Takeda *et al.*, "Reduction of Cavity Length in λ-Scale Embedded Active-region Photonic Crystal (LEAP) Lasers," *2018 IEEE International Semiconductor Laser Conference (ISLC)*, pp. 1-2, 2018.

[66] S. Matsuo, A. Shinya, T. Kakitsuka, K. Nozaki, T. Segawa, T. Sato, Y. Kawaguchi, and M. Notomi, "High-speed ultracompact buried heterostructure photonic-crystal laser with 13 fJ of energy consumed per bit transmitted," *Nature Photonics*, vol. 4, pp. 648-654, 2010.

[67] S. Matsuo, K. Takeda, T. Sato, M. Notomi, A. Shinya, K. Nozaki, K. Hasebe, and T. Kakitsuka, "10-Gbit/s direct modulation of electrically driven photonic crystal nanocavity laser," *Optical Fiber Communication Conference*, 2012.

[68] S. Matsuo, K. Takeda, T. Sato, M. Notomi, A. Shinya, K. Nozaki, H. Taniyama, K. Hasebe, and T. Kakitsuka, "Room-temperature continuous-wave operation of lateral current injection wavelength-scale embedded active-region photonic-crystal laser," *Optics Express*, vol. 20, pp. 3773-3780, 2012.

[69] K. Takeda, T. Sato, A. Shinya, K. Nozaki, W. Kobayashi, H. Taniyama, M. Notomi, K. Hasebe, T. Kakitsuka, and S. Matsuo, "Few-fJ/bit data transmissions using directly modulated lambda-scale embedded active region photonic-crystal lasers," *Nat. Photonics*, vol. 7, no. 7, pp. 569–575, 2013.

[70] A. Levi, R. Slusher, S. McCall, T. Tanbun-Ek, D. Coblentz, and S. Pearton, "Room temperature operation of microdisc lasers with submilliamp threshold current," *Electronics Letters*, vol. 28, pp. 1010-1012, 1992.

[71] L. Rayleigh, "CXII. The problem of the whispering gallery," *The London, Edinburgh, and Dublin Philosophical Magazine and Journal of Science*, vol. 20, pp. 1001-1004, 1910.

[72] C. Garrett, W. Kaiser, and W. Bond, "Stimulated emission into optical whispering modes of spheres," *Physical Review*, vol. 124, p. 1807, 1961.

[73] S. McCall, A. Levi, R. Slusher, S. Pearton, and R. Logan, "Whispering-gallery mode microdisk lasers," *Applied Physics Letters*, vol. 60, p. 289, 1992.

[74] J. Xavier, S. Vincent, F. Meder and F. Vollmer, "Advances in optoplasmonic sensors - combining optical nano/microcavities and photonic crystals with plasmonic nanostructures and nanoparticles," *Nanophotonics*, vol. 7, pp. 1-38, 2018.

[75] A. Zolotukhina, A, Spiridonov, E. Karchevskii and A. Nosich, "Electromagnetic analysis of optimal pumping of a microdisk laser with a ring electrode," Applied Physics B, vol. 123, pp. 32, 2017.

[76] M. Fujita, R. Ushigome, and T. Baba, "Continuous wave lasing in GaInAsP microdisk injection laser with threshold current of 40 μA," *Electronics Letters*, vol. 36, pp. 790-791, 2000.

[77] J. Van Campenhout, P. Rojo-Romeo, P. Regreny, C. Seassal, D. Van Thourhout, S. Verstuyft, L. Di Cioccio, J.-M. Fedeli, C. Lagahe, and R. Baets, "Electrically pumped InP-based microdisk lasers integrated with a nanophotonic silicon-on-insulator waveguide circuit," *Optics Express*, vol. 15, pp. 6744-6749, 2007.

[78] Y. Wan, D. Jung, C. Shang, N. Collins, I. MacFarlane, J. Norman, M. Dumont, A. C. Gossard, and J. E. Bowers, "Low-threshold continuous-wave operation of electrically pumped 1.55 μm InAs quantum dash microring lasers," *ACS Photonics*, vol. 6, no. 2, pp. 279-285, 2018.

[79] Y. Wan, D. Inoue, D. Jung, J. C. Norman, C. Shang, A. C. Gossard, and J. E. Bowers, "Directly modulated quantum dot lasers on silicon with a milliampere threshold and high temperature stability," *Photon. Res*., vol. 6, pp. 776-781, 2018.

[80] X.-W. Ma, Y.-Z. Huang, L.-X. Zou, B.-W. Liu, H. Long, H.-Z. Weng, Y.-D. Yang, and J.-L. Xiao, "Narrow-linewidth microwave generation using AlGaInAs/InP microdisk lasers subject to optical injection and optoelectronic feedback," *Opt. Express*, vol. 23, no. 16, pp. 20321-20331, 2015.

[81] N. C.-Z. Ning, "Semiconductor nanolasers and the size-energy-efficiency challenge: a review," *Adv. Photonics*, vol. 1, p. 014002, 2019.

[82] P. Berini and I. De Leon, "Surface plasmon–polariton amplifiers and lasers," *Nat. Photonics*, vol. 6, pp. 16–24, 2011.

[83] R.F. Oulton, "Surface plasmon lasers: sources of nanoscopic light," *Mater. Today*, vol. 15, pp. 26–34, 2012.

[84] R.-M. Ma, R.F. Oulton, V.J. Sorger, and X. Zhang, "Plasmon lasers: coherent light source at molecular scales," *Laser Photonics Rev*, vol. 7, pp. 1–21, 2013.

[85] S. Gwo and C.-K. Shih, "Semiconductor plasmonic nanolasers: current status and perspectives," *Rep. Prog. Phys*., vol. 79, p. 086501, 2016.

[86] X. Yang, P. N. Ni, P. T. Jing, *et al*., "Room temperature electrically driven

ultraviolet plasmonic lasers," *Adv. Opt. Mater.*, vol. 0, p. 1801681, 2019.

[87] W. L. Barnes, A. Dereux, and T. W. Ebbesen, "Surface plasmon subwavelength optics," *Nature*, vol. 424, pp. 824–830, 2003.

[88] A. V. Zayats, I. I. Smolyaninov, and A. A. Maradudin, "Nano-optics of surface plasmon polaritons," *Phys. Rep.*, vol. 408, pp. 131–314, 2005.

[89] D. K. Gramotnev and S. I. Bozhevolnyi, "Plasmonics beyond the diffraction limit," *Nat. Photonics*, vol. 4, pp. 83–91, 2010.

[90] Q. Shang, S. Zhang, Z. Liu, *et al.*, "Surface plasmon enhanced strong exciton–photon coupling in hybrid inorganic–organic perovskite nanowires," *Nano Lett.*, vol. 18, pp. 3335–3343, 2018.

[91] M. T. Hill, M. Marell, E. S. P. Leong, *et al.*, "Lasing in metal-insulator-metal sub-wavelength plasmonic waveguides," *Opt. Express*, vol. 17, pp. 11107–11112, 2009.

[92] K. Ding, L. Yin, M. T. Hill, Z. Liu, P. J. van Veldhoven, and C.-Z. Ning, "An electrical injection metallic cavity nanolaser with azimuthal polarization," *Appl. Phys. Lett.*, vol. 102, p. 041110, 2013.

[93] Y. Suematsu, S. Arai, and K. Kishino, “Dynamic single-mode semiconductor lasers with a distributed reflector,” *Journal of Lightwave Technology*, vol. 1, pp. 161-176, 1983.

[94] Y. Suematsu and S. Arai, “Single-mode semiconductor lasers for long-wavelength optical fiber communications and dynamics of semiconductor lasers,” *IEEE Journal of Selected Topics in Quantum Electronics*, vol. 6, pp. 1436-1449, 2000.

[95] H. Kogelnik and C. Shank, “Stimulated emission in a periodic structure,” *Applied Physics Letters*, vol. 18, p. 152, 1971.

[96] H. Kogelnik and C. Shank, “Coupled - wave theory of distributed feedback lasers,” *Journal of Applied Physics*, vol. 43, pp. 2327-2335, 1972.

[97] E. Kapon, A. Hardy, and A. Katzir, “The effect of complex coupling coefficients on distributed feedback lasers,” *IEEE Journal of Quantum Electronics*, vol. 18, pp. 66-71, 1982.

[98] K. Utaka, S. Akiba, K. Sakai, and Y. Matsushima, “Effect of mirror facets on lasing characteristics of distributed feedback InGaAsP/InP laser diodes at 1.5 µm range,” *IEEE Journal of Quantum Electronics*, vol. 20, pp. 236-245, 1984.

[99] K. David, G. Morthier, P. Vankwikelberge, and R. Baets, “Yield analysis of non-AR-coated DFB lasers with combined index and gain coupling,” *Electronics Letters*, vol. 26, pp. 238-239, 1990.

[100] K. David, G. Morthier, P. Vankwikelberge, R. G. Baets, T. Wolf, and B. Borchert,

"Gain-coupled DFB lasers versus index-coupled and phase shifted DFB lasers: A comparison based on spatial hole burning corrected yield," *IEEE Journal of Quantum Electronics*, vol. 27, pp. 1714-1723, 1991.

[101] K. Nakahara, T. Tsuchiya, T. Kitatani, K. Shinoda, T. Taniguchi, T. Kikawa, *et al.*, "40-Gb/s direct modulation with high extinction ratio operation of 1.3-μm InGaAlAs multiquantum well ridge waveguide distributed feedback lasers," *IEEE Photonics Technology Letters*, vol. 19, pp. 1436-1438, 2007.

[102] M. Allovon and M. Quillec, "Interest in AlGaInAs on InP for optoelectronic applications," *IEEE Proceedings J - Optoelectronics*, pp. 148-152, 1992.

[103] J. Yong, J. M. Rorison, and I. H. White, "1.3-μm quantum-well InGaAsP, AlGaInAs, and InGaAsN laser material gain: a theoretical study," *IEEE Journal of Quantum Electronics*, vol. 38, pp. 1553-1564, 2002.

[104] W. Kobayashi, T. Yamanaka, M. Arai, N. Fujiwara, T. Fujisawa, K. Tsuzuki, T. Ito, T. Tadokoro, and F. Kano, "Wide Temperature Range Operation of a 1.55- μ m 40-Gb/s Electroabsorption Modulator Integrated DFB Laser for Very Short-Reach Applications," *IEEE Photonics Technology Letters*, vol. 21, no. 18, pp. 1317-1319, 2009.

[105] N. Nunoya, M. Nakamura, H. Yasumoto, S. Tamura, and S. Arai, "Low Threshold GaInAsP/InP Distributed Feedback Lasers with Periodic Wire Active Regions Fabricated by CH4/H2 Reactive Ion Etching," *Japanese Journal of Applied Physics*, vol. 38, pp. L1323-L1326, 1999.

[106] N. Nunoya, H. Yasumoto, H. Midorikawa, S. Tamura, and S. Arai, "Low threshold current density operation of GaInAsP/InP lasers with strain-compensated multiple-layered wirelike active regions," *Japanese Journal of Applied Physics*, vol. 39, pp. 1042-1045, 2000.

[107] N. Nunoya, M. Nakamura, H. Yasumoto, S. Tamura, and S. Arai, "GaInAsP/InP multiple-layered quantum-wire lasers fabricated by CH4/H2 reactive-ion etching," *Japanese Journal of Applied Physics*, vol. 39, pp. 3410-3415, 2000.

[108] N. Nunoya, M. Nakamura, H. Yasumoto, M. Morshed, K. Fukuda, S. Tamura, and S. Arai, "Sub-milliampere operation of 1.55 μm wavelength high index-coupled buried heterostructure distributed feedback lasers," *Electronics Letters*, vol. 36, pp. 1213-1214, 2000.

[109] K. Komori, A. Shigehisa, Y. Suematsu, and I. ARIMA, "Proposal of distributed reflector (DR) structure for high efficiency dynamic single mode (DSM) lasers," *IEICE Transactions (1976-1990)*, vol. 71, pp. 318-320, 1988.

[110] K. Komori, S. Arai, Y. Suematsu, I. Arima, and M. Aoki, "Single-mode

properties of distributed-reflector lasers," *IEEE Journal of Quantum Electronics*, vol. 25, pp. 1235-1244, 1989.

[111] T. Shindo, S. Lee, D. Takahashi, N. Tajima, N. Nishiyama, and S. Arai, "Low-threshold and high-efficiency operation of distributed reflector laser with wirelike active regions," *IEEE Photonics Technology Letters*, vol. 21, pp. 1414-1416, 2009.

[112] S. Lee, D. Takahashi, T. Shindo, K. Shinno, T. Amemiya, N. Nishiyama, and S. Arai, "Low-Power-Consumption High-Eye-Margin 10-Gb/s Operation by GaInAsP/InP Distributed Reflector Lasers with Wirelike Active Regions," *IEEE Photonics Technology Letters*, vol. 23, pp. 1349-1351, 2011.

[113] D. Takahashi, S. Lee, M. Shirao, T. Shindo, K. Shinno, T. Amemiya, N. Nishiyama, and S. Arai, "Carrier-Transport-Limited Modulation Bandwidth in Distributed Reflector Lasers with Wirelike Active Regions," *IEEE Journal of Quantum Electronics*, vol. 48, pp. 688-695, 2012.

[114] K. Oe, Y. Noguchi, and C. Caneau, "GaInAsP lateral current injection lasers on semi-insulating substrates," *Photonics Technology Letters*, IEEE, vol. 6, pp. 479-481, 1994

[115] T. Aihara, T. Hiraki, K. Takeda, T. Fujii, T. Kakitsuka, T. Tsuchizawa, and S. Matsuo "Membrane buried-heterostructure DFB laser with an optically coupled III-V/Si waveguide", *Optics Express*, vol. 27, no. 25, p. 36438, 2019.

[116] T. Okumura, T. Koguchi, H. Ito, N. Nishiyama, and S. Arai, "Injection-type GaInAsP/InP membrane buried heterostructure distributed feedback laser with wirelike active regions," *Applied Physics Express*, vol. 4, pp. 042101-1, 2011.

[117] D. Inoue, T. Hiratani, Y. Atsuji, T. Tomiyasu, T. Amemiya, N. Nishiyama, and S. Arai, "Monolithic integration of membrane-based butt-jointed built-in DFB lasers and p-i-n photodiodes bonded on Si substrate," *IEEE J. Sel. Top. Quantum Electron.*, vol. 21, pp. 1–7, 2015.

[118] S. Matsuo, K. Takeda, T. Sato, M. Notomi, A. Shinya, K. Nozaki, H. Taniyama, K. Hasebe, and T. Kakitsuka, "Room-temperature continuous-wave operation of lateral current injection wavelength-scale embedded active-region photonic-crystal laser," *Opt. Express*, vol. 20, pp. 3773–3780, 2012.

[119] H. C. C. Jr and E. Buehler, "Evidence for low surface recombination velocity on n-type InP," *Appl. Phys. Lett.*, vol. 30, pp. 247–249, 1977.

[120] S. Sakai, M. Umeno, and Y. Amemiya, "Measurement of diffusion coefficient and surface recombination velocity for P-InGaAsP grown on InP," *Japan. J. Appl. Phys.*, vol. 19, pp. 109–113, 1980.

[121] T. Okumura, D. Kondo, H. Ito, S. Lee, T. Amemiya, N. Nishiyama, S. Arai,

"Lateral Junction Waveguide-Type Photodiode Grown on Semi-Insulating InP Substrate," Japanese Journal of Applied Physics, vol. 50, no. 2, pp. 020206-1-020206-3, 2011.

[122] T. Okamoto, N. Nunoya, Y. Onodera, S. Tamura, and S. Arai, "Continuous wave operation of optically pumped membrane DFB laser," *Electronics Letters*, vol. 37, pp. 1455-1457, 2001.

[123] T. Okamoto, N. Nunoya, Y. Onodera, S. Tamura, and S. Arai, "Low-threshold single mode operation of membrane BH-DFB lasers," *Electronics Letters*, vol. 38, pp. 1444-1446, 2002.

[124] T. Okamoto, N. Nunoya, Y. Onodera, S. Tamura, and S. Arai, "Single-mode operation of optically pumped membrane buried heterostructure distributed-feedback lasers," *Jpn. J. Appl. Phys*., vol. 41, p. L249, 2002.

[125] T. Okamoto, T. Yamazaki, S. Sakamoto, S. Tamura, and S. Arai, "Low-threshold membrane BH-DFB laser arrays with precisely controlled wavelength over a wide range," *IEEE Photonics Technology Letters*, vol. 16, pp. 1242-1244, 2004.

[126] T. Okamoto, N. Nunoya, Y. Onodera, T. Yamazaki, S. Tamura, and S. Arai, "Optically pumped membrane BH-DFB lasers for low-threshold and single-mode operation," *IEEE J. Sel. Top. Quantum. Electron.*, vol. 9, pp. 1361-1366, 2003.

[127] S. Sakamoto, T. Okamoto, T. Yamazaki, S. Tamura, and S. Arai, "Multiple-wavelength membrane BH-DFB laser arrays," *IEEE J. Sel. Top. Quantum. Electron.*, vol. 11, pp. 1174-1179, 2005.

[128] S. Sakamoto, H. Naitoh, M. Ohtake, Y. Nishimoto, S. Tamura, T. Maruyama, *et al*., "Strongly index-coupled membrane BH-DFB lasers with surface corrugation grating," *IEEE J. Sel. Top. Quantum. Electron.*, vol. 13, pp. 1135-1141, 2007.

[129] T. Okumura, T. Maruyama, H. Yonezawa, N. Nishiyama, and S. Arai, "Injection-type GaInAsP–InP–Si distributed-feedback laser directly bonded on silicon-on-insulator substrate," *IEEE Photonics Technology Letters*, vol. 21, pp. 283-285, 2009.

[130] T. Okumura, M. Kurokawa, M. Shirao, D. Kondo, H. Ito, N. Nishiyama, *et al*., "Lateral current injection GaInAsP/InP laser on semi-insulating substrate for membrane-based photonic circuits," *Optics Express*, vol. 17, pp. 12564-12570, 2009.

[131] T. Okumura, H. Ito, D. Kondo, N. Nishiyama, and S. Arai, "Continuous wave operation of thin film lateral current injection lasers grown on semi-insulating InP substrate," *Jpn. J. Appl. Phys*., vol. 49, p. 0205, 2010.

[132] T. Shindo, T. Okumura, H. Ito, T. Koguchi, D. Takahashi, Y. Atsumi, *et al*.,

"GaInAsP/InP lateral-current-injection distributed feedback laser with a-Si surface grating," *Optics Express*, vol. 19, pp. 1884-1891, 2011.

[133] T. Shindo, T. Okumura, H. Ito, T. Koguchi, D. Takahashi, Y. Atsumi, *et al.*, "Lateral-current-injection distributed feedback laser with surface grating structure," *IEEE J. Sel. Top. Quantum. Electron.*, vol. 17, pp. 1175-1182, 2011.

[134] T. Shindo, T. Okumura, M. Futami, R. Osabe, H. Ito, T. Koguchi, T. Amemiya, N. Nishiyama, and S. Arai, "Lateral current injection distributed feedback laser with wirelike active regions," *Compound Semiconductor Week (CSW/IPRM), 2011 and 23rd International Conference on Indium Phosphide and Related Materials*, pp. 1-4, 2011.

[135] M. Futami, T. Shindo, T. Koguchi, K. Shinno, T. Amemiya, N. Nishiyama, and S. Arai, "GaInAsP/InP Lateral Current Injection Laser with Uniformly Distributed Quantum-Well Structure," *IEEE Photonics Technology Letters*, vol. 24, pp. 888-890, 2012.

[136] M. Futami, K. Shinno, T. Shindo, T. Amemiya, N. Nishiyama, and S. Arai, "Improved quantum efficiency of GaInAsP/InP top air-clad lateral current injection lasers," *IEEE Optical Interconnects Conference*, pp. 34-35, 2012.

[137] T. Okumura, T. Koguchi, H. Ito, N. Nishiyama, and S. Arai, "Injection-type GaInAsP/InP membrane buried heterostructure distributed feedback laser with wirelike active regions," *Applied Physics Express*, vol. 4, pp. 042101-1, 2011.

[138] T. Shindo, M. Futami, T. Okumura, R. Osabe, T. Koguchi, T. Amemiya, *et al.*, "Lasing operation of lateral-current-injection membrane DFB laser with surface grating," *16th Opto-Electronics and Communications Conference*, 2011.

[139] T. Shindo, M. Futami, T. Okumura, R. Osabe, T. Koguchi, T. Amemiya, *et al.*, "Lateral-Current-Injection Type Membrane DFB Laser with Surface Grating," *IEEE Photonics Technology Letters*, vol. 25, 2013.

[140] M. Futami, T. Shindo, K. Doi, T. Amemiya, N. Nobuhiko, and A. Shigehisa, "Low-threshold operation of LCI-membrane-DFB lasers with Be-doped GAInAs contact layer," *presented at the The 24th International Conference on Indium Phosphide and Related Materials (IPRM2012)*, Santa Barbara, CA, USA, 2012.

[141] T. Shindo, M. Futami, K. Doi, T. Amemiya, N. Nishiyama, and S. Arai, "Design of Lateral-Current-Injection-Type Membrane Distributed-Feedback Lasers for On-Chip Optical Interconnections," *IEEE J. Sel. Top. Quantum. Electron.*, vol. 19, p. 1502009, 2013.

[142] K. Doi, T. Shindo, J. Lee, T. Amemiya, N. Nishiyama, and S. Arai, "Thermal analysis of lateral-current-injection membrane distributed feedback laser," *IEEE*

J. Quantum Electron., vol. 50, pp. 321-326, 2014.
[143] K. Doi, T. Shindo, M. Futami, J. Lee, T. Hiratani, D. Inoue, S. Yang, T. Amemiya, N. Nishiyama, and S. Arai, "Room-temperature continuous-wave operation of lateral current injection membrane laser," presented at the The 25th International Conference on Indium Phosphide and Related Materials (IPRM2013), Kobe, Japan, 2013.
[144] D. Inoue, J. Lee, K. Doi, T. Hiratani, Y. Atsuji, T. Amemiya, N. Nishiyama, and S. Arai, "Room-temperature continuous-wave operation of GaInAsP/InP lateral-current-injection membrane laser bonded on Si substrate," Applied Physics Express, vol. 7, p. 072701, 2014.
[145] T. Hiratani, D. Inoue, T. Tomiyasu, Y. Atsumi, K. Fukuda. T. Amemiya, N. Nishiyama and S. Arai, "Room-temperature continuous-wave operation of membrane distributed-reflector laser," *Appl. Phys. Express*, vol. 8, no. 112701, pp. 1–4, 2015.
[146] T. Tomiyasu, T. Hiratani, D. Inoue, N. Nakamura, K, Fukuda, T. Uryu, T. Amemiya N. Nishiyama and S. Arai, "High-differential quantum efficiency operation of GaInAsP/InP membrane distributed-reflector laser on Si", *Appl. Phys. Express*, vol. 10. p. 062702. 2017.
[147] T. Hiratani, D. Inoue, T. Tomiyasu, K, Fukuda, N. Nakamura, T. Amemiya, N. Nishiyama and S. Arai, "High Efficiency Operation of GaInAsP/InP Membrane Distributed-Reflector Laser on Si," *Appl. Phys. Express*, vol. 10, p. 62701, 2017.
[148] S. Matsuo, T. Fujii, K. Hasebe, K. Takeda, T.Sato, and T. Kakitsuka, "Directly modulated buried heterostructure DFB laser on SiO_2/Si substrate fabricated by regrowth of InP using bonded active layer", *Optics Express*, vol. 22, pp. 12139-12147, 2014.
[149] T. Fujii, T. Sato, K. Takeda, K. Hasebe, T. Kakitsuka and S. Matsuo, "InGaAsP/InP buried heterostruture on SiO_2/Si substrate using epitaxial growth after direct bonding of thin active layer," *26th International Conference on Indium Phosphide and Related Materials (IPRM)*, pp. 1-2, 2014.
[150] K. Takeda, S. Matsuo, T. Fujii, K. Hasebe, T. Sato, and T. Kakitsuka, "Epitaxial growth of InP to bury directly bonded thin active layer on SiO2/Si substrate for fabricating distributed feedback lasers on silicon," *IET Optoelectron.*, vol. 9, no. 4, pp. 151–157, 2015.
[151] S. Matsuo, T. Fujii, K. Hasebe, K. Takeda, T. Sato, and T. Kakitsuka, "Directly modulated DFB laser on SiO_2/Si substrate for datacenter networks," *J. Lightwave Technol.*, vol. 33, pp. 1217-1222, 2015.

[152] H. Nishi, T. Fujii, K. Takeda, K. Hasebe, T. Kakitsuka, T. Tsuchizawa, T. Yamamoto, K. Yamada, and S. Matsuo, "Membrane distributed-reflector laser integrated with SiOx-based spot-size converter on Si substrate," *Opt. Express*, vol. 24, pp. 18346-18352, 2016.

[153] T. Kimoto and J. A. Cooper, "Fundamentals of Silicon Carbide Technology," *River*, 2018.

[154] C. Xu, S. Wang, G. Wang, J. Liang, S. Wang, L. Bai, J. Yang, and X. Chen, "Temperature dependence of refractive indices for 4H- and 6H-SiC," *J. Appl. Phys*., vol. 115, no. 11, p. 113501, 2014.

[155] S. Yamaoka, R. Nakao, T. Fujii, K. Takeda, T. Hiraki, H. Nishi, T. Kakitsuka, T. Tsuchizawa, and S. Matsuo, "High-Temperature Continuous-Wave Operation of Membrane Distributed Reflector Lasers on SiC", *CLEO 2019*, pp. 1-2, 2019.

[156] S. Yamaoka, N.-P. Diamantopoulos, H. Nishi, R. Nakao, T. Fujii, K. Takeda, T. Hiraki, T. Tsurugaya, S. Kanazawa, H. Tanobe, T. Kakitsuka, T. Tsuchizawa, F. Koyama, and S. Matsuo, "Directly modulated membrane lasers with 108 GHz bandwidth on a high-thermal-conductivity silicon carbide substrate", *Nature Photonics*, vol. 15, no. 1, pp. 28-35, 2021.

[157] B. Corbett, R. Loi, W. Zhou, D. Liu, and Z. Ma, "Transfer print techniques for heterogeneous integration of photonic components," *Prog. Quantum Electron*., vol. 52, pp. 1–17, 2017.

[158] Z. Wang, A. Abbasi, U. Dave, A. De Groote, S. Kumari, B. Kunert, C. Merckling, M. Pantouvaki, Y. Shi, B. Tian, K. Van Gasse, J. Verbist, R. Wang, W. Xie, J. Zhang, Y. Zhu, J. Bauwelinck, X. Yin, Z. Hens, J. Van Campenhout, B. Kuyken, R. Baets, G. Morthier, D. Van Thourhout, and G. Roelkens, "Novel light source integration approaches for silicon photonics," *Laser Photon. Rev.*, vol. 11, 2017, Art. no. 1700063.

[159] H. Yang, D. Zhao, S. Chuwongin, J.-H. Seo, W. Yang, Y. Shuai, J. Berggren, M. Hammar, Z. Ma and W. Zhou, "Transfer-printed stacked nanomembrane lasers on silicon," *Nature Photon*., vol. 6, no. 9, pp. 615–622, 2012.

[160] J. Justice, C. Bower, M. Meitl, M. B. Mooney, M. A. Gubbins, and B. Corbett, "Wafer-scale integration of group III–V lasers on silicon using transfer printing of epitaxial layers," *Nature Photon*., vol. 6, pp. 610–614, 2012.

[161] A. De Groote, P. Cardile, A. Z. Subramanian, A. M. Fecioru, C. Bower, D. Delbeke, R. Baets, and G. Roelkens, "Transfer-printing-based integration of single-mode waveguide-coupled III-V-on-silicon broadband light emitters," *Opt. Exp*., vol. 24, no. 13, pp. 13754–13762, 2016.

[162] Y. Maeda, T. Aihara, T. Fujii, T. Hiraki, K. Takeda, T. Tsuchizawa, H. Sugiyama, T. Sato, T. Segawa, Y. Ota, S. Iwamoto, Y. Arakawa, and S. Matsuo, "Micro-Transfer-Printed Membrane Distributed Reflector Lasers on Si Waveguide Modulated With 50-Gbit/s NRZ Signal," *Journal of Lightwave Technology*, vol. 41, no. 12, pp. 3866-3873, June 15, 2023.

Chapter 2

Theoretical analysis of membrane laser for low-power consumption operation

2.1 Introduction 44

2.2 Basic theory of semiconductor lasers 45

2.2.1 Threshold current and external differential quantum efficiency 45

2.2.2 Transfer matrix method (TMM) 48

2.2.3 Frequency response 53

2.3 Analysis of optical confinement structure for lateral direction 57

2.3.1 Internal loss and differential resistance 57

2.3.2 Design of buried-ridge-waveguide (BRW) structure 60

2.4 Analysis for optical confinement structure for cavity direction 66

2.4.1 Carrier density analysis 66

2.4.2 Design of asymmetric corrugation-pitch-modulation (ACPM) grating 67

2.5 Estimation of consumption power 74

2.6 Conclusion 82

Reference 84

2.1 Introduction

Semiconductor membrane lasers have a structure that can improve laser performance by increasing the refractive index difference in the vertical direction and increasing optical confinement. The optical confinement factor is an important component in fundamental laser characteristics such as threshold current and modulation efficiency. In this chapter, the methods for analyzing these laser characteristics are reviewed, and optimal device structures are discussed from the viewpoint of optical confinement.

Membrane lasers have high optical confinement in the vertical direction, and horizontal and resonance axis directions will also be considered. Although higher optical confinement leads to lower threshold and higher modulation efficiency, there are concerns about reduction of optical output power and spatial hole-burning. Based on theoretical analysis, the optimal structure is investigated.

2.2 Basic theory of semiconductor lasers

2.2.1 Threshold current and external differential quantum efficiency

First, fundamental characteristics of semiconductor lasers, such as threshold current and optical output efficiency, are derived from the rate equations. The rate equations for carrier density and photon density can be written as

$$\frac{dN}{dt} = \frac{\eta_i I}{qV_a} - (R_{sp} + R_{nr}) - R_{st} \tag{2.1}$$

$$\frac{dS}{dt} = \xi R_{st} + \xi \beta_{sp} R_{sp} - \frac{S}{\tau_p}, \tag{2.2}$$

where, N is the carrier density, S is the photon density, I is the injection current, η_i is the internal quantum efficiency, V_a is the active volume, R_{sp} is the spontaneous emission rate, R_{nr} is the nonradiative recombination rate, R_{st} is the net stimulated emission rate, ξ is the optical confinement factor, β_{sp} is the spontaneous emission factor, and τ_p is the photon life time. The recombination terms unrelated to the stimulated emission can be expressed as follows

$$R_{sp} + R_{nr} \approx AN + BN^2 + CN^3 = \frac{N}{\tau}, \tag{2.3}$$

where A is the non-radiative recombination coefficient, B is the spontaneous emission coefficient, C is the auger recombination coefficient and τ is the carrier lifetime. In

GaInAsP-based strain-compensated lasers, $B = 1.6 \times 10^{-10}$ cm^3/s and $C = 5.0 \times 10^{-29}$ cm^6/s have been reported [1][2]. Defining the material gain of the active layer as g, the increase in photon density ΔS when a small interval Δz is advanced can be expressed as follows,

$$S + \Delta S = S\exp(1 + g\Delta z) \approx S + gS\Delta z\,. \tag{2.4}$$

Therefore, the recombination rate R_{st} of the stimulated emission light using the group velocity v_g can be written as

$$R_{st} = v_g gS\,. \tag{2.5}$$

The photon density τ_p is the average time that a single photon is confined in the cavity, and its reciprocal $1/\tau_p$ is expressed using the threshold gain g_{th} by

$$\frac{1}{\tau_p} = \xi v_g g_{th}\,. \tag{2.6}$$

Thus, we can now rewrite the carrier and photon density rate equations for values in the active region,

$$\frac{dN}{dt} = \frac{\eta_i I}{qV_a} - (AN + BN^2 + CN^3) - v_g gS \tag{2.7}$$

$$\frac{dS}{dt} = \xi v_g gS + \xi\beta_{sp}(AN + BN^2 + CN^3) - \xi v_g g_{th} S\,. \tag{2.8}$$

By solving the simultaneous equations (2.7) and (2.8) as a steady state, the carrier density and photon density for any given injection current can be obtained. The threshold current can then be obtained by looking at the rise of the photon density with injection current on the horizontal axis. Here, to obtain the threshold current in a simplified way, we will transform the rate equation for the carrier density using an approximation. The recombination rate that does not contribute to induced emission is approximated by

$$R_{sp} + R_{nr} \approx AN + BN^2 + CN^3 \approx B_{eff}N^2\,, \tag{2.9}$$

where B_{eff} represents the effective recombination rate. Solving equation (2.7) for the steady state with $S = 0$ below the threshold, I_{th} is given by

$$I_{\mathrm{th}} = \frac{qV_{\mathrm{a}}}{\eta_{\mathrm{i}}} B_{\mathrm{eff}} N_{\mathrm{th}}^{2}\,. \tag{2.10}$$

Various approximations have been proposed for the relationship between carrier density and gain, and when approximated in logarithmic form, N_{th} can be expressed using the gain coefficient, g_0, by

$$N_{\mathrm{th}} = N_{\mathrm{tr}} \exp\left(\frac{g_{\mathrm{th}}}{g_0}\right). \tag{2.11}$$

In this approximation, N_{tr} is the transparency carrier density and the differential gain, $\partial g/\partial N \equiv g'$, is given by

$$\frac{\partial g}{\partial N} = g' = \frac{g_0}{N}. \tag{2.12}$$

The value for differential gain g' is determined by the slope of the tangent to the gain curve at the threshold point. From this, equation (2.10) can be rewritten as

$$I_{\mathrm{th}} = \frac{qV_{\mathrm{a}}}{\eta_{\mathrm{i}}} B_{\mathrm{eff}} N_{\mathrm{tr}}^{2} \exp\left(\frac{2g_{\mathrm{th}}}{g_0}\right). \tag{2.13}$$

From eq. (2.13) we can now calculate a steady-state photon density above threshold where $g = g_{\mathrm{th}}$, that is

$$S = \frac{\eta_{\mathrm{i}}(I - I_{\mathrm{th}})}{q v_{\mathrm{g}} g_{\mathrm{th}} V_{\mathrm{a}}}. \tag{2.14}$$

To obtain the power out, first calculate the light energy stored in the cavity, expressed by multiplication of photon energy and photon number. Then multiply this by the energy loss rate of the mirror, $v_{\mathrm{g}}\alpha_{\mathrm{m}} = 1/\tau_{\mathrm{m}}$, to obtain the optical power output from the mirror,

$$P_{\mathrm{o}} = v_{\mathrm{g}} a_{\mathrm{m}} h\nu S V_{\mathrm{a}}\,. \tag{2.15}$$

Substituting from Eq.(2.14),

$$P_\mathrm{o} = \eta_\mathrm{i}\left(\frac{a_\mathrm{m}}{a_\mathrm{i}+a_\mathrm{m}}\right)\frac{hv}{q}(I-I_\mathrm{th}) = \eta_\mathrm{d}\frac{hv}{q}(I-I_\mathrm{th})\,. \tag{2.16}$$

This shows that η_d is the differential quantum efficiency, defined as the number of photons out per electron in from a measured *P–I* characteristic. To calculate the threshold current and external differential quantum efficiency of DFB lasers, the coupled wave theory or the transfer matrix method is used to calculate the mirror loss and threshold gain. The transfer matrix method will be described in section 2.4.1.

2.2.2 Transfer matrix method

There are two main methods for analyzing periodic refractive index structures such as DFB lasers. One is the coupled wave theory (CWT) [19][20] and the other is the transfer matrix method (TMM) [21]-[24]. The CWT method involves expressing the index and gain perturbation using a cosine function. This is done under the assumption of small index and gain changes. Additionally, the grating section is represented as a single matrix to simplify calculations and save time. However, this method cannot be applicable when dealing with membrane lasers due to their large refractive index contrast. The index coupling coefficient in membrane lasers is notably higher (more than 10 times) compared to conventional DFB lasers. In order to introduce the exact index structure to the analysis, TMM is useful. The TMM is a method of expressing reflections and transmissions in each region of a diffraction grating as a matrix and multiplying them by the total matrix. In this

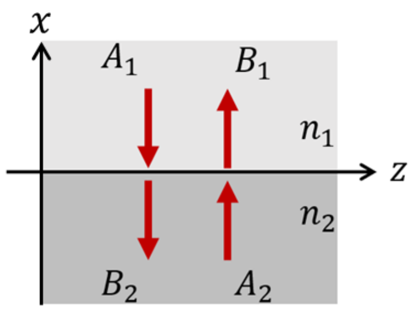

Fig. 2.1 Transfer matrix at the boundary.

study, the TMM was used to analyze the refractive index as if it were distributed along the resonance axis in accordance with the distribution of carrier density. First, the transfer matrices at the boundaries of the regions with different refractive indexes as shown in Fig. 2.1 are considered. The y-axis components of the electric field intensity at the boundary, E_{1y} and E_{2y} are expressed as follows,

$$E_{1y} = (A_1 \exp(-jk_{1x}x) + B_1 \exp(jk_{1x}x)) \exp(jk_{1z}z) \tag{2.17}$$

$$E_{2y} = (A_2 \exp(-jk_{2x}x) + B_1 \exp(jk_{2x}x)) \exp(jk_{2z}z)\,. \tag{2.18}$$

Here, since the boundary conditions E_y and H_z are continuous at $x = 0$, we obtain the following equation,

$$A_1 + B_1 = A_2 + B_2 \tag{2.19}$$

$$\frac{k_{1x}}{\omega\mu_1}(A_1 - B_1) = \frac{k_{2x}}{\omega\mu_2}(A_2 - B_2)\,. \tag{2.20}$$

In the model in Fig. 2.1, $\theta_i = 0$, $\mu_1 = \mu_2$, and using the relation $k_i = k_0 n_i$, the following equations can be obtained from the simultaneous equations (2.19) and (2.20),

$$\begin{cases} A_2 = \dfrac{n_2 + n_1}{2\sqrt{n_1 n_2}} A_1 + \dfrac{n_2 - n_1}{2\sqrt{n_1 n_2}} B_1 \\ B_2 = \dfrac{n_2 - n_1}{2\sqrt{n_1 n_2}} A_1 + \dfrac{n_2 + n_1}{2\sqrt{n_1 n_2}} B_1 \end{cases} \tag{2.21}$$

Thus, the transfer matrix at the boundary is as follows,

$$\begin{bmatrix} A_2 \\ B_2 \end{bmatrix} = \frac{1}{2\sqrt{n_1 n_2}} \begin{bmatrix} n_2 + n_1 & n_2 - n_1 \\ n_2 - n_1 & n_2 + n_1 \end{bmatrix} \begin{bmatrix} A_1 \\ B_1 \end{bmatrix} \tag{2.22}$$

Using the above equations, the transfer matrix of the grating structure model shown in Fig. 2.2 can be expressed as follows,

$$\mathbf{M_m} = \begin{bmatrix} \exp(-j\beta_m l_m) & 0 \\ 0 & \exp(j\beta_m l_m) \end{bmatrix} \tag{2.23}$$

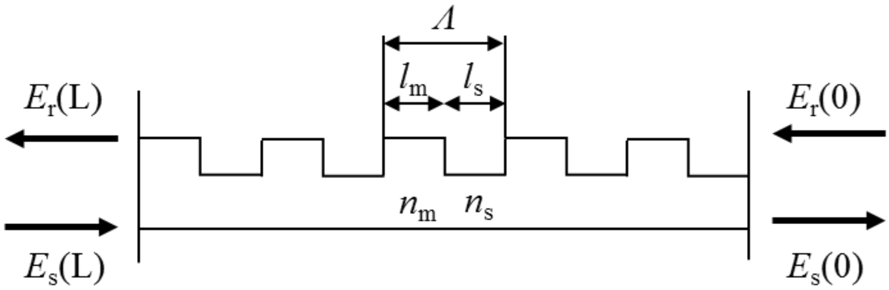

Fig. 2.2 TMM calculation model of the grating structure.

$$\mathbf{M_{ms}} = \frac{1}{2\sqrt{n_m n_s}} \begin{bmatrix} n_s + n_m & n_s - n_m \\ n_s - n_m & n_s + n_m \end{bmatrix} \tag{2.24}$$

$$\mathbf{M_s} = \begin{bmatrix} \exp(-j\beta_s l_s) & 0 \\ 0 & \exp(j\beta_s l_s) \end{bmatrix} \tag{2.25}$$

$$\mathbf{M_{sm}} = \frac{1}{2\sqrt{n_m n_s}} \begin{bmatrix} n_m + n_s & n_m - n_s \\ n_m - n_s & n_m + n_s \end{bmatrix}, \tag{2.26}$$

where the region with large equivalent refractive index n_{eq} is the m-region and the region with small equivalent refractive index n_{eq} is the s-region, where $\mathbf{M_i}$ is the propagation matrix in each region, $\mathbf{M_{ij}}$ is the propagation matrix at the boundary from region j to i, l_m is the width of the m region, l_s is the width of the s region, and Λ is the grating period. The propagation constant β_i and complex refractive index n_i in each region are expressed using the propagation constant k_0 (= 2π/λ) in vacuum as follows

$$\beta_m = k_0 n_m, \qquad \beta_s = k_0 n_s \tag{2.27}$$

$$n_m = n_{eqm} + j\frac{g_m}{2k_0}, \qquad n_s = n_{eqs} + j\frac{g_s}{2k_0}, \tag{2.28}$$

where n_{eqm} and n_{eqs} are the equivalent refractive index, g_i represents the mode gain of each region and is given by

$$g_m = \xi_m g - \alpha_{im}, \qquad g_s = \xi_s g - \alpha_{is}, \tag{2.29}$$

where ξ is the optical confinement factor to the active layer, g is the active layer gain, and

α_i is the internal loss.

Using the above equation, the matrix **F** of the entire cavity is obtained by multiplying the matrices of each region throughout. The electric field at $z = L$ is expressed as

$$\begin{bmatrix} E_r(L) \\ E_s(L) \end{bmatrix} = \mathbf{F} \begin{bmatrix} E_r(0) \\ E_s(0) \end{bmatrix} = [\mathbf{M_{m0}} \cdot \mathbf{M_m} \cdots \mathbf{M_{sm}} \cdot \mathbf{M_s} \cdot \mathbf{M_{ms}} \cdot \mathbf{M_m} \cdots \mathbf{M_{0m}}] \begin{bmatrix} E_r(0) \\ E_s(0) \end{bmatrix}. \quad (2.30)$$

The power reflectivity and transmissivity are expressed as,

$$R = \left| \frac{E_s(0)}{E_r(0)} \right|^2 = \frac{|F_{21}|^2}{|F_{22}|^2} \quad (2.31)$$

$$T = \left| \frac{E_r(L)}{E_r(0)} \right|^2 = \frac{|F_{11}F_{22} - F_{12}F_{21}|^2}{|F_{22}|^2} = \frac{1}{|F_{22}|^2}, \quad (2.32)$$

where the determinant of the matrix $|F_{11}F_{22}\text{-}F_{12}F_{21}|$ reduces to one. The lasing condition is that the output exists when the external input is zero in equation (2.30), thus applying this condition gives the following equation,

$$\begin{bmatrix} E_r(L) \\ 0 \end{bmatrix} = \mathbf{F} \begin{bmatrix} 0 \\ E_s(0) \end{bmatrix} = \begin{bmatrix} F_{11} & F_{12} \\ F_{21} & F_{22} \end{bmatrix} \begin{bmatrix} 0 \\ E_s(0) \end{bmatrix}. \quad (2.33)$$

Since this equation is needed to hold, the lasing condition can be expressed as

$$F_{22} = 0\,. \quad (2.34)$$

Solving for the gain g for wavelength λ, the lowest gain that satisfies the condition in Equation (2.30) is the threshold gain g_{th}, and the wavelength at that time is the oscillation wavelength λ_{th}. By substituting the threshold gain g_{th} into equation (2.13), the threshold of the laser with grating can be calculated.

In a grating structure, reflection occurs in the grating and the forward wave E_r and backward wave E_s are coupled. The grating coupling coefficient κ is defined as an expression of the degree of this coupling [25]. In TMM, the grating coupling coefficient κ of the TE mode is expressed as

$$\kappa = \frac{1}{\Lambda}\ln\left(\frac{\beta_m}{\beta_s}\right). \tag{2.35}$$

Next, the electric field intensity distribution inside the cavity is determined. As shown in Fig. 2.3, the inside of the cavity is divided by $z = l$, and the transfer matrices in each region are defined as $\mathbf{F_1}$ and $\mathbf{F_2}$. The threshold gains and the lasing wavelength obtained from the condition in Eq. (2.34) were assigned to these matrices. In this case, the electric field at $z = l$ satisfies the following relation

$$\begin{bmatrix} E_r(l) \\ E_s(l) \end{bmatrix} = \mathbf{F_1}\begin{bmatrix} E_r(0) \\ E_s(0) \end{bmatrix} = \begin{bmatrix} F_{11}^1 & F_{12}^1 \\ F_{21}^1 & F_{22}^1 \end{bmatrix}\begin{bmatrix} 0 \\ E_s(0) \end{bmatrix} \tag{2.36}$$

$$\begin{bmatrix} E_r(L) \\ E_s(L) \end{bmatrix} = \begin{bmatrix} E_r(L) \\ 0 \end{bmatrix} = \mathbf{F_2}\begin{bmatrix} E_r(l) \\ E_s(l) \end{bmatrix}. \tag{2.37}$$

These equations can be rearranged as

$$\begin{cases} E_r(l) = F_{12}^1 E_s(0) \\ E_s(l) = F_{22}^1 E_s(0) \end{cases}. \tag{2.38}$$

Here the electric field intensity is expressed as follows,

$$E = |E_r|^2 + |E_s|^2\,. \tag{2.39}$$

Therefore, the normalized electric field intensity distribution from Equations (2.38) and (2.39) can be expressed using the normalization constant E_0 as

$$E(z) = E_0\left(\left(F_{12}^{(z)}\right)^2 + \left(F_{22}^{(z)}\right)^2\right). \tag{2.40}$$

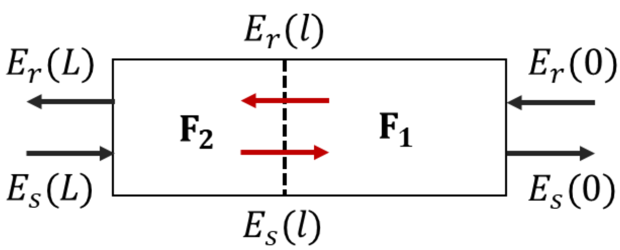

Fig. 2.3 TMM calculation model of the grating structure for electric field intensity distribution.

2.2.3 Frequency response

When data transmission is considered, the power consumption of a semiconductor laser is determined by the bias current that satisfies both the optical output power required for light detection and the modulation speed. For conditions based on optical output, equation (2.16) can be used to determine the bias current to obtain the necessary optical output for light receiving. On the other hand, the modulation speed condition is determined by the relaxation oscillation frequency of the laser. The relaxation oscillation frequency f_r can be expressed as follows,

$$f_r = \frac{1}{2\pi}\sqrt{\frac{\xi(dg/dN)v_g\eta_i}{qV_a}(I_b - I_{th})}\,. \tag{2.41}$$

Here, ξ is the optical confinement factor, dg/dN is the differential gain, v_g is the group velocity, η_i is the internal quantum efficiency, V_a is the active volume, I_b is the bias current. It can be seen that the relaxation oscillation frequency is increased by increasing the bias current. The slope is expressed by the following equation,

$$\text{Modulation efficiency} = \frac{1}{2\pi}\sqrt{\frac{\xi(dg/dN)v_g\eta_i}{qV_a}}\,. \tag{2.42}$$

This is the slope of f_r as a function of bias current and is an important parameter for obtaining high speed operation under low bias current conditions. The 3dB bandwidth is given by the frequency at which the power of the response is halved. Using the damping factor γ, the relationship between f_{3dB} and f_r is given as follows at low damping,

$$\begin{aligned} f_{3dB} &= f_r\sqrt{1-\frac{1}{2}\left(\frac{\gamma}{2\pi f_r}\right)^2+\sqrt{1+\left[1-\frac{1}{2}\left(\frac{\gamma}{2\pi f_r}\right)^2\right]^2}} \\ &\approx f_r\sqrt{1+\sqrt{2}} \approx 1.55 f_r\,. \end{aligned} \tag{2.43}$$

Based on the discussion of the rise and fall times of the large-signal response of semiconductor lasers [15], the relationship between the 3-dB bandwidth and the maximum achievable data rate for a non-return-to-zero (NRZ) signal is

$$\text{Data rate} = 1.3 f_{3\text{dB}} \,. \tag{2.44}$$

This relation gives the information for the large signal modulation from the bandwidth.

Using the above equation, semiconductor laser power consumption is discussed. For data transmission, a semiconductor laser needs to meet two requirements. One is that the laser emits sufficient optical output intensity for the photodetector to detect the signal, and the other is that the laser can modulate at the desired modulation speed. The power

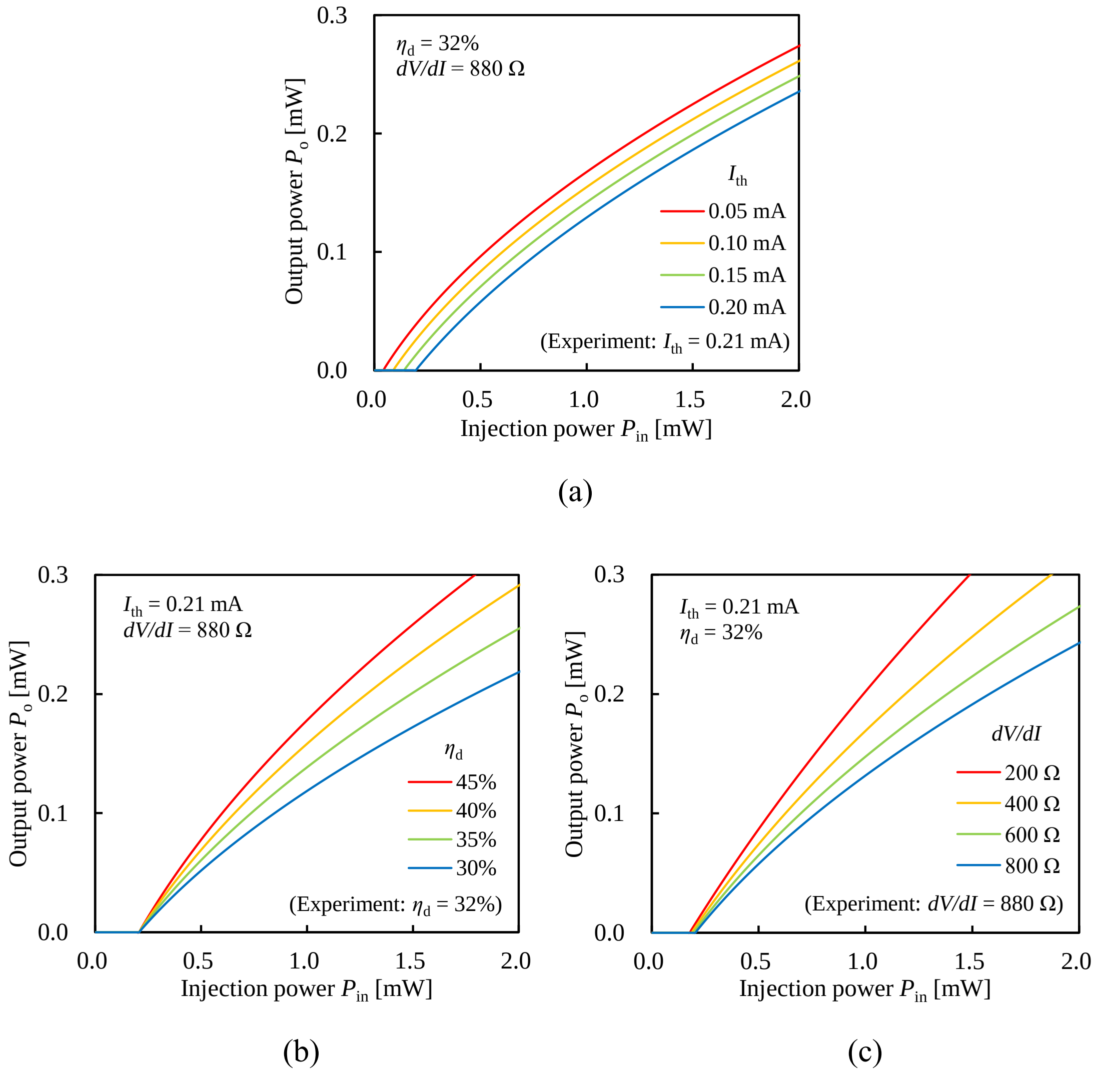

Fig. 2.4 Comparison of power consumption for the required light output power with various laser characteristics.

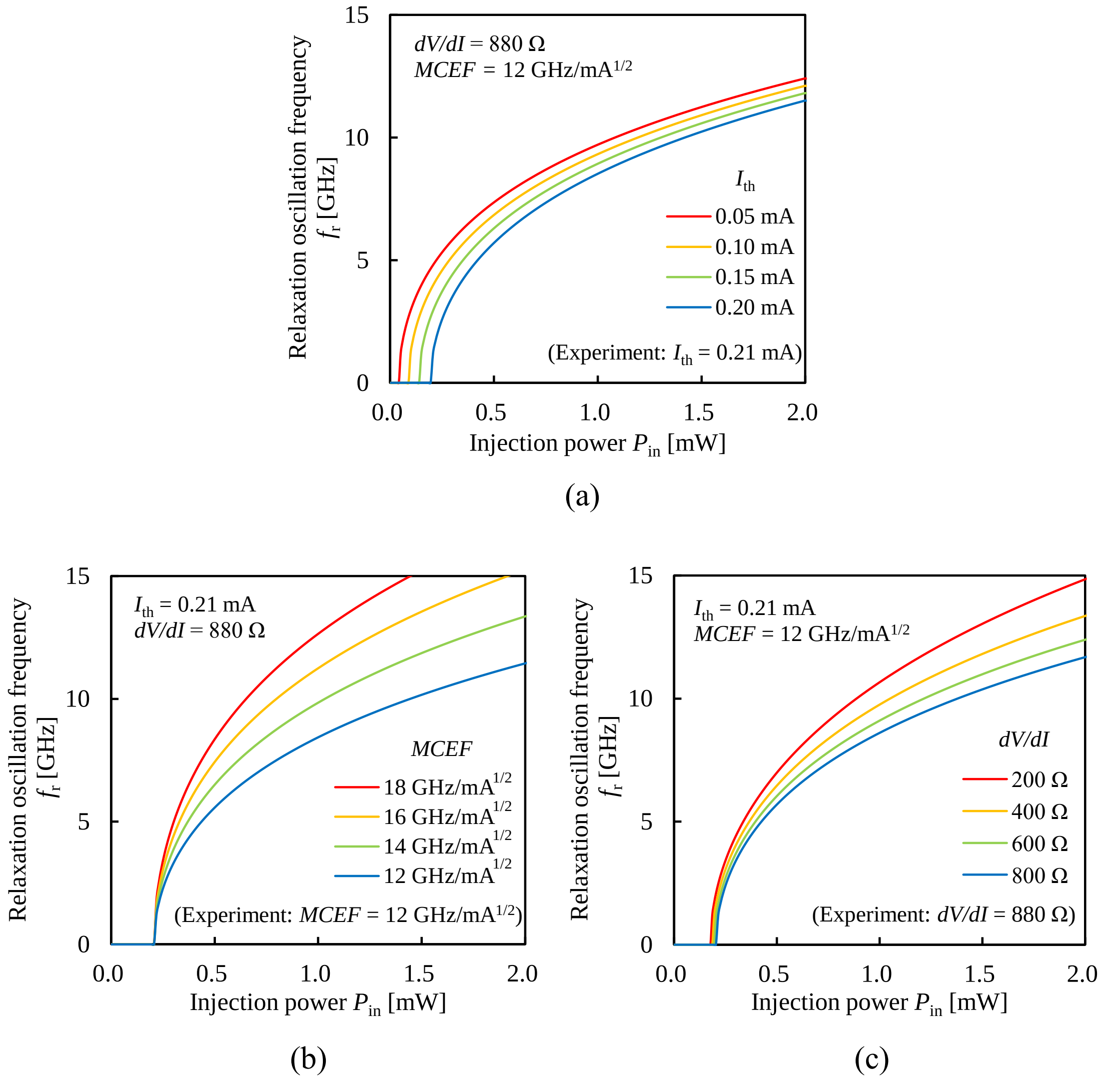

Fig. 2.5 Comparison of relaxation oscillation frequency as functions of the injection power with various laser characteristics.

consumption of a semiconductor laser is determined by the bias current and bias voltage when both requirements are satisfied. These requirements vary depending on the application of the semiconductor laser. Membrane lasers have a low threshold current and high-power conversion efficiency at low injection power, giving them an advantage in relatively short distance communications. Fig. 2.4 and Fig. 2.5 show the relationships between laser characteristics and power consumption using eqs. (2.16) and (2.41). The horizontal axis of Fig. 2.4 shows the injection power and the vertical axis shows the optical output. The optical output of a semiconductor laser at a given bias current is determined by the threshold current and the external differential quantum efficiency. The injection power is also determined by the multiplication of the bias current by the bias voltage, which is related to the differential resistance. Each parameter is based on the results obtained by previous experiments [16]. When the required optical output is high, improving the external differential quantum efficiency and differential resistance can have a significant effect on reducing power consumption, but the smaller the required optical output, the greater the impact of the threshold current on power consumption. Also, Fig. 2.5 shows the relationship between relaxation oscillation frequency f_r and injected power. As shown in equations (2.43) and (2.44), the modulation speed is related to f_r. To operate at low power consumption, a high f_r needs to be obtained at low injection power. When considering modulation with NRZ signals, the modulation speed is approximately twice that of f_r. When operating at 20 Gbit/s or higher modulation rates, the modulation current efficiency factor (MCEF) is significantly related to power consumption. Thus, semiconductor lasers have different power consumption depending on their application, and the characteristics that affect their reduction are different. It is then necessary to understand the relationship between laser structure parameters and lasing characteristics to improve these laser characteristics. Since increasing optical confinement is expected to improve threshold current, differential resistance, and MCEF, the next section will focus on optical confinement.

2.3 Analysis of optical confinement structure for lateral direction

This section describes a study of introducing a buried-ridge-waveguide (BRW) structure as a lateral optical confinement structure to reduce the power consumption of semiconductor membrane lasers. First, the analysis of internal loss and differential resistance is described, and a theoretical analysis of a semiconductor membrane lasers with a BRW structure is performed. Then, the parameters of the BRW structure are determined based on the obtained differential resistance results.

2.3.1 Internal loss and differential resistance

- **Internal loss**

The internal loss can be determined from the laser structure and absorption coefficient by modal calculation. Fig. 2.6 shows the cross-sectional structure of a semiconductor membrane laser. The *p*-InP side cladding layer is grown to a doping concentration of 5×10^{17} cm^{-3}. The doping concentration in the region below the contact layer was set to 4×10^{18} cm^{-3} considering the diffusion of dopant from the high

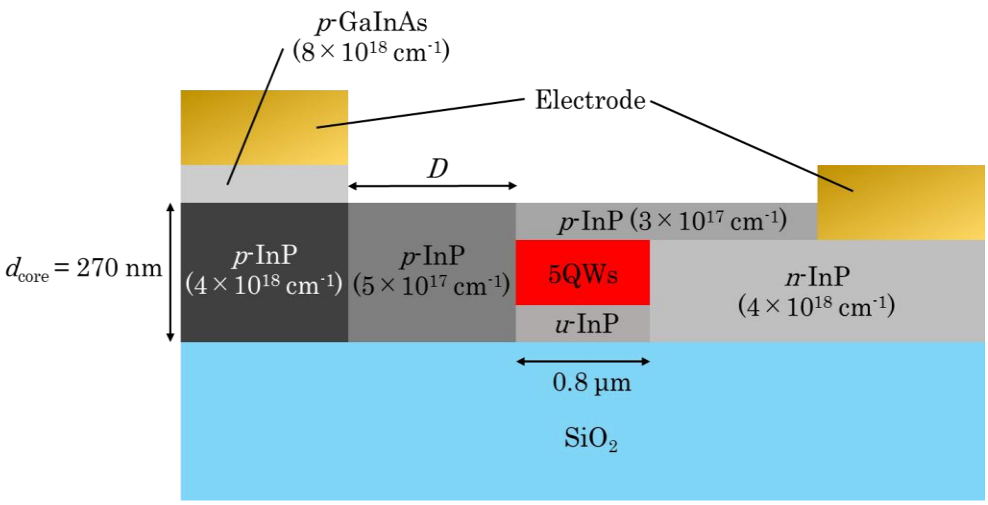

Fig. 2.6 Calculation model

Table 2.1 Material parameter

Material	Doping concentration [cm^{-3}]	Absorption coefficient [cm^{-1}]
Au	-	798000
p-GaInAs (contact)	8×10^{18}	5000
GaInAsP (well)	-	100
	4×10^{18}	80
p-InP	5×10^{17}	10
	3×10^{17}	6
n-InP	4×10^{18}	2

concentration contact layer. Table 2.1 shows the material parameters used in the calculations. The absorption coefficient α of the active layer is set to 100 cm^{-1} [3] and that of the *n*-InP side cladding layer to 2 cm^{-1} [4]. The absorption coefficient of the *p*-InP side cladding layer can be expressed as

$$\alpha = 20 \times \frac{N_\mathrm{A}}{10^{18}} \ \ [\mathrm{cm}^{-1}]\,, \tag{2.45}$$

for the 1.5 μm wavelength band using the impurity concentration N_A from fitting the experimental values [5]. Using these absorption coefficients, a modal calculation yields the complex equivalent refractive index. The complex equivalent refractive index is expressed by

$$\tilde{n} = n_\mathrm{eq} + j\kappa\,. \tag{2.46}$$

The relationship between the internal loss and the extinction coefficient κ is expressed as

$$\alpha_\mathrm{i} = 2k_0\kappa = \frac{4\pi\kappa}{\lambda}, \tag{2.47}$$

based on the propagation constant of optical power [6], and the internal loss was obtained by substituting the extinction coefficient obtained from the mode calculation.

- **Differential resistance**

The resistance components of semiconductor membrane lasers can be divided into contact resistance and active layer resistance, *p*-InP side cladding layer resistance, and *n*-InP side cladding layer resistance. Contact resistance and active layer resistance are much smaller than side cladding layer resistance, and side cladding layer resistance is assumed to be dominant. To determine the side cladding layer resistance, the resistivity of InP is determined by

$$\rho_{\mathrm{InP}} = \frac{1}{eN_{\mathrm{A}}\mu}, \tag{2.48}$$

where N_{A} is the impurity concentration and μ is the mobility. There are many experimental results on InP mobility [7]-[9] and fitting functions [10]. Here we assume low field mobility [11] and use equation,

$$\mu(N,T) = \mu_{\min} + \frac{\mu_{\max} \times 300\mathrm{K}\left(\frac{300\mathrm{K}}{T}\right)^{\theta_1} - \mu_{\min}}{1 + \left(\frac{N}{N_{\mathrm{ref}} \times 300\mathrm{K} \times \left(\frac{T}{300\mathrm{K}}\right)^{\theta_2}}\right)^{\lambda}}, \tag{2.49}$$

which is a Caughey-Thomas-like model [12]. This was obtained by fitting to experimental values from several references. Each parameter is shown in Table 2.2 for InP, where $\mu_{\min}$ is the minimum mobility value, $\mu_{\max}$ is the maximum mobility value, N_{ref} is the impurity concentration for reference, and θ_1, θ_2, and λ are the fitting parameters.

The resistivity of InP obtained using Eqs. (2.48) and (2.49) is shown in Fig. 2.7. The

Table 2.2 Parameters for mobility of InP [9]

Carrier	$\mu_{\max}$(300K) [cm^2/Vs]	$\mu_{\min}$ [cm^2/Vs]	N_{ref}(300K) [cm^{-3}]	λ	θ_1	θ_2
Electron	5200	400	3.0×10^{17}	0.47	2.0	3.25
Hole	170	10	4.87×10^{17}	0.62	2.0	3.0

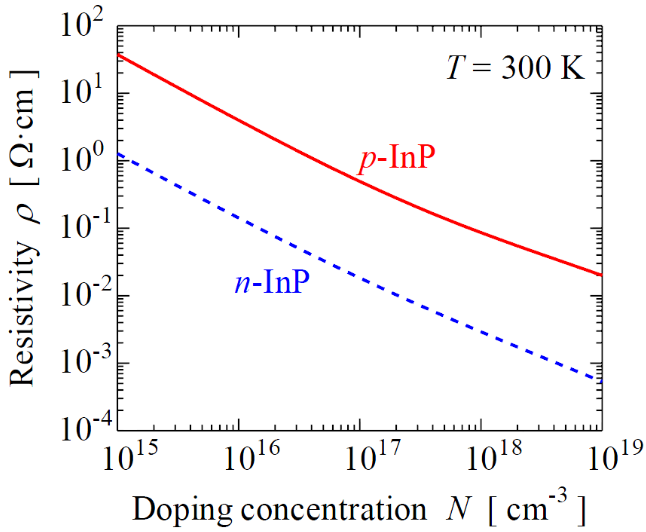

Fig. 2.7 Resistivities of the *p*-InP and *n*-InP as a function of the doping concentration [10].

impurity concentration of *n*-InP is 4 × 10^{18} cm^{-3}, and that of *p*-InP is 4 × 10^{18} cm^{-3} and 5 × 10^{17} cm^{-3}, respectively. Therefore, Fig. 2.7 shows that the resistivity of *p*-InP is more than one order of magnitude larger than that of *n*-InP. We also ignored the contact resistance of the *p*-side and *n*-side by assuming the ideal contact resistance of approximately 10^{-6} $\Omega\cdot cm^2$ [13][14]. Therefore, the *p*-InP side cladding resistance is regarded as the most dominant element resistance, and only the *p*-InP side cladding resistance is assumed as the device resistance in the following calculations. From the above, the device resistance is expressed as

$$R_{\text{InP}} = \rho_{\text{InP}} \frac{D}{L_{\text{DFB}} d_{\text{core}}} = \frac{1}{eN_{\text{A}}\mu} \frac{D}{L_{\text{DFB}} d_{\text{core}}}, \tag{2.50}$$

where D is the distance from the active layer edge to the electrode edge, L_{DFB} is the DFB region length, and d_{core} is the active layer thickness.

2.3.2 Design of buried-ridge-waveguide (BRW) structure

In the previous section, we mentioned that the *p*-InP side cladding resistance is dominant in the differential resistance of semiconductor membrane lasers and is

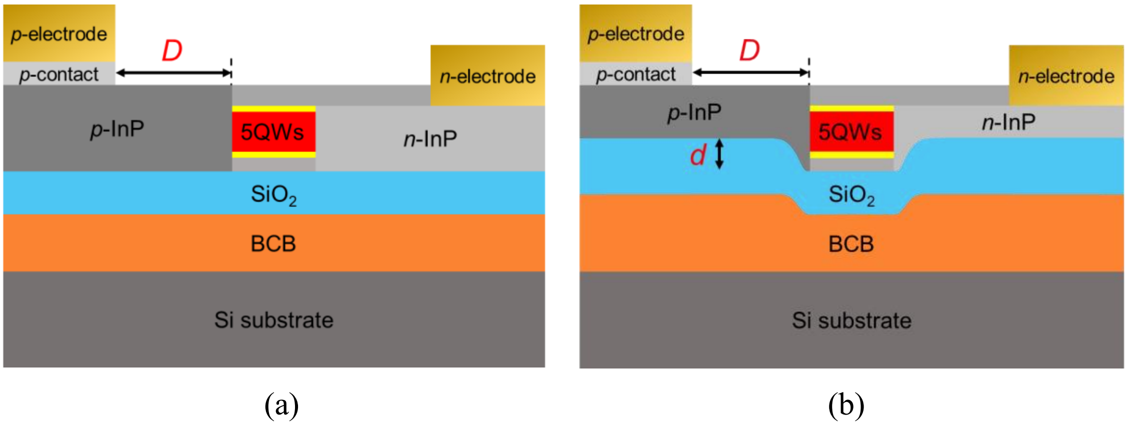

Fig. 2.8 Cross sectional view of membrane laser with (a) the conventional flat structure and (b) the BRW structure.

proportional to the distance *D* from the active layer edge to the electrode edge. Thus, the differential resistance can be reduced by shortening the distance between the electrode and the active layer. However, the distance *D* between the electrode and the active layer must consider the mode distribution inside the active layer. If the electrode is placed too close to the active layer, the internal loss will increase due to high absorption loss by the electrode. Therefore, by strengthening the lateral optical confinement, not only a reduction of the bias current by increasing the confinement factor ξ but also a reduction of the differential resistance by shortening the distance *D* between the electrode and the active layer is expected. Buried-ridge-waveguide (BRW) structure was proposed as a structure that can achieve this strong lateral optical confinement.

The BRW structure is a structure in which the thickness of the side cladding layer is thinner than that of the active layer. This structure provides strong optical confinement and shortens the distance between the electrode edge and the active layer edge. Fig. 2.8 shows the calculation model of the conventional structure and the BRW structure. In the previous study, the boundary between the active layer and the side cladding layer was calculated based on a calculation model assuming an ideal ridge structure, but this time, in consideration of the formation of the BRW structure by OMVPE, a slope width W_d, which occurs in actual growth, was introduced in the mode calculation.

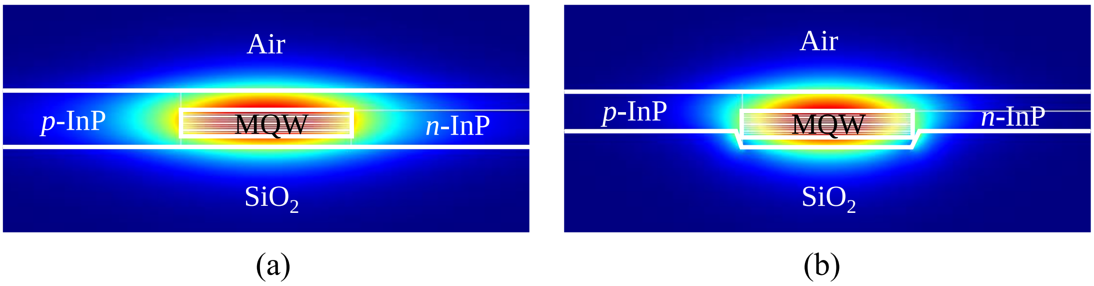

Fig. 2.9 Calculated optical intensity distribution of (a) the conventional flat structure and (b) the BRW structure (d = 50 nm).

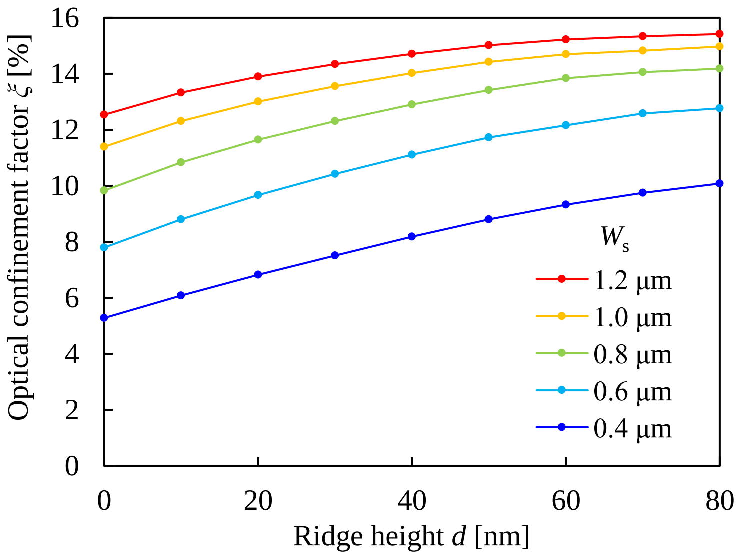

Fig. 2.10 Distribution of electric field density in the lateral direction at each thickness difference *d*.

First, the thickness difference d was examined. Fig. 2.9 shows the mode distribution in the BRW structure with d = 50 nm. Compared to the conventional structure, the BRW structure reduces the light intensity leakage in the lateral direction. Fig. 2.10 shows the optical confinement factor at each thickness difference d. It can be confirmed that the transverse optical confinement increases as the step d increases. This means that the BRW structure can bring the electrode closer to the active layer due to the strong lateral confinement. Although shortening the distance between the electrode and the active layer can reduce the differential resistance, there is a trade-off: if the distance is shortened to the position where absorption by the electrode occurs, the internal loss will increase.

Therefore, assuming that the electrode distance can be shortened until the internal loss increases by 5% from the value at *D* = 3 μm, where absorption by the electrode can be ignored, the minimum electrode-active layer distance D_{min} was determined for each thickness difference *d*. Fig. 2.11 shows the dependence of the internal loss on the distance between the electrode and the active layer for each thickness difference *d*. As observed,

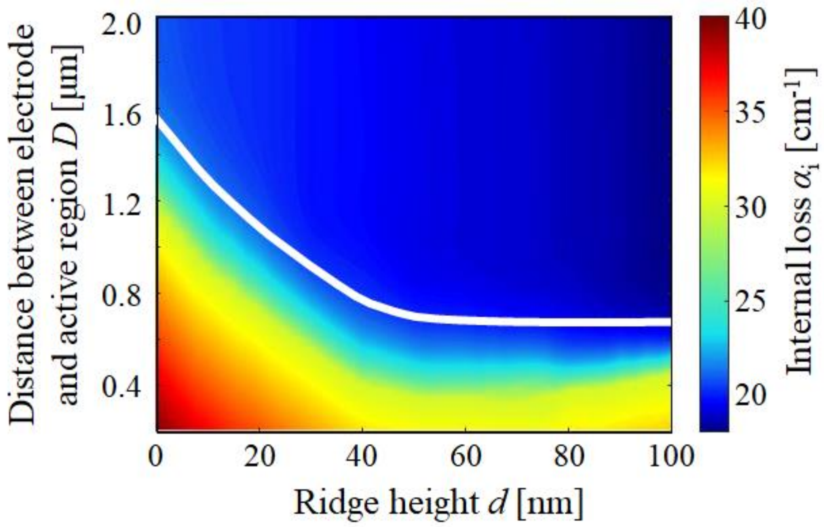

Fig. 2.11 Calculated internal loss α_i with various ridge height *d* and distance *D* between the *p*-electrode and the active region.

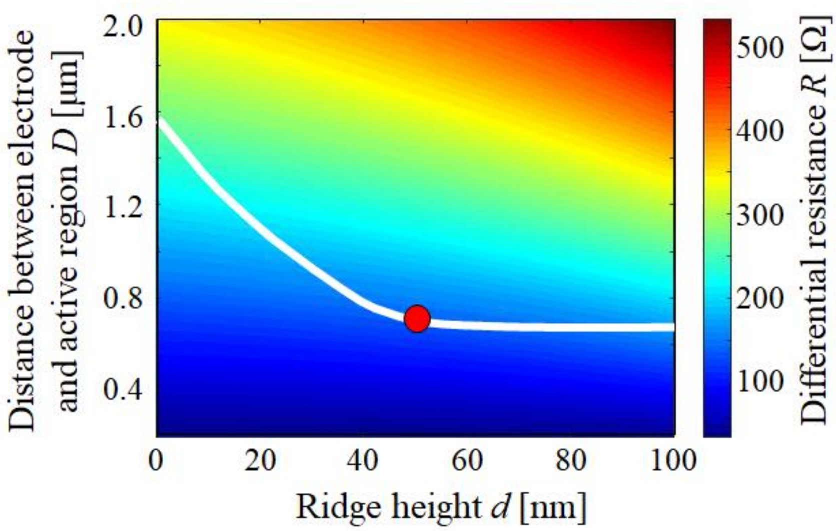

Fig. 2.12 Calculated resistance *R* with various ridge height *d* and distance *D* between the *p*-electrode and the active region.

the minimum distance D_{min} can be decreased by increasing the ridge height (D_{min} = 1.6 μm at d = 0, whereas D_{min} = 0.7 μm at d > 50 nm).

Next, the obtained minimum electrode active layer distance D_{min} is used to calculate the differential resistance. The differential resistance of semiconductor membrane lasers is dominated by the p-InP side cladding resistance, as described in the previous section, and is given by equation (2.50). Fig. 2.12 shows the calculated resistance R, when the ridge height d, and distance D, are changed. Here, the DFB region length is calculated as L_{DFB} = 30 μm, and the resistivity of the InP side cladding is calculated as ρ_{InP} = 0.14 Ω·cm from equation (2.49). The increase in the ridge height causes thinning of the current pass and an increase in the resistance per unit length. Therefore, the resistance is the lowest at d = 50 nm on the borderline. At this value, a resistance reduction of 40% can be realized when compared to that of the conventional flat structure.

Next, we will discuss the slope width W_d. The formation method of the BRW structure is described in the next chapter, but in the case of OMVPE formation, a slope is generated at the boundary between the active layer and the side cladding layer in the actual growth. Since previous calculations have shown that the differential resistance can be reduced most at a step d = 50 nm, we set the step d to 50 nm and examined how much the slope width affects the results. Fig. 2.13 shows the calculation model. The mode calculations were performed for each electrode-active layer distance in the same manner

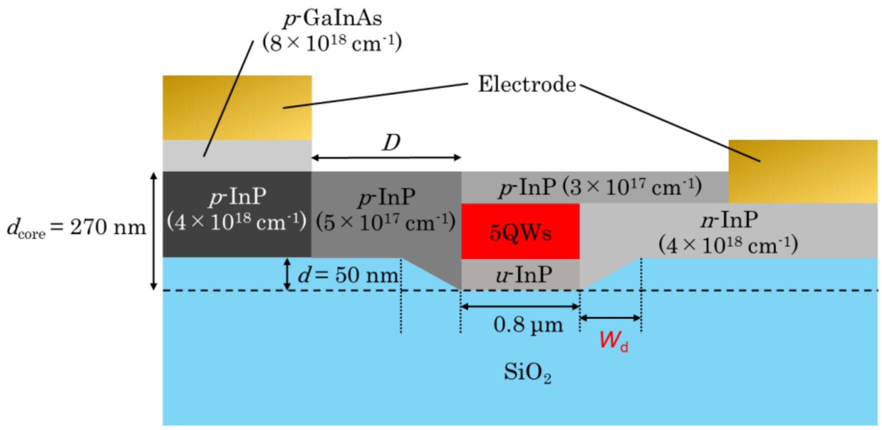

Fig. 2.13 Calculation model considering slope by OMVPE.

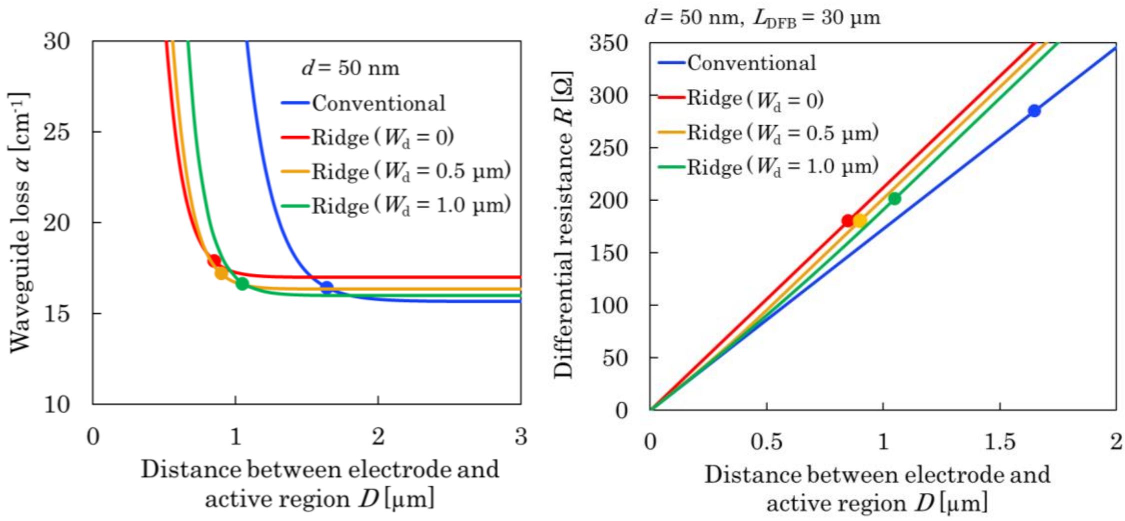

(a) (b)

Fig. 2.14 Internal loss and differential resistance at each slope width W_d.

as the calculation method described above, and the result of plotting the minimum electrode-active layer distance D_{min} from the obtained internal loss is shown in Fig. 2.14(a). As the slope width increases, the change in refractive index between the active layer and the side cladding layer becomes gradual, resulting in a slight weakening of optical confinement to the active layer. The result of obtaining the differential resistance from the obtained D_{min} is shown in Fig. 2.14(b). In the case of a slope area, the thickness near the active layer is slightly larger than that near the electrode, which must also be considered in the differential resistance calculation equation. The differential resistance when the slope term is included is expressed as

$$R_{\mathrm{InP}} = \rho_{\mathrm{InP}} \frac{D - W_{\mathrm{d}}}{L_{\mathrm{DFB}}(d_{\mathrm{core}} - d)} + \rho_{\mathrm{InP}} \frac{1}{L_{\mathrm{DFB}}} \int_0^{W_{\mathrm{d}}} \frac{1}{d(x)} \mathrm{d}x \,. \tag{2.51}$$

Fig. 2.14 shows that the differential resistance remains unchanged at $W_d = 0$ and 0.5 μm, and at 1.0 μm, it is lower than that of the conventional structure, but higher than that of $W_d = 0$ and 0.5 μm.

These results indicate that the BRW structure with a step of $d = 50$ nm and a slope width of $W_d \leq 0.5$ μm has the lowest differential resistance as a BRW structure.

2.4 Analysis for optical confinement structure for cavity direction

This section describes a laser analysis for periodic distributions in the cavity direction. The analysis that takes into account the carrier density distribution inside the cavity, which is not generally taken into account, will be explained. Finally, the results of the analysis of the diffraction grating of the membrane laser using these methods are described.

2.4.1 Carrier density analysis

In performing a laser analysis for the period distribution in the cavity direction, it is also necessary to determine the carrier density distribution inside the cavity. The rate equation for general carrier density is restated as

$$\frac{dN}{dt} = \frac{\eta_{\mathrm{i}} I}{q V_{\mathrm{a}}} - (AN + BN^2 + CN^3) - v_{\mathrm{g}} g S \,. \tag{2.52}$$

This equation is the most basic equation for analyzing laser characteristics, but the distribution in the cavity direction is assumed to be uniform. Considering the distribution in the cavity direction, the rate equation for the carrier density is expressed by the following equation,

$$\frac{dN(z)}{dt} = \frac{\eta_{\mathrm{i}} I}{q V_{\mathrm{a}}} - [AN(z) + BN(z)^2 + CN(z)^3] - v_{\mathrm{g}} g(z) S(z) + D_n \frac{d^2 N(z)}{dz^2}\,, \tag{2.53}$$

where D_{n} is the carrier diffusion constant and the injected current I is assumed to be uniform in the cavity direction [26]. The last term on the right-hand side represents the diffusion of carriers in the cavity direction due to the carrier density distribution. From the above, the electric field intensity distribution obtained by the TMM, and the rate equation can be used to obtain the distribution of carrier density in the cavity direction. There is a close relationship between carrier density and refractive index. This is called the free carrier effect: as the free carrier concentration increases, the imaginary part of the refractive index increases while the real part decreases [27]. The relationship between carrier density and refractive index can be expressed as

$$\Delta n = -\frac{\alpha_0 \lambda_0 g' \Delta N}{4\pi}, \tag{2.54}$$

where α_0 is the linewidth enhancement factor and g' is the differential gain. Therefore, since the refractive index is also distributed according to the carrier density distribution, it is necessary to calculate the threshold gain g_{th} and electric field intensity distribution $E(z)$ using the TMM method again, taking Δn into account. By repeating these calculations until the carrier density converges, laser characteristics that take into account the distribution along the cavity direction can be obtained.

2.4.2 Design of asymmetric corrugation-pitch-modulation (ACPM) grating

The grating selectively reflects light at the Bragg wavelength in the opposite direction, but to make a cavity, the light must be reflected again in the original direction. Considering the amount of phase shift of the reflected light at the Bragg wavelength, the uniform grating does not oscillate at the Bragg wavelength that has traveled around the cavity because the light weakens each other, and in principle, lasing occurs at two symmetric wavelengths that are off from the Bragg wavelength. In cleaved DFB lasers, the probability of their single-mode operation depends on the corrugation phase at the mirror facets [28]. Therefore, a λ/4-shifted DFB laser, which introduces a phase-shifted region equivalent to a quarter of the wavelength in the center of the grating (Fig. 2.15), has been proposed in 1976 by Haus and Shank [29]. The inserted phase-shift region compensates for the phase change of the reflected light, and single-wavelength lasing at the most stable Bragg wavelength can be obtained as shown in Fig. 2.16. However, at higher output light intensities, it tends to oscillate in multimode. Soda *et al*. explained in

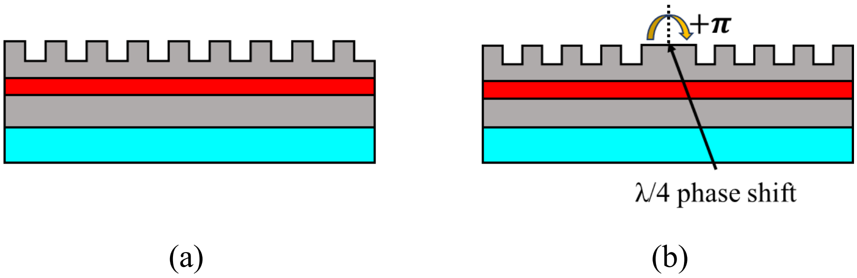

Fig. 2.15 Schematics of the structure with (a) uniform grating and (b) λ/4 phase-shifted grating.

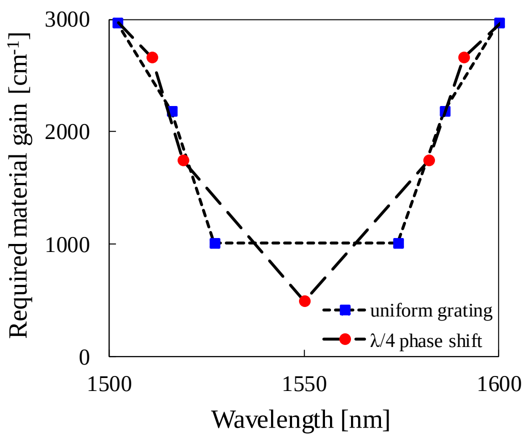

Fig. 2.16 Relationship between wavelength of lasing mode and required material gain.

1987 that this phenomenon was caused by spatial hole burning [30]. In λ/4 phase-shift grating, the electric field is concentrated at the phase-shift position and the supply of carriers cannot follow, resulting in spatial hole-burning. To reduce the spatial hole-burning effect, a corrugation-pitch-modulated (CPM) grating structure was proposed [31][32]. As shown in Fig. 2.17, the ACPM grating has a structure in which the grating period is slightly increased over several periods at the phase shift position. The CPM grating generates an effective λ/4 phase-shift with several length, whereas the grating phase changes suddenly at the center of the λ/4 phase-shifted grating. This makes it possible to disperse the concentration of electric field and is therefore expected to suppress spatial hole burning. Longitudinal spatial hole-burning in λ/4 phase-shifted gratings is also found to affect the roll-off response of lasers at low frequencies. In 2013,

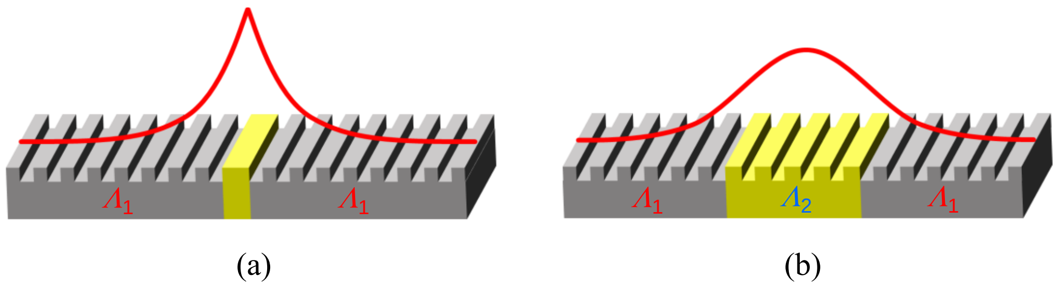

Fig. 2.17 Schematics of the structure with (a) λ/4 phase- shifted grating and (b) CPM grating. The yellow regions indicate the phase array region, and the red lines indicate the electric field intensity distribution inside the cavity.

the application of asymmetric CPM (ACPM) gratings to a laser structure with a high reflectivity (HR) coating on one side to suppress hole-burning was reported [33]. Compared to λ/4 shifted gratings, ACPM lasers have a smaller laser roll-off at lower frequencies and direct modulation at 28 Gb/s was reported. Thus, ACPM grating has already been reported by several institutes and is expected to be particularly effective in laser structures with high κL. Therefore, I considered that ACPM grating could be effective for membrane DR lasers with high κL and investigated its adoption.

The key factors in designing ACPM gratings are the insertion position of the phase-shift and the ratio of the phase arrange region (PAR). First, the insertion position of the phase shift was examined. Since the DR laser has an asymmetric structure with a highly reflective DBR mirror behind the active region, the optimal insertion position of the phase shift is not in the center of the active region. Fig. 2.18 shows the relationship between the insertion position of the phase shift and the threshold material gain. The length of the active region is represented by L_{DFB}, and the length from the back end of the active region to the center of the phase shift is represented by L_{phase}. In this calculation, the length of the DBR is 100 μm in order to obtain sufficient reflectance. As can be seen from the results, the insertion position of the phase shift that results in the minimum threshold gain is toward the rear. This is due to the fact that the effective optical path length in the backward direction is longer due to the high reflectivity of the DBR, and thus the effective center of the entire cavity is located in the backward direction. The results indicate that a phase shift should be inserted at the position where the length from the back end is 0.28

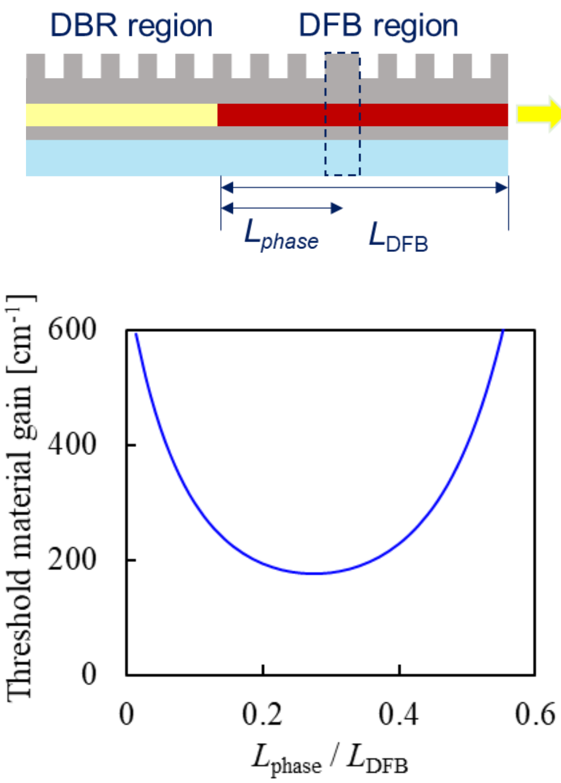

Fig. 2.18 Relationship between the insertion position of the phase shift and the threshold material gain.

L_{DFB}.

Next, the analysis to determine the length of the phase arrange region of CPM grating is described. In this analysis, it is necessary to calculate the electric field intensity distribution inside the cavity for each grating structure and analyze the carrier density distribution to satisfy the rate equation in the distribution. The electric field intensity distribution can be calculated using equation (2.53). Fig. 2.19 shows the electric field intensity distribution inside the cavity for λ/4 phase-shifted gratings and ACPM grating (PAR = 0.3, 0.5). In this analysis, the electric field intensities are normalized to be equal to the sum of the electric field intensities in the cavity direction. Also, for simplicity, the phase shift was placed in the center of the cavity in this analysis. As can be seen in this figure, the electric field is very strongly concentrated at the phase shift in the λ/4 phase-shifted gratings indicated by the blue line. On the other hand, in the ACPM grating, the electric field is dispersed as PAR is increased, and at PAR = 0.5, the concentration of the

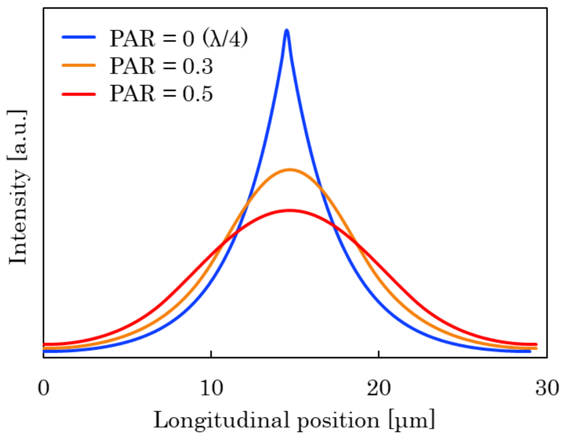

Fig. 2.19 Electric field intensity distribution inside the cavity for each grating structure.

electric field is reduced to about half that of the λ/4 phase-shifted gratings.

The carrier density distribution in the cavity can be obtained by solving the rate equation considering the distribution along the resonance axis as shown in Equation (2.53), feeding back the refractive index change to the TMM, and performing the calculation repeatedly. Fig. 2.20 shows the results of analyzing the carrier density distribution inside the cavity at each injection current. Fig. 2.20(a) shows the carrier density distribution of λ/4 phase-shifted gratings, which shows a large dip in the carrier density at the phase-shifted position due to the strong electric field concentration. As the injection current is increased, the optical output is also increased, so that more carriers are consumed at the phase shift position. As a result, the threshold gain increases, and the overall carrier density increases. Carrier density is closely related to gain, and as carrier density decreases, gain also decreases. As the gain of the lasing mode is reduced, the gain difference between the lasing mode and the side mode becomes smaller, causing unstable operation. On the other hand, in the ACPM grating (PAR = 0.3) shown in Fig. 2.20(b), the carrier density distribution is also moderate due to the relaxation of the concentration of the electric field.

This analysis of the TMM in combination with the rate equation confirms that the carrier density distribution is moderate in ACPM grating, but it is necessary to establish

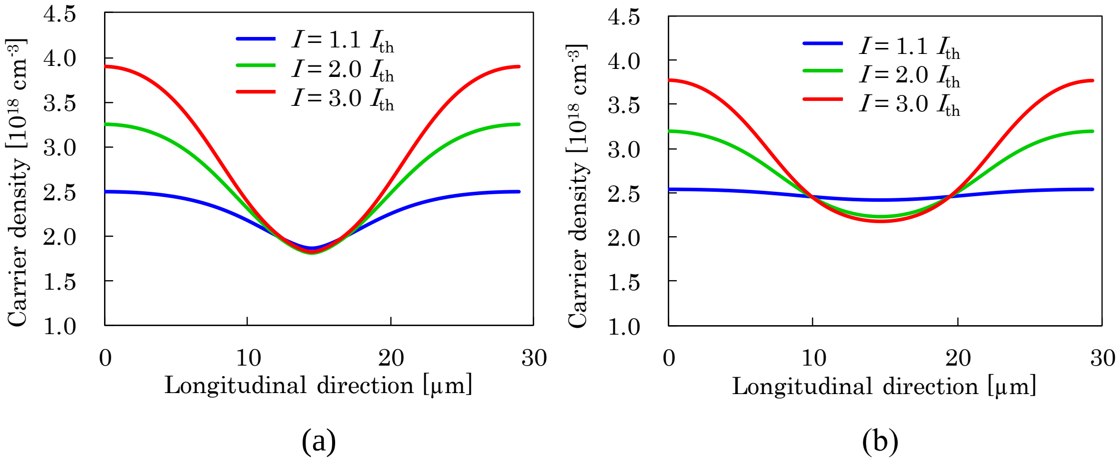

Fig. 2.20 Carrier density distribution inside the cavity at each injection current with (a) λ/4 phase-shifted gratings and (b) ACPM grating (PAR = 0.3).

guidelines in designing a structure that can suppress spatial hole-burning the most. In this analysis, the structure was designed using the gain difference between lasing mode and side mode as an indicator. Fig. 2.21 shows the relationship between injection current and threshold gain difference obtained from the analysis. The vertical axis of the graph represents the normalized gain difference between the lasing mode and the side mode with the next lowest threshold gain. The gain difference at threshold is largest for $\lambda/4$ phase-shifted gratings, represented by the blue line, because the behavior of ACPM grating with longer PAR becomes more similar to that of uniform grating. However, as the injection current is increased, the gain difference shrinks due to the effect of hole burning. This shrinkage is more gradual the longer the PAR. The slope of this decrease and the gain difference at the threshold can uniquely determine the optimal PAR length. The relation between PAR length and gain difference at an injection current of $I = 10\ I_{th}$ is shown in Fig. 2.22. The blue and red lines show the analyses for a DFB region length of 30 μm ($\kappa L = 4.8$) and 40 μm ($\kappa L = 6.4$), respectively, when the grating depth is 50 nm for the membrane DR laser. From this result, it can be estimated that the PAR lengths of 0.25 and 0.31 give the largest gain difference for $\kappa L = 4.8$ and $\kappa L = 6.4$, respectively. This analysis shows that as κL increases, the concentration of the electric field also increases, requiring a longer PAR to mitigate it. From the above analysis, a study to optimize the

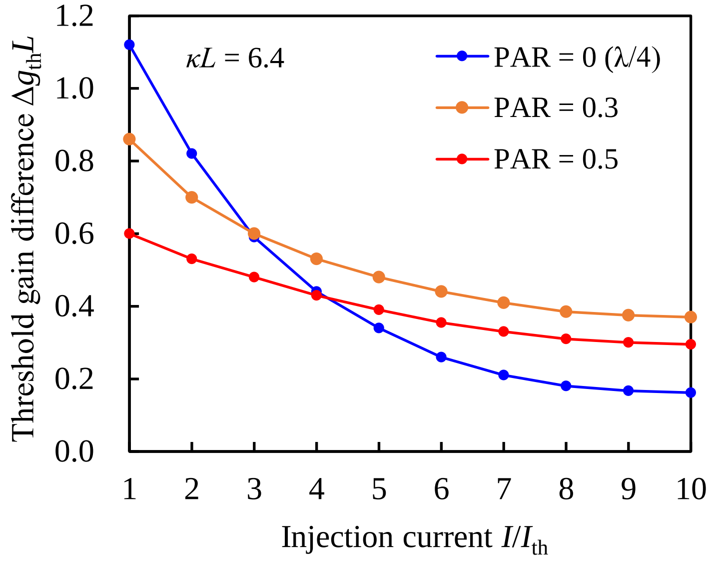

Fig. 2.21 Normalized threshold gain difference between the main mode and the side mode as a function of normalized injection current.

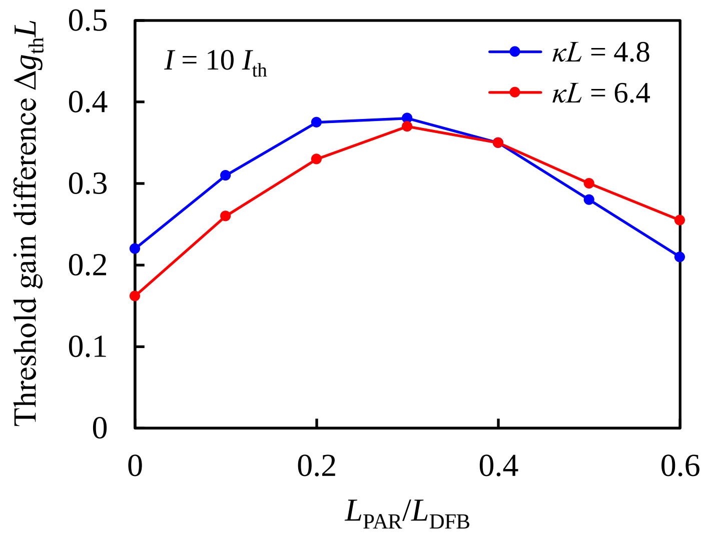

Fig. 2.22 Normalized threshold gain difference between the main mode and the side mode as a function of phase arrange region length.

optical confinement in the cavity direction was indicated.

2.5 Estimation of consumption power

Using the above calculation, the power consumption required for data transmission was estimated. Each parameter used in the laser characteristics analysis is shown in Table 2.3. In this calculation, an internal quantum efficiency η_i of 75%, which were obtained experimentally in previous works, were used [17][18]. The other parameters used in this calculation are typical values for the GaInAsP/InP strain compensated MQWs [1].

Fig. 2.23 shows the relationship between each parameter and ridge depth, obtained from the modal calculations. It can be seen that optical confinement increases with increasing ridge depth. As the optical confinement changes, the mode shape changes, and the internal loss changes accordingly. The p-side cladding layer is a region of relatively high absorption, and increasing the ridge depth reduces overlap with the side cladding layer, which also reduces internal losses. Fig. 2.24 shows the DFB region length dependence of the threshold current for each ridge depth. The threshold current is found to be decreasing as optical confinement increases with increasing ridge depth for all grating structures. Threshold currents are lower than for uniform gratings due to the introduction of phase shift. On the other hand, the external differential quantum efficiency,

Table 2.3 Parameters for laser analysis.

Parameters	Value
Internal quantum efficiency η_i	0.75
Stripe width W_s	0.8 μm
Total thickness of core d_{core}	5 × 5.4 nm
Bimolecular recombination coefficient B	1.6×10^{-10} cm^3/s
Auger coefficient C	5×10^{-29} cm^6/s
Transparent carrier density N_{tr}	1.5×10^{18} cm^{-3}
Gain coefficient g_0	1500 cm^{-1}
Differential gain dg/dN	7.2×10^{-16} cm^2

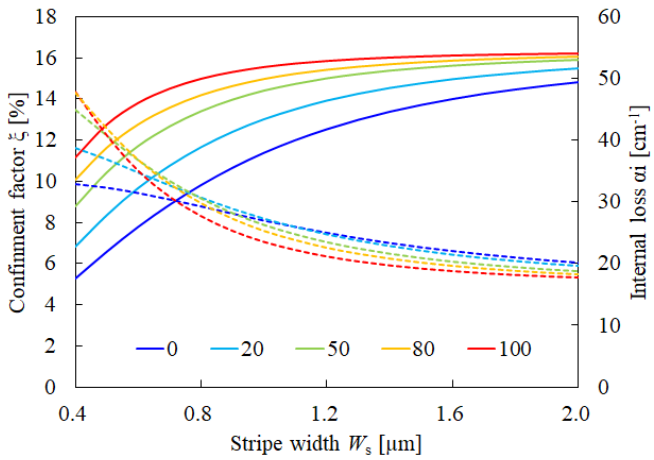

Fig. 2.23 Relationship between each parameter and ridge depth from mode calculation.

shown in Fig. 2.24, decreases rapidly with increasing resonator length for phase-shifted grating laser. This is because the light is strongly confined with respect to the emitting direction of the light, which is mitigated in the ACPM grating compared to the λ/4-shift grating. The external differential quantum efficiency shows a value that varies little with ridge depth, which is due to the internal loss does not change significantly with the ridge depth.

Using these obtained basic characteristic parameters, the power consumption of the semiconductor laser can be calculated. As an example, the calculation is first performed under the condition settings that have been used in previous studies. Assuming that the optical intensity at which the photodetector can receive signals error-free at 10 Gbit/s operation is -13 dBm and the total coupling loss is 5 dB, the optical output required for the laser is 0.16 mW. Since the power required for the photodetector increases by a factor of √n when the modulation speed increases by a factor of n, the optical output power required for the laser is 0.22 mW at 20 Gbit/s operation. The power consumption can be obtained by multiplying the bias current by the bias voltage, where the voltage is related to the differential resistance. The differential resistance can be obtained from the results discussed in Section 2.3.2. Fig. 2.25 (a) shows the power consumption required to output the required optical output of 0.16 mW for the laser at 10 Gbit/s operation. As the ridge

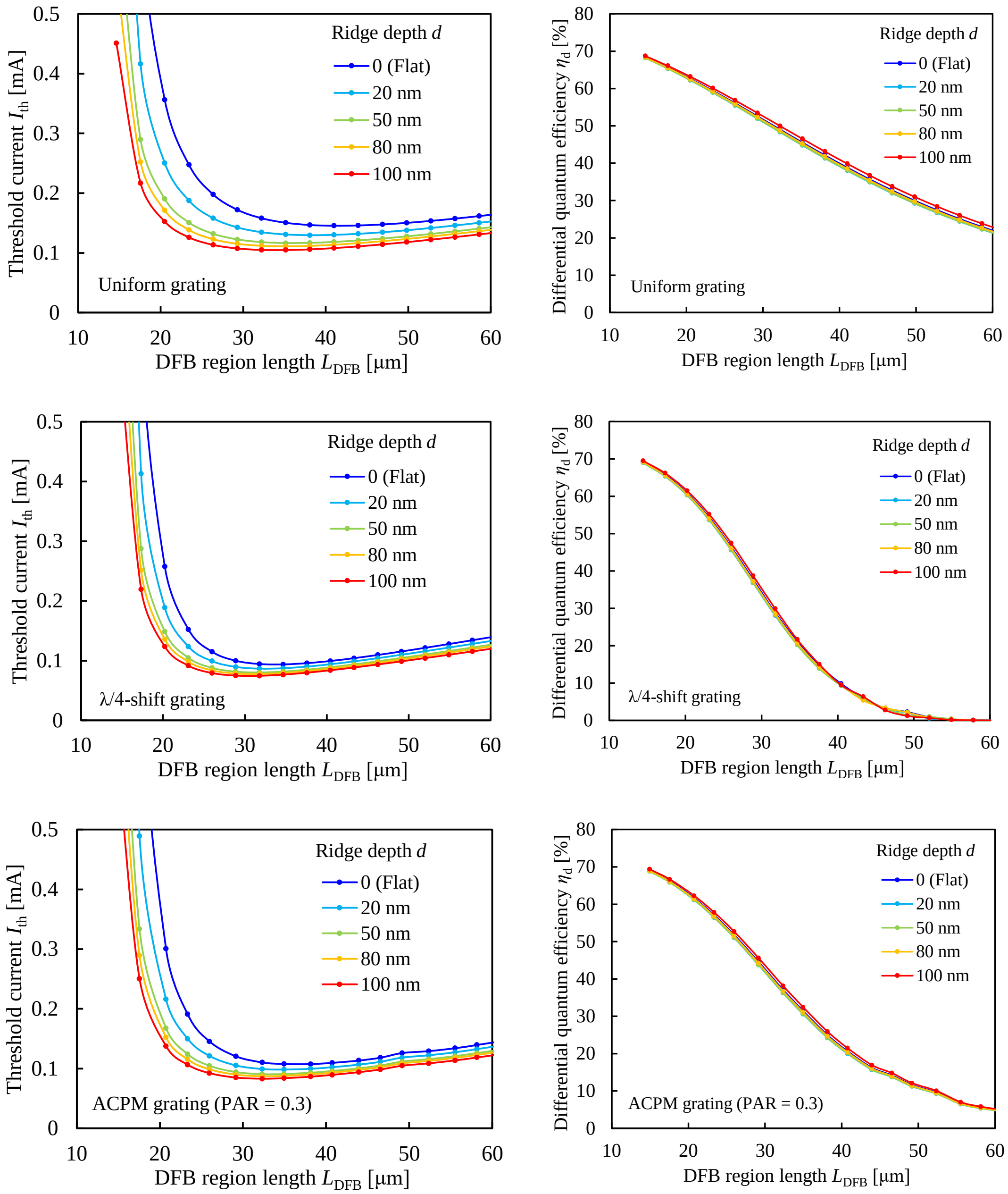

Fig. 2.24 DFB region dependence of threshold current and differential quantum efficiency for each grating.

depth is increased, the differential resistance increases after d = 50 nm, but the injection current is minute, resulting in a larger contribution to the reduction of the threshold current. Fig. 2.25 (b) shows the power required to operate at 10 Gbit/s. The modulation speed is affected by the parameters of optical confinement, threshold current, and active layer volume, resulting in the lowest power consumption near a DFB region length of 30

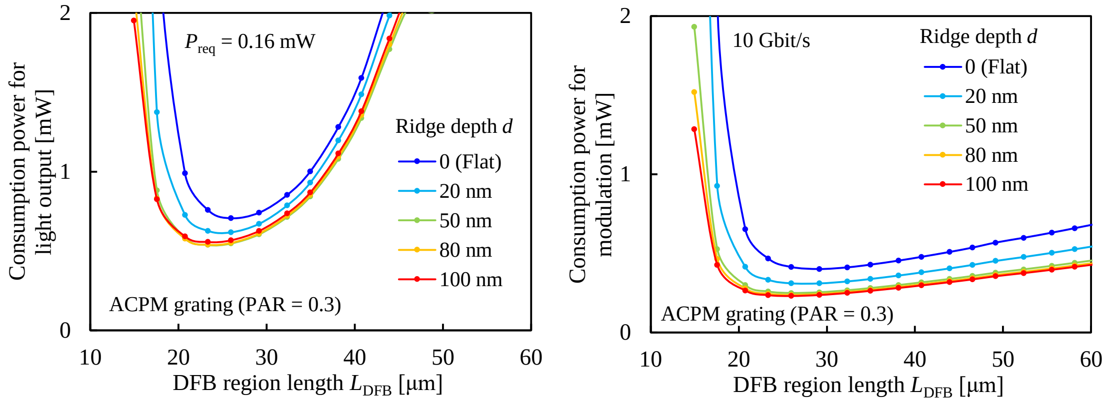

(a) (b)

Fig. 2.25 DFB region dependence of consumption power for 10 Gbit/s.

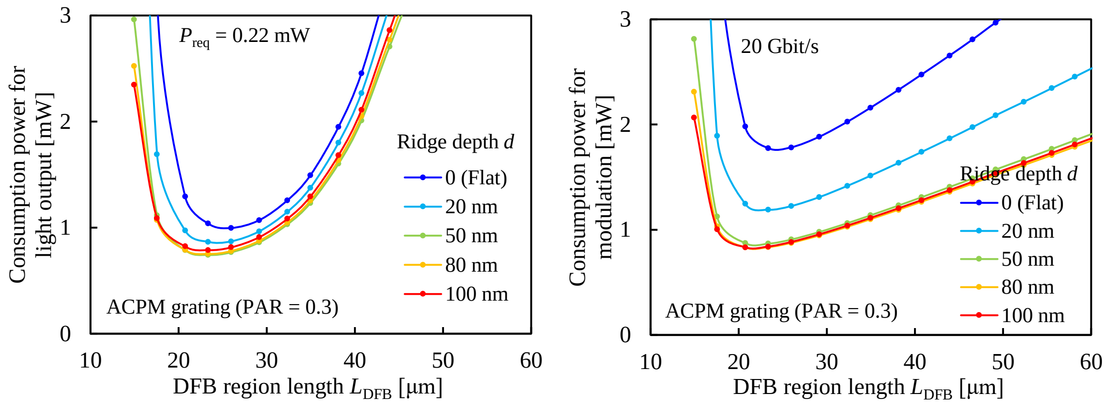

(a) (b)

Fig. 2.26 DFB region dependence of consumption power for 20 Gbit/s.

μm. Lasers for signal transmission need to satisfy both requirements based on optical output power and requirements based on modulation speed. Therefore, at 10 Gbit/s operation, the power consumption is ruled by the optical output requirement, and the energy cost is 52 fJ/bit. On the other hand, the 20 Gbit/s operation shown in Fig. 2.26 is limited by the modulation speed, indicating that the optimal structure is determined by the combination of required optical output and modulation speed.

The above outlines a method for determining power consumption, but in determining the optimal structure, it is necessary to select the parameters to be varied. The number of quantum wells is one of the structural parameters that can be varied, and high-speed

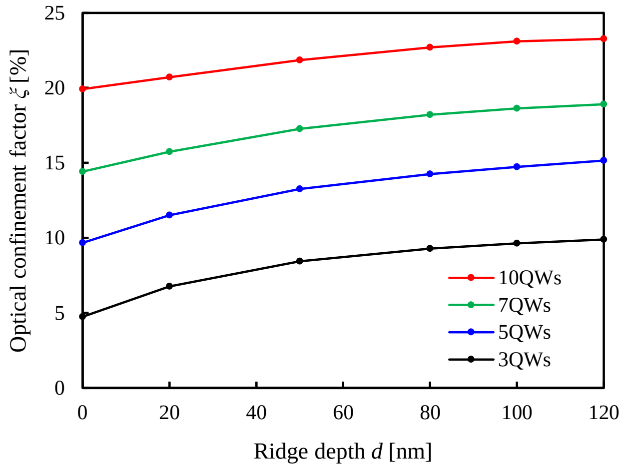

Fig. 2.27 Relationship between optical confinement factor and ridge depth with various quantum well number.

modulation is expected by increasing the number of wells. However, increasing the number of active layers also leads to an increase in active layer volume, so it cannot be said that increasing the number of active layers is generally effective in reducing power consumption. Calculations were made to determine if the number of active layers needs to be changed in terms of power consumption. Fig. 2.27 shows the relationship between optical confinement factor and ridge depth for each number of active layers. The optical confinement factor increases with increasing ridge depth and well number. Using these values, the results obtained for the threshold current are shown in the Fig. 2.28. The threshold current is affected by how the optical confinement per layer varies with the number of wells. Therefore, increasing the number of wells basically results in an increase in the threshold current. Next, assuming the same configuration as before, the Fig. 2.29 shows the results of calculating the power consumption required to output 0.22 mW or more light at 20 Gbit/s operation. First, with respect to the requirement by optical output, the power consumption is also higher because the threshold current increases while the internal loss remains almost unchanged for an increase in the number of wells. On the other hand, with respect to the modulation speed requirement, the increase in differential gain due to the reduction in the threshold carrier density has improved the modulation

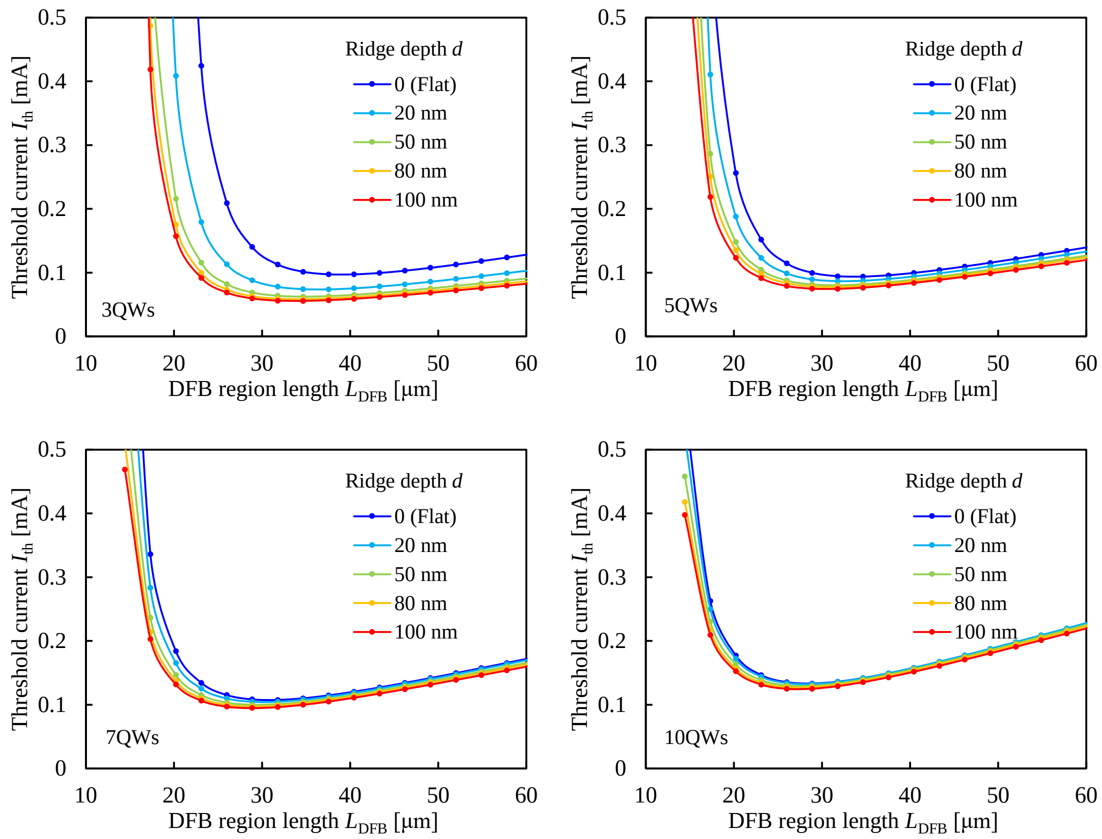

Fig. 2.28 DFB region dependence of threshold current for each well number.

efficiency, resulting in lower power consumption in flat structures and at d = 20 nm with an increase in wells. However, for d > 50 nm, the contribution of the increase in threshold current due to the increase in active layer volume is significant, and the minimum power consumption is found to be at 5QWs. Therefore, in subsequent calculations, the number of wells was fixed at 5 layers.

As mentioned above, the power consumption of the laser must satisfy both optical output and modulation speed requirements. These requirements vary depending on the application. Therefore, structures that give the minimum power consumption are calculated for 10 Gbit/s and 20 Gbit/s, respectively, assuming various optical output power requirements, and the results are summarized in Table 2.4. The red region represents the requirement for optical output, while the blue region represents the requirement for modulation speed to be disciplined. A comparison of 10 Gbit/s and 20 Gbit/s operation shows that 20 Gbit/s operation is capable of lower power consumption

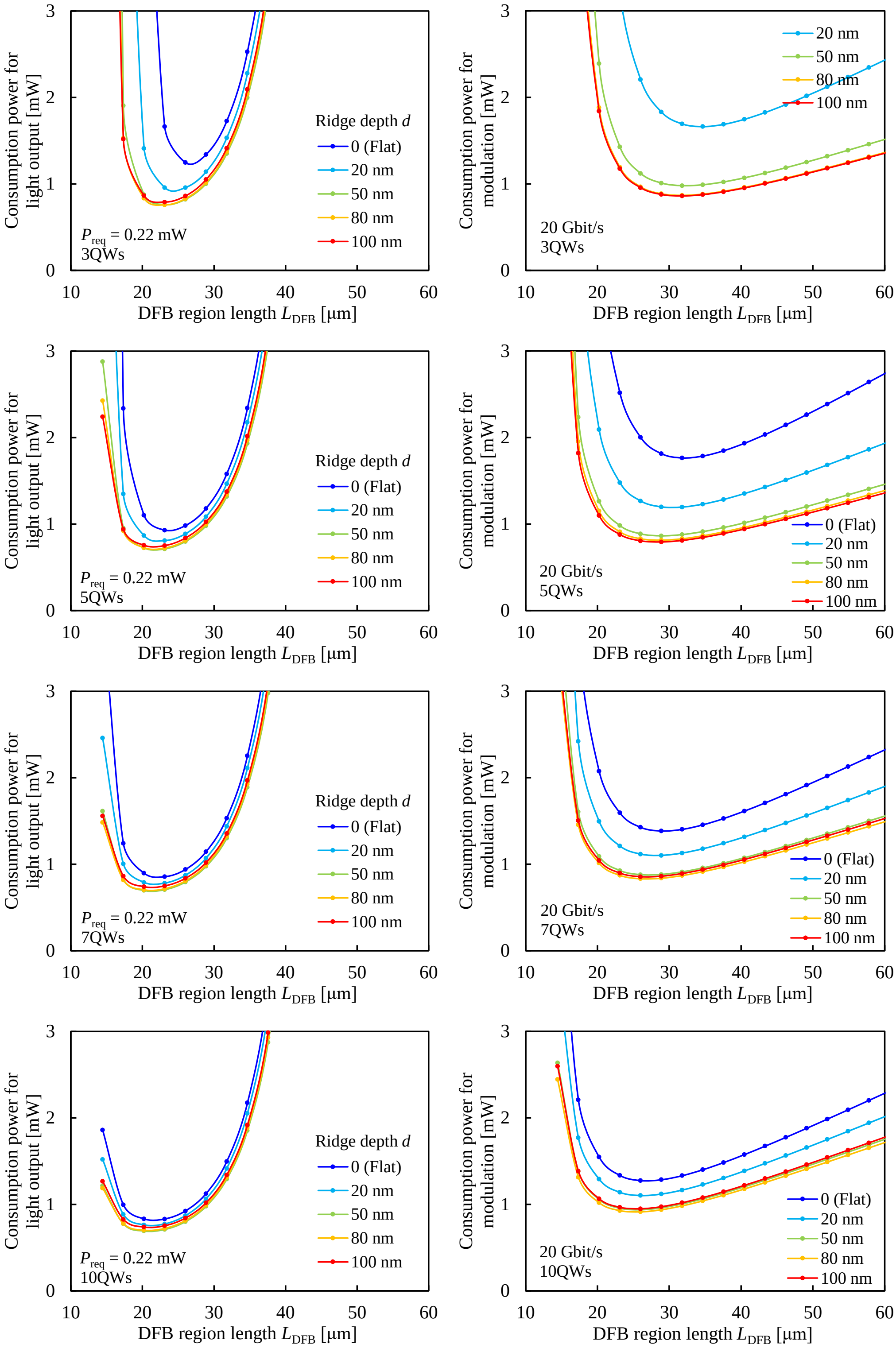

Fig. 2.29 DFB region dependence of consumption power for each number of wells.

when both are limited by optical output. However, 20 Gbit/s operation requires more power to achieve modulation speed, and 10 Gbit/s operation can be transmitted at lower

Table 2.4 Optimal structures for each performance requirement.

Required power [dBm]	Required power [mW]	10 Gbit/s d [nm]	10 Gbit/s L_{DFB} [μm]	10 Gbit/s Energy cost [fJ/bit]	20 Gbit/s d [nm]	20 Gbit/s L_{DFB} [μm]	20 Gbit/s Energy cost [fJ/bit]
-3	0.50	50	20	188	50	20	94
-4	0.40	50	20	141	50	20	70
-5	0.32	50	20	110	50	20	55
-6	0.25	50	20	83	100	23	43
-7	0.20	50	23	64	100	26	40
-8	0.16	50	23	52	100	29	40
-9	0.13	50	23	41	100	29	40
-10	0.10	50	23	34	100	29	40
-11	0.08	50	23	28	100	29	40
-12	0.06	50	23	23	100	29	40
-13	0.05	100	26	21	100	29	40
-14	0.04	100	29	21	100	29	40
-15	0.03	100	29	21	100	29	40
-20	0.03	100	29	21	100	29	40
-25	0.03	100	29	21	100	29	40
-30	0.03	100	29	21	100	29	40

energy cost when transmission is possible with a small optical output.

2.6 Conclusion

In this chapter, we analyzed semiconductor membrane lasers, focusing on key parameters such as threshold current, external differential quantum efficiency, and optical confinement in the lateral and cavity directions. The objective was to identify methods for analyzing the fundamental characteristics and overall performance, and to explore ways to optimize these lasers. Membrane lasers offer a promising approach to enhancing optical confinement and improving laser performance by increasing the vertical refractive index difference. There, investigation of structures that can further reduce power consumption by improving the optical confinement in the lateral and cavity directions was conducted.

First, for the lateral optical confinement structure, a buried-ridge-waveguide (BRW) structure, in which the side cladding layer is thinner than the active layer, was proposed and investigated. Focusing on the fundamental characteristics of internal loss and differential resistance, the ridge depth was designed to minimize these parameters while increasing optical confinement, and d = 50 nm was found to be optimal. Also, by considering the slope near the active layer, which is caused by the fabrication process, the experimental guideline of W_d < 0.5 μm was obtained.

Next, the introduction of asymmetric corrugation pitch modulation (ACPM) as an optical confinement structure in the cavity direction is examined. The transfer matrix method (TMM), which is commonly used in the analysis of DFB lasers, is clarified in detail, and the rate equation is extended to the cavity direction to analyze the distribution of carrier density inside the cavity as well. Using these methods, a method was established to obtain the optimal design in the membrane DR laser of ACPM gratings, which is expected to suppress spatial hole-burning. When hole burning occurs, the supply of carriers is insufficient, and the main mode gain is reduced. The gain difference between the main and side modes was analyzed for each structure, and it was estimated that the most stable operation with the best gain difference is achieved when the phase arrange region (PAR) length is 0.25 and 0.31 at cavity lengths of 30 μm and 40 μm, respectively.

And for the power consumption analysis, we first calculated the laser fundamental characteristics such as threshold current and external differential quantum efficiency using the calculation method and parameters described above. The relationship between the ridge depth and optical confinement factor of the BRW structure and the number of quantum wells was clarified. Although increasing the number of quantum wells is expected to improve the modulation speed, 5QWs was found to be optimal in terms of power consumption. Since the power consumption of semiconductor lasers varies depending on the application, we calculated the optimum structure for varying power requirements at 10 Gbit/s and 20 Gbit/s, and presented guidelines for semiconductor laser design based on the required performance.

Reference

[1] L. A. Coldren, S. W. Corzine, and M. L. Mashanovitch, *Diode lasers and photonic integrated circuits.* New York, NY, USA: Wiley-Interscience, 1995.

[2] M. Fujita, A. Sakai, and T. Baba, “Ultrasmall and ultralow threshold GaInAsP-InP microdisk injection lasers: design, fabrication, lasing characteristics, and spontaneous emission factor,” *IEEE Journal of selected topics in Quantum Electronics,* vol. 5, pp. 673-681, 1999.

[3] N. Nunoya, M. Nakamura, M. Morshed, S. Tamura, and S. Arai, “High-performance 1.55-µm wavelength GaInAsP-InP distributed-feedback lasers with wirelike active regions,” *IEEE Journal of Selected Topics in Quantum Electronics,* vol. 7, pp. 249-258, 2001.

[4] M. Bugajski and W. Lewandowski, “Concentration-dependent absorption and photoluminescence of n-type InP,” *Journal of Applied Physics,* vol. 57, pp. 521-530, 1985.

[5] H. Casey Jr and P. Carter, “Variation of intervalence band absorption with hole concentration in p-type InP,” *Applied Physics Letters,* vol. 44, pp. 82-83, 1984.

[6] E. Hecht, "Optics," *Addison-Wesley*, 2002.

[7] C. Hilsum, “Simple empirical relationship between mobility and carrier concentration,” *Electronics Letters,* vol. 10, pp. 259-260, 1974.

[8] W. Walukiewicz, J. Lagowski, L. Jastrzebski, P. Rava, M. Lichtensteiger, C. Gatos, *et al.*, “Electron mobility and free-carrier absorption in InP; determination of the compensation ratio,” *Journal of Applied Physics,* vol. 51, pp. 2659-2668, 1980.

[9] D. Anderson, N. Apsley, P. Davies, and P. Giles, “Compensation in heavily doped n-type InP and GaAs,” *Journal of applied physics,* vol. 58, pp. 3059-3067, 1985.

[10] M. Sotoodeh, A. Khalid, and A. Rezazadeh, “Empirical low-field mobility model for III–V compounds applicable in device simulation codes,” *Journal of applied physics,* vol. 87, pp. 2890-2900, 2000.

[11] M. Littlejohn, J. Hauser, and T. Glisson, “Velocity-field characteristics of Ga1− xInxP1− yAsy quaternary alloys,” *Applied Physics Letters,* vol. 30, pp. 242-244, 1977.

[12] D. Caughey and R. Thomas, “Carrier mobilities in silicon empirically related to doping and field,” *Proceedings of the IEEE,* vol. 55, pp. 2192-2193, 1967.

[13] A. Katz, W. Dautremont-Smith, S. Chu, P. Thomas, L. Koszi, J. Lee, et al.,

"Pt/Ti/p-In0. 53Ga0. 47As low-resistance nonalloyed ohmic contact formed by rapid thermal processing," *Applied Physics Letters*, vol. 54, pp. 2306-2308, 1989.

[14] G. Franz and M. C. Amann, "Extremely Low Contact Resistivity of Ti/Pt/Au Contacts on p+-InGaAs as Determined by a New Evaluation Method," *Journal of The Electrochemical Society*, vol. 140, pp. 847-850, 1993.

[15] R. Tucker, J. Wiesenfeld, P. Downey, and J. Bowers, "Propagation delays and transition times in pulse-modulated semiconductor lasers," *Applied Physics Letters*, vol. 48, pp. 1707-1709, 1986.

[16] T. Tomiyasu, T. Hiratani, D. Inoue, N. Nakamura, K, Fukuda, T. Uryu, T. Amemiya N. Nishiyama and S. Arai, "High-differential quantum efficiency operation of GaInAsP/InP membrane distributed-reflector laser on Si", Appl. Phys. Express, vol. 10. p. 062702. 2017.

[17] D. Inoue, J. Lee, K. Doi, T. Hiratani, Y. Atsuji, T. Amemiya, et al., "Room-temperature continuous-wave operation of GaInAsP/InP lateral-current-injection membrane laser bonded on Si substrate," *Applied Physics Express*, vol. 7, pp. 072701, 2014.

[18] T. Tomiyasu, T. Hiratani, D. Inoue, K. Fukuda, N. Nakamura, T. Amemiya, N. Nishiyama, S. Arai, "Waveguide Loss Reduction of Lateral-current-injection Type GaInAsP/InP Membrane Fabry-Perot Laser," *Japanese Journal of Applied Physics*, Vol. 56, No. 5, pp. 050311, 2017.

[19] H. Kogelnik and C. Shank, "Stimulated emission in a periodic structure," *Applied Physics Letters*, vol. 18, pp. 152-154, 1971.

[20] R. Bonello and I. Montrosset, "Analysis of multisection and multielectrode semiconductor lasers," *Journal of lightwave technology*, vol. 10, pp. 1890-1900, 1992.

[21] G. Bjork and O. Nilsson, "A new exact and efficient numerical matrix theory of complicated laser structures-Properties of asymmetric phase-shifted DFB lasers," *Journal of lightwave technology*, vol. 5, pp. 140-146, 1987.

[22] T. Makino and J. Glinski, "Transfer matrix analysis of the amplified spontaneous

emission of DFB semiconductor laser amplifiers," *IEEE journal of quantum electronics*, vol. 24, pp. 1507-1518, 1988.

[23] J. Hong, W. Huang, and T. Makino, "On the transfer matrix method for distributed-feedback waveguide devices," *Journal of lightwave technology*, vol. 10, pp. 1860-1868, 1992.

[24] T. Makino, "Threshold condition of DFB semiconductor lasers by the local-normal-mode transfer-matrix method: correspondence to the coupled-wave method," *Journal of lightwave technology*, vol. 12, pp. 2092-2099, 1994.

[25] J. Hong, W. Huang, and T. Makino, "On the transfer matrix method for distributed-feedback waveguide devices," *Journal of lightwave technology*, vol. 10, pp. 1860-1868, 1992.

[26] M. Yamada and Y. Suematsu, "Analysis of gain suppression in undoped injection lasers," *J. Appl. Phys*., vol. 1, April 1981.

[27] R. A. Soref and B. R. Bennett, "Electrooptical effects in silicon," *IEEE J. Quantum Electron*., vol. 23, no. 1, pp. 123–129, Jan. 1987.

[28] W. Streifer, D. Scifres and R. Burnham, "Coupling coefficients for distributed feedback single- and double-heterostructure diode lasers," in *IEEE Journal of Quantum Electronics*, vol. 11, no. 11, pp. 867-873, 1975.

[29] H. Haus and C. Shank, "Antisymmetric taper of distributed feedback lasers," in *IEEE Journal of Quantum Electronics*, vol. 12, no. 9, pp. 532-539, 1976.

[30] H. Soda, Y. Kotaki, H. Sudo, H. Ishikawa, S. Yamakoshi and H. Imai, "Stability in single longitudinal mode operation in GaInAsP/InP phase-adjusted DFB lasers," in *IEEE Journal of Quantum Electronics*, vol. 23, no. 6, pp. 804-814, 1987.

[31] M. Okai, N. Chinone, H. Taira and T. Harada, "Corrugation-pitch-modulated phase-shifted DFB laser," in *IEEE Photonics Technology Letters*, vol. 1, no. 8, pp. 200-201, 1989.

[32] M. Okai, "Spectral characteristics of distributed feedback semiconductor lasers and their improvements by corrugation-pitch-modulated structure," *J. of Appl. Phys*., Vol. 75, pp. 1-29, 1994.

[33] K. Nakahara, Y. Wakayama, K. Hiruma, T. Kitatani, K. Shinoda, T. Fukamachi, Y. Sakuma, and S. Tanaka, "28-Gb/s Directly Modulated InGaAlAs ACPM DFB Lasers with High Mask Margin of 22% at 55°C," *Optical Fiber Communication Conference/National Fiber Optic Engineers Conference 2013*, OTh4H.3, 2013.

[34] W. Fang, "Study of High Temperature and High Efficiency Operation of Membrane Photonic Integrated Circuits on Si Substrate" Doctoral Thesis, Tokyo institute of technology, 2022.

[35] D. A. Miller, "Device requirements for optical interconnects to silicon chips," *Proceedings of the IEEE,* vol. 97, pp. 1166-1185, 2009.

Chapter 3
Fabrication technologies for membrane photonic devices

3.1 Introduction	88
3.2 Fabrication process and equipment	89
3.3 Selective area regrowth using organo-metallic vapor-phase epitaxy (OMVPE)	109
3.4 Surface grating formation using electron beam lithography	115
3.4.1 Grating design	115
3.4.2 Fabrication process	120
3.5 Conclusion	125
Reference	127

3.1 Introduction

In this chapter, fabrication techniques for membrane lasers are discussed. A structure to improve optical confinement was introduced in Chapter 2, and the proposed BRW structure can be realized by controlling the thickness of the side cladding layers that embed the active layer. First, the membrane laser fabrication process and the equipment used are reviewed, then focus on the realization of the BRW structure using selective regrowth of organo-metallic vapor-phase epitaxy (OMVPE) and discuss the growth conditions. The latter part of this chapter focuses on the formation of grating. First, the design principle of the grating for the membrane DR laser is described, and based on this design, experimental conditions are investigated. Then, problems in the conventional grating fabrication process are discussed, and improvements made to solve them are described.

3.2 Fabrication process and equipment

This section describes the semiconductor membrane DR laser fabrication process and the equipment used in each process. Table 3.1 shows the initial substrate structure of the semiconductor membrane laser fabricated in this study, and Fig. 3.1 shows a

Table 3.1 Initial wafer layer structure

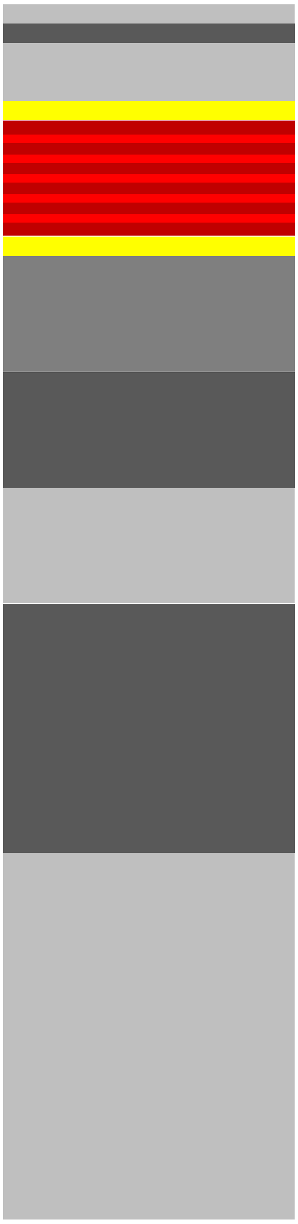

Layer	Material	Thickness [nm]
Protection	*u*-InP	10
Protection	$Ga_{0.47}In_{0.53}As$	10
Cap	*u*-InP	50
u-OCL	$Ga_{0.21}In_{0.79}As_{0.46}P_{0.54}$	15
TS barrier	$Ga_{0.26}In_{0.74}As_{0.49}P_{0.51}$	10
CS well	$Ga_{0.22}In_{0.78}As_{0.81}P_{0.19}$	5.4
TS barrier	$Ga_{0.26}In_{0.74}As_{0.49}P_{0.51}$	10
CS well	$Ga_{0.22}In_{0.78}As_{0.81}P_{0.19}$	5.4
TS barrier	$Ga_{0.26}In_{0.74}As_{0.49}P_{0.51}$	10
CS well	$Ga_{0.22}In_{0.78}As_{0.81}P_{0.19}$	5.4
TS barrier	$Ga_{0.26}In_{0.74}As_{0.49}P_{0.51}$	10
CS well	$Ga_{0.22}In_{0.78}As_{0.81}P_{0.19}$	5.4
TS barrier	$Ga_{0.26}In_{0.74}As_{0.49}P_{0.51}$	10
CS well	$Ga_{0.22}In_{0.78}As_{0.81}P_{0.19}$	5.4
TS barrier	$Ga_{0.26}In_{0.74}As_{0.49}P_{0.51}$	10
u-OCL	$Ga_{0.21}In_{0.79}As_{0.46}P_{0.54}$	15
Cap	*u*-InP	100
p-contact	*p*-$Ga_{0.47}In_{0.53}As$	100
InP etch stop	*u*-InP	100
GaInAs etch stop	*u*-$Ga_{0.47}In_{0.53}As$	300
Substrate	*u*-InP	

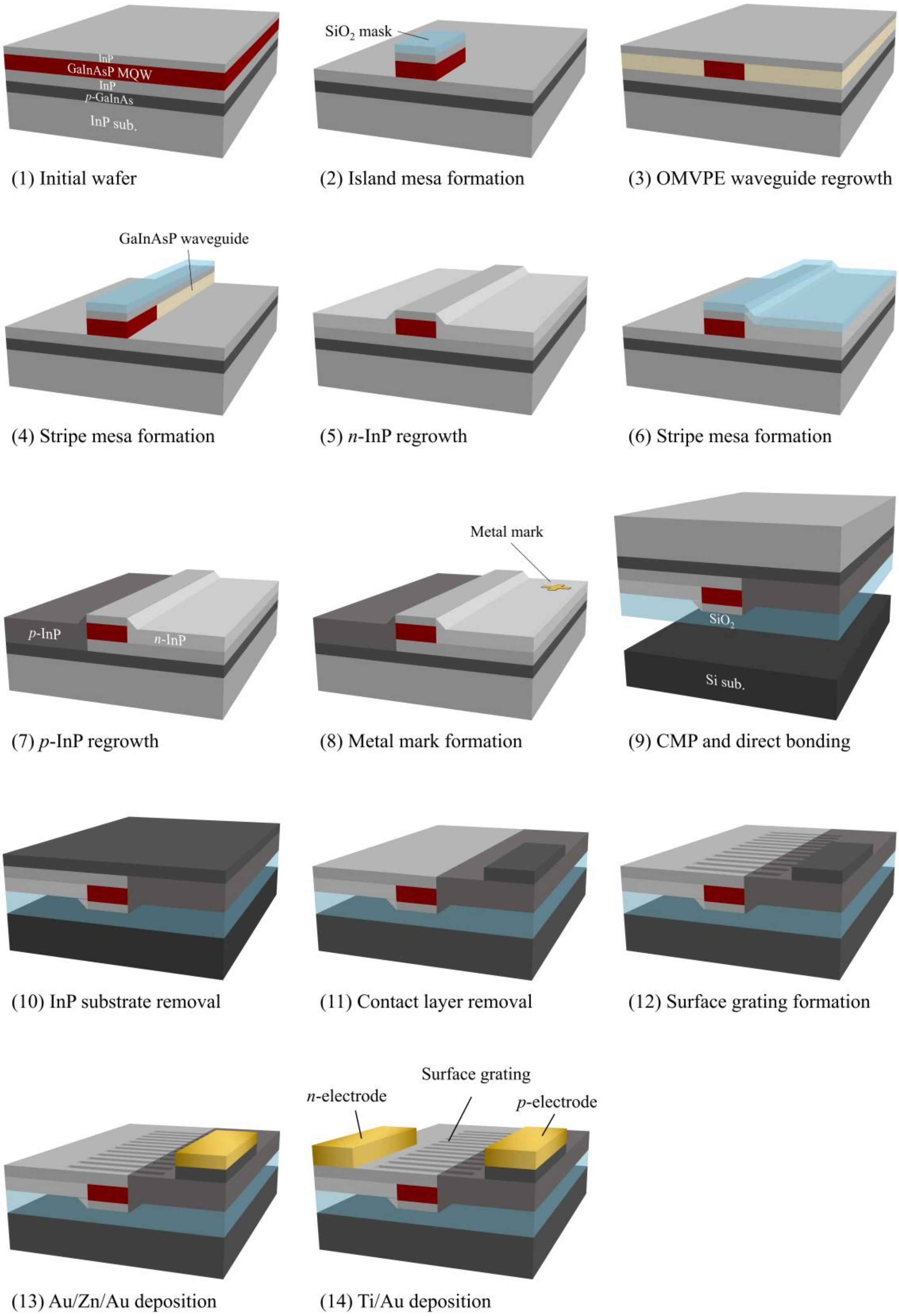

Fig. 3.1 Fabrication process of membrane DR laser

schematic of the fabrication process. The initial wafer comprises five GaInAsP/GaInAsP quantum wells (QWs) with InP cap layers to suppress surface recombination. The *p*-GaInAs contact layer is formed beneath the bottom InP layer on the InP substrate, which later becomes the top side after bonding. The process involves three selective regrowth steps using OMVPE for waveguide regrowth and p-i-n junction. Subsequently, wafer bonding to a Si substrate takes place, with the bonding technologies. After the InP substrate is removed by wet chemical etching, selective etching of the unnecessary contact layer is performed. Finally, the DFB or DR structure is formed by employing electron beam lithography (EBL) and dry etching to create a surface grating, followed by metal deposition. The detailed process and fabrication condition were shown as follow:

(1) Initial wafer

The structure of initial wafer is given in Table 3.1. Active layers consist of five 1% compressively strained $Ga_{0.22}In_{0.78}As_{0.81}P_{0.19}$ quantum wells with six 0.15% tensile strained $Ga_{0.26}In_{0.74}As_{0.49}P_{0.51}$ barriers sandwiched by optical confinement layers (OCLs).

(2) Island mesa formation

The fabrication process was started from the removal of protective cap layers. Then GaInAsP QWs island was formed by combining dry-etching and wet-etching. Firstly, 50-nm-thick SiO_2 mask was deposited on the wafer by PECVD using condition of エラー! 参照元が見つかりません。. The island pattern was exposed by maskless photolithography system with the exposure power of ~ 80 mJ/cm^2 and speed of 3.6 mm/sec. S1818 was used as the photoresist for lithography, and spin-coating was performed under the conditions shown in the Table 4.3. After development using MF320, residual resist was removed by O_2 ashing. Secondly, CF_4 RIE dry etching was performed under the conditions in Table 3.3 to transfer the resist pattern to SiO_2, and then S1818 photoresist was removed by acetone spray. The third step is the transfer of the pattern to the semiconductor. This step is divided into two stages, first using CH_4/H_2 RIE dry etching to etch the InP and GaInAsP active layers. The condition of dry etching is shown in Table 3.4. The remaining GaInAsP active layer is then removed by wet etching using the chemical solution of $H_2SO_4 : H_2O_2 : H_2O = 1 : 1 : 40$. The etching amount of dry and wet etching was determined to control the side wall shape and side etching amount.

(3) OMVPE regrowth of the passive layer

Passive waveguide layers were selectively regrown around the GaInAsP by OMVPE. Butt-joint built-in (BJB) structures were formed by precisely controlling the wet etching time and regrowth time. The regrowth thickness was determined to minimize the reflection at the interface between active and passive region. The detailed condition research is shown in previous study [1]. After regrowth, the SiO_2 mask was removed with 7% buffered HF (BHF) for 1 min.

(4) Stripe mesa formation and (5) *n*-InP regrowth

A 10-µm-width stripe mesa was formed by using the same lithography and etching method described in (3). In this study, the BRW structure is formed by this regrowth process. The shape and thickness are related to the condition of wet etching, mask width and regrowth time. The detail will be described in the next section.

(6) Stripe mesa formation and (7) *p*-InP regrowth

A 40-µm-width stripe mesa was formed by the same way described in (3). In this step, the regrown *n*-InP and bottom 100-nm-thick *p*-InP were removed together by chemical solution of $HCl : CH_3COOH = 1 : 3$. The *p*-InP would be grown on the GaInAsP (1.3Q) contact layer.

(8) Metal mark formation

After the bonding process, the 150 nm thick semiconductor on top layer makes the alignment mark blurred and difficult to detect automatically. Thus, we addressed this problem by transferring to a clear metal mark before bonding. The metal mask pattern was exposed by maskless photolithography system with the exposure power of ~ 25 mJ/cm^2 and speed of 3.6 mm/sec. AZ5218 was used as the photoresist for lithography and spin-coating was performed under the conditions shown in the Table 4.6. Then, after reversal baking at 120°C for 120 seconds on a hot plate, full exposure was performed at an exposure power of 250 mJ. After development using MIF300, residual resist was removed by O_2 ashing. Dry etching was performed until the bottom 100 nm InP layer was removed so that the deposited metal appeared on the surface after bonding. A Ti/Au (25 nm/200 nm) was evaporated by EB evaporation.

(9) Chemical mechanical polishing and surface activated bonding

Although surface flatness is important for direct bonding, the BRW structure grows the cladding thinner than the core, resulting in a maximum thickness difference of about 100 nm. Chemical mechanical polishing (CMP) was therefore introduced to flatten the surface. 2-μm SiO_2 was deposited by PECVD, then, the wafer was polished ~1 μm. After polishing, the wafer was cleaned by PVA brush using megasonic system. Then III-V wafer was bonded to Si substrate by using a-Si assisted surface activated bonding technique. More detail about this bonding technique is discussed in a previous study [1].

(10) InP substrate removal

After bonding, 350-μm-thick InP substrate was removed by HCl for approximately 1 hour. GaInAs etch-stop layer was removed by $H_2SO_4 : H_2O_2 : H_2O = 1 : 1 : 40$ for 6 min, and InP etch-stop layer was removed by $HCl : CH_3COOH = 1 : 4$ for 1 min.

(11) Contact layer removal

The contact layer was etched by selective wet etchant of $H_2SO_4 : H_2O_2 : H_2O = 1 : 1 : 40$, except for the *p*-side electrode region. The lithography method was the same as described in (2).

(12) Surface grating formation

A 25-nm-thick SiO_2 mask was deposited by PECVD. As an EB lithography resist, 300-nm-thick ZEP 520A was coated on substrate. A surface grating pattern of SiO_2 was formed by electron-beam lithography with dose amount of 140 μC/cm^2. After formation of grating pattern SiO_2 mask, this pattern was transferred on a surface InP by using dry etching, which condition is shown in Table 3.4.

(13) Au/Zn/Au deposition

The *p*-side electrode was deposited on the contact layer by using AZ5218 and maskless lithography. Before deposition, the surface of p^+-GaInAs was processed by $H_2SO_4 : H_2O_2 : H_2O = 1 : 1 : 40$ for 3 sec to clean the surface. Then, Au/Zn/Au = 25/50/300 nm metal layers were evaporated by resistive thermal evaporation. The deposited metal was annealed at 350°C for 1 min in N_2 ambient to alloying the Au and Zn.

(14) Ti/Au deposition

The electrode pattern was formed both *p*- and *n*-side by using AZ5218 and maskless lithography. Before deposition, the top *p*-InP cap layer at n-electrode region was etched by CH_4/H_2 RIE. After that, Ti/Au = 25 nm/200 nm was deposited by EB evaporation.

Finally, the processed substrate is cleaved into bars at the waveguide or DFB section to measure the optical output characteristics.

The following section describes the equipment used in the series of fabrication procedures for the membrane DFB/DR lasers described above.

Organo-metallic vapor phase epitaxy (OMVPE)

Fig. 3.2 OMVPE equipment of HR3255.

Molecular beam epitaxy (MBE) and organo-metallic vapor phase epitaxy (OMVPE) are suitable for obtaining uniform thin films over large areas. MBE is a method of epitaxial growth on a substrate crystal by feeding raw materials with molecular beams in an ultrahigh vacuum. In most cases, the raw materials are heated in an ultrahigh vacuum growth chamber and supplied with molecular beams that have a mean free path sufficiently longer than the chamber size. Because the growth takes place in an ultrahigh vacuum, crystals of extremely high purity can be grown. OMVPE is a semiconductor crystal growth method using organo-metallic and material gases, and in addition to being able to grow large-area crystals, it is highly controllable. The organometallic materials used for crystal growth are liquid or solid at room temperature but have high saturation vapor pressure. Hence, they can be supplied to the reaction chamber as a gas by using H_2 as a carrier gas, and crystals are grown on the substrate surface at high temperature. MBE have difficulty in regrowth due to the high sticking coefficients of group III atoms on the mask materials and polycrystalline islands are easily formed on the mask during the growth. Therefore, OMVPE is generally used for selective growth.

In this study, HR-3255 from TAIYO NIPPON SANSO CORPORATION was used for initial wafer growth, regrowth of GaInAsP waveguides and InP side cladding. As a material source, group-III material (metal organic) of tri-methyl-indium (TMI), tri-ethyl-gallium (TEG), and tri-methyl-gallium (TMG) and group-V material of AsH_3 (arsine) and PH_3 (phosphine) are implemented. Epitaxial growth was performed on a carbon susceptor coated with SiC at 82 Torr pressure and 12 rpm substrate rotation.

Plasma enhanced chemical vapor phase deposition (PECVD)

PECVD equipment deposits materials on substrates by applying high-frequency voltage to parallel plate electrodes at the top and bottom of the chamber; the appearance of the PECVD equipment PD-100ST manufactured by SAMCO is shown in Fig. 3.3. In this laboratory, TEOS (tetraethyl orthosilicate) and oxygen O_2 are used as material gases, mainly for SiO_2 deposition. PECVD uses plasma to decompose the source gases, resulting

Fig. 3.3 Plasma-enhanced chemical vapor phase deposition (PECVD) system.

Table 3.2 Deposition conditions of SiO_2.

Parameters	Value
TEOS flow	3 sccm or 1 sccm
O_2 gas flow	233 sccm
RF power	30 W
Pressure	70 Pa
Temperature	280°C
Deposition rate	~50 nm/min or ~25 nm/min

in lower deposition temperatures and less strain. In addition, the ability to form the film uniformly over a large area with good step coverage is also an advantage.

Reactive ion etching (RIE)

This dry etching system is used for transferring resist patterns onto SiO_2 or SiO_2 patterns onto semiconductors. In this system, a high-frequency voltage is applied to a parallel plate electrode into which a material gas is introduced to radicalize the reaction gas. The radicalized gas is irradiated onto the substrate surface to perform etching.

Fig. 3.4 Reactive-ion-etching (RIE) system (RIE-10NR SAMCO)

Compared to wet etching using a chemical solution, the damage to the substrate surface is greater, but a highly perpendicular etching shape can be obtained. In this study, CF_4 gas is used for etching SiO_2 and CH_4/H_2 gas for etching semiconductors. In the etching process using CH_4/H_2 gas, the polymers generated tend to interfere with the vertical etching profile. By inserting an ashing process using O_2 plasma between the CH_4/H_2 etching process and repeating this cycle, high verticality can be achieved. **エラー! 参照元が見つかりません。** shows the appearance of reactive-ion-etching system of 10-NR (SAMCO).

Table 3.3 Etching conditions of SiO_2 using CF_4 RIE.

Parameters	Value
CF_4 gas flow	10 sccm
Pressure	1 Pa
RF power	25 W
Time	10 min (~50 nm)

Table 3.4 Etching conditions of III-V semiconductor using CH_4/H_2 RIE.

Parameters	Step 1	Step 2
CH_4 gas flow	10 sccm	-
H_2 gas flow	40 sccm	-
O_2 gas flow	-	30 sccm
Pressure	6 Pa	10 Pa
RF power	100 W	50 W
Time	60 sec	40 sec

Maskless photolithography system

Fig. 3.5 shows the appearance of the maskless exposure system (manufactured by Japan Science Engineering), and Fig. 3.6 shows the principle. The maskless exposure system uses a digital micromirror device (DMD) as the exposure pattern generator, and a CCD camera is used to scan the substrate, eliminating the need for a mask. In addition,

Fig. 3.5 Maskless photolithography system (DNK IP-1007-2(MX-1204))

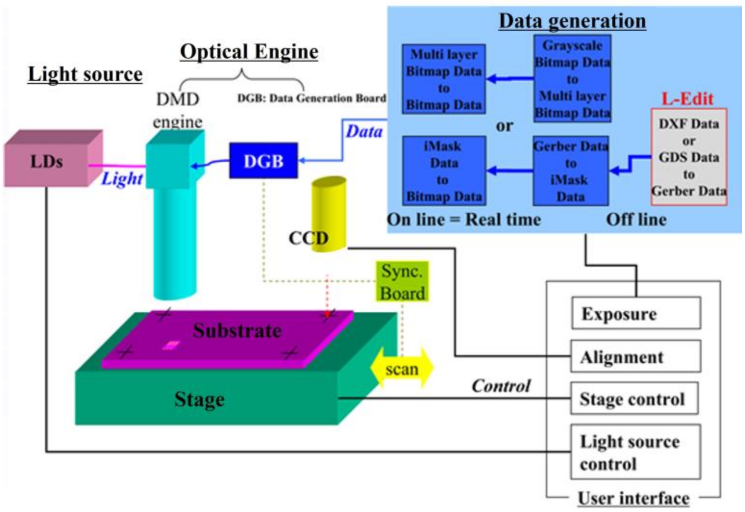

Fig. 3.6 Maskless exposure system principle

since alignment is performed automatically, alignment error can be kept within ±100 nm. The improved alignment accuracy enables structures such as stripes and electrodes to be formed at positions close to their design values, regardless of the operator's skill. Also, since no mask is required and the pattern is imported from CAD data each time, the pattern can be changed as needed. The elimination of mask fabrication enables cost reduction and shortening of time to exposure. It is also powerful for small-quantity, high-mix production and research and development applications.

O2 plasma reactor

After etching the SiO_2 mask using RIE, resist removal is performed by acetone spraying with heated acetone. Since there may be resist that has not been sufficiently removed, an ashing process is performed using the plasma reactor RP301 manufactured

Table 3.5 Conditions of maskless lithography using S1818 photoresist.

	Process	Value
(1)	OAP spin coating (step 1)	1000 rpm, 3 sec
(2)	OAP spin coating (step 2)	6000 rpm, 60 sec
(3)	S1818 spin coating (step 1)	1000 rpm, 3 sec
(4)	S1818 spin coating (step 2)	6000 rpm, 60 sec
(5)	Prebake	110°C, 60 sec
(6)	Exposure	~ 80 mJ/cm^2
(7)	Development	MF320, 60 sec
(8)	Post bake	110°C, 30 sec

Table 3.6 Conditions of maskless lithography using AZ5218 photoresist.

	Process	Value
(1)	OAP spin coating (step 1)	1000 rpm, 3 sec
(2)	OAP spin coating (step 2)	5000 rpm, 30 sec
(3)	AZ5218 spin coating (step 1)	1000 rpm, 3 sec
(4)	AZ5218 spin coating (step 2)	5000 rpm, 60 sec
(5)	Prebake	100°C, 90 sec
(6)	Pattern exposure	~ 25 mJ/cm^2
(7)	Reversal bake	120°C, 120 sec
(8)	Full exposure	250 mJ
(9)	Development	AZ300MIF, 60 sec

by YAMATO SCIENTIFIC. The appearance of the plasma reactor system is shown in Fig. 3.7. In the reactor, introduced oxygen gas is made into plasma by non-ionizing radiation, and a chemical reaction occurs when the oxygen radicals in the plasma combine with the photoresist, causing the photoresist to be removed.

Surface activated bonding

Surface activated bonding (SAB) is one of the room temperature bonding technologies that bond two materials without adhesives, heat, or pressure by surface treating and activating the bonding surfaces of the materials in a vacuum. Since surface activation bonding can be performed at room temperature, no heat is applied to the base material. This makes it possible to bond heterogeneous materials that could not be bonded

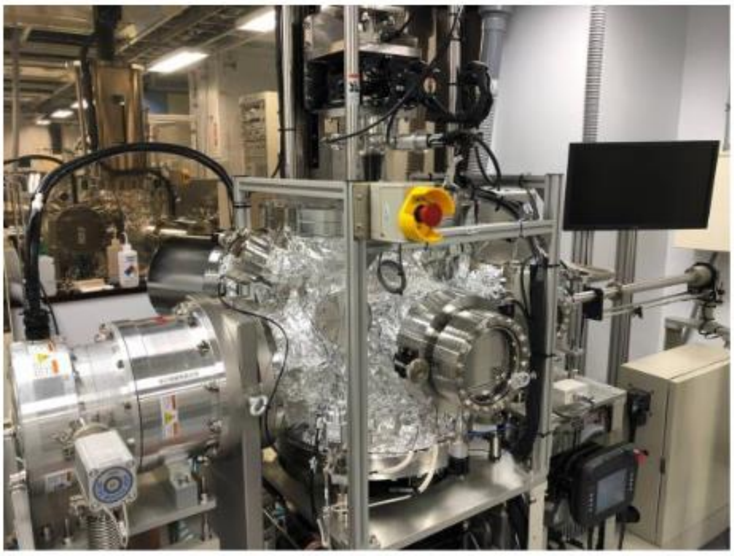

Fig. 3.8 Surface activated bonding equipment (Musashino engineering)

Table 3.7 Conditions of surface activated bonding.

Process	Value	
	Sputtering irradiation	Activating irradiation
Current	100 mA	50 mA
Voltage	1.5 kV	1.2 kV
Time	15 min	90 sec
Ar gas flow	30 sccm	30 sccm
	Bonding	
Load	500 kgf	
Time	5 min	
Pressure	< 10^{-5} Pa	

due to their different thermal expansion coefficients. Because the base materials are bonded to each other at the atomic level, the bonding is stronger and more durable than bonding with adhesives. The thickness of the adhesion layer can also be reduced, enabling device miniaturization. In the case of heat-applied bonding, it takes time for the temperature to rise and fall. Surface-activated bonding does not apply heat, so the processing time is reduced. In addition, surface activation bonding, which does not use adhesives, is more reliable than existing processing methods and allows for the manufacture of finer products. In this study, Ar was used as the activation gas, though various gases such as Ne, Kr, Xe, and N_2 can be used. The conditions of SAB are shown in Table 3.7.

Electron beam lithography (EBL)

In electron beam lithography (EBL), electron beams emitted from an electron gun are passed through electron lenses, apertures, deflectors, etc., and irradiated onto a mask blank while the X-Y-Z stage is finely controlled to expose the desired pattern. Compared to photolithography, EBL is not suitable for mass production due to its long exposure time, but its high resolution makes it suitable for fabricating ultra-fine devices. Since a mask is not required for each exposure, patterning of any shape is possible, and it is mainly used for research and development and small-quantity, high-mix production. The EBL system consists of an electron gun, electronics system, and stage main unit, which are configured in a vacuum chamber, and a computer for control. The electron gun has an emitter made

Fig. 3.9 Electron-beam lithography (EBL) system of JEOL JBX-6300FS.

of tungsten fixed to the tip of a filament, which is heated by passing an electric current and emits electrons in a thermal field by applying a voltage. The JEOL JBX-6000FS has an acceleration voltage of 50 kV and is capable of imaging ultra-fine structures as small as 10 nm. In this study, it is used to form diffraction grating patterns.

Resistive thermal evaporation

In thermal evaporation, raw materials are placed in a resistance coil. By passing a large current through the resistance coil, the coil as well as the raw material is heated, and the thermally evaporated metal is deposited on the target substrate. The thermal evaporation system is a common technique for depositing metals because it is simpler in structure than the electron beam deposition method. This method allows for a gradual increase in the temperature of the raw material; metals with low thermal conductivity, such as Zn, are preferably evaporated by thermal evaporation to avoid explosive boiling. In this study, this system is used to form electrodes with the Au/Zn/Au/Ti/Au structure, for which good ohmic contact was obtained in a previous study. Fig. 3.10 shows the appearance of the resistance heating evaporation system (TOKYO vacuum, EG-240).

Fig. 3.10 Thermal evaporation system (TOKYO VACUUM, EG-240).

Electron beam evaporation

Electron beam evaporation is a form of physical vapor deposition. The target material to be deposited is evaporated by irradiating an electron beam from a charged tungsten filament. The gas-phase metal in contact with the substrate and cooled precipitates to form a thin film coating. When the electron beam strikes the surface of the evaporator, its kinetic energy is converted to heat by impact. Although the energy emitted by a single electron is small, the number of electrons is large, so the total amount of energy emitted is quite high, typically several million watts or more per square inch. This makes this system a suitable method for depositing metals such as Ti, which has a high melting point. In the membrane laser fabrication, Ti/Au was used for the *n*- and *p*-type electrodes. The appearance of electron beam evaporation system is shown in Fig. 3.11.

Fig. 3.11 Electron beam evaporation system (ULVAC, EX-300)

Rapid thermal annealing (RTA) system

This equipment is a lamp heating system for semiconductor substrates that rapidly heats one side of the top of the substrate using a radiant surface-reflecting infrared lamp

Fig. 3.12 Rapid thermal annealing system (RTP-6, ADVANCE RIKO)

to perform annealing in a short time. The laboratory owns an RTP-6 from ADVANCE RIKO, which can raise the temperature from room temperature to a maximum of 1000 °C. In this study, it was used for alloying the Au/Zn/Au electrode, which is the *p*-side electrode.

300 mm fully automated probe system

Silicon Photonics Probing system by FormFactor offers advanced capabilities for precise calibration and testing of photonics components. Key features include revolutionary wafer and die-level probing technology, real-time in-situ calibrations, and true die-level edge coupling. The system supports horizontal and wafer-level edge coupling with high accuracy, low coupling loss, and automated fiber-to-facet alignment. Vertical coupling adheres to industry standards with precise calibration and automated optimization features. The integrated solution includes thermal capability for stable measurements across a wide temperature range. Automated calibration functions and a robust measurement assistant ensure accurate and repeatable results. The SiPh-Tools

Fig. 3.13 Automated probe system (CM300-Ph, FormFactor)

software package automates tasks, while the Photonics Controller Interface allows manual control and setup. The reconfigurable fiber arm provides flexibility and quick calibration after changes. Overall, the system demonstrates FormFactor's commitment to innovation and precision in silicon photonics testing.

3.3 Selective area regrowth using organometallic vapor-phase epitaxy (OMVPE)

In the previous chapter, the optimal design parameters for the BRW structure were determined to be a step of d = 50 nm and a slope width of $W_d \leq 0.5$ μm. One method to form this structure is to etch the side cladding layer after growing it so that it is flat with the active layer, and another method is to control the time for regrowth by OMVPE. The former method produces an ideal ridge structure with a small slope width, but requires an additional process compared to the conventional process. However, in the latter method, if the slope width can be reduced to 0.5 μm or less, the BRW structure can be formed without adding any new steps to the conventional process.

Fig. 3.14 shows a conceptual diagram of regrowth by OMVPE. Organometallic compounds are thermodynamically unstable and decompose upon heating, releasing metals. In OMVPE, atoms that reach the substrate surface migrate to a more stable location, resulting in a flat substrate surface [3]-[5].

In selective regrowth, atoms decomposed on the SiO_2 mask cannot bond with the SiO_2 mask, so they diffuse across the surface to the mask edge and then migrate and bond

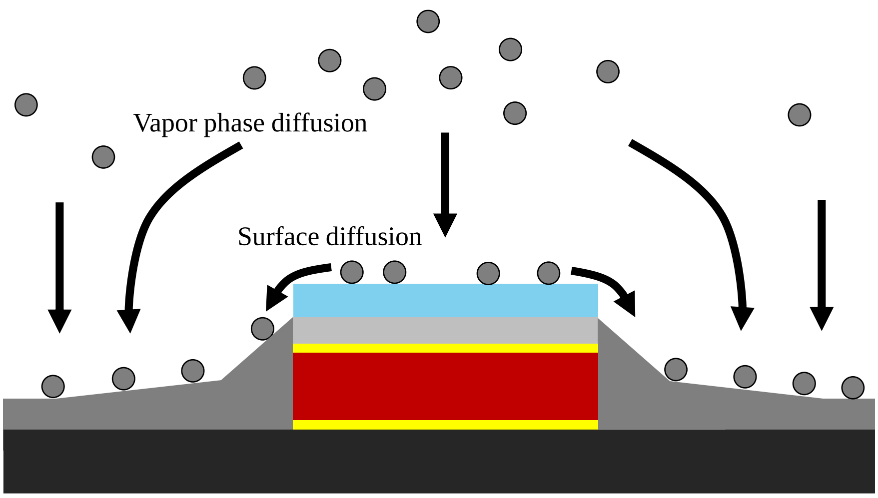

Fig. 3.14 Conceptual diagram of regrowth by OMVPE.

at the mask edge. In this process, a concentration gradient of deposition species occurs in the stagnant layer on the SiO_2 mask and on the growth surface, so that deposition species diffuse in the gas phase and grow with a gradual slope [6]-[9]. In selective regrowth, growth is determined by both surface diffusion and gas-phase diffusion, but surface diffusion dominates in the vicinity of the SiO_2 mask, creating a slope of about 1 µm. In this section, we describe the OMVPE condition study performed to obtain the desired BRW structure.

In the fabrication process of semiconductor membrane lasers in our laboratory, *p*-InP side cladding and *n*-InP side cladding are grown separately. Fig. 3.15 shows the InP

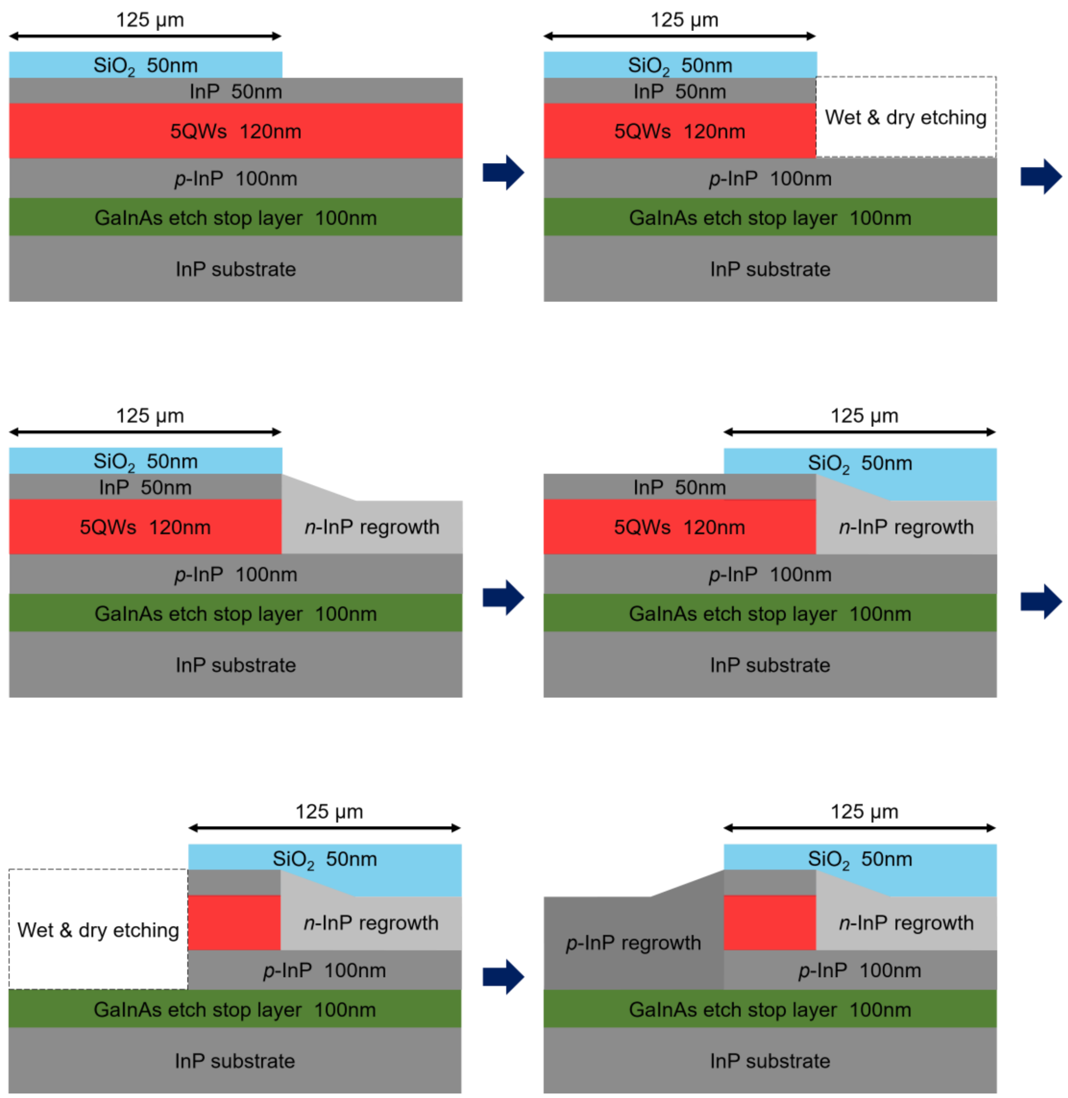

Fig. 3.15 Schematic of *n*- and *p*-InP regrowth process

regrowth process. In the *n*-InP regrowth process, the active layer and 50 nm-thick InP are etched and regrown, whereas in the *p*-InP regrowth process, the 100 nm-thick InP underneath is also etched. In addition, *p*-InP regrowth requires a mask of a certain width to protect the *n*-InP region regrown in the previous process.

Transition of InP growth film with time

To form the BRW structures, it is necessary to check how the thickness and shape of the grown film near the mask varies with growth time and mask width. First, using a mask with a width of 125 μm, GaInAs were inserted between the InP growth as markers to check the growth rate and shape with respect to the growth time in the vicinity of the mask. The growth by OMVPE is performed under the condition shown in Table 3.8. The growth period of the InP and GaInAs aimed at thicknesses of 40 nm and 10 nm is 47 s and 8 s, respectively. Fig. 3.16 shows a cross-sectional SEM image of the substrate on which the growth was performed. From this figure, it can be confirmed that the growth rate is indeed faster in the vicinity of the mask than in the distant area. After the film near the mask is flattened, the growth rate in the distant area increases, instead of further deposition and uplift of the film in its vicinity. This is related to the fact that molecules are grown to their lowest energy state in OMVPE. The results for the thickness of the grown film at each growth time in the vicinity of the mask are shown in Fig. 3.17. The growth rate is slow until it stabilizes due to the low partial pressure of the deposited species in the reactor for a while after the start of growth. From these results, it was found that the deposition rate after stabilization is 40 nm/min at a mask width of 125 μm.

Table 3.8 Condition of OMVPE (Organic-Metal Vapor Phase Epitaxy).

Parameters	Value
Precursors of groups V and III	PH_3, TMI
Pressure	76 Torr
Temperature	600°C
V/III ratio	550

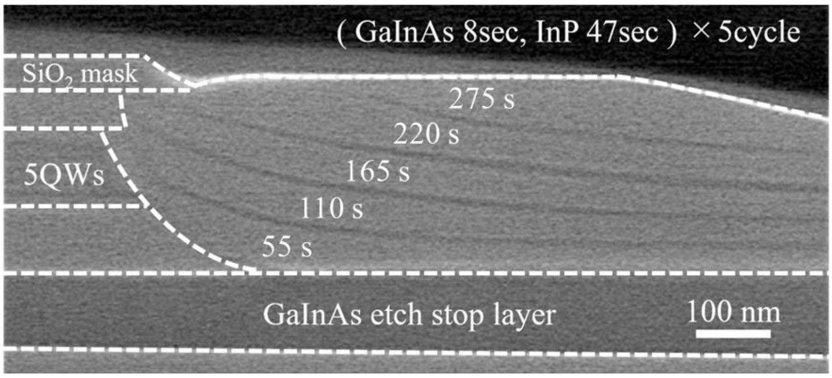

Fig. 3.16 OMVPE embedding growth pattern of InP with intervals of a GaInAs marker.

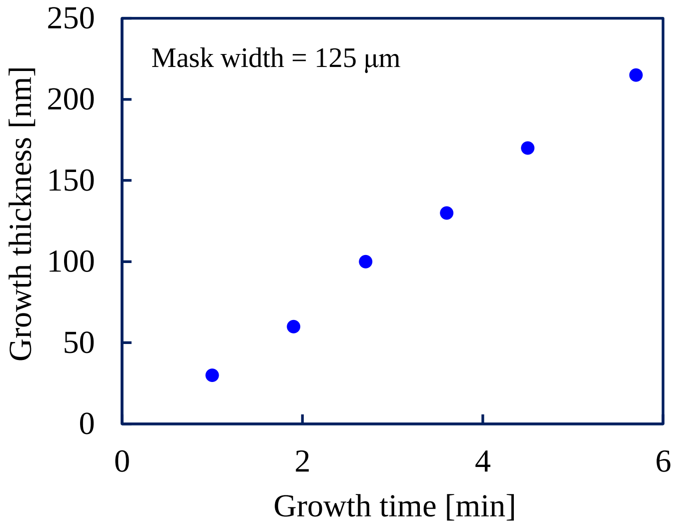

Fig. 3.17 Relationship between growth time and growth thickness in the vicinity of the mask.

Experiments to determine the relationship between growth time and growth film thickness for different mask widths are shown in the figure. Since the slope near the mask is derived from the diffusion of molecules decomposed in the mask area, the smaller the mask width, the smaller the slope width is expected to be. However, the mask used in *p*-InP regrowth also protects the *n*-InP region regrown in the previous process, so a certain width is necessary. In this study, the mask width was determined to be 40 μm considering the size of the electrode pad.

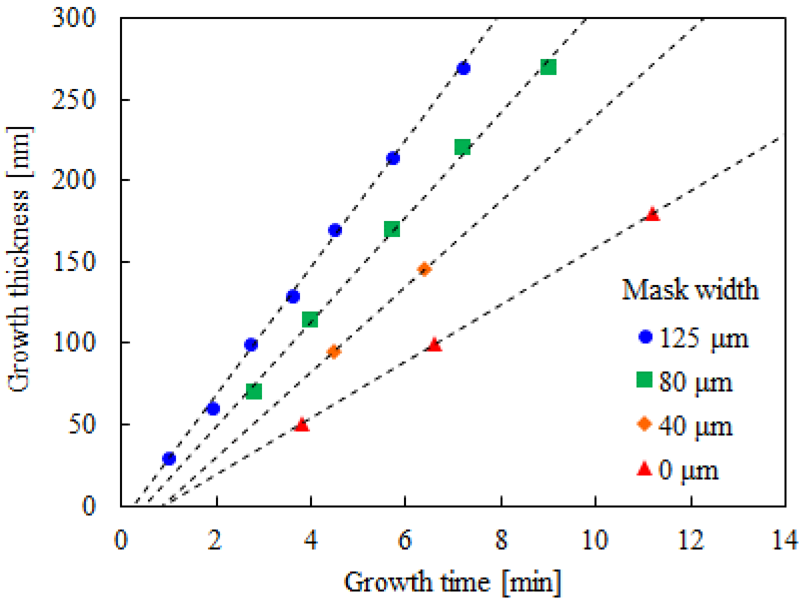

Fig. 3.18 Relationship between growth time and growth thickness in the vicinity of the mask for each mask width.

Side etching dependence

The side etching dependence was investigated by changing the wet etching time to reduce the width W_d of the slope. In the regrowth process for semiconductor membrane lasers, regrowth is performed after dry and wet etching the areas that will become the side cladding. In wet etching, the active layer shrinks due to isotropic etching, so the side etching under the SiO_2 mask increases as the wet etching time is increased. When InP is regrown on a substrate with large side-etched layers, atoms diffused from the SiO_2 mask migrate to fill the area, which is expected to reduce the W_d [10]. The conventional process uses a wet etching time of 5 minutes. In this study, we performed regrowth on substrates with several wet etching time to examine the side etching dependence of the slope width W_d.

Fig. 3.19 shows the cross-sectional SEM images of the regrowth substrate at each wet etching time. When the wet etching time was set to 5, 8, and 10 minutes, the amount of side etching was 100 nm, 150 nm, and 180 nm, respectively, indicating that the amount of side etching increased proportionally with time. The slope widths W_d were 0.7 μm, 0.6 μm, and 0.3 μm, respectively. These results indicate that the wet etching time should be

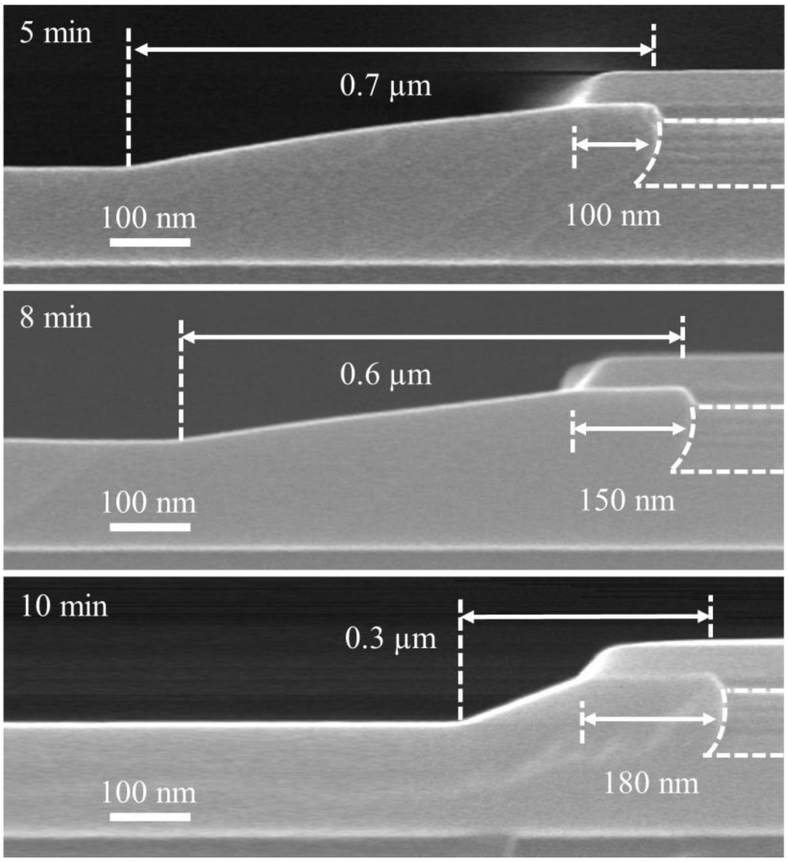

Fig. 3.19 Side etching dependence of regrowth film.

set to 10 minutes to achieve $W_d \leq 0.5$ μm, which was calculated theoretically. Increasing the wet etching time to 10 minutes results in a reduction of the active layer by about 0.2 μm on one side, or about 0.4 μm in total. Therefore, by properly designing the width of the mask, the desired structure can be obtained without changing the stripe width.

3.4 Surface grating formation using electron beam lithography

3.4.1 Grating design

First, the design of the membrane DR laser structure is described. Fig. 3.20 and Fig. 3.21 shows the schematic structure and cross-section of a membrane DR laser, respectively. The membrane DR laser consists of an active DFB section, a passive DBR section, and a waveguide section. The DBR has high reflectivity in a specific wavelength band, which enhances the optical output from the front side by feedback of the backward emitted light to the active layer. To realize a highly efficient membrane DR laser, matching the lasing wavelength with the Bragg wavelength in the DBR region is

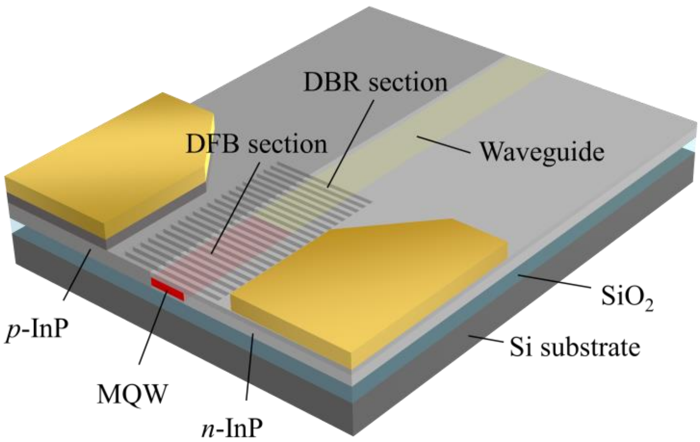

Fig. 3.20 Schematic of the membrane DR laser.

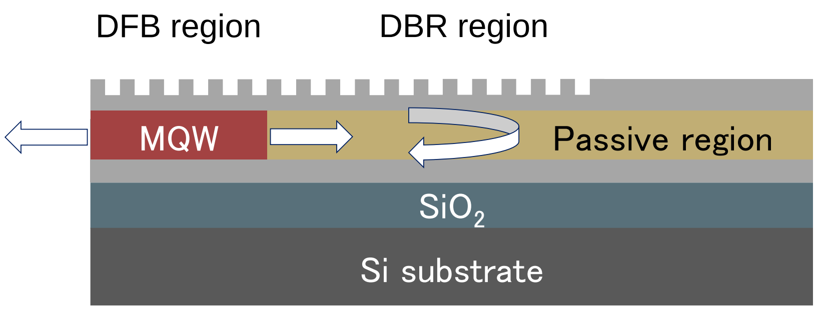

Fig. 3.21 Cross sectional image of the cavity.

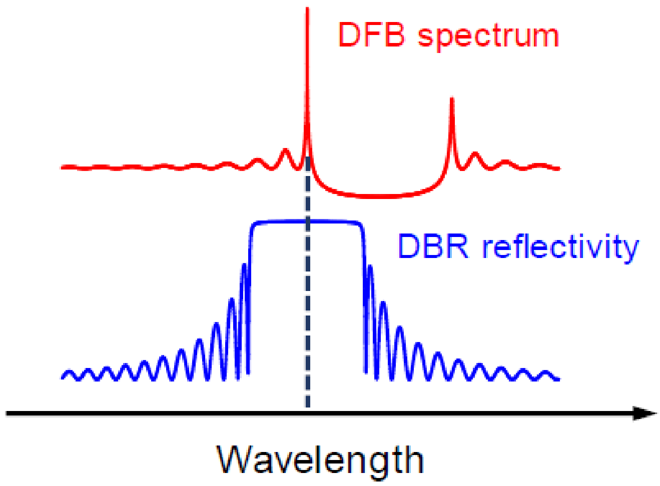

Fig. 3.22 Spectrum characteristics of the membrane DR laser.

important [11]. Fig. 3.22 shows an image of the spectrum characteristics of the membrane DR laser. In general, a DFB laser with a uniform grating has two wavelengths with the minimum threshold gain, and the lasing wavelength is determined by the combination with the material gain of the active layer. This wavelength is determined by κL, where κ is the refractive index coupling coefficient and L is the cavity length. In other words, considering only the parameters for forming gratings with EBL, the wavelength depends on the grating period, grating depth, and cavity length.

Fig. 3.23(a) shows normalized plots of threshold gain and threshold wavelength for a membrane DFB laser with uniform grating. This result was calculated using the transfer matrix method and only the lowest order mode is indicated. As we often see, for a typical laser, the lasing conditions are simultaneously satisfied at wavelengths equally spaced on each side of the Bragg wavelength if there is no reflection from the end. In the case of membrane lasers, however, the threshold gain of the shorter wavelength mode is slightly lower. This is due to the relatively large difference in confinement factors within the grating region for membrane lasers with high κ. The electric field of the short wavelength mode is higher in the low refractive index region, resulting in a slightly higher modal gain for the short wavelength mode. Fig. 3.23(b) also shows the relationship between κL and

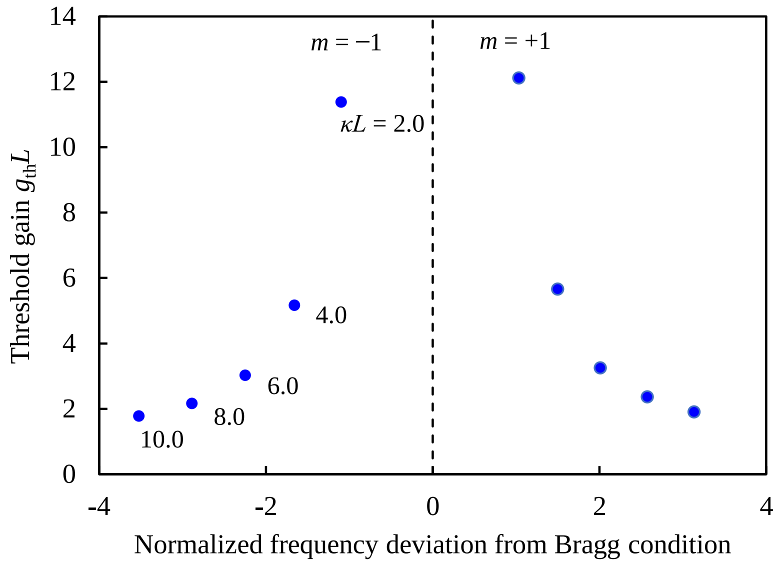

(a)

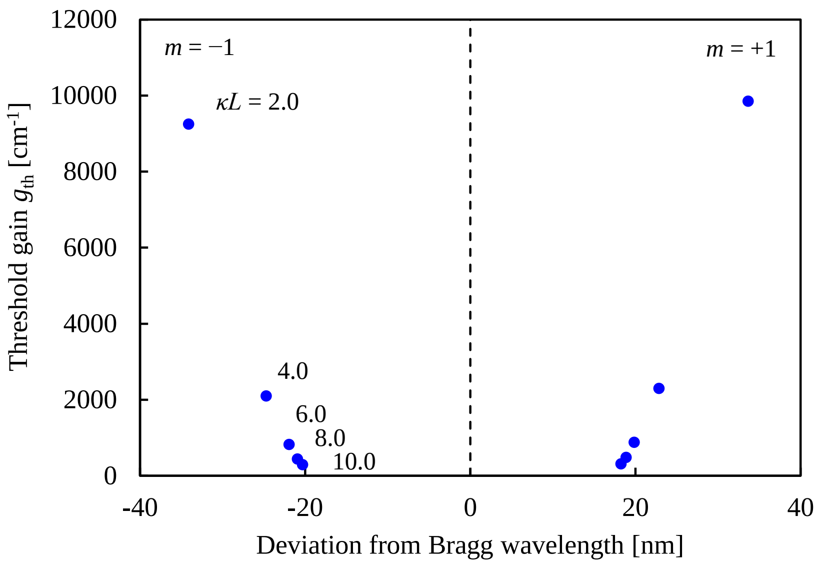

(b)

Fig. 3.23 (a) Normalized plots of threshold gain and wavelength for different modes. (b) Relationship between threshold gain and deviation from the Bragg wavelength.

the lasing mode, though the values on the horizontal axis are converted to deviation from the Bragg wavelength. As shown in Chapter 2, the membrane DR laser has a minimum threshold current at a DFB region length of 30 μm when the grating depth d_g is 50 nm. In this case, κL is 4.8, indicating that the wavelength variation is small with respect to the

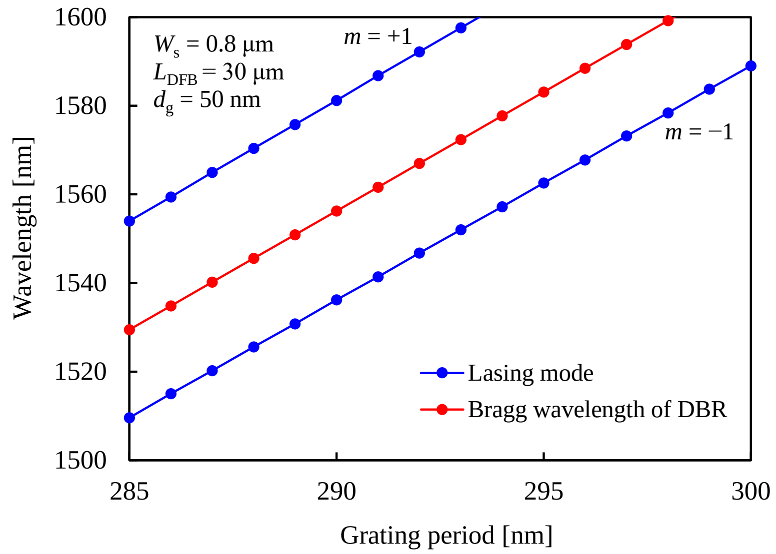

Fig. 3.24 The relationship between lasing mode of DFB laser and stop band of DBR.

variation of the grating depth due to fabrication errors. In addition, since the DFB and DBR regions are formed at the same time, the relative positions of the stop bands hardly change because the Bragg wavelengths of both regions transition similarly with fluctuations in grating depth. Therefore, it is important to determine the relationship between each grating period and wavelength. Fig. 3.24 shows the relationship between each grating period and wavelength. The blue line shows the change in the lowest order mode of the membrane DFB laser, calculated with a DFB region length of 30 μm and a grating depth d_g of 50 nm. The red line shows the relationship between the DBR period and the Bragg wavelength, which does not match that of the DFB region at the same period due to a slight difference in the refractive index between the DFB and DFB regions.

Next, we fabricated devices based on these results and confirmed them experimentally. First, Fig. 3.25 shows the spectra of the membrane DFB laser with different grating periods. The stripe width is 0.8 μm and the DFB region length is 40 μm. As the grating period is increased to 292nm, 293nm, and 294nm, the spectrum shifts to the longer wavelength side accordingly. Fig. 3.26 shows the spectra of the membrane DBR laser with different grating periods. The stopband of a passive device can be observed by inputting light from an external source and measuring its transmittance or

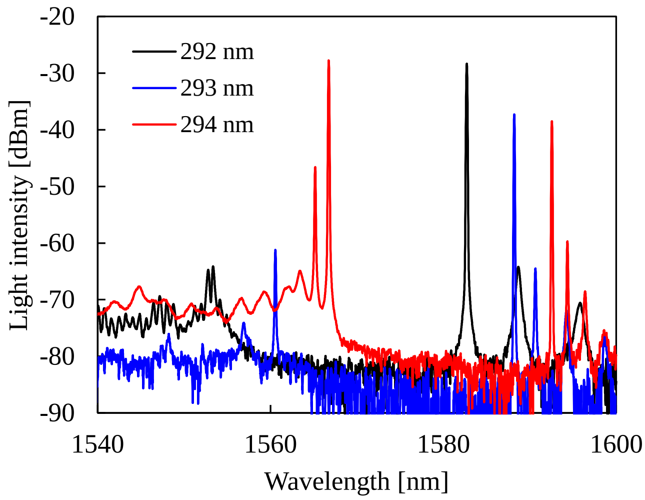

Fig. 3.25 Spectrum of membrane DFB laser with various grating period. The stripe width is 0.8 μm and the DFB region length is 40 μm.

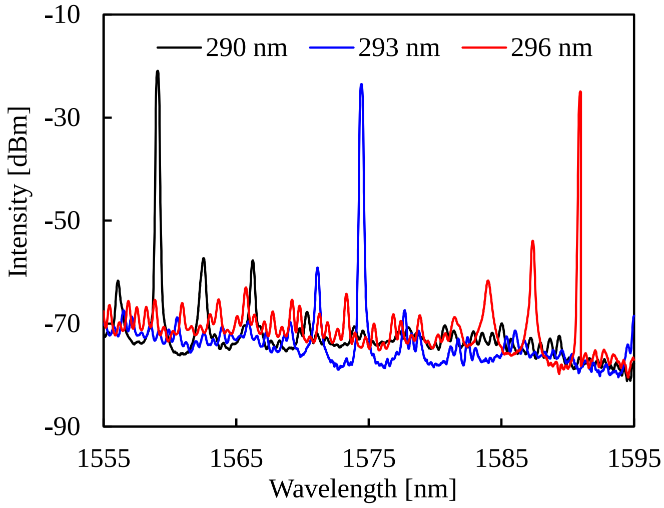

Fig. 3.26 Spectrum of membrane DBR laser with various grating period. The front and rear DBR length were 30 μm and 100 μm, respectively.

reflectance. However, membrane lasers using GaInAsP embedded waveguides require almost as much effort as laser fabrication due to the need for regrowth to fabricate the waveguide and the inability to fabricate a bent waveguide. DBR lasers are easier to evaluate and closer to actual situations. The fabricated DBR laser was formed with a DBR length of 100 μm in the back to obtain sufficient reflectivity and 30 μm in the front. The stripe width is 0.8 μm and the cavity length is 70 μm. The DBR was formed with a length

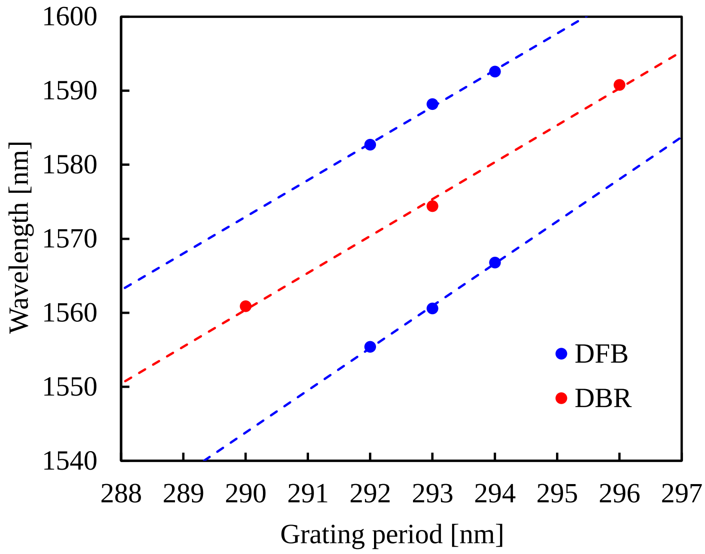

Fig. 3.27 Experimental results of lasing mode with various grating period.

of 100 μm in the back to obtain sufficient reflectivity and 30 μm in the front. Since the DBR laser oscillates in a mode depending on the resonator length defined by the front and rear DBRs, the lasing wavelength and Bragg wavelength do not necessarily coincide. However, since the wavelength difference should be less than the FSR = 3.5 nm, it was determined to be within the acceptable range from the consideration of the stopband width. Fig. 3.27 shows the summarized results of the lasing wavelengths of the DFB and DBR lasers. Compared to the theoretical calculation shown in Fig. 3.24, the wavelength is slightly shifted to the short wavelength side relative to the grating period. This was probably due to the deviation of the stripe width and the grating depth. Based on these experimental results, we conclude that the DFB period should be 291 nm and the DBR period should be 288 nm for a DR laser lasing at 1550 nm.

3.4.2 Fabrication process

Fig. 3.28 shows SEM images of membranes lasers fabricated by the conventional fabrication process. In this fabrication process, the surface grating was formed by EBL after the electrode was deposited. Therefore, the metal repelled the ZEP resist, and the

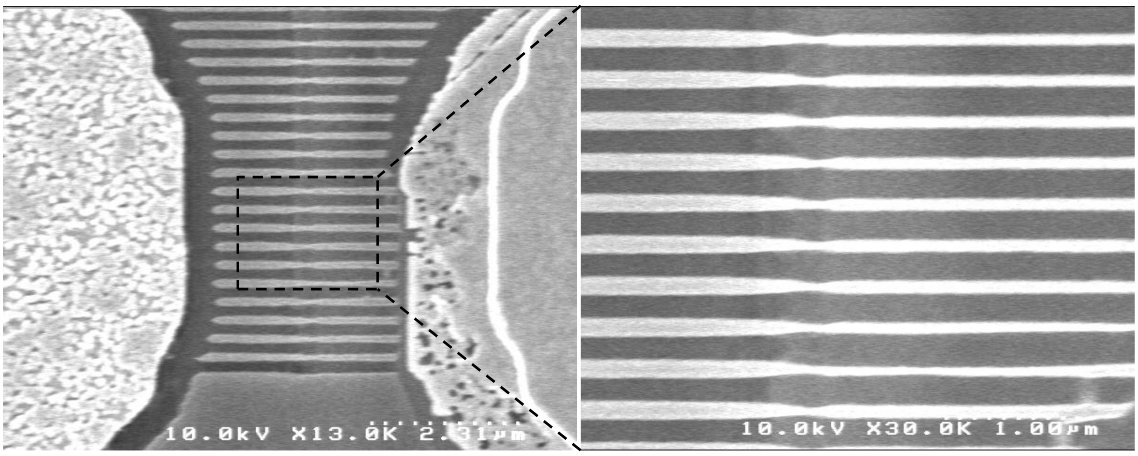

Fig. 3.28 SEM images of the fabricated device in previous study.

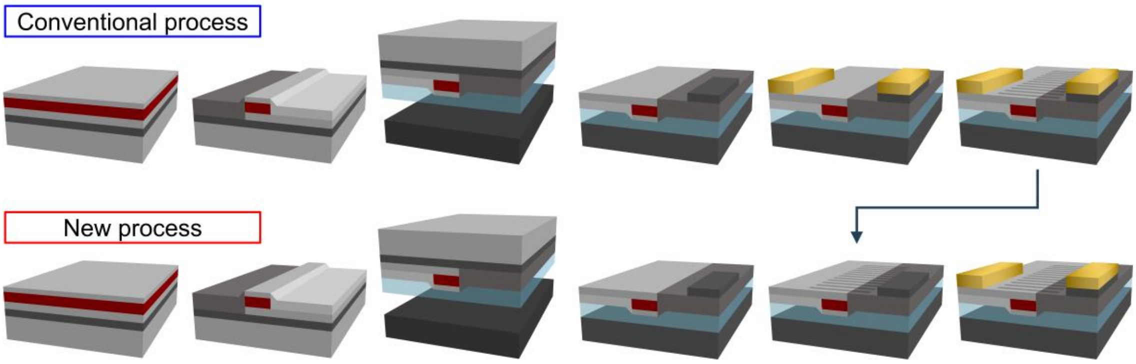

Fig. 3.29 Schematic of fabrication process of membrane DR laser.

area around the metal was etched without being protected by the resist. In addition, the grating pattern was transferred to the semiconductor by wet etching due to concerns about damage to the active layer caused by dry etching. However, the InP on the *p*-side was regrown on GaInAs and the top surface consists of mixed crystals. This slight difference in composition caused a difference in reactivity of the wet etching solution, resulting in non-uniform grating as shown in Fig. 3.28.

Therefore, process changes were considered. First, as shown in Fig. 3.29, we changed the sequence of grating formation before electrode deposition and also considered changing to dry etching. Fig. 3.30 shows an experiment to evaluate the damage to the active layer, which is a concern in dry etching. First, an initial substrate with an active layer is bonded onto a Si substrate. After 25-nm-thick SiO_2 was formed

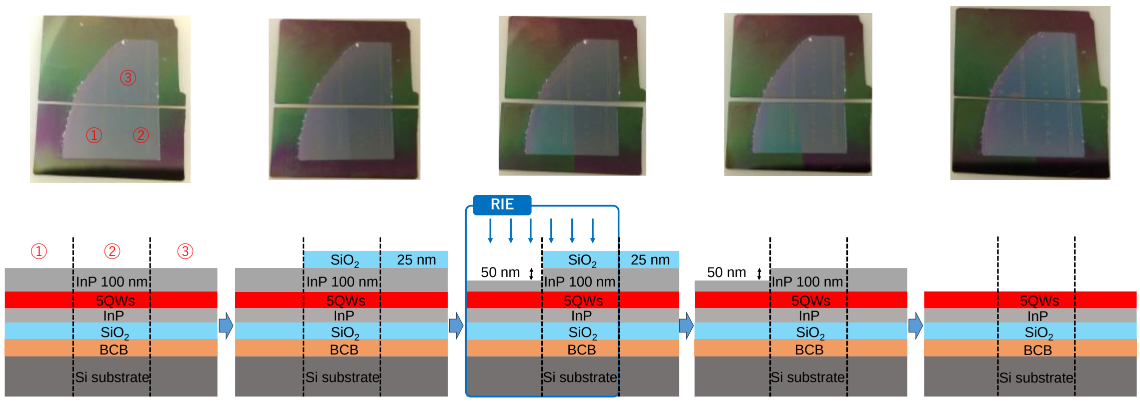

Fig. 3.30 Experimental process for evaluation of dry etching damage to the active region.

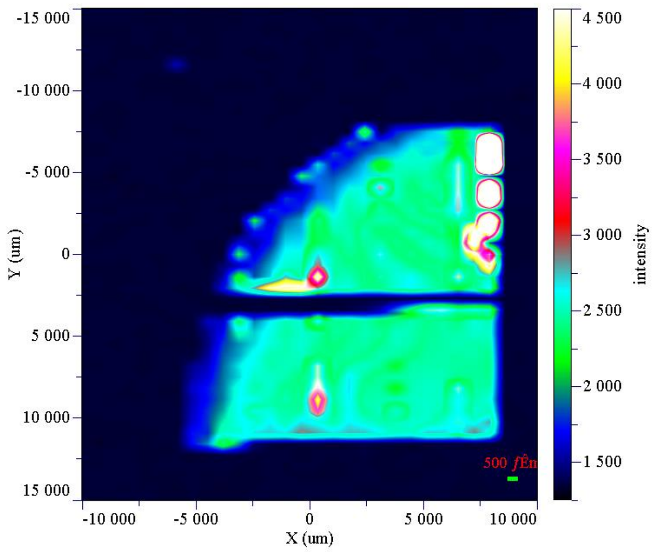

Fig. 3.31 Photo luminescence intensity mapping image.

using PECVD, it was divided into three areas. The SiO_2 in one of the regions was removed, and 50 nm of InP was removed by dry etching, the same amount as the grating formation. Finally, top InP of all substrates was removed by wet etching to avoid photoluminescence intensity changes due to different film thicknesses.

Photoluminescence properties were evaluated to investigate the damage caused by dry etching. Photoluminescence (PL) measurements are based on the principle that carriers are excited by an excitation light source with an energy larger than the band gap of the target semiconductor and emitted when the carriers recombine. Since the emitted photons correspond to the intrinsic band gap of each semiconductor material, the emission spectrum can be used to determine the optical properties of the material. The measurement system consists of light sources with wavelengths of 640 nm or 1064 nm (VORTRAN LASER TECHNOLOGY) and the detector (HORIBA, synapse) and the spectrometer (HORIBA, iHR320). Fig. 3.31 shows the PL mapping measurements. The positional relationship of the measured substrates is the same as that shown in Fig. 3.30. From the measurement results, there is almost no change in PL intensity, and it is concluded that damage to the active layer due to dry etching is negligible.

As the process was changed from wet etching to dry etching, the EBL conditions were also reexamined. Since it is more difficult to obtain anisotropy in wet etching than in dry etching, it was necessary to take into account the change in duty ratio due to side etching. In dry etching, it is possible to maintain the duty ratio of the resist pattern almost as it is. The etching time of dry etching also needs to be considered. In dry etching, the etching rate of fine patterns is slower than that of patterns with larger aperture widths due to the micro-loading effect [12][13]. Therefore, experiments were conducted to find the conditions for a duty ratio of 50% and grating depth of 50 nm.

First, the relationship between exposure dose and duty ratio was investigated. CAD patterns with duty ratios varying from 0.3 to 0.5 were fabricated, and these patterns were exposed with five different doses from 120 to 160 $\mu C/cm^2$. The grating patterns were transferred to SiO_2 by CF_4 RIE and top InP was etched by CH_4/H_2 RIE. Fig. 3.32 shows SEM images of the gratings fabricated under each condition. The more the exposure dose and duty ratio are increased, the wider the etching area becomes. There are multiple combinations of exposure and duty ratio that result in a duty ratio of 0.5 after etching. Considering the uniformity of verticality pattern, the condition of (140 $\mu C/cm^2$, 40%) was chosen. Fig. 3.33 shows SEM images of the gratings fabricated under the condition of (140 $\mu C/cm^2$, 40%). The semiconductor layer was etched by CH_4/H_2 RIE for 90 sec, and the etching depth was found to be 60 nm.

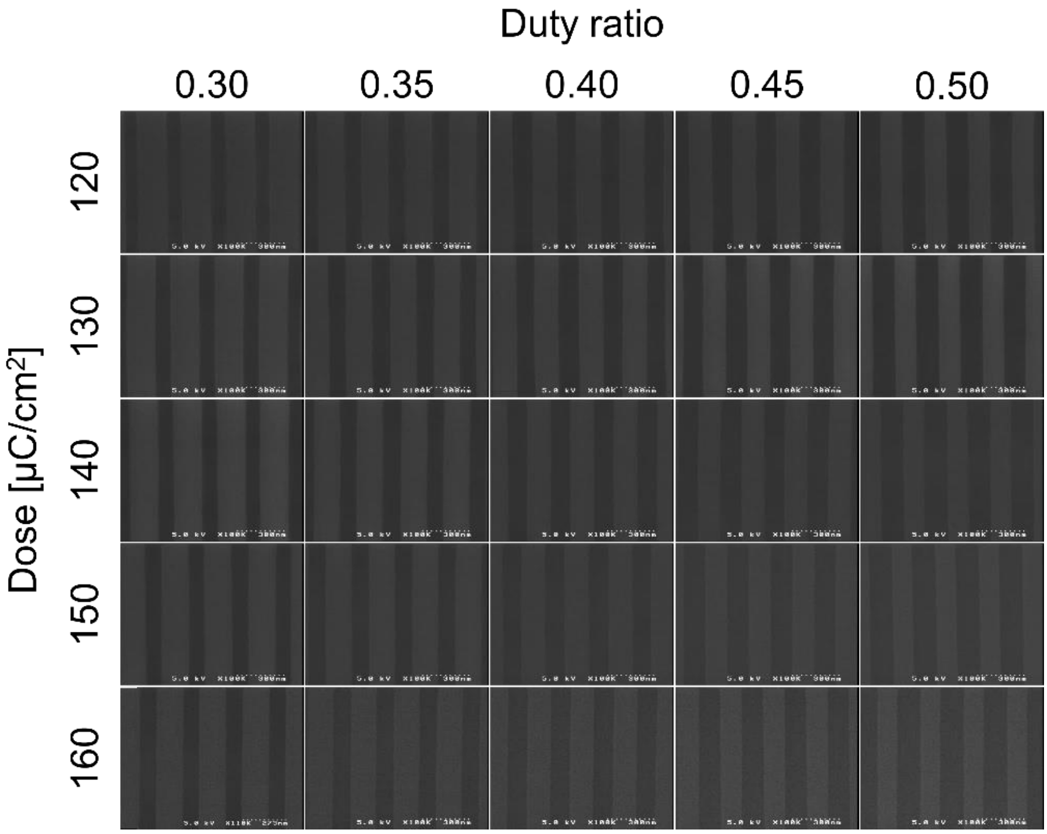

Fig. 3.32 SEM images of fabricated grating of each dose and duty ratio.

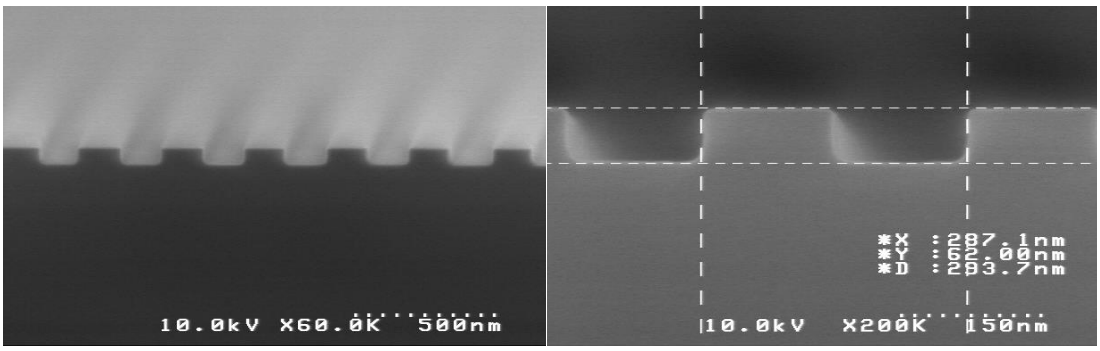

Fig. 3.33 Cross sectional SEM image of the grating of 50% duty ratio.

With the above, consideration of the concerns arising from the process change was confirmed, and the devices were fabricated using the new process, as shown in Fig. 3.34. Problems such as pattern non-uniformity and metal repelling resist, which had occurred in previous studies, were successfully solved by the new process. The effect of the change from wet etching to dry etching on laser characteristics will be discussed in Chapter 4.

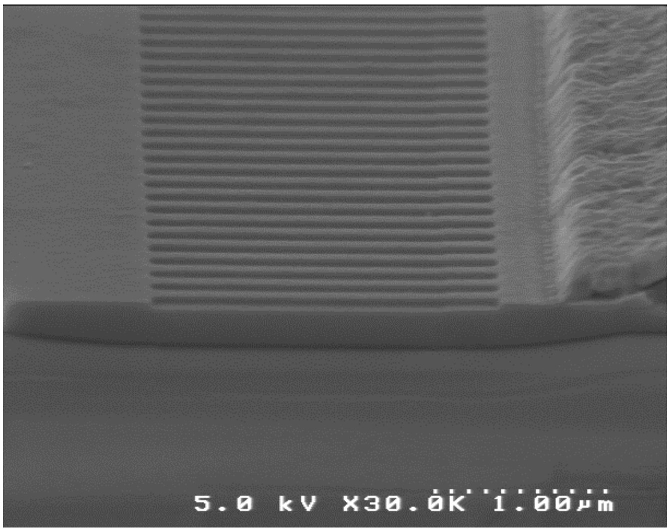

Fig. 3.34 SEM image of fabricated device with new fabrication process.

3.5 Conclusion

This chapter delves into the details of membrane laser fabrication techniques, with particular focus on the realization of ridge-buried-waveguide (BRW) structures and the formation of grating. Selective regrowth using organometallic vapor phase epitaxy (OMVPE) is then discussed and optimal design parameters for the BRW structures are examined closely. Two matters are considered to achieve the desired BRW structure, including etching of the side cladding layers and control of the regrowth time. Detailed examination of the OMVPE conditions reveals the interaction between mask width and growth thickness, and the regrowth time to obtain a ridge depth of d = 50 nm for each mask width is experimentally determined. An investigation was also conducted to achieve a slope width (W_d) of 0.5 μm or less, which was obtained by calculation. Experimental results emphasize the importance of wet etching time in determining W_d, and a wet etching time of 10 minutes was found to be optimal for achieving the desired structure.

The second half of the chapter moves on to the formation of grating on surfaces using electron beam lithography (EBL) and closely outlines the principles of grating design for DR lasers. Theoretical considerations are validated through experiments to determine the grating period for optimal laser performance. The challenges encountered in previous studies have been improved by revising the fabrication process. The formation of grating was rearranged and the transition from wet etching to dry etching was examined. It was shown that the damage to the active layer by dry etching was negligible, and this process improvement solved the problem of the previous study and enabled uniform fabrication.

Reference

[1] D. Inoue, J. Lee, T. Hiratani, Y. Atsuji, T. Amemiya, N. Nishiyama, S. Arai, "Sub-milliampere Threshold Operation of Butt-jointed Built-in Membrane DFB Laser Bonded on Si Substrate," *Optics Express*, Vol. 23, Issue 6, pp. 7771-7778, 2015.

[2] W. Fang, N. Takahashi, Y. Ohiso, T. Amemiya, N. Nishiyama, "High-quality, room-temperature, surface-activated bonding of GaInAsP/InP membrane structure on silicon," *Japanese Journal of Applied Physics*, Vol. 59, pp. 060905, 2020.

[3] Y. Sakata, Y. Inomoto, and K. Komatsu, "Surface migration effect and lateral vapor-phase diffusion effect for InGaAsP/InP narrow-stripe selective metal-organic vapor-phase epitaxy," *Journal of crystal growth*, vol. 208, pp. 130-136, 2000.

[4] O. Kayser, "Selective growth of InP/GaInAs in LP-MOVPE and MOMBE/CBE," *Journal of crystal growth*, vol. 107, pp. 989-998, 1991.

[5] J. S. Chang, K. W. Carey, J. E. Turner, and L. A. Hodge, "Compositional non-uniformities in selective area growth of GaInAs on InP grown by OMVPE," *Journal of Electronic Materials*, vol. 19, pp. 345-348, 1990.

[6] O. Kayser, R. Westphalen, B. Opitz, and P. Balk, "Control of selective area growth of InP," *Journal of Crystal Growth*, vol. 112, no. 1, pp. 111-122, 1991.

[7] T. Van Caenegem, I. Moerman, and P. Demeester, "Selective area growth on planar masked InP substrates by metal organic vapor phase epitaxy (MOVPE)," *Progress in Crystal Growth and Characterization of Materials*, vol. 35, no. 2–4, pp. 263-288, 1997.

[8] Y. D. Galeuchet, P. Roentgen, V. Graf, "GaInAs/InP selective area metalorganic vapor phase epitaxy for one-step-grown buried low-dimensional structures," *J. Appl. Phys.*, 15, 1990.

[9] E. J. Thrush, J. P. Stagg, M. A. Gibbon, R. E. Mallard, B. Hamilton, J. M. Jowett, E. M. Allen, "Selective and non-planar epitaxy of InP/GaInAs(P) by MOCVD," *Materials Science and Engineering: B*, vol. 21, no. 2–3, pp. 130-146, 1993.

[10] A. Catana, R. F. Broom, R. Germann, P. Roentgen, "Regrowth of InP by MOVPE on dry-etched heterostructures of InP-GaInAsP," *Journal of Crystal Growth*, vol. 129, no. 3–4, pp. 779-782, 1993.

[11] K. Ohira, T. Murayama, H. Yagi, S. Tamura, and S. Arai, "Low threshold current distributed-reflector laser with phase-shifted DFB and high-reflection DBR sections," *The 17th International Conference on Indium Phosphide and Related*

Materials (IPRM2005), pp. 558-561, 2005.

[12] C. Hedlund, H.-O. Blom, S. Berg, "Microloading effect in reactive ion etching," *J. Vac. Sci. Technol. A*, vol. 12, no. 4, pp. 1962–1965, 1994.

[13] J. Yeom, Y. Wu, J. C. Selby, M. A. Shannon, "Maximum achievable aspect ratio in deep reactive ion etching of silicon due to aspect ratio dependent transport and the microloading effect," *J. Vac. Sci. Technol. B*, vol. 23, no. 6, pp. 2319–2329, 2005.

Chapter 4
Characteristics of membrane distributed-reflector lasers

4.1 Introduction 129
4.2 OMVPE growth conditions and initial epi-wafer 130
4.3 Membrane Fabry-Perot laser with BRW structure 138
4.4 Low threshold current membrane DR laser 142
4.4.1 Static characteristics 143
4.4.2 Dynamic characteristics 147
4.5 Discussion of consumption power of membrane DR laser 150
4.6 Conclusion 152
Reference 153

4.1 Introduction

In this chapter, membrane lasers are characterized and discussed based on experimental results for what is the ideal semiconductor laser. Semiconductor lasers are characterized by both material and structural parameters. Since laser structures are analyzed on the basis of material parameters, proper evaluation and improvement can lead to optimal structures. First, the initial epi-wafer, which is the basis of the semiconductor laser, was improved while evaluating laser characteristics. Then, membrane DR lasers with the BRW structure and ACPM grating discussed in the previous chapters were fabricated and characterized. Based on the experimental results, power consumption in various applications will then be discussed, concluding the discussion on the ideal laser.

4.2 OMVPE growth conditions and initial epi-wafer

Thermal characteristics improvement by thinner quantum wells

In previous studies, optical output saturated at an injection current of about 3 mA due to high differential resistance, high thermal resistance, and other reasons [1][2]. This saturation of optical output due to heat leads to an increase in injection power to output enough optical power, causing an increase in power consumption. To solve this problem, efforts were made by co-worker Dr. Fang to reduce thermal resistance [3], and a different approach was to improve the active layer structure of the initial substrate. The energy gap in a well is determined by its composition. However, in a quantum well structure, the electrons in the well are confined to a discrete energy state that satisfies a certain wave function. This wavefunction varies with the well thickness, and the thinner the well, the higher the energy as shown in Fig. 4.1 The energy of the second level is also increased, which reduces the probability of a transition to the second level when the energy of the electrons is broadened by heat. That is, a thinner well thickness is expected to suppress the decrease in gain at higher temperatures and improve temperature characteristics.

The composition of the wells must also be changed because simply reducing the thickness of the well film shifts the gain peak to the short wavelength side. In the material of GaInAsP, the energy gap and lattice constant can be tuned by changing its composition. The growth condition was controlled at 5.4 nm, which is 10% thinner than the conventional well film thickness of 6 nm. To achieve the desired energy gap and strain, repeated experiments are required to change the flow rate of the material, check the peak

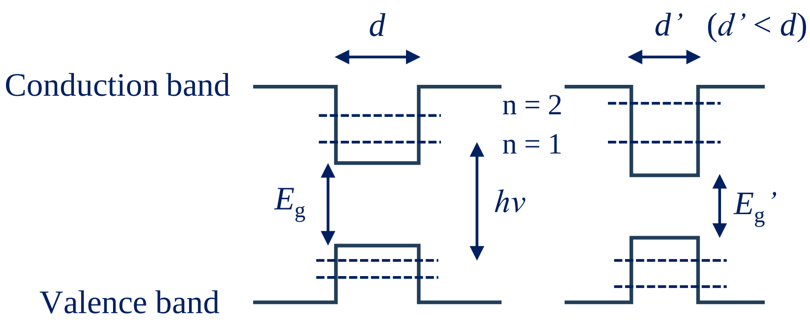

Fig. 4.1 Schematic of energy band diagram for quantum wells.

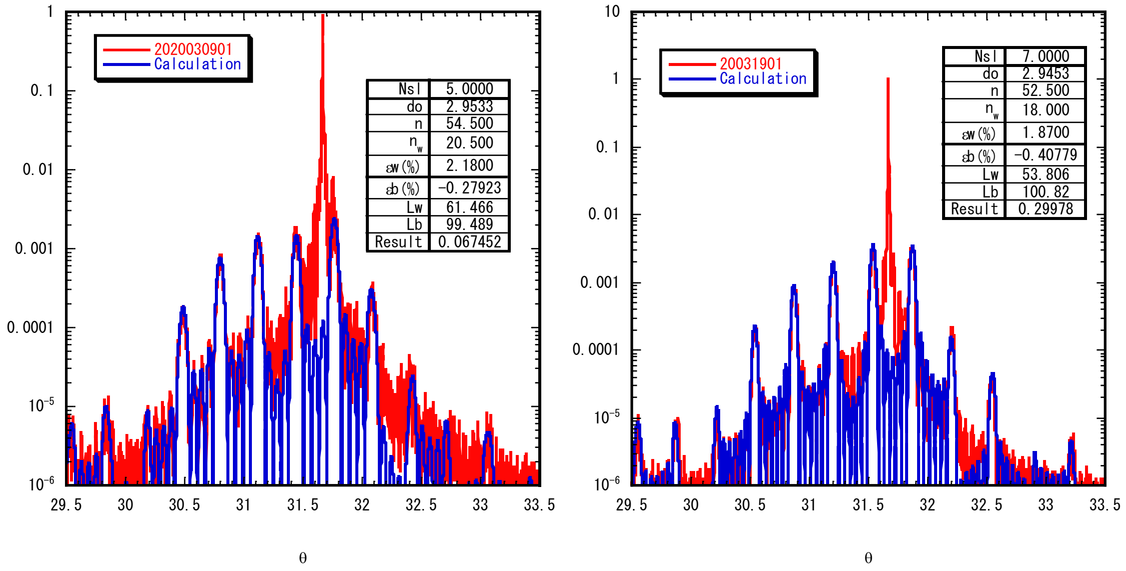

(a) (b)

Fig. 4.2 X-ray diffraction measurements and calculation with (a) conventional recipe and (b) new recipe.

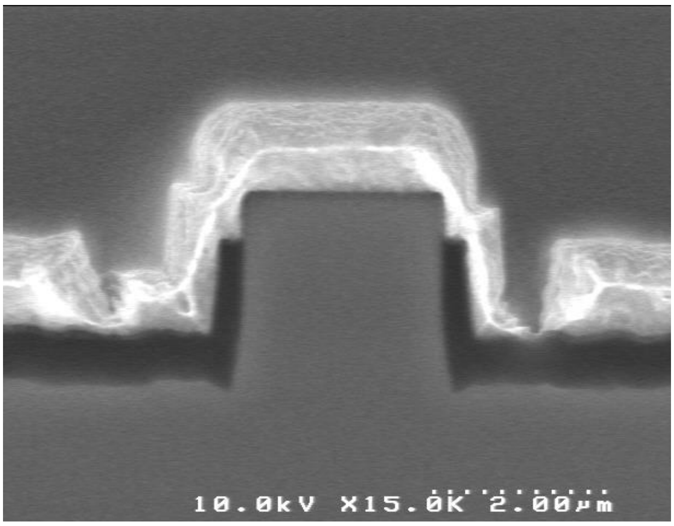

Fig. 4.3 SEM image of fabricated ridge stripe laser.

wavelength and strain amount. Fig. 4.2 shows the results of X-ray diffraction (XRD) measurements under the growth conditions of OMVPE obtained after repeated experiments. The red line shows the measurement results, and the blue line shows the fitted results. Fig. 4.2(a) shows the active layer fabricated with the conventional recipe,

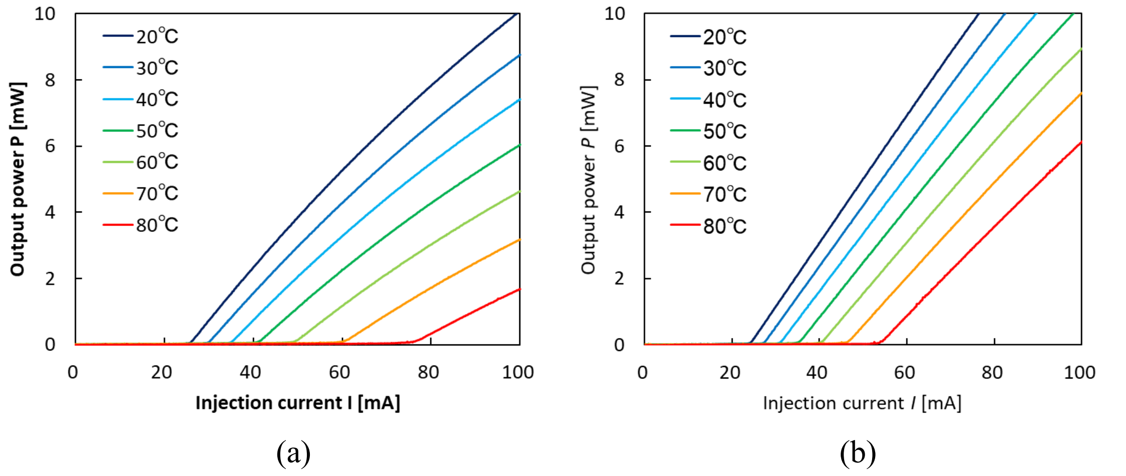

Fig. 4.4 *I-L* characteristics in various stage temperature of fabricated FP lasers with (a) conventional recipe and (b) new recipe.

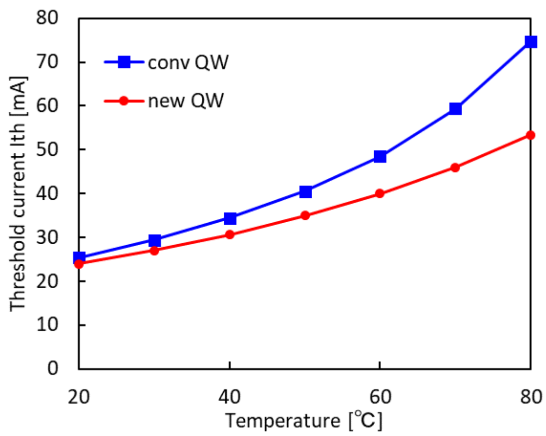

Fig. 4.5 Comparison of stage temperature dependence of threshold current.

and Fig. 4.2(b) shows the result of the active layer fabricated with the new recipe. The fitting results show that the desired values of the well and barrier film thicknesses of 5.4 nm and 10 nm were obtained, respectively. In terms of strain, well and barrier are +0.94% and -0.20%, respectively, which are almost comparable to those of the conventional design.

Ridge stripe Fabry-Perot lasers were fabricated using these active layers to evaluate temperature characteristics. The fabrication was performed by collaborator Ohiso, and the process was summarized in detail by Eissa [4]. Fig. 4.3 shows the SEM image of the fabricated device with stripe width of 3 μm. The insulator is etched only on the top of the mesa and successfully contacted with the electrode. Fig. 4.4 shows the measurement results of the fabricated devices. The devices were measured at room temperature in pulses. For devices with a stripe width of 5 μm and a cavity length of 420 μm, threshold currents of 24 mA and 23 mA at room temperature were obtained for the conventional and new recipes, respectively, which are almost the same values. However, as the temperature of the stage is increased, the devices fabricated with the conventional recipe show a marked increase in threshold current. Fig. 4.5 shows the change in threshold current at each stage temperature. The threshold current is known to increase exponentially with temperature, and the temperature characteristic of device is evaluated using the characteristic temperature T_0. Compared to the conventional active layer, the new active layer increased T_0 from 56 K to 75 K, a 30% increase.

Doping concentration of contact layer

In a previous study, it was reported that the internal loss was reduced to 22 cm^{-1} by reducing the doping concentration in *p*-InP regrowth from 2×10^{18} cm^{-1} to 5×10^{17} cm^{-1}. The initial substrate had to be changed due to a change in the fabrication process, so the conditions of the OMVPE were reexamined. In the conventional initial substrate, DMZn was used to grow the contact layer at the maximum flow rate of 520 sccm to achieve high doping concentration in GaInAs. However, the Zn doping concentration saturates at a

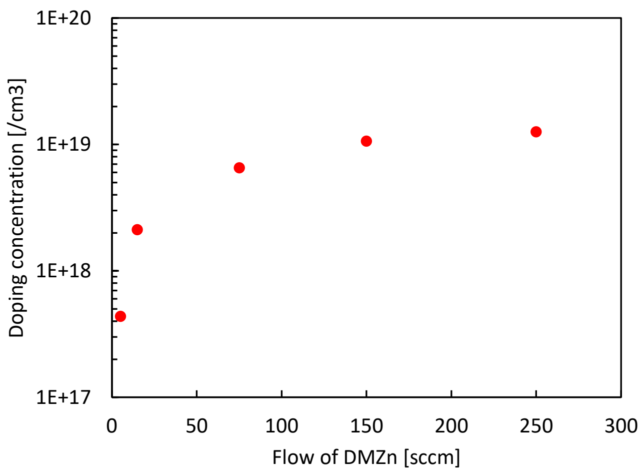

Fig. 4.6 Relationship between the DMZn flow rate and doping concentration measured with a CV profiler.

certain DMZn flow rate, and even if the flow rate is increased further, the doping concentration does not increase and diffuses to the bottom layer. This excess DMZn diffuses Zn into the InP cladding layer and OCL, causing absorption and increasing internal loss. Also, when contacting the electrode and *p*-InP, a layer of highly doped *p*-GaInAs is placed between them to make ohmic contact. However, the difference in band gap between InP and GaInAs is large, and there is concern that a barrier may be created due to the band discontinuity, resulting in a resistive component. Therefore, it is expected that a layer of GaInAsP with a band gap wavelength of 1.3 µm, which is between the band gaps of InP and GaInAs, will reduce the differential resistance by mitigating the band discontinuities. This GaInAsP (1.3Q) layer is expected both to reduce the differential resistance and to suppress the diffusion of Zn into the active layer.

First, the flow rate of DMZn in the contact layer was examined. Fig. 4.6 shows the measured relationship between the DMZn flow rate and doping concentration measured with a CV profiler. In the conventional process, the flow rate was set at 520 sccm, but it can be seen that the doping concentration saturates at a flow rate above 150 sccm. This excess diffuses and possibly has a significant effect on the internal loss, so the flow rate was changed to 150 sccm. In the InP cladding layer after deposition of the contact layer, the V/III ratio was increased by setting the flow rate of TMI to 1/4 and the flow rate of

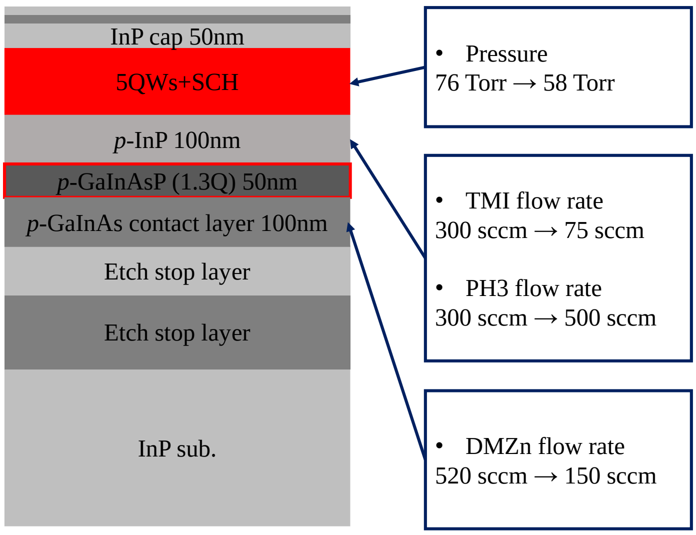

Fig. 4.7 OMVPE condition change in epi-wafer growth.

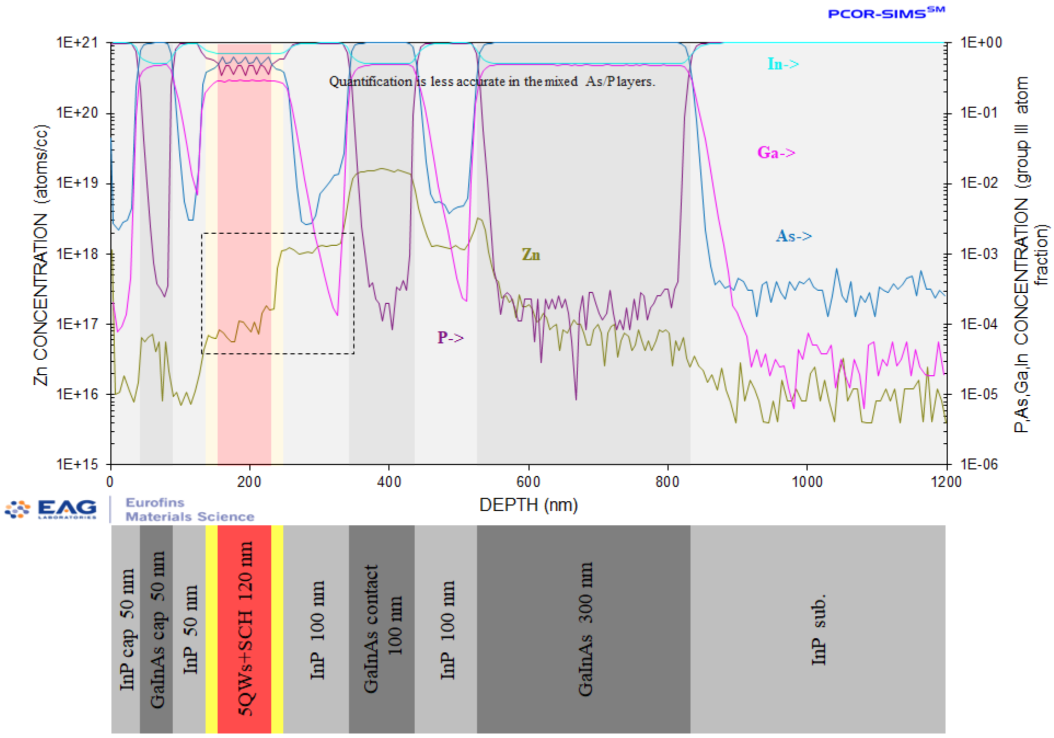

(a)

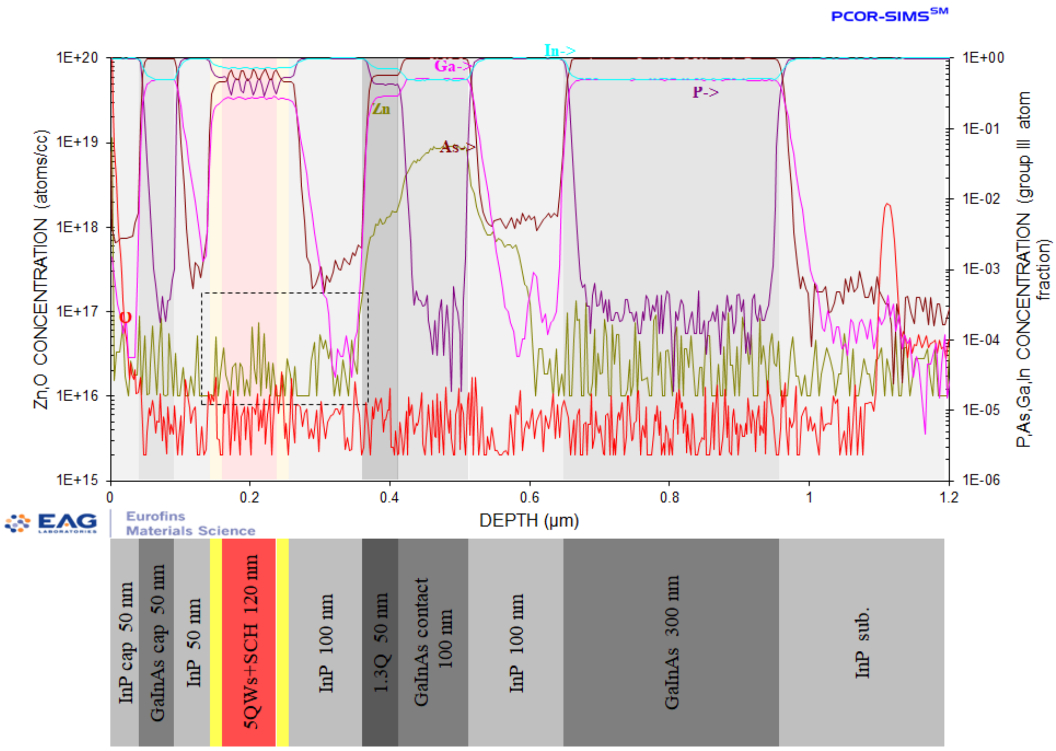

(b)

Fig. 4.8 SIMS analysis results with (a) high DMZn flow rate recipe and (b) low DMZn flow rate recipe.

PH_3 to the maximum of 500 sccm to suppress the replacement of P and Zn. In addition, the reactor pressure during active layer deposition was set to the lowest feasible value to improve the crystal quality of the active layer. The changes in OMVPE condition are summarized in Fig. 4.7.

First, initial substrates were prepared using a conventional recipe and a recipe with modified growth conditions, and the results of Zn diffusion confirmed by SIMS analysis are shown in Fig. 4.8. Focusing on the active layer and InP circled by the dashed line, it can be seen that 1×10^{18} cm^3 was doped into the InP layer even though DMZn was not flowing during the growth of that layer. This diffusion also slightly reaches the active

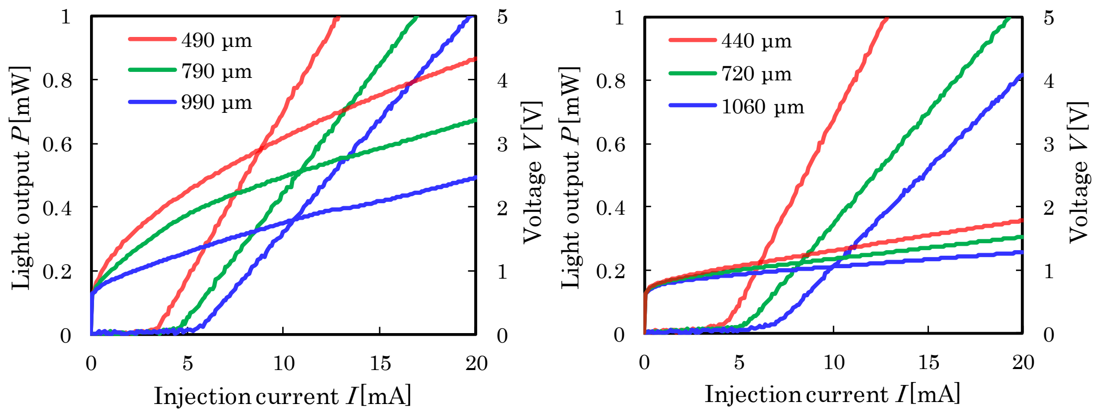

(a) (b)

Fig. 4.9 *I-L* and *I-V* characteristics with (a) conventional recipe and (b) new recipe.

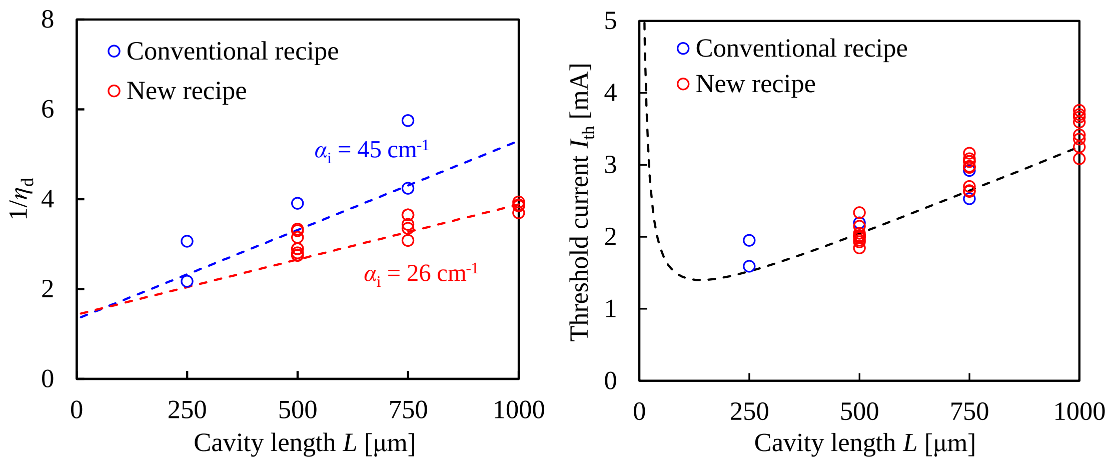

(a) (b)

Fig. 4.10 Comparison of (a) internal loss and (b) threshold current.

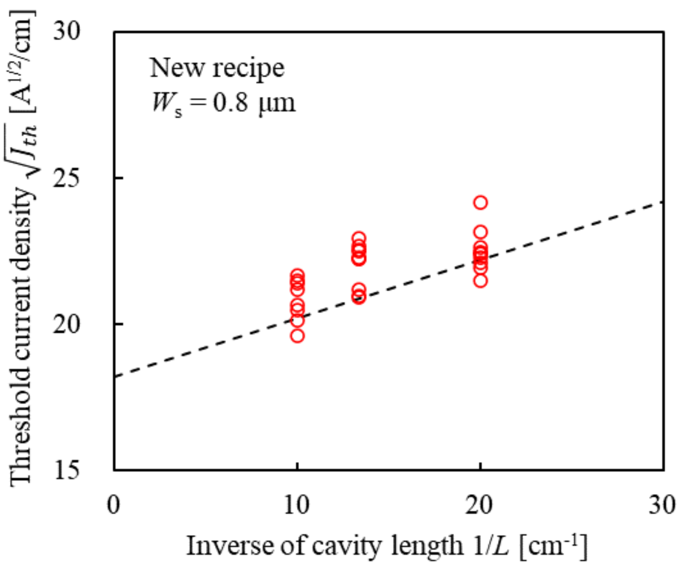

Fig. 4.11 Threshold current density as a function of the inverse cavity length.

layer, which is expected to be the cause of absorption. On the other hand, in the recipe with adjusted flow rate, the doping concentration in the contact layer is slightly reduced, but is maintained at 1×10^{19} cm^3 on the interface side with the electrode. Zn concentrations in the InP and active layer were below the detection limit, confirming that diffusion was suppressed.

Membrane FP lasers were fabricated and characterized using the recipe above. The *I-L* and *I-V* characteristics of the fabricated devices with different cavity lengths are shown in Fig. 4.9. In the device with the conventional recipe shown in Fig. 4.9(a), the resistance increases nonlinearly with the injection current. This is expected to be due to the InAsP generated at the GaInAs/InP interface, which acts as a barrier and a series resistance component. In contrast, the device with GaInAsP (1.3Q) layer shows almost ideal *I-V* characteristics as shown in Fig. 4.9(b). The cavity length dependence is shown in Fig. 4.10. Although there was no significant difference in the threshold current, the relationship between the inverse of the external differential quantum efficiency and the cavity length showed that the internal loss was 26 cm^{-1}, which is almost equivalent to the internal loss of the Be-doped substrate [5]. Fig. 4.11 shows the plot of the threshold current density of the fabricated FP lasers as a function of the inverse cavity length. A differential gain *dg/dN* of 7.2 × 10^{-16} cm^2 was obtained from the slope and the intercept of the fitting line. From these results, the basic properties of the membrane lasers were indicated.

4.3 Membrane Fabry-Perot laser with BRW structure

In this section, the results of fabrication and characterization of Fabry-Perot lasers are presented to confirm the property improvement by the BRW structure. Fig. 4.12 shows the cross-sectional SEM images of the fabricated devices. The SEM images were colored for clear visual. These were fabricated on the same initial substrate. The stripe width W_s and slope width W_d of the fabricated device are 1.8 μm and 0.5 μm, respectively. The thickness difference between the active layer and the side cladding layer is also confirmed to be 50 nm. Fig. 4.13 shows typical optical output and voltage characteristics for devices with conventional and BRW structures. The cavity length L = 560 μm, and the distance D between the electrode and the active layer is 1.7 μm for the conventional structure and

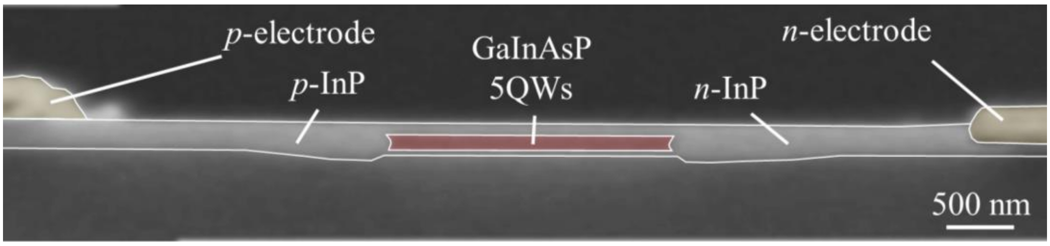

(a)

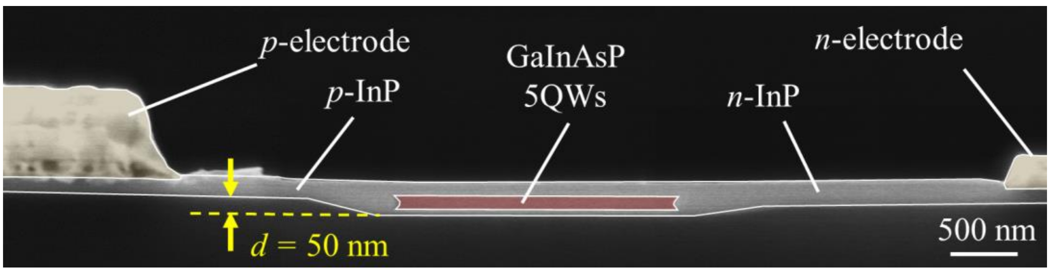

(b)

Fig. 4.12 Cross-sectional SEM images of fabricated membrane Fabry-Perot lasers with (a) the conventional flat structure and (b) the BRW structure. (Artificially colored)

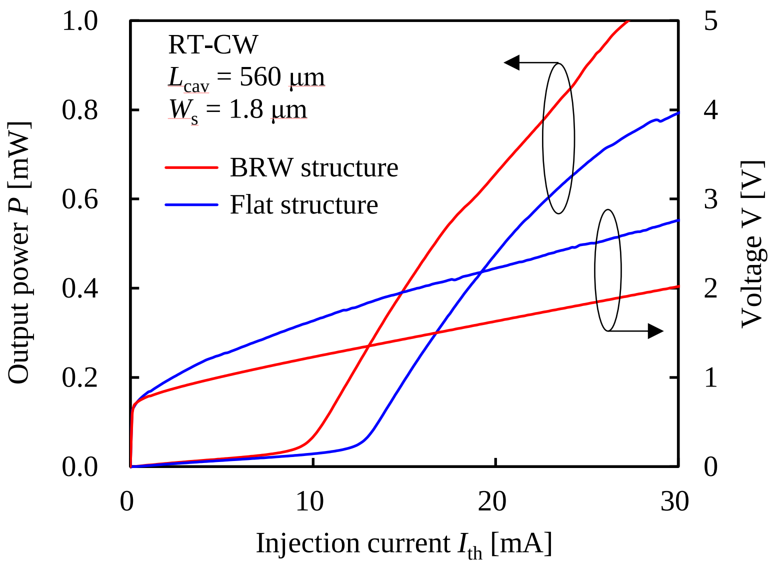

Fig. 4.13 *I-L* and *I-V* characteristics of FP laser with cavity length of 560 µm and stripe width of 1.8 µm.

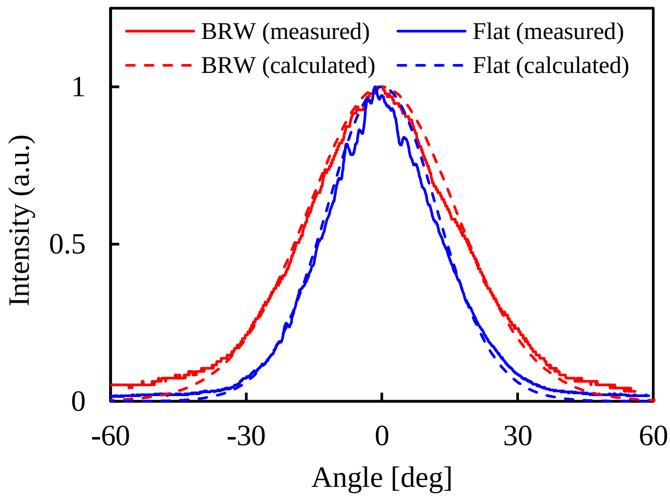

Fig. 4.14 Horizontal component of far field pattern for the BRW structure and the flat structure.

0.8 µm for the BRW structure. As shown in Fig. 4.13, the threshold current I_{th} = 12.1 mA (J_{th} = 1.0 kA/cm^2) and differential resistance dV/dI = 31 Ω are obtained for the BRW structure, while the threshold current I_{th} = 14.1 mA (J_{th} = 1.3 kA/cm^2) and differential resistance dV/dI = 59 Ω for the conventional flat structure. Fig. 4.14 shows the horizontal component of the far-field pattern when a current of 20 mA was applied. The

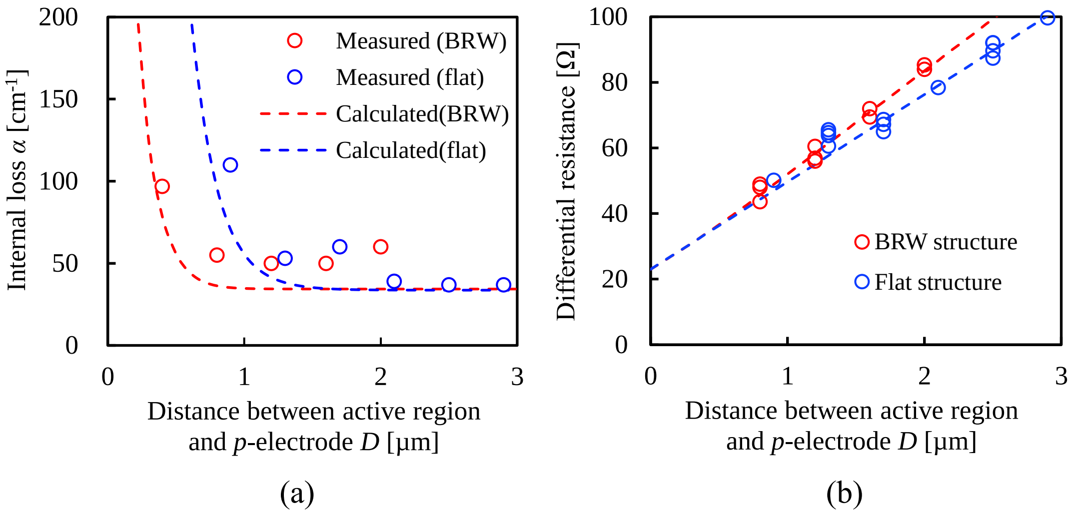

Fig. 4.15 Relationship between electrode distance and (a) internal loss and (b) differential resistance.

measurement results are shown as solid lines, with the red line indicating the BRW structure and the blue line indicating the flat structure. The full width at half maximum (FWHM) of the BRW and flat structures were calculated to be 38.0° and 27.8°, respectively. The dotted lines indicate the far-field patterns of each structure as analyzed by simulation. The parameters described in Chapter 2 were used in the analysis. The results obtained from the experiments are close to these analytical results, confirming that the expected optical confinement effect was achieved.

Next, comparison of the characteristics for several devices are shown. Fig. 4.15 shows the relationship between internal loss and distance between active region and *p*-electrode. As explained in Chapter 2, there is a relationship between electrode distance and internal loss. Since the electrode has a very large absorption coefficient, the internal loss increases rapidly when the electrode is closer to the active layer within a certain distance. Fig. 4.15(a) shows the results of the analysis with dotted lines, showing the internal loss at flat structure and the BRW structure with ridge depth d = 50 nm. For the experimental values, the internal loss calculated from the cavity length dependence are shown for each electrode distance. The internal loss increased rapidly as the electrodes were placed closer, and the minimum distances between active region and electrode at

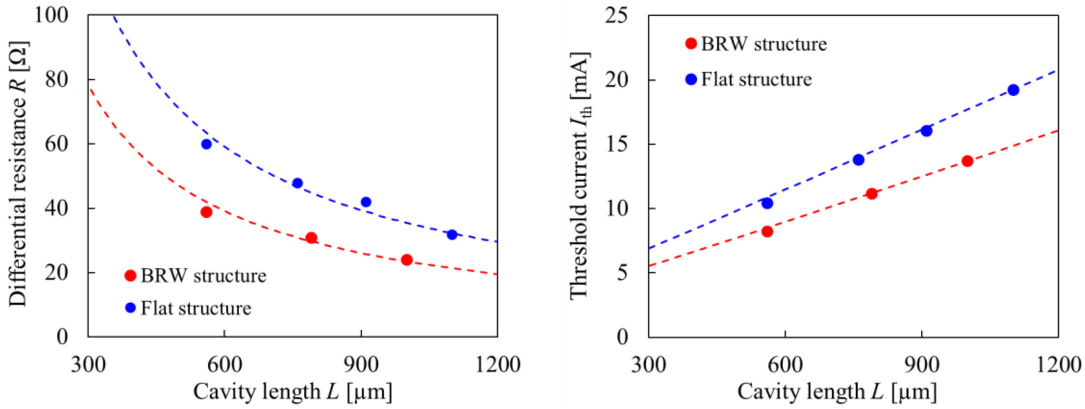

(a) (b)

Fig. 4.16 Comparison of cavity length dependence of (a) threshold current and (b) differential resistance.

which the internal loss was not increased were 0.8 μm and 1.7 μm, respectively. Also, the relationship between differential resistance and distance between active region and *p*-electrode is shown in Fig. 4.15(b). Since the differential resistance is inversely proportional to the cavity length, the value of differential resistance is converted to a cavity length of 500 μm. The side cladding layer is the current path, resulting in a higher differential resistance for devices with the same electrode distance in the BRW structure. However, as shown in Fig. 4.15 the BRW structure can reduce the electrode distance, and consequently reduce the differential resistance.

Fig. 4.16(a) shows the dependence of differential resistance on cavity length. The blue line shows a flat structure with $D = 1.7$ μm and the red line shows the BRW structure with $D = 0.8$ μm. The electrode could be placed closer to the active layer, resulting in a 35% reduction in differential resistance from the flat structure. The cavity length dependence of the threshold current is shown in Fig. 4.16(b). The threshold current is related to the optical confinement factor to the active layer, and the larger the confinement factor, the lower the threshold current. The BRW structure with a ridge depth of $d = 50$ nm increased the optical confinement factor, resulting in a 15% reduction in the threshold current. The above results experimentally demonstrate that the introduction of the BRW structure increases optical confinement and improves laser characteristics.

4.4 Low threshold current membrane DR laser

In the previous section, the effect of the BRW structure was confirmed by fabricating FP lasers. In this section, membrane DR lasers with ACPM grating were fabricated and characterized.

Fig. 4.17 shows a schematic diagram of the fabricated membrane DR laser with stripe width of 0.7 μm. The re-grown laser substrates were bonded onto the Si substrate by the a-Si assisted direct bonding technique established by co-worker Fang [3]. Fig. 4.18 shows a detailed description of the grating section. The grating was designed using the refractive index at a grating depth of 50 nm, and the basic grating period of the DFB region is 293 nm. The grating period of the phase shift region is determined by the cavity

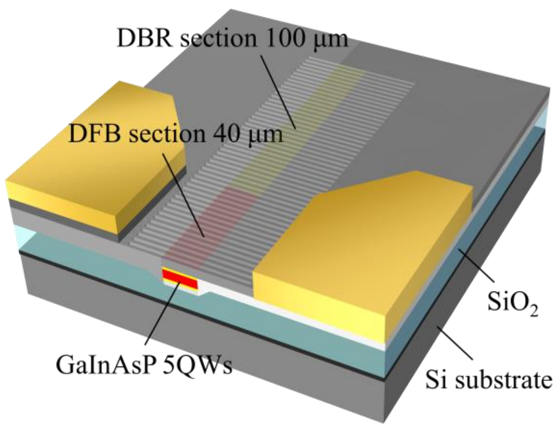

Fig. 4.17 Schematic of fabricated membrane DR laser with the BRW structure and ACPM grating.

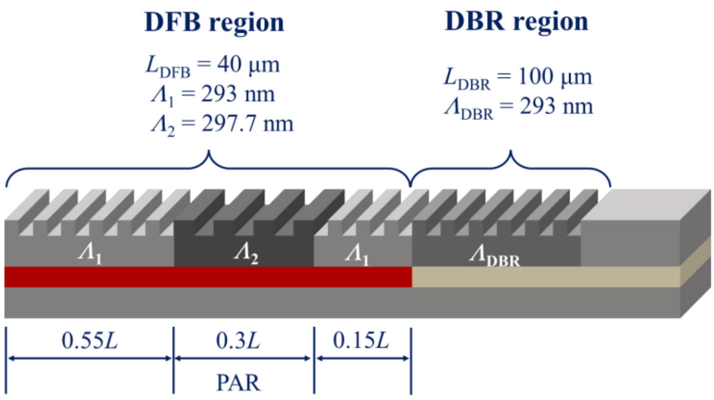

Fig. 4.18 Cross sectional view for detailed description of the grating section.

length and the length of the phase arrange region (PAR). In this design, the DFB region length was set to 40 μm and the PAR to 0.3. The grating period for the phase shift of π was calculated to be 297.7 nm. The DBR region was designed so that the stopband overlapped with the lasing wavelength, resulting in a grating period of 293 nm. The DBR length was 100 μm to obtain sufficient reflectivity.

4.4.1 Static characteristics

Fig. 4.19 shows the *I-L* and *I-V* characteristics of the fabricated device. The threshold current of 0.13 mA and external differential quantum efficiency from front facet of 23% were obtained. The threshold current is 40% lower than the threshold current of 0.21 mA for the flat structure and uniform grating in the previous study, due to the increase in optical confinement factor by the BRW structure and the reduction in threshold gain by the phase shift of the ACPM grating. The differential resistance was also successfully reduced to 480 Ω by bringing the distance between the electrode and the active layer to 0.8 μm. In addition, the change in active layer thickness and the improvement of thermal resistance by direct bonding resulted in an increase in saturation injection current up to 5

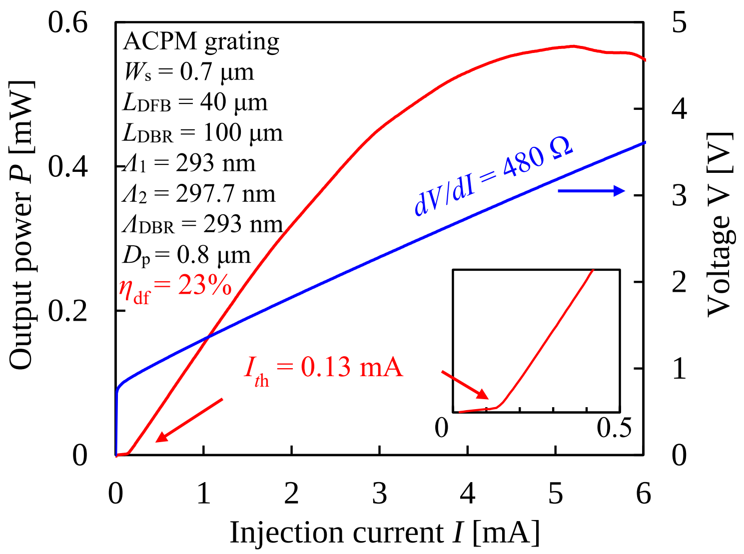

Fig. 4.19 *I-L* and *I-V* characteristics of the fabricated membrane DR laser with ACPM grating.

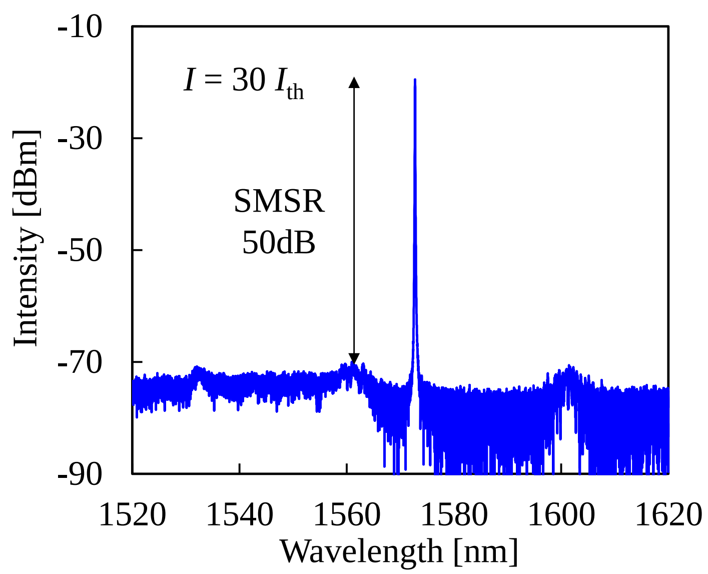

Fig. 4.20 Lasing spectrum with injection current $I = 30\ I_{th}$.

mA, despite the short cavity of 40 μm. Fig. 4.20 shows the spectrum of the fabricated device at injection current of I = 30 I_{th}. The SMSR of 50 dB is obtained even at high injection currents, confirming that hole-burning is suppressed by the ACPM grating. The lasing wavelength is 1570 nm, which is slightly shorter than the center of the adjacent side modes. This is because this device has a cleaved end facet, and the design parameters were calculated by assuming zero reflection from the end facet. Also, the device is cleaved on the active layer. If a waveguide is formed on the front side, FP mode is generated at the boundary between the front cleaved facet and the active layer, and the operation becomes unstable. Therefore, the DFB length shift due to cleavage is also a cause. These can be solved by applying an anti-reflective coating to the cleaved facet or are not a problem in optical link applications because they have no cleavage. Uniform and λ/4-shifted grating were also fabricated on the same substrate. The characteristics of the devices with the lowest threshold among the fabricated devices are shown in Fig. 4.21. Both devices have a stripe width of 0.7 μm, a DFB length of 30 μm, and a DBR length of 100 μm. A threshold current of 0.18 mA was obtained for the uniform grating, confirming the reduction of the threshold current due to the BRW structure even for the DR laser. For devices with λ/4-shifted gratings, the threshold current was 0.15 mA due to the reduction

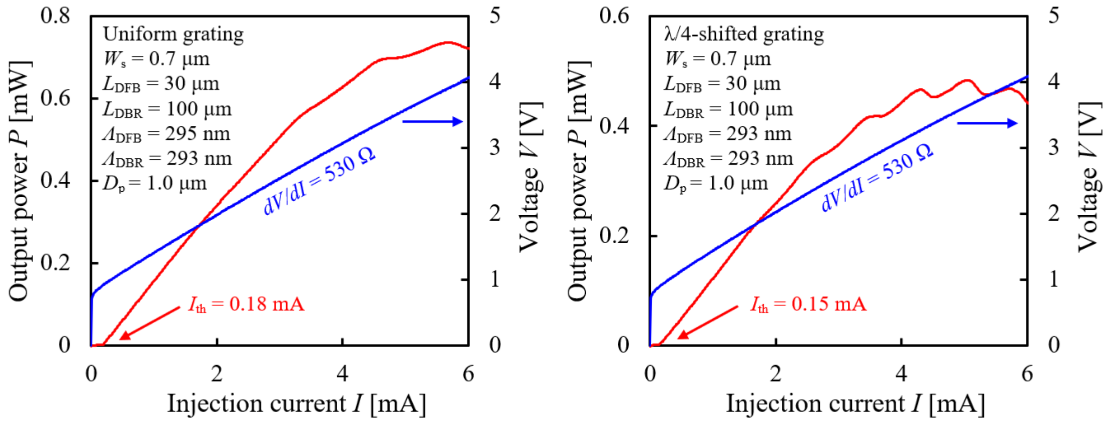

Fig. 4.21 *I-L* and *I-V* characteristics of the fabricated membrane DR lasers with (a) uniform grating and (b) λ/4-shifted grating.

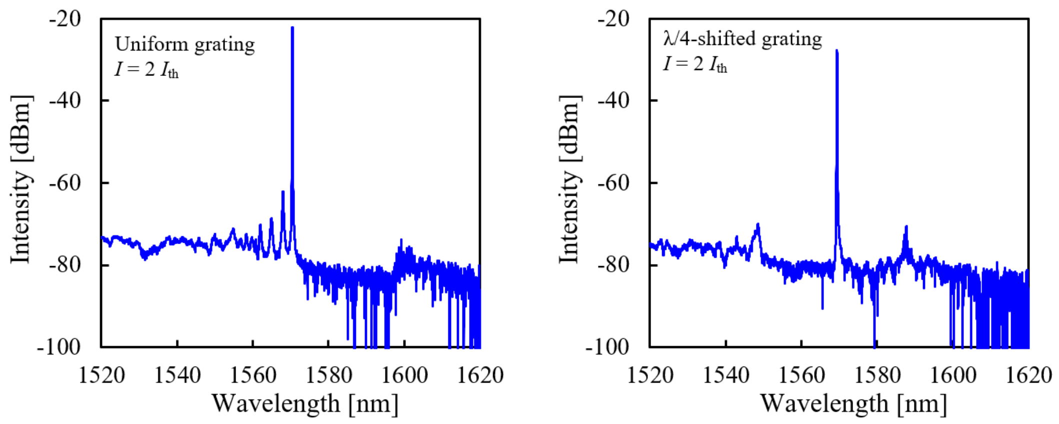

Fig. 4.22 Lasing spectrum of the fabricated membrane DR lasers with (a) uniform grating and (b) λ/4-shifted grating.

in threshold gain caused by the phase shift. The index-coupling coefficient κ_i was calculated to be 1370 cm^{-1} from the stopband width of 30 nm in Fig. 4.22(a). For the device with λ/4-shifted grating, single mode lasing was observed near the center of the stopband due to the phase shift as shown in Fig. 4.22(b). The lasing wavelength is slightly shifted from the center, possibly due to a fabrication error in the width of the phase shift.

Next, the cavity length dependence of the fabricated devices is presented. Fig. 4.23. shows the obtained threshold current for each grating as a function of the DFB region length. The dashed line shows the theoretical curve with an internal quantum efficiency

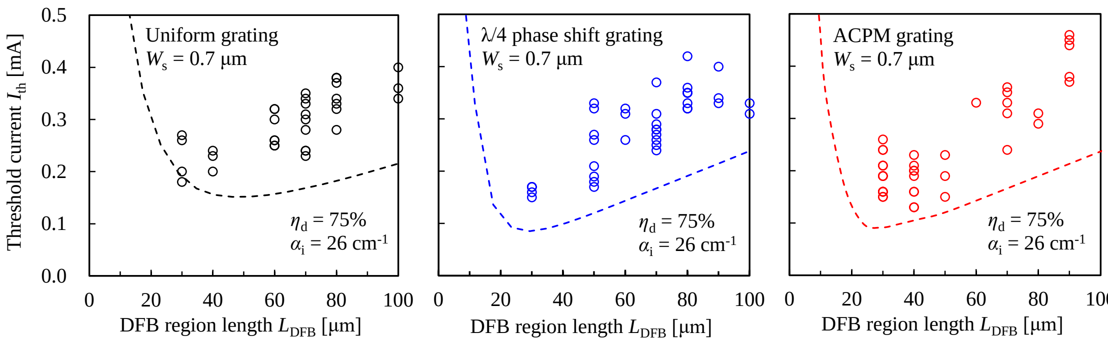

(a) (b) (c)

Fig. 4.23 DFB length dependence of threshold current for each grating structure.

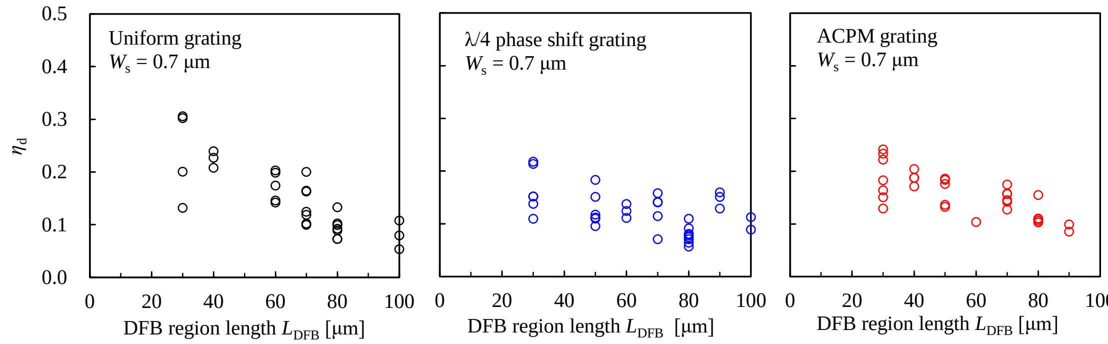

(a) (b) (c)

Fig. 4.24 DFB length dependence of differential quantum efficiency for each grating structure.

of 75% and internal loss of 26 cm^{-1}, which were experimentally obtained from FP laser characteristics. As the DFB region length increases, the threshold current increases because the active layer volume increases. The results obtained from experiments show similar tendency to the theoretical curves. However, the values are slightly higher than the theoretical values for all structures. This is possibly due to leakage currents through the passive region. Fig. 4.24 shows the DFB length dependence of the external differential quantum efficiency. As the DFB region length increases, the external differential quantum efficiency decreases because the mirror loss becomes smaller. Comparing the external differential quantum efficiencies for λ/4-shifted grating and ACPM grating, the λ/4-shifted grating tends to be lower over the entire cavity length. This could be attributed to the decrease in output caused by the decrease in gain as the injection current increases due to the effect of hole burning.

4.4.2 Dynamic characteristics

In this part, the dynamic characteristics of the membrane DR laser, including small-signal measurements and large-signal data transmission, are investigated. First, small-signal measurements are performed using a vector network analyzer (VNA). The microwave frequency from 40 MHz to 65 GHz is available. An electrical modulation signal was applied to the device via a 40 GHz high-speed ground-signal (GS) RF probe. The light output from the facet was coupled to a spherical-lensed single-mode fiber. The coupled optical signal was finally detected by a 20-GHz PIN-trans-impedance amplifier (TIA) photoreceiver. The measurement was performed for the device with the DFB region length of 40 μm, shown in Fig. 4.17.

The small-signal response S_{21} of the membrane DR laser with various bias current from 0.25 mA to 1.5 mA are shown in Fig. 4.25. The relaxation frequency f_r and the 3-dB bandwidth f_{3dB} both increased with increasing current up to an injection current of 1.5 mA. At a bias current of 0.9 mA, f_{3dB} reached 14.1 GHz, which implies that 20-Gbit/s

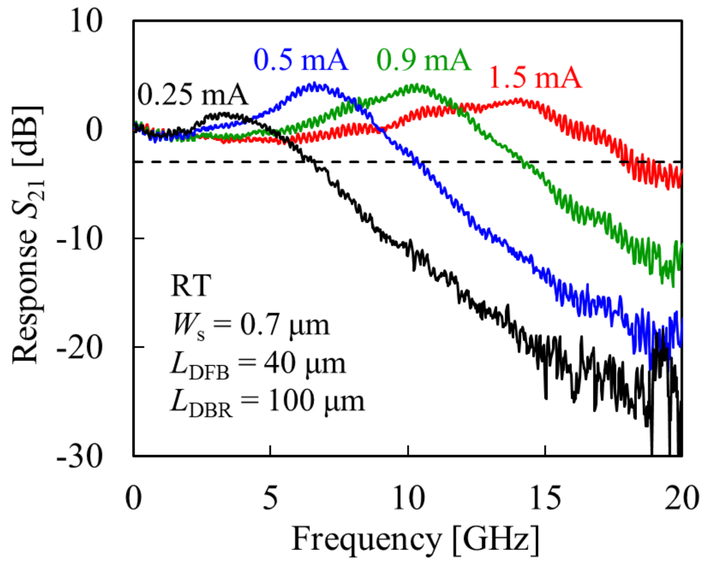

Fig. 4.25 Small signal response S_{21} of the membrane DR laser with ACPM grating.

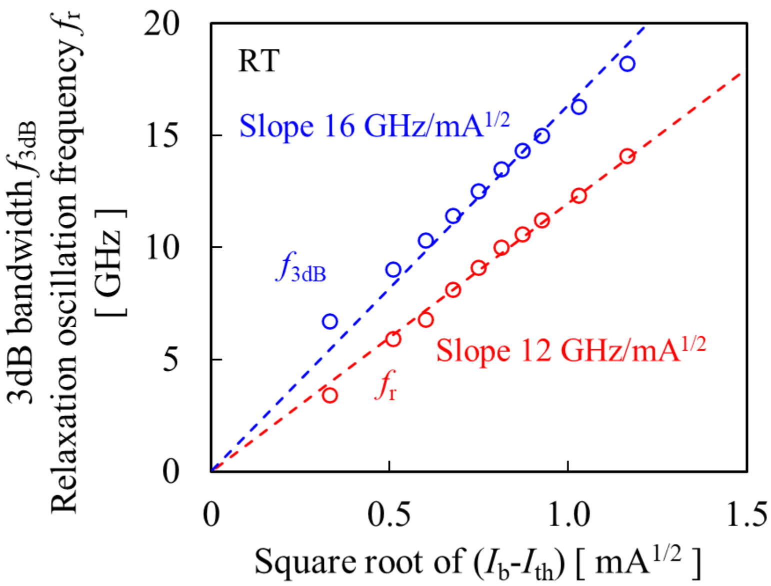

Fig. 4.26 Relaxation oscillation frequency f_r and 3dB bandwidth f_{3dB} as a function of the square root of I_b-I_{th}.

operation can be expected with a bias current of approximately 1.0 mA. The maximum f_r of 14.1 GHz and f_{3dB} of 18.5 GHz were obtained at bias current of 1.5 mA. The modulation efficiency was determined by the slope of the f_r and f_{3dB} as a function of the square root of I_b - I_{th} as shown in Fig. 4.26 Relaxation oscillation frequency f_r and 3dB bandwidth f_{3dB} as a function of the square root of I_b-I_{th}.. The modulation current efficiency factor (MCEF) and the slope of f_{3dB} were 12 GHz/mA$^{1/2}$ and 16 GHz/mA$^{1/2}$, respectively. In previous studies, f_{3dB} saturated at around 13 GHz due to high differential resistance and high thermal resistance [1], but these improvements have significantly increased the 3-dB bandwidth. As for the MCEF, it was expected to be improved due to increased optical confinement, but the results were almost the same as previous studies. Since f_r is expressed by Eq. (2.24), the cause is the decrease in differential gain due to the change in the active layer.

Next, the large signal modulation was performed. Fig. 4.27 shows the measurement setup of large signal measurement. An electrical data signal of the non-return-to-zero (NRZ) modulation scheme with a pseudo-random bit sequence (PRBS) with a word

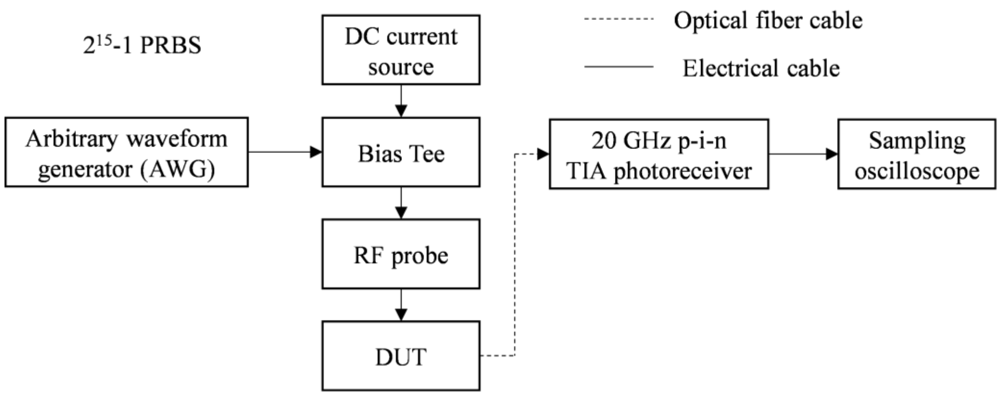

Fig. 4.27 Measurement setup for large signal modulation.

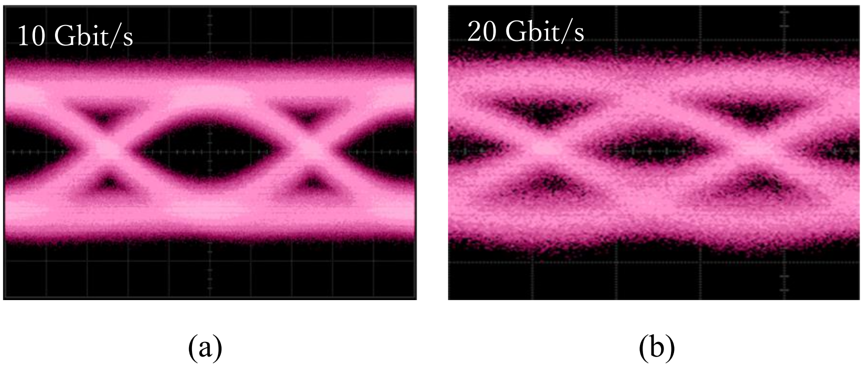

Fig. 4.28 Eye diagrams of membrane DR laser biased at 3.0 mA for 10 Gbit/s, 20 Gbit/s.

length of 2^{15} - 1 was generated by an arbitrary waveform generator (AWG). The optical signal from the device was received by photodetector after attenuated using a variable optical attenuator. Fig. 4.28 shows the eye pattern of the 10 Gbit/s and 20 Gbit/s NRZ signal. The bias current of the device and the modulation voltage swing were set to 3.0 mA and 0.75 Vpp, respectively. A clear eye opening was obtained at relatively high injection current, while at lower injection currents the eye pattern was unclear. Since the optical output was not amplified by the EDFA in this measurement, it was considered that the signal power was insufficient to detect. The eye diagram in Fig. 4.28(b) shows no waveform collapse, which implies that a clear eye opening can be observed even at low injection currents if the optical signal is properly amplified.

4.5 Discussion of consumption power of membrane DR laser

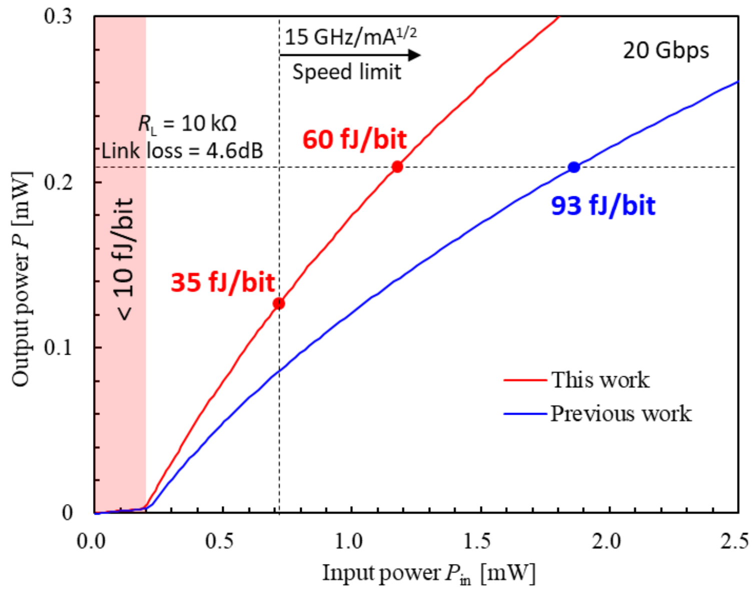

Fig. 4.29 Consumption power for 20 Gbit/s operation.

Using the above results, the power consumption of the membrane laser was estimated. In a previous study, transmission experiments with a membrane DR laser and a fiber-coupled receiver reported an energy cost of 93 fJ/bit at 20 Gbit/s operation [1]. In this experiment, the optical output received by the photodetector was affected by the loss of fiber coupling and amplification by the Er-doped fiber amplifier (EDFA). The I-V characteristics indicate that the optical output is 0.21 mW at an injection current that gives 93 fJ/bit, so this device meets the requirements for an optical link with a load resistance of 10 kΩ and a link loss of 4.6dB. Assuming a comparable optical link, 60 fJ/bit transmission is estimated to be possible with the device fabricated in this study, as shown in Fig. 4.29. A large portion of this reduction in energy costs is due to the reduction in differential resistance and threshold current. By designing a higher load resistance or reducing link loss, the required optical output is expected to decrease, and the energy cost can be reduced to 35 fJ/bit. To further reduce energy costs, the requirement by modulation speed needs to be lowered. Fig. 4.30 shows the relationship between each laser

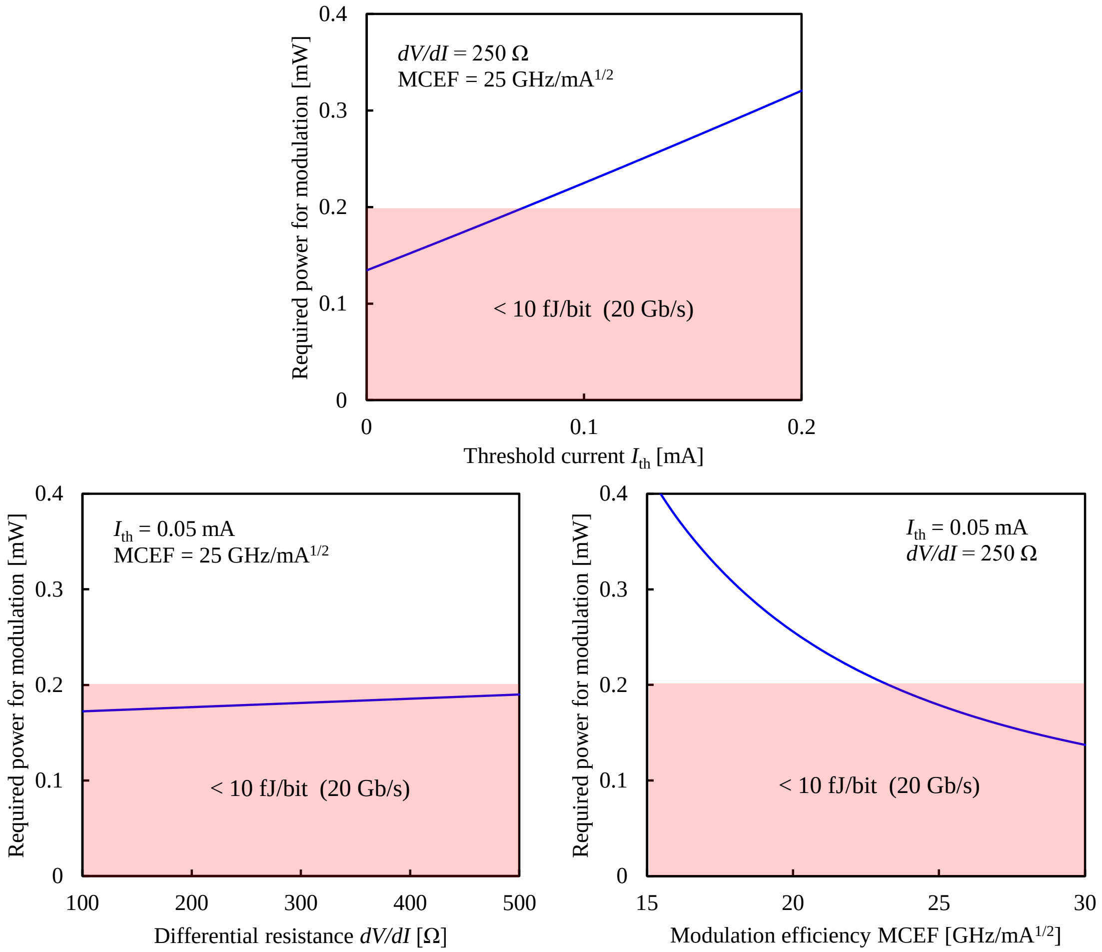

Fig. 4.30 Comparison of power consumption for the modulation with various laser characteristics.

characteristic and the power consumption required for 20 Gbit/s operation. The results show that the threshold current and MCEF are significantly related to the modulation speed. As for the threshold current, it is expected that it can be reduced to 0.07 mA by reducing the leakage current flowing through the waveguide. As for the MCEF, the relaxation oscillation frequency was expected to increase due to the increase in optical confinement, but the experimental results were almost the same as in the previous study. A possible cause is that the differential gain has been reduced by changing the active layer strain. In addition, the cavity length was designed to minimize the threshold current in this design, but the optimum cavity length could be slightly shorter in a structure that also takes modulation into account. As for differential resistance, differential resistance does not have a significant impact on power consumption at low injection currents, so further deepening the ridge depth to further strengthen lateral optical confinement is also a candidate.

4.6 Conclusion

In summary, this chapter delved into the characterization and analysis of membrane lasers with a focus on achieving the ideal semiconductor laser. The exploration involved a thorough examination of semiconductor laser structures, considering both material and structural parameters. The enhancement process commenced with an improvement in the initial epi-wafer, the foundational element of semiconductor lasers. Subsequently, membrane DR lasers with the BRW structure and ACPM grating, previously discussed in preceding chapters, were fabricated and subjected to detailed characterization. The experimental results provided valuable insights into laser characteristics, paving the way for a comprehensive evaluation of power consumption in various applications. In the fabricated DR laser with a ridge depth of 50 nm and a DFB region length of 40 um, a low threshold current operation of 0.13 mA was achieved, a 40% reduction from the previous study. The differential resistance was also significantly reduced from 860Ω in the previous study. The energy cost was calculated to be 60 fJ/bit, assuming the same link loss as in the previous study. This discussion on the ideal laser sets the stage for informed advancements and further refinements in semiconductor laser design and application.

Reference

[1] T. Tomiyasu, T. Hiratani, D. Inoue, N. Nakamura, K, Fukuda, T. Uryu, T. Amemiya N. Nishiyama and S. Arai, "High-differential quantum efficiency operation of GaInAsP/InP membrane distributed-reflector laser on Si", *Appl. Phys. Express*, vol. 10. p. 062702. 2017.

[2] T. Hiratani, D. Inoue, T. Tomiyasu, K, Fukuda, N. Nakamura, T. Amemiya, N. Nishiyama and S. Arai, "High Efficiency Operation of GaInAsP/InP Membrane Distributed-Reflector Laser on Si," *Appl. Phys. Express*, vol. 10, p. 62701, 2017.

[3] W. Fang, N. Takahashi, Y. Ohiso, T. Amemiya, N. Nishiyama, "High-quality, room-temperature, surface-activated bonding of GaInAsP/InP membrane structure on silicon," *Japanese Journal of Applied Physics*, vol. 59, p. 060905, 2020.

[4] M. Eissa, "Study of InP/Si Hybrid Lasers with High-quality Si Waveguide Fabrication by Electron Beam Lithography" Doctoral Thesis, Tokyo institute of technology, 2022.

[5] T. Tomiyasu, T. Hiratani, D. Inoue, K. Fukuda, N. Nakamura, T. Amemiya, N. Nishiyama, S. Arai, "Waveguide Loss Reduction of Lateral-current-injection Type GaInAsP/InP Membrane Fabry-Perot Laser," *Japanese Journal of Applied Physics*, vol. 56, No. 5, p. 050311, 2017.

Chapter 5
Future prospects: extension of applications of membrane lasers

5.1 Introduction	154
5.2 Application for on-chip optical interconnect	155
5.2.1 Short distance optical communication	155
5.2.2 Requirements of on-chip optical interconnect	160
5.2.3 Optical link with InP waveguide	166
5.3 Application for optical neural network	173
5.3.1 Optical neural network using photonic integrated circuit	173
5.3.2 Concept of all optical neural network using membrane laser	178
5.3.3 Characterization and future prospect	180
5.4 Application for B5G/6G communication system	186
5.4.1 Radio-over-fiber (RoF)	186
5.4.2 Photon-photon resonance (PPR) for high-speed modulation	188
5.4.3 Characterization and future prospect	192
5.5 Conclusion	198
Reference	199

5.1 Introduction

This chapter discusses various applications that take advantage of the low power consumption and fast response of semiconductor membrane lasers. In the previous chapter, ideal semiconductor lasers were discussed with on-chip optical interconnection as an application example. Section 5.2 provides an overview of the background of optical interconnection and discusses the challenges and approaches for on-chip interconnection, which has the shortest communication distance. The remaining issues to be solved for the optical interconnection approach are discussed. Section 5.3 discusses the application of membrane lasers to deep learning. Demand for deep learning has exploded in recent years, and research on reducing the time and power consumption required for these learning processes using optical circuits has attracted much attention in recent years. A method to utilize a semiconductor membrane laser as an activation function is proposed and experimentally demonstrated. Section 5.4 examines the application of membrane lasers as a light source for analog radio-over-fiber, which is expected to be a next-generation communication technology.

5.2 Application for on-chip optical interconnect

5.2.1 Short distance optical communication

Communications using optical fiber have contributed greatly to the development and spread of the Internet, and optical communication technology has also advanced due to the demand for wider bandwidth. In recent years, not only long-distance optical communications through metro networks and long-distance trunk lines, but also communication traffic in short-distance optical communications within data centers has been rapidly increasing. In line with this trend, the server has been evolving remarkably over the past several years. In addition, the performance of servers, which have evolved remarkably over the past several years, must be further improved. Factors on the hardware side that limiting server performance include the communication bandwidth limit of the

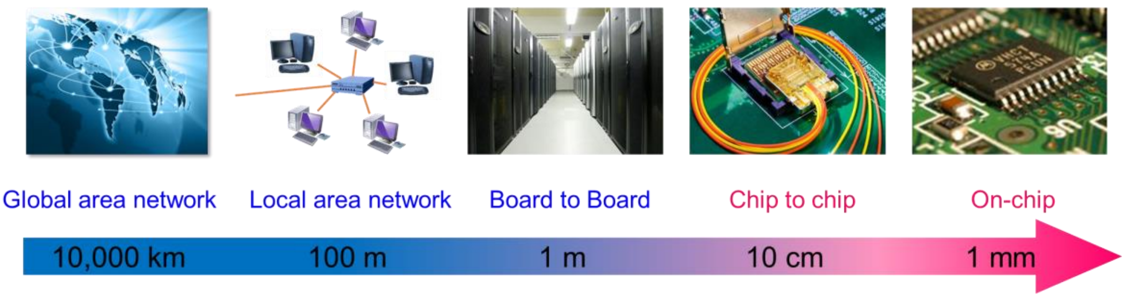

Fig. 5.1 Optical communication systems for various distances.

Ethernet local area network (LAN) connecting the server to the network backbone and server rack, communication between boards in the rack, and communication between CPU and memory in the board. Ethernet LANs have been developed in the early 1970s, and since then, the speed of Ethernet LANs has increased. Optical fiber was first introduced to Ethernet LANs in the 10BASE-F standard, which used a wavelength of 0.85 μm and had lower loss than coaxial cables but did not spread because of its high installation cost. Later, not only the 0.85 μm band but also the 1.3 μm band was introduced, and after transmission speeds exceeded 1 Gb/s from the late 1990s, many standards using optical fiber were seen. In 2019, 400GbE was standardized and is being deployed for optical communications within data centers [1]. Vertical cavity surface emitting laser (VCSEL) and multi-mode fiber (MMF) are used for short distance communications between racks, and VCSEL and single-mode fiber (SMF) are used for connections over 2 km, such as for router connections in data centers. 400GBASE-SR is the standard used for connections within 100 m, and four-pulse amplitude modulation (PAM-4) is used as the modulation scheme.

As the communication bandwidth in Ethernet LANs has been improved, research on optical interconnection has been conducted in recent years to increase the bandwidth for inter-board communication within racks ranging from several tens of centimeters to several meters and for chip-to-chip communication within boards, to handle the increasing amount of information being communicated. For board-to-board communication, several methods have been proposed, including direct transmission free-space systems [2][3], free-space systems using total reflection [4]-[6], systems using optical fibers [7], and planar lightwave circuit (PLC) systems using waveguides[8]-[16]. Recently, an 8 Gb/s transmission experiment [17] has been reported using a printed circuit board (PCB) embedded with polymer waveguides, in which a VCSEL array, MMF, and microlens array are integrated. Transmission experiments using optical fiber at 4 × 10 Gb/s [18] and 4 × 28 Gb/s using optical transceivers in a 65 nm CMOS process [19] have been reported, raising expectations for practical applications. On the other hand, for chip-to-chip communication within a board, research using polymer waveguides, which have

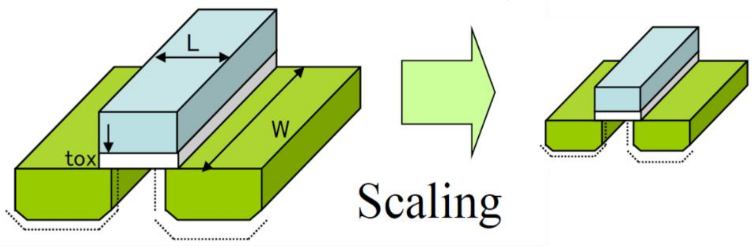

Device/Circuit parameter	Scaling Factor
Device dimensions L, W, Tox	1/S
Doping concentration	S
Voltage	1/S
Field	1
Current	1/S
Gate Delay	1/S
Power dissipation/device	$1/S^2$

Fig. 5.2 Scaling law on single device [27].

low manufacturing costs, has taken center stage. Furthermore, since polymers exhibit low loss, especially for wavelengths of 850 nm [20], optical links with VCSELs, polymer waveguides, and photodetectors are commonly used [20]-[23]. Recent studies have reported signal transmission at 16 × 10 Gb/s and 16 × 15 Gb/s using 4 × 4 VCSEL arrays [23] and high-density integration of chip modules [24], followed by board-to-board optical interconnects.

As transmission capacity increases, optical communication is expanding its application to shorter distance communications, and optical wiring is now being used for inter-board wiring in data centers, and there are high expectations for the practical application of optical wiring for chip-to-chip connections within boards. And even shorter-range communication, on-chip optical interconnection, is also being actively researched. Large-scale integrated circuits (LSIs) have achieved high speed and high integration based on the scaling rule [25]. The scaling rule is a design guideline for transistors published by Dennard *et al.* in 1974, which states that when transistor dimensions are increased by a factor of 1/S, current and voltage are increased by a factor of 1/S, circuit delay time is increased by a factor of 1/S, and integration is increased by a factor of S^2 as shown in Fig. 5.2. However, as wiring becomes finer along with the

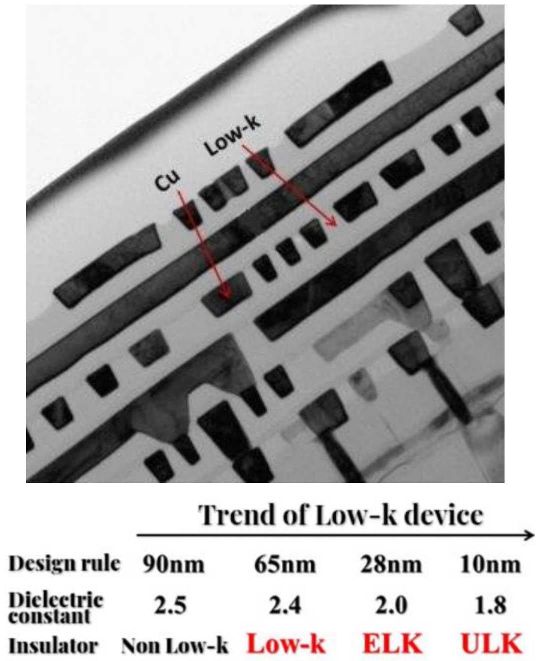

Fig. 5.3 Cu/low-k interconnects [29].

elements, the resistance of the wiring becomes higher. Since information transmission by electricity is limited by resistance and capacitance, power consumption increases at high bit rates [26]. In addition, processor performance is still improving according to Moore's law, but the delay time of individual transistors has already saturated, and performance improvements are being realized through parallelization and other means [27]. However, this delay becomes a problem when true low-delay processing is required. Methods to solve these problems include the use of low-*k* materials as dielectric materials between wires and the insertion of repeater buffers. Low-*k* materials are low-dielectric materials with a relative dielectric constant k of 3.0 or less (Fig. 5.3). Low-*k* materials can be used as interlayer dielectric materials to lower interconnection capacitance and reduce interconnection delay, and many low-*k* materials with low dielectric constant have been proposed [28][29]. In addition, since the time constant RC increases in proportion to the square of the wiring length, delay can be suppressed by shortening the wiring and connecting the wiring with a repeater circuit [30][31]. However, the inclusion of repeater circuits is not a fundamental solution because it leads to increased power consumption and chip size. Therefore, as shown in Fig. 5.4, three-dimensional integration, in which

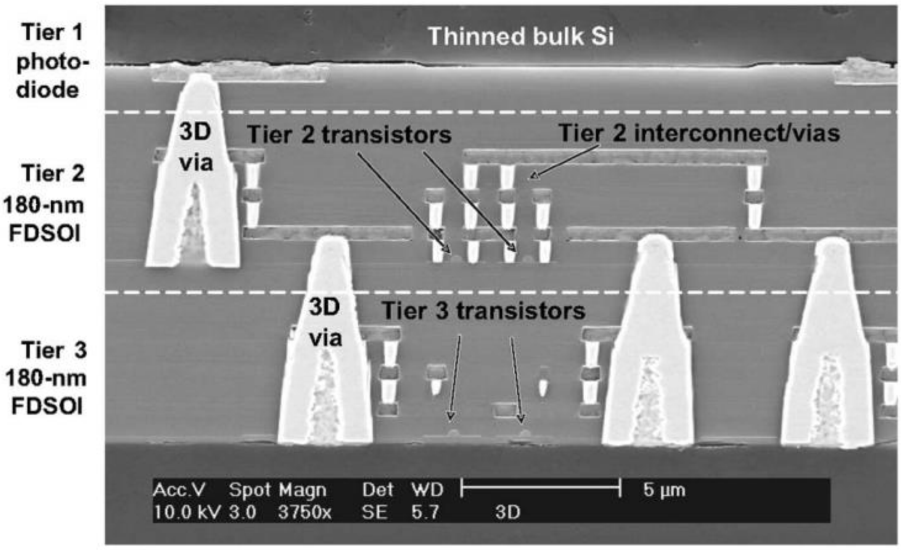

Fig. 5.4 Three-dimensional (3-D) integrated circuit [32].

LSI layers are stacked top to bottom and connected at the top and bottom through an insulating layer, has been actively studied in recent years. This method can shorten the distance between blocks by stacking chips three-dimensionally and can shorten the wiring length compared to wiring on the same plane, thus enabling higher speeds [32]. However, this three-dimensional integration technology has problems such as alignment tolerance between stacked boards, lower yield, and less freedom in wiring layout.

Therefore, as another approach to solve the problem in global electrical wiring, on-chip optical wiring has been proposed to replace global electrical wiring with optical wiring [33]-[35]. Since information transmission by light is not limited by RC, it is more advantageous than electrical wiring in terms of power consumption at higher bit rates. Also, by applying the multiplexing technology cultivated in long-distance communications, large-capacity communications are possible. Other advantages include the fact that there is almost no skew because the delay varies little with distance, and the restrictions on wiring spacing due to crosstalk and electromagnetic interference can be greatly reduced. Furthermore, on-chip optical interconnects are highly compatible with chip-to-chip optical interconnects, and these studies are expected to be useful for their mutual development [36].

5.2.2 Requirements of on-chip optical interconnect

To realize on-chip optical interconnection, a semiconductor laser that can operate with extremely low power consumption is required. The power consumption is determined by the bias current, and the bias current must satisfy both requirements by optical output and modulation speed. The requirement by optical output is due to the optical power required for error-free operation of the photodetector. The requirement by modulation speed is due to the bias current required to modulate the semiconductor laser. Since the 3-dB bandwidth f_{3dB} of a semiconductor laser is proportional to the square root of I_b-I_{th}, a bias current above a certain level is required to transmit signals at the desired modulation speed. The power consumption is determined by the injection current that satisfies both requirements, and the power consumption required to transmit one bit is one of the indicators of laser characteristics as energy cost. Energy costs required to realize on-chip optical interconnects are estimated by D.A.B. Miller [37]. This roadmap is based on ITRS 2007 technology node parameters, on- and off-chip clock frequencies, and signal I/O pins. Fig. 5.5 shows trends and predictions of energy cost for off-chip and on-chip interconnects. According to this prediction, the available energy cost of one

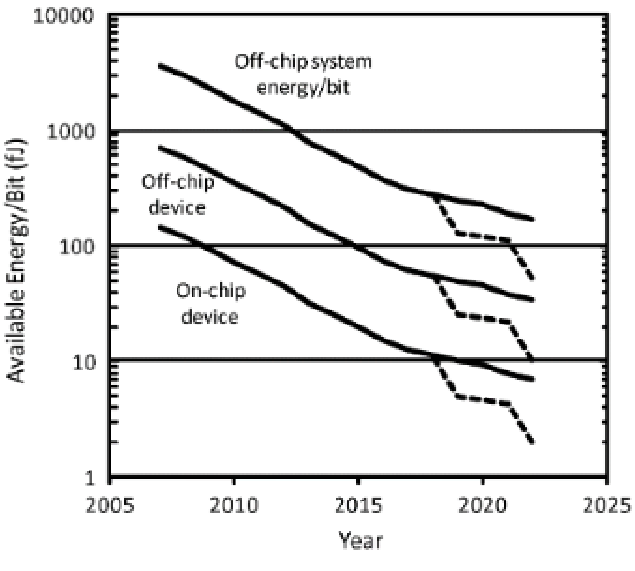

Fig. 5.5 The trend of energies per bit for off-chip devices and on-chip devices [37].

directly modulated laser should be at least less than 10 fJ/bit. Therefore, 10 Gbit/s is the target operating speed, but speeds as high as 20 Gbit/s are also possible.

Here, an estimation was performed for on-chip optical interconnection, which is one of the applications of membrane lasers. A configuration in which a laser and a photodetector are coupled by a waveguide was considered. When considering on-chip interconnection, the energy cost required for the laser is estimated to be <10 fJ/bit [37]. To achieve low power consumption of membrane lasers (<10 fJ/bit), it is necessary to reduce the required light-receiving power and link loss of the PD. Previous studies have reported that a PD absorption length of 12 μm (stripe width = 0.8 μm) can reduce the junction capacitance and increase the load resistance. The relationship between the load resistance and the required power of the photodetector is calculated by co-worker Dr. Fang [39]. The larger the load resistance, the smaller the required receive power and the 3 dB bandwidth of the PD. The relationship between bit-error-rate (BER) and signal-to-noise ratio (SNR) in an intensity-modulation-direct-detection (IM-DD) method is expressed as follows

$$BER = \frac{1}{2} erfc\left(\frac{\sqrt{SNR}}{2\sqrt{2}}\right). \tag{5.1}$$

SNR is related to a *Q* factor, and they can be expressed as follow

$$SNR = \frac{\overline{i_s^2}}{\overline{i_n^2}} = 4Q^2, \tag{5.2}$$

$$Q = \frac{I_1 - I_0}{\sigma_1 + \sigma_0}, \tag{5.3}$$

where, $\overline{i_s^2}$ and $\overline{i_n^2}$ are the mean square of signal photocurrent and noise photocurrent, respectively. *Q* factor is a function of the I_1 as the signal current of level "1", I_0 as the signal current of level "0", σ_1 as the noise current of level "1", and σ_0 as the noise current of level "0". Then, $\overline{i_s^2}$ and $\overline{i_n^2}$ are estimated by following equation

$$\overline{i_s^2} = R^2 P_{in}^2, \tag{5.4}$$

$$\overline{i_n^2} = \left(2q(i_s + i_d) + \frac{4k_BT}{R_{eq}}\right) f_{BW}, \tag{5.5}$$

where, R is the responsivity of the photodiode, P_{in} is the received power of the output optical signal from laser, q is the electron charge, i_d is the dark current, k_B is the Boltzmann constant, T is the temperature, R_{eq} is the equivalent resistance of the received circuit and f_{BW} is the bandwidth. The minimum received optical power required by the total noise P_{in_n} can be expressed as follows

$$P_{in\_n} = \frac{1}{R}\sqrt{\left(2q(i_s + i_d) + \frac{4k_BT}{R_{eq}}\right) f_{BW} \cdot SNR}. \tag{5.6}$$

On the other hand, the required minimum received optical power for supplying a sufficient output voltage P_{in_o} is defined as follows

$$P_{in\_o} = \frac{i_s}{R} = \frac{V_{out}}{RR_L}, \tag{5.7}$$

where R_L is the load resistance. Although the drive voltage varies depending on the driver configuration, the required optical output can be controlled to some extent by appropriately designing the load resistance. If the required output voltage is 200mV, the relationship between load resistance and required optical output is expressed as shown in the Fig. 5.6. For a photodetector with a stripe width of 0.8 μm and a PD absorption length of 12 μm, the input light intensity to the photodetector was estimated to be -23.01 dBm

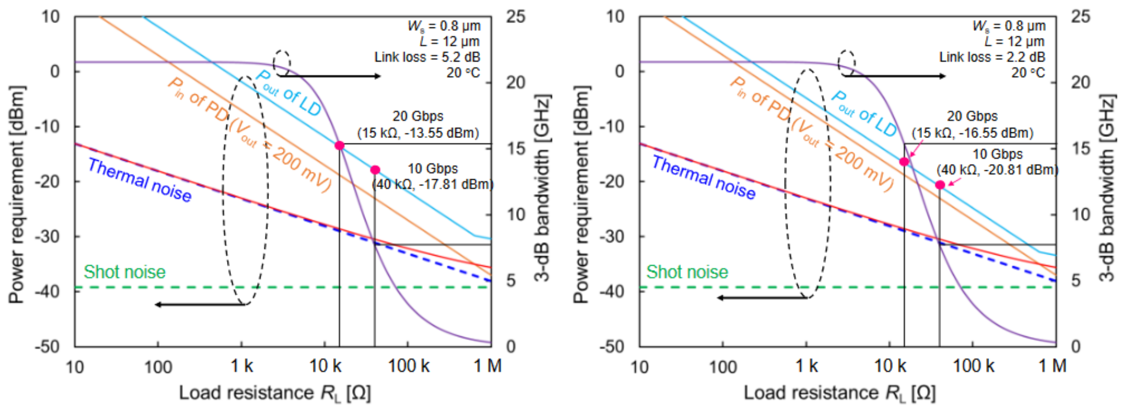

Fig. 5.6 Power requirement of membrane laser in on-chip optical interconnection [39].

Table 5.1 Light output power condition of the membrane laser.

Required received power of PD (W_s = 0.8 μm, L = 12 μm)	-23.01 dBm (10 Gbit/s, R_L = 40 kΩ) -18.72 dBm (10 Gbit/s, R_L = 15 kΩ)
Coupling loss	0.1 dB × 2
Propagation loss (2 cm)	1 dB/cm × 2
Margin	3 dB
Required light output power of LD	**17 μW (10 Gbit/s)** **44 μW (20 Gbit/s)**

with a load resistance of 40 kΩ at 10 Gbit/s operation. At 20 Gbit/s operation, required input power was estimated to be -18.72 dBm when the load resistance was 15 kΩ. Then, the total coupling loss was calculated to be 5.2 dB, assuming that the coupling loss between waveguide and LD, waveguide and PD was 0.1 dB, the propagation loss was 2 dB for 2cm propagation, and margin was 3 dB. Therefore, the optical output required for the laser was calculated to be -17.81 dBm (16.56 μW) and -13.55 dBm (44.16 μW) at 10 Gbit/s and 20 Gbit/s operation, respectively. The light output power condition of the membrane laser is summarized in Table 5.1. Using these conditions, the laser characteristics were analyzed, and the power consumption was calculated from the required optical output and modulation speed.

Table 5.2 shows the power consumption required to each optical output, which shown in Chap. 2. As can be seen from these results, in the case of on-chip optical interconnection applications, the power consumption is governed by the modulation rate for both 10 Gbit/s and 20 Gbit/s operation, and <10 fJ/bit cannot be achieved with only the parameters under consideration. Therefore, we studied the case where the active layer was changed from GaInAsP to AlGaInAs, which has higher differential gain. In AlGaInAs system-based quantum-well which can create deep conduction band offset, a differential gain higher than GaInAsP-based quantum-well was reported. The differential gain of 1.1×10^{-15} cm^2 has been experimentally realized [37]. As shown in the figure,

Table 5.2 Optimal structures for each performance requirement.

Required power [dBm]	[mW]	10 Gbit/s d [nm]	L_{DFB} [μm]	Energy cost [fJ/bit]	20 Gbit/s d [nm]	L_{DFB} [μm]	Energy cost [fJ/bit]
-3	0.50	50	20	188	50	20	94
-4	0.40	50	20	141	50	20	70
-5	0.32	50	20	110	50	20	55
-6	0.25	50	20	83	100	23	43
-7	0.20	50	23	64	100	26	40
-8	0.16	50	23	52	100	29	40
-9	0.13	50	23	41	100	29	40
-10	0.10	50	23	34	100	29	40
-11	0.08	50	23	28	100	29	40
-12	0.06	50	23	23	100	29	40
-13	0.05	100	26	21	100	29	40
-14	0.04	100	29	21	100	29	40
-15	0.03	100	29	21	100	29	40
-20	0.03	100	29	21	100	29	40
-25	0.03	100	29	21	100	29	40
-30	0.03	100	29	21	100	29	40

although the high differential gain reduced the power consumption due to modulation, the power consumption was still limited by the modulation rate, with energy costs of 15 fJ/bit and 26 fJ/bit for 10 Gbit/s and 20 Gbit/s operation, respectively. There are several ways to further reduce energy costs. The first is to increase the doping concentration of the p-InP side cladding layer to reduce differential resistance. Since this layer affects the internal loss, the concentration has been lowered. However, since the influence on the

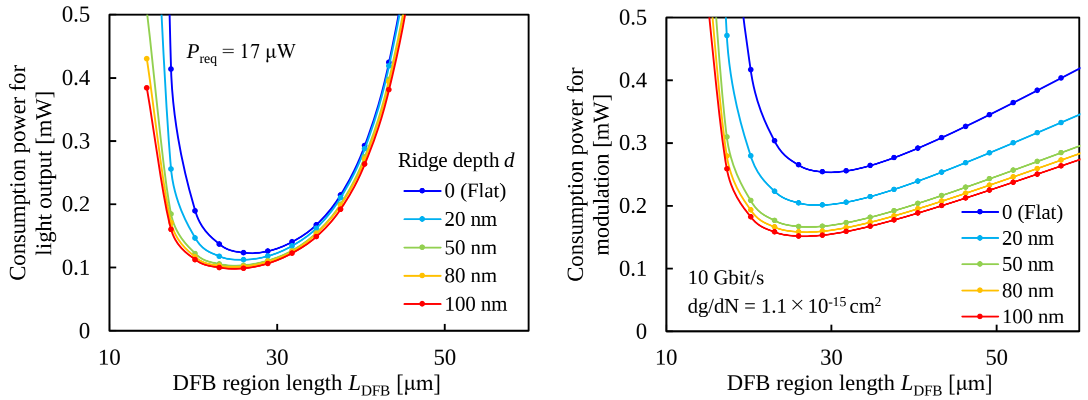

(a) (b)

Fig. 5.7 Consumption power for 10 Gbit/s operation with AlGaInAs quantum wells.

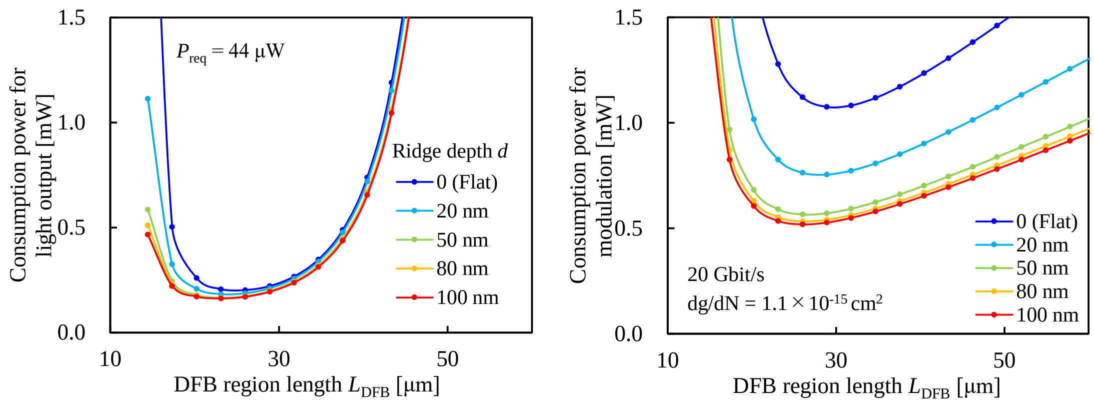

(a) (b)

Fig. 5.8 Consumption power for 20 Gbit/s operation with AlGaInAs quantum wells.

internal loss is becoming smaller due to stronger lateral optical confinement, it is expected that increasing the doping concentration to an appropriate level will reduce the differential resistance. Another approach is to suppress leakage current through the waveguide, which we believe can be achieved by semiconductor lasers using InP waveguides. In the next section, we describe experiments on a semiconductor laser with an InP waveguide and an optical link that uses the InP waveguide.

5.2.3 Optical link with InP waveguide

The membrane DR lasers fabricated in the previous study used GaInAsP embedded waveguides. A butt-jointed built-in process for membrane lasers was established by D. Inoue *et al*. and a 4 dB/cm low loss was reported. In this structure, the passive region is formed at the same time as the active region is formed, enabling no misalignment. In addition, because regrowth is performed by OMVPE, regrowth thickness and composition are stable. Therefore, the coupling loss between the active and passive regions is very small. However, GaInAsP embedded waveguides are formed by regrowth, which is affected by the wafer surface orientation, causing difficulties in fabricating bending waveguides. For this reason, it cannot be applied to integration that requires bending waveguides, limiting its application to straight waveguides only. In addition, the

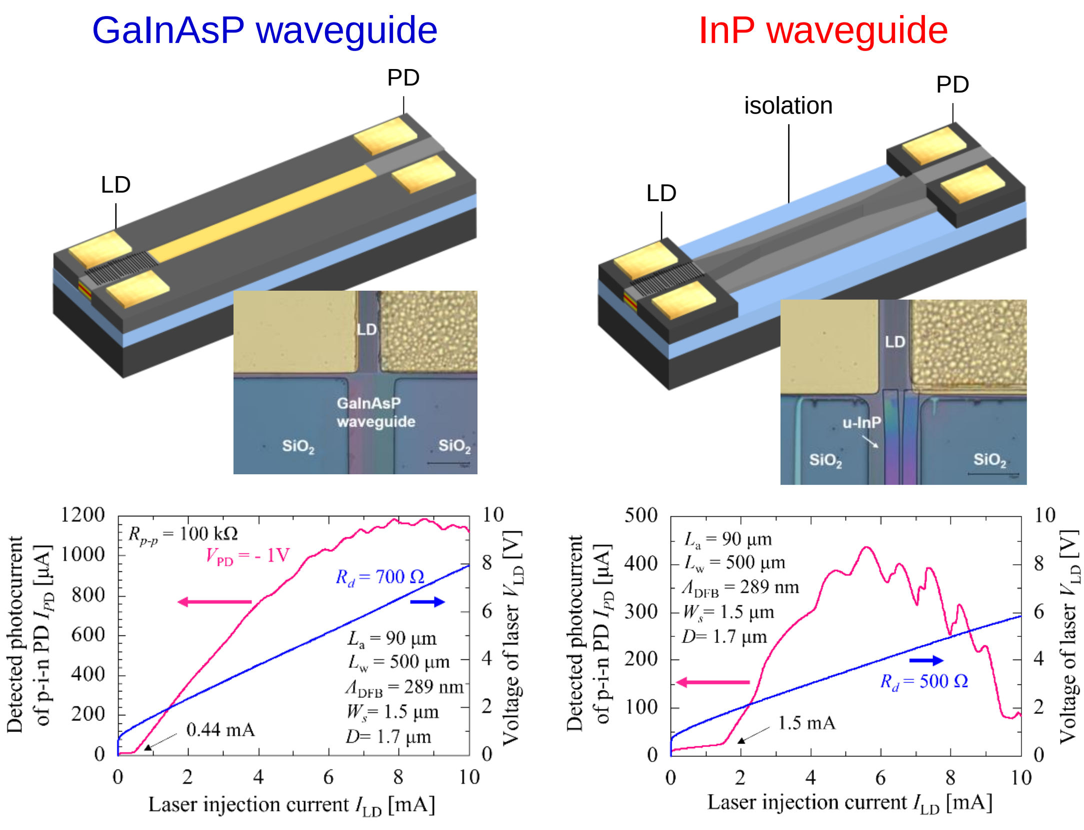

(a) (b)

Fig. 5.9 Schematics of membrane laser and characteristics of fabricated devices with (a) GaInAsP waveguide and (b) InP waveguide [39].

cladding of the waveguide is also doped, which may increase the waveguide loss. To solve these problems, a change from GaInAsP embedded waveguides to InP waveguides has been studied [39][40]. However, a comparison of the fabricated devices showed that the InP waveguide lasers had higher threshold currents and lower differential efficiencies than the GaInAsP embedded waveguide lasers. This was considered to be due to the non-uniformity of regrowth thickness in the waveguide region caused by misalignment during *n*-InP and *p*-InP regrowth, and a proposal has been made to change the waveguide formation sequence. Membrane lasers with InP waveguides fabricated in previous studies followed the fabrication sequence of GaInAsP embedded waveguides, growing InP for the waveguide and then forming the p-i-n junction. In this fabrication process, *n*-InP and *p*-InP regrowth was performed while the waveguide section was covered by a mask, and alignment errors were induced in the process. As a result, the edges of *n*-InP and *p*-InP were not aligned with the boundaries of the active and passive regions, and increased

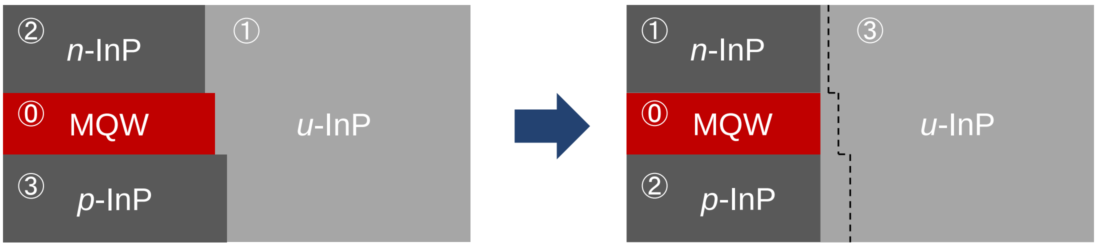

Fig. 5.10 New process flow of forming p-i-n junction and waveguide.

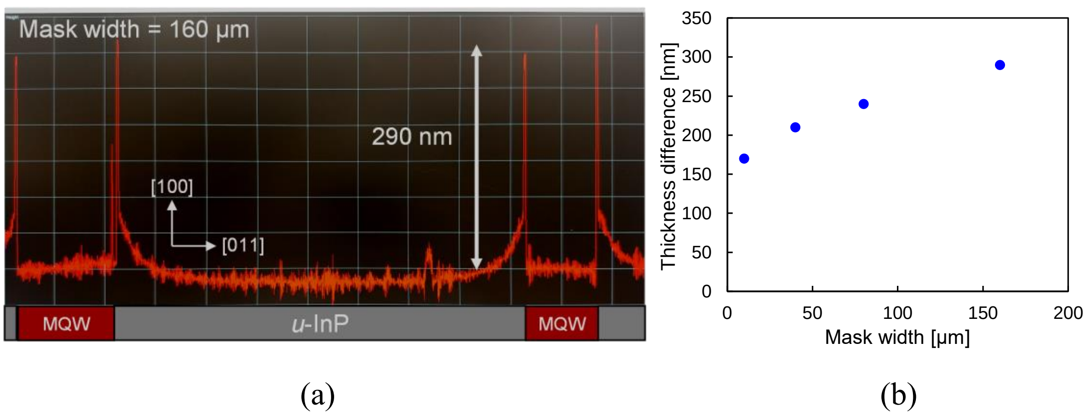

Fig. 5.11 Measured thickness profile with mask width of 160 μm and mask width dependence of thickness difference.

reflection due to non-uniform film thickness and increased absorption loss due to non-uniform currents were concerned. Therefore, as shown in Fig. 5.10, the fabrication process was changed to perform *n*-InP and *p*-InP regrowth followed by waveguide formation. Although the effect of misalignment could be avoided by this sequence, it was confirmed that a 290 nm rabbit ear was formed at 270 nm-thick waveguide regrowth as shown in Fig. 5.11(a) because the area covered by the mask during waveguide formation was larger than that in the previous sequence. Since this thickness variation affects the optical modes, it is expected that the coupling efficiency will decrease if the tapers are fabricated based on simulations performed on a flat waveguide structure. Therefore, an investigation was first performed to obtain the relationship between mask width and regrowth thickness variation during waveguide formation. Narrowing the mask width reduces the molecules that decompose on the mask, thus reducing the increase in thickness near the mask due to surface diffusion. The thickness difference can be suppressed by decreasing the mask width, as shown in Fig. 5.11(b). However, even with a mask width of 20 µm, the thickness difference was more than half of the waveguide thickness, indicating that other approaches are necessary. As another approach, side etching and mask shape were examined. By increasing the amount of side etching, atoms decomposed on the mask migrate to the side-etched area under the mask, reducing the amount of growth at the mask edge, and preventing growth in the [1 0 0] direction on the

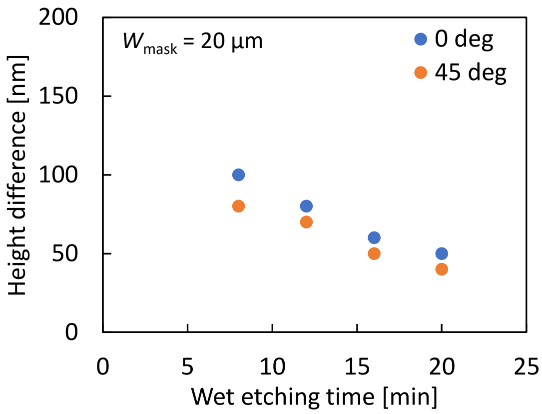

(a)

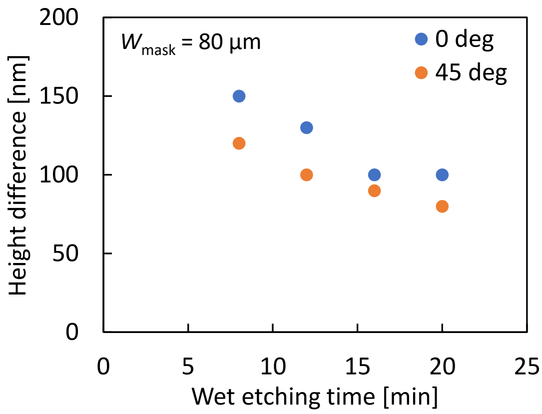

(b)

Fig. 5.12 Growth thickness difference with various condition.

(0 1 1) plane. The optimum amount of side etching depends on the growth rate and V-III ratio and should be investigated for each growth condition. It is also considered effective to avoid the (0 1 1) plane, where rabbit ears are likely to occur, by changing the mask shape and adding an angle to the mask. Fig. 5.12 shows the results of growth thickness difference when growth was performed at different etching times and mask angles. The growth thickness difference is suppressed by increasing the wet etching time before regrowth. This is due to the undercut of the wet etching, and the amount of undercut was 20 nm/min in the previous experiment. The growth thickness difference was also suppressed by changing the mask angle to 45°, but there was almost no difference at a

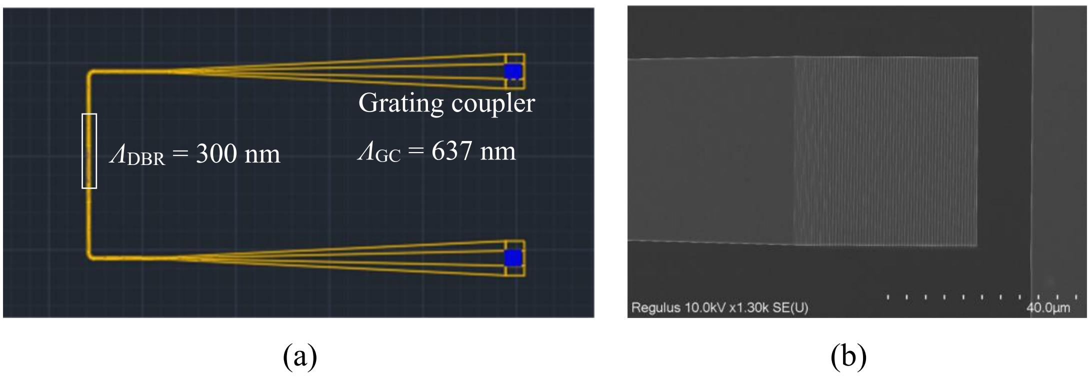

Fig. 5.13 **(a)** CAD design of InP waveguide with grating coupler and (b) SEM image of fabricated grating coupler.

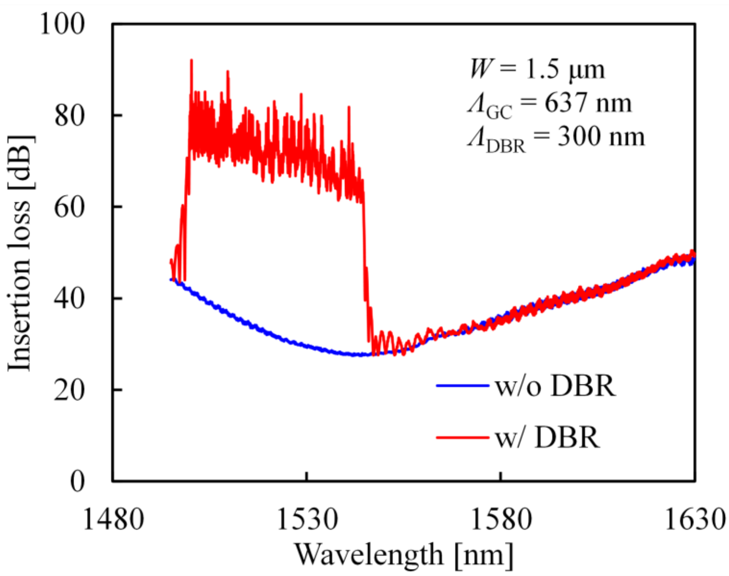

Fig. 5.14 Insertion loss measured using grating coupler.

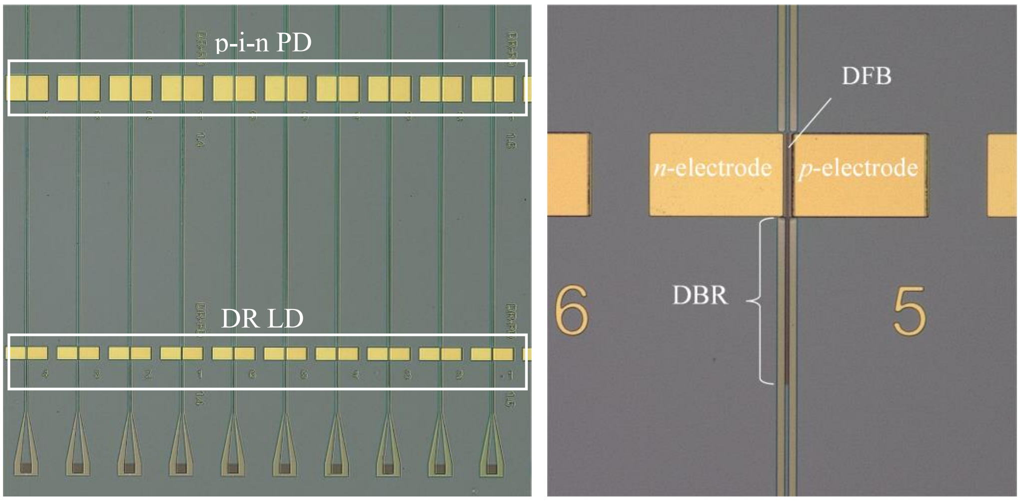

Fig. 5.15 Optical microscope images of fabricated device.

mask width of 20 µm. As a result, the growth thickness difference could be suppressed to 50 nm by using a mask width of 20 µm and performing wet etching for 20 minutes.

Next, grating condition was performed with grating coupler. In changing from GaInAsP embedded waveguides to InP waveguides, it is necessary to examine the conditions of DBRs formed in the passive region. The waveguide shown in Fig. 5.13(a) was fabricated and the stopband of the DBR was confirmed using a grating coupler. The InP-rib waveguide has a core thickness of 270 nm, rib thickness of 50 nm, and a grating coupler with a period of 637 µm, where the duty ratio is distributed in the light propagation direction [41]. Both grating depth of DBR and grating coupler were 50 nm. Fig. 5.14 shows the measured Insertion loss. The blue line shows the measurement result without DBR, and the loss is smallest around 1550 nm. The red line shows the insertion loss with DBR, and a 45 nm-wide stopband centered at 1525 nm was observed. The average refractive index was 2.53, close to the theoretical value of 2.57 for a DBR grating with a depth of 50 nm. From this result, it was found that for the stop band to be centered at 1550 nm, the grating period should be 306 nm.

Fig. 5.15 shows optical microscope images of the fabricated InP waveguide membrane DR laser. The DFB region length and DBR length of the LD are 50 µm and 100 µm, respectively, and a grating coupler for backward output confirmation is located behind the DBR region. InP waveguide of 2.0 μm width and 500 μm length was formed in the front of LD, coupled to a 100 μm long PD. Fig. 5.17 shows the measured I_{LD}-I_{PD} and I_{LD}-V_{LD} characteristics, with no electrical isolation between the LD and PD, and the PD bias voltage of 0V. The red line shows the characteristics of a DR laser with a DBR of 100 μm and the blue line shows the characteristics of a DFB laser. The threshold currents were 0.16 mA and 0.22 mA, respectively, which is comparable to that of a laser

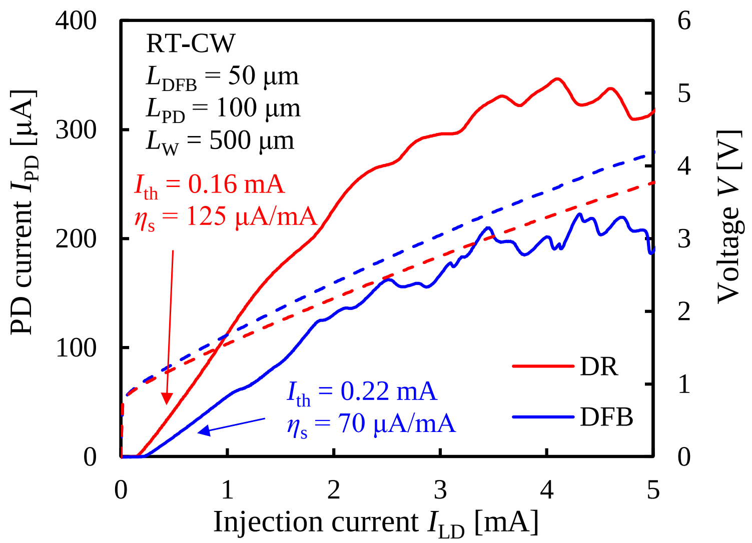

Fig. 5.16 Comparison of DR and DFB laser characteristics with InP waveguide.

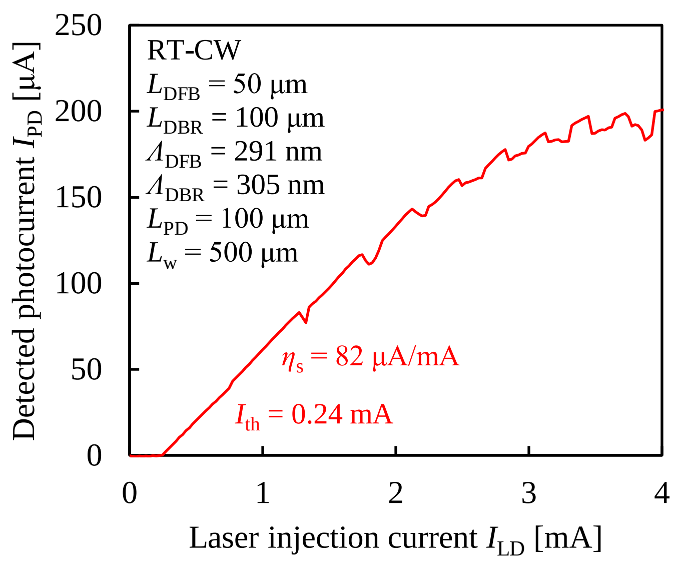

Fig. 5.17 I_{LD}-I_{PD} characteristics of fabricated device with InP waveguide.

fabricated with a GaInAsP embedded waveguide. In the slope efficiencies of the DR and DFB lasers, 125 μA and 70 μA were obtained, respectively, with the DR laser having higher efficiency due to feedback of backward emission by the DBR. In all devices measured, there was a kink in their properties as shown in Fig. 5.17. The optical output from the rear was very weak and the spectrum could not be observed, but the kink was equally spaced with respect to the injected power, which is thought to be due to the FP mode of the waveguide. This means that reflections occur at the boundary between the active and passive regions. This could be due to misalignment during InP waveguide formation or non-uniform growth thickness, which causes a reflection and decrease in coupling efficiency. Improving this coupling efficiency will be a future challenge.

5.3 Application for optical neural network

5.3.1 Optical neural network using photonic integrated circuit

Machine learning has developed remarkably as one of the methods that play a central role in today's artificial intelligence. Among machine learning methods, deep learning (deep learning) has attracted much attention in recent years. Deep learning is a method of learning rules and knowledge from data using a model called a neural network (NN), and using the learned model, various tasks such as prediction, recognition, and generation can be realized [42]-[45]. The basic structure of NNs used in deep learning is shown in Fig. 5.18. The multilayer perceptron consists of three layers: an input layer, a hidden layer, and an output layer. Multiple hidden layers improve the accuracy of the output relative to the input. This is often used in deep learning and is called a deep neural network. In deep neural networks, input data is propagated from the input layer through the network in a forward direction to produce output. The error between the predicted data and the correct data is calculated by a loss function. Then, for parameters such as weights and biases in the network, partial derivatives are calculated in the reverse order from the output layer to the input layer, and the parameters are updated. Learning is performed by repeating these steps.

Neural networks have received a dramatic amount of attention in recent years, and

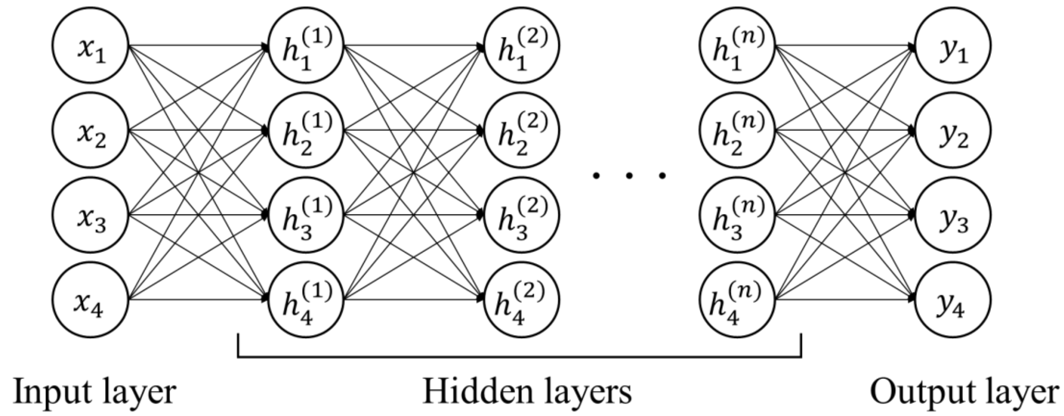

Fig. 5.18 General artificial neural network architecture composed of an input layer hidden layers and an output layer.

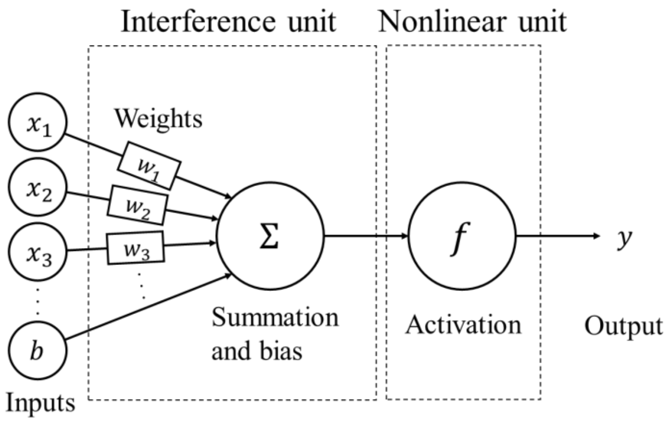

Fig. 5.19 Interference and nonlinear units that compose each layer of the artificial neural network.

one of the factors behind this remarkable development is the computational power of computers and the availability of large amounts of data. On the other hand, it is said that Moore's law [46], which represents the current technological progress of computers, is about to come to an end, and with the increase in computing demand, innovative computing technologies are being pioneered with the post-Moore era in mind. Optical computing is a concept that already emerged in the 1960s, but several differences can be cited between the past and the present. One of them is the progress of machine learning technology and the emergence of new information processing concepts. This progress has strongly encouraged the research and development of optical computing platforms. Various optical neural networks (ONNs) have recently been developed by taking advantage of the unique properties of optics [47]-[51]. These enable parallel computation of NNs at ultra-high speed and ultra-low power consumption [52]-[55] and are expected to be key devices that will drastically change the exponentially growing power problem of deep learning processing. Each node of the NN consists of an interference unit that is multiplied by a weight and added together, and a nonlinear unit that activates the result, as shown in Fig. 5.19.

The optical linear unit, which performs the matrix operations of linear transformations in optical NNs, is relatively easy to realize in Mach-Zehnder interferometers (MZI) and micro-ring resonators (MRRs). The MZI consists of two interference couplers and two arms, each with a phase shifter. The phase shifter can easily control the amount of phase shift by thermally adjusting the heater, allowing arbitrary 2 × 2 unitary matrix operations. Arbitrary N × N unitary matrices can be represented by properly arranging such MZIs on the silicon substrate. In 2017, Shen *et al*. proposed a cascaded MZI-based optical deep learning architecture on a silicon platform, showing the potential of this method to significantly accelerate computational speed and improve power efficiency [56] (Fig. 5.20). This led to a rapid increase in research on MZI schemes [57][58].

The method using wavelength-division multiplexing (WDM) and MRR can increase the device integration density because the radius of the microring can be reduced to a few

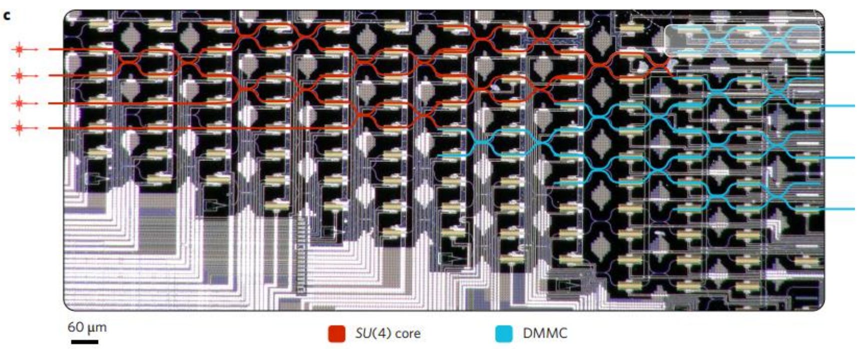

Fig. 5.20 Optical interference unit using Mach-Zehnder interferometers (MZI) [56].

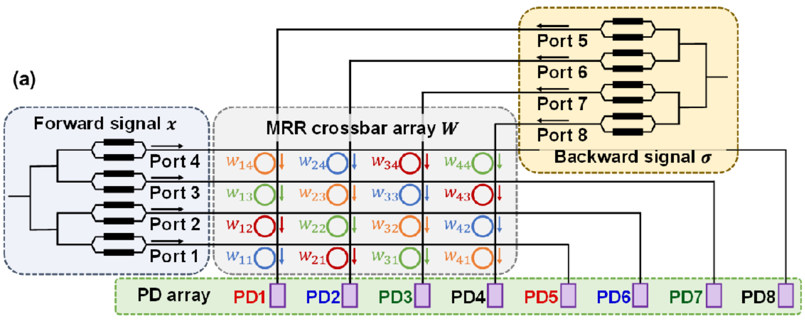

Fig. 5.21 Optical interference unit using micro-ring resonators (MRRs) [63].

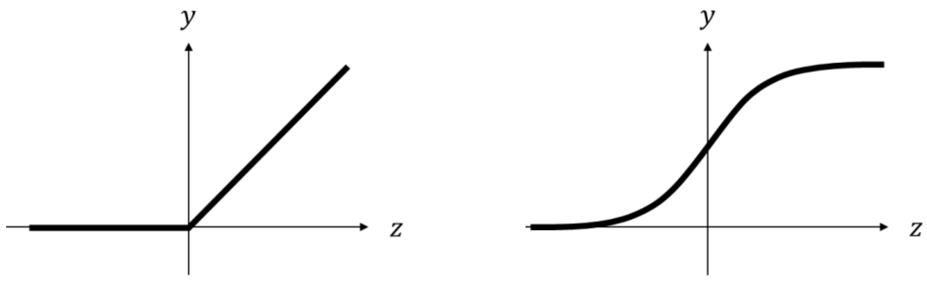

$$f(z) = \begin{cases} z & (z \geq 0) \\ 0 & (z < 0) \end{cases}$$

(a)

$$f(z) = \frac{1}{1 + e^{-z}}$$

(b)

Fig. 5.22 Commonly used activation functions (a) rectified linear unit (ReLU) function and (b) sigmoid function.

µm on a silicon platform. Thus, the footprint problem of the MZI method can be improved. This method uses multiple microrings with different wavelengths of light and different resonance wavelengths (Fig. 5.21). The coupling ratio of the wavelength channels can be adjusted independently by each microring, and the matrix can be calculated by incoherent addition of light at each wavelength. However, since the operation is based on light intensity, it is not possible to represent negative numbers in this way. Therefore, it is necessary to acquire signals from both the drop and through ports of the micro ring using a balanced photoreceiver and output the difference signal. This method has been developed since 2012, when Yang *et al*. proposed a matrix vector multiplier based on a microring array [59] and Tait *et al*. proposed a "broadcast-and-weight" method to realize optical NNs [60][61]. In 2010, Xu *et al*. proposed an optical convolutional neural network architecture using WDM and succeeded in increasing the computation speed [62], which is expected to improve both computation speed and energy consumption by an order of magnitude. These devices have been widely reported using mature CMOS processes to achieve low cost and space savings.

As described above, there have been many reports on interference units based on mature Si photonics technology. On the other hand, in the nonlinear unit, the realization of a low-power, high-sensitivity nonlinear optical device still remains a challenge. In most

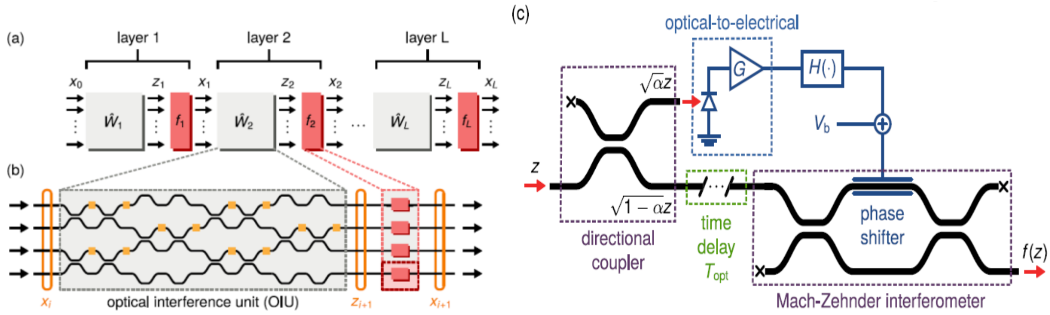

Fig. 5.23 Electro-optic nonlinear activation functions for optical neural network [69].

of the currently reported ONNs, only the interference unit is implemented with an optical circuit, while the nonlinear region is handled electrically. The activation function is a function that performs a nonlinear transformation applied after the linear transformation of the inputs and weights. It determines how the sum of the input signals is activated and prepares the values to be passed to the next layer. Generally, a perceptron consisting of only input and output layers uses a step function as its activation function, while a multilayer perceptron uses a sigmoid function, rectified linear unit (ReLU) function, or softmax function as its activation function (Fig. 5.22). Since optical devices basically respond linearly to their inputs, it is difficult to fabricate nonlinear units in optical circuits. Several optical nonlinear units utilizing nonlinear optical effects in semiconductor optical amplifiers have been reported [64]-[67]. Saturated absorbers have been reported as nonlinear units that are relatively easy to form on silicon platforms but require very large input light to achieve a nonlinear response [68]. Also shown in the Fig. 5.23 is a reported nonlinear unit that responds at low input light using MZI [69]. In this configuration, the input light is divided into signal light and control light, and the control light is converted to voltage by a light receiver to change the split ratio of the MZI in the subsequent stage. This configuration can operate with low input, but the configuration is complex and requires electrical processing. Therefore, a simple optical nonlinear unit that operates at low power consumption on a Si platform is expected to be realized. This study proposed the use of a semiconductor membrane laser as an optical nonlinear unit.

5.3.2 Concept of all optical neural network using membrane laser

There are various types of activation functions, but in deep neural networks, the ReLU function is commonly used to avoid the gradient vanishing problem. The gradient vanishing problem is a problem in which the gradient becomes almost zero in a neural network with deep layers in the back propagation method, and it takes a very long time to learn. In the back propagation method, the gradient is multiplied from the output to the input, and it is known that the gradient disappearance problem is likely to occur if the

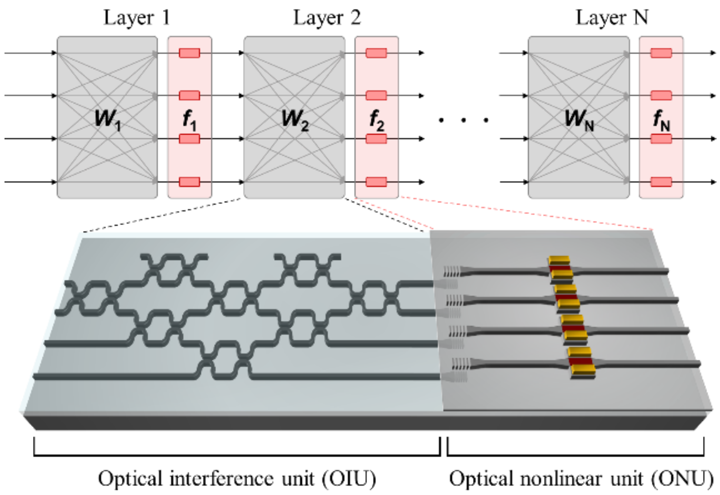

Fig. 5.24 Schematic of the proposed all-ONN with membrane optical nonlinear units.

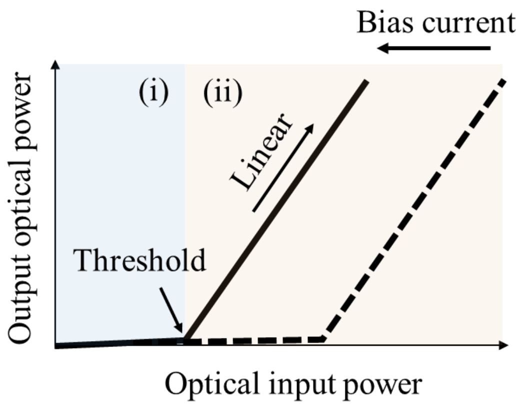

Fig. 5.25 Nonlinear operation of the membrane laser depending on bias current: (i) below the threshold and (ii) linear output above the threshold.

activation function is used such that the gradient value becomes small. ReLU is a function whose output value is always zero if the input value to the function is less than zero, and whose output value is the same as the input value if the input value is above zero. Since the shape of this function resembles the optical output characteristics of a semiconductor laser, it was proposed to use it as a nonlinear unit.

The principle of operation is explained. The configuration is as shown in Fig. 5.24. Signals from the interference unit using MZI are coupled to the III/V layer and input to a semiconductor laser that functions as a nonlinear unit. An ONN using MZIs as an interference unit propagates light intensity as a signal. To operate as an optical nonlinear unit, the optical output must respond nonlinearly to the input light. It can function as a ReLU function by driving the semiconductor laser around the threshold. If the optical input is below the threshold, the laser acts as an absorber and the output is almost zero as shown in Fig. 5.25(i). As the optical input increases and the carrier density inside the active layer reaches a threshold value, the optical output increases linearly with input light shown in Fig. 5.25(ii). Non-linear effects can be achieved when the input optical intensity crosses the threshold. By controlling the bias current that is added to the laser, the threshold to the optical input can be varied.

This response is a characteristic of semiconductor lasers and is not unique to membrane lasers. However, when considering actual integration, membrane lasers have several significant advantages. Typical semiconductor lasers have small optical confinement, and the cavity length is about 1 mm, which is very long to obtain sufficient κL. Therefore, when light is input from the outside, the carrier density differs between the front and the rear, resulting in non-uniformity inside the cavity. Only the rear part is to act as an absorber and the output is expected to increase slowly with respect to the input near the threshold. In addition, when the cavity length is longer, the increase in carrier density decreases for the same input intensity, resulting in lower sensitivity to the input. The threshold for nonlinear output can be changed by adding bias current, but membrane lasers can be driven with low power consumption because the threshold current is very low. Therefore, membrane lasers could be very effective in realizing the ReLU function using laser characteristics.

5.3.3 Characterization and future prospect

To confirm that the membrane laser works as a ReLU function, experiments were performed with only nonlinear units. The SEM image of the fabricated device is shown in Fig. 5.26. The device was cleaved with a waveguide, the forward waveguide was 20 μm long. Fig. 5.27(a) shows the output characteristics of the current-driven membrane laser. The fabricated device was a DR structure consisting of a 293-nm pitch DFB grating and a 295-nm pitch DBR grating. The threshold current was 0.5 mA for a device with a DFB region length of 90 μm and a stripe width of 0.8 μm. Comparing the fiber coupling

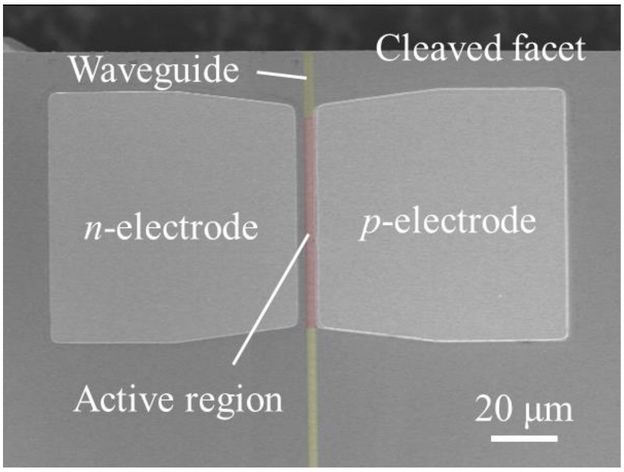

Fig. 5.26 SEM image of the fabricated membrane DR laser.

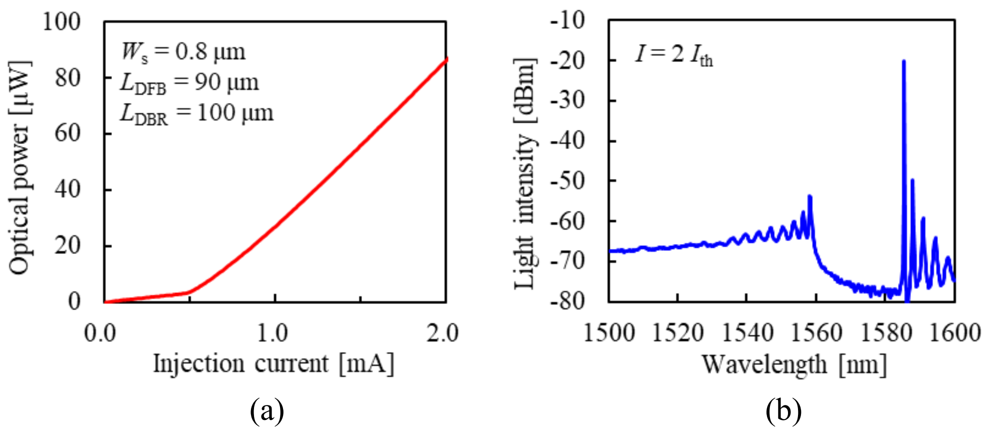

Fig. 5.27 (a) Output power versus injection current of the device and (b) spectrum with an injection current of 1.0 mA ($2I_{th}$).

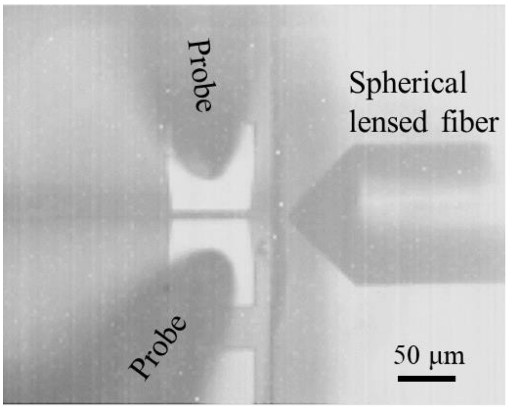

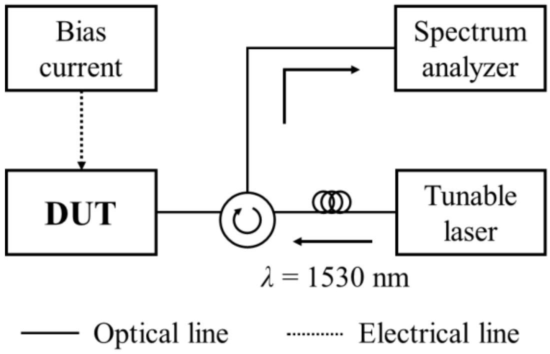

(a) (b)

Fig. 5.28 (a) Microscope image of the device under test (DUT) and (b) schematic of the experimental setup.

output to the photodetector output, the coupling loss between the membrane laser and the fiber was about 10 dB. Fig. 5.27(b) shows the spectrum at a bias current $I_b = 2I_{th}$ (1.0 mA), confirming the lasing wavelength to be 1585 nm. Fig. 5.28 shows the measurement system configuration. Excitation light from the wavelength tunable laser (signal light from interference unit) was coupled to the cleaved facet of the waveguide by a lensed fiber, and the output of the membrane laser was observed using an analyzer via a circulator. As shown in Fig. 5.26, the cavity length of the membrane laser used in this study was very small (90 μm), enabling uniform pumping in the cavity by the incident light (signal light). To increase the pumping efficiency, the wavelength of the pumping light was set to 1530 nm, which is shorter than the lasing wavelength of the membrane laser, 1585 nm. Fig. 5.29. shows the results of the measurement with bias current of 0.1 mA. The horizontal axis shows the input light, and the vertical axis shows the optical output received. For power injected into the device below 0.6 mW, the optical output was almost zero, and for higher power input, the optical output increased linearly. Note that the power inside chip should be approximately 0.06 mW according to our previous experiment of the fiber coupling efficiency (10%). Output power is also 10 times higher than the values. Fig. 5.30 shows the spectra at input power before and after lasing. Fig. 5.30(a) shows the spectrum at an input power of 0.1 mW, and a peak is observed only at

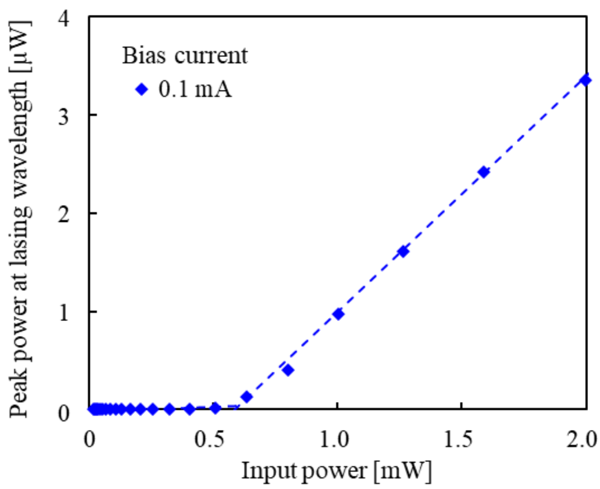

Fig. 5.29 Response of the membrane nonlinear activation unit with bias current of 0.1 mA.

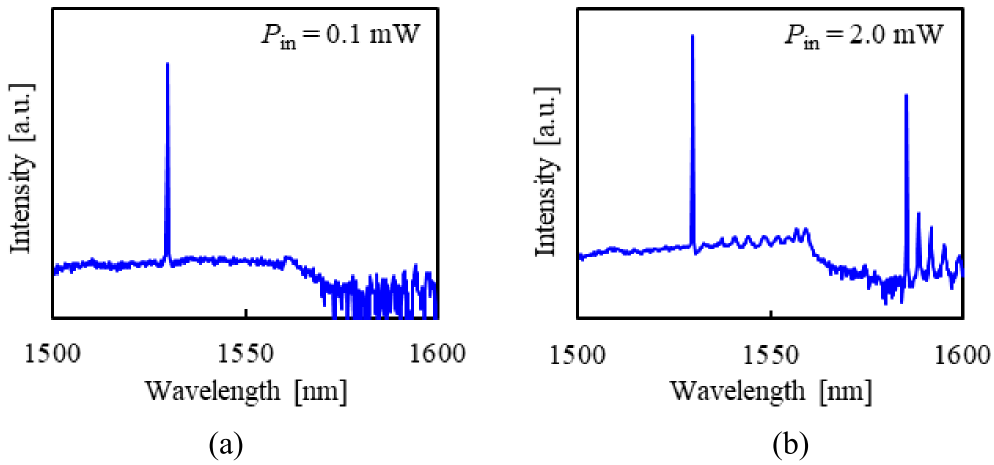

Fig. 5.30 Spectrum at injection power of (a) 0.1 mW (before the threshold) and (b) 2.0 mW (after the threshold).

1530 nm of the input light. At input light of 2.0 mW, the amplified spontaneous emission increases, indicating that the carrier density is increased by the injected light as shown in Fig. 5.30(b). Also, lasing was observed at 1585 nm, the same as lasing by current injection. Fig. 5.31. shows the response to input light at different bias currents. As the bias current increases, the carrier density at zero input power increases, thus the threshold value decreases. Changing the bias current resulted in almost no change in the slope of the

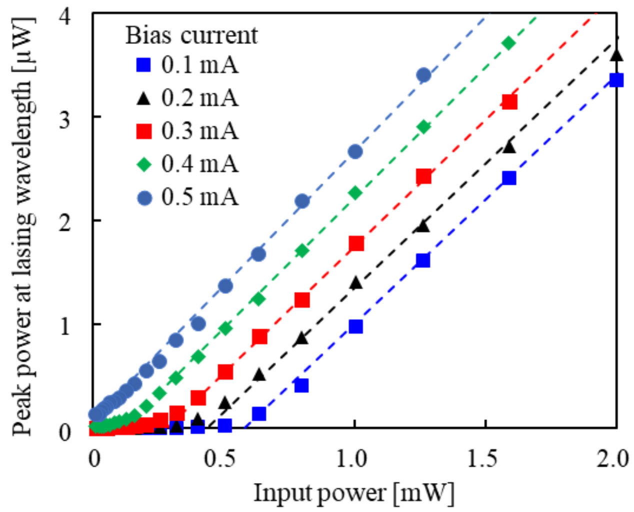

Fig. 5.31 Response of the membrane nonlinear activation unit with various bias current.

output relative to the input. As the bias current is increased, the spontaneous emission of light increases because the excitation is more uniform than excitation by light. Therefore, the slope below the threshold value tends to increase with increasing bias current. This trend differs from the ideal ReLU function where the output is zero below a threshold value. However, activation functions, such as the exponential linear unit (ELU) function derived from the ReLU function, have been proposed that allow learning to proceed even on negative inputs. These functions learn better with negative inputs but have the disadvantage of more complex error functions. It is expected that this part can be calculated at high speed by using light instead of electrical processing.

The measured optical ReLU were applied to the convolutional neural network (CNN) for the MNIST handwritten digit classification. After formulating the optical ReLU considering coupling efficiency from the results of Fig. 5.27, which was given by

$$f(x) = \begin{cases} 0.0003e^{12.3x} \ (x < 0.3394) \\ 0.24x - 0.062 \quad (x \geq 0.3394) \end{cases}, \tag{5.8}$$

constructed the CNN shown in Fig. 5.32. The MNIST database contains of 60,000 training images and 10,000 testing images. For this classification task, the batch size was set to 100, the learning rate to 0.001, and convolution was performed with a kernel size

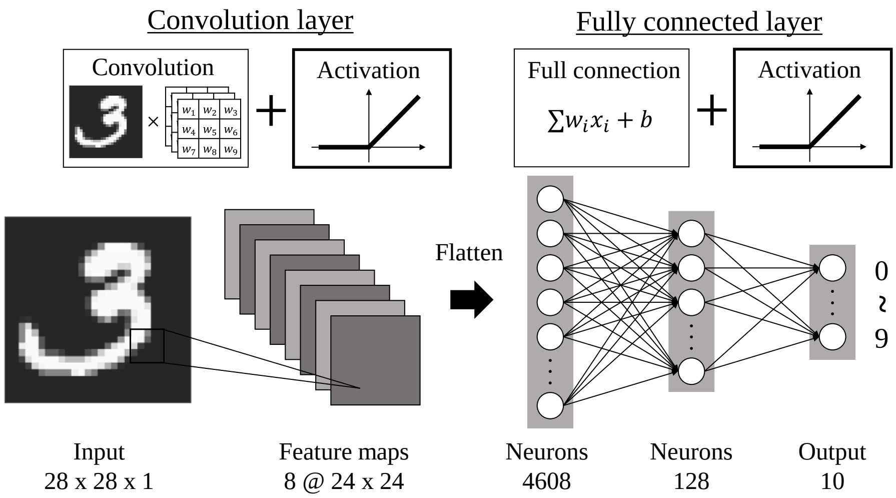

Fig. 5.32 Architecture of convolutional neural network.

Table 5.3 Test Accuracy of CNN with Nonlinear Active Functions.

Type	Activation Function	Epoch	Test Accuracy
1	Optical ReLU	10	98.22%
2	ReLU	10	98.32%
3	ELU	10	98.05%
4	Sigmoid	10	97.71%
5	Softplus	10	97.75%

of 5 × 5 and a stride of 1. Table 5.3 shows the test accuracy of the network after training with various nonlinear activation functions: the accuracy of the optical ReLU applied to the NN is 98.22%, which is comparable to the accuracy of the ideal ReLU applied to the same NN. These results indicate that the optical ReLU obtained in this study is valid as a nonlinear activation function.

The above results are the results of an experiment to confirm the membrane device works as a ReLU function. The relationship between the parameters of the laser structure and the learning results was analyzed by co-worker Sakai [70]. The correlation between the slope of the ReLU function and the CNN correct response rate was examined, respectively, and it was clarified that the CNN correct response rate is highly dependent on the slope efficiency (Fig. 5.33). The CNN correctness rate was then calculated for each structure, and it was shown that the rate was comparable to that obtained when the ReLU

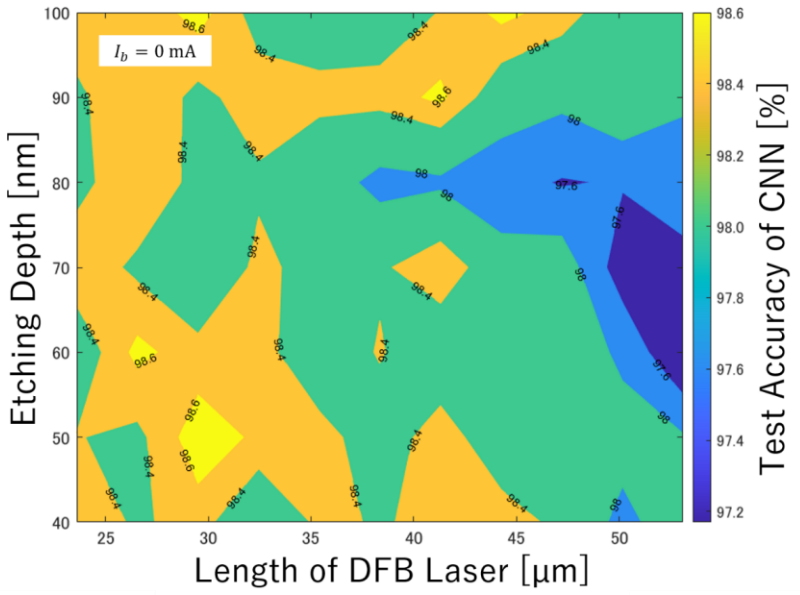

Fig. 5.33 Test accuracy of CNN using membrane lasers with each structural parameter as activation function [70].

function was applied (98.32 %) over a wide range of values. The slope efficiency analysis for each structure was then presented, and it was again confirmed that there is a positive correlation between the slope efficiency and the CNN positive response rate. The oscillation delay was also analyzed, and a minimum laser oscillation delay time τ_d = 0.69 ns was obtained for a grating depth of d = 80 nm and a DFB region length of L = 26.55 μm when the bias current I_b = 0 mA. These results indicate the optimal structure when using membrane lasers as ReLU functions, and the power consumption and computational speed of the calculations are discussed.

As described above, semiconductor membrane lasers are expected to be applied to optical neural networks, taking advantage of their short cavity and low power consumption. In actual integration, various problems need to be solved, such as the method of integrating the interference unit and nonlinear unit, and the wavelength dependence of the membrane laser. However, when semiconductor fabrication technology advances and these problems are solved, membrane lasers will be one of the most promising candidates for realizing ONNs.

5.4 Application for B5G/6G communication system

5.4.1 Radio-over-fiber (RoF)

6G communications, also known as Beyond 5G, refers to the next-generation mobile communications system that further advances the performance of 5G, which is currently in widespread use. When 6G is put into practical use, it will be possible to realize advanced communications such as high speed, high capacity, low latency, and multiple simultaneous connections. For such high-capacity communications, it is necessary to use radio waves in high-frequency bands such as millimeter waves, which have high directivity and attenuation [71][72]. Therefore, to cover a large area, a large number of wireless base stations must be densely deployed. In addition, a wireless base station had to be installed for each wireless system. Therefore, as high-frequency band wireless systems diversify in line with increasingly diverse needs, a huge number of wireless base stations will have to be installed. Therefore, a system configuration that allows multiple wireless systems to share a wireless base station is required to drastically reduce the number of wireless base stations. One approach that has been proposed is the introduction of analog radio-over-fiber (RoF) [73]-[75]. A-RoF is a technology that modulates optical signals with wireless signals in intensity and transmits optical signals in the form of

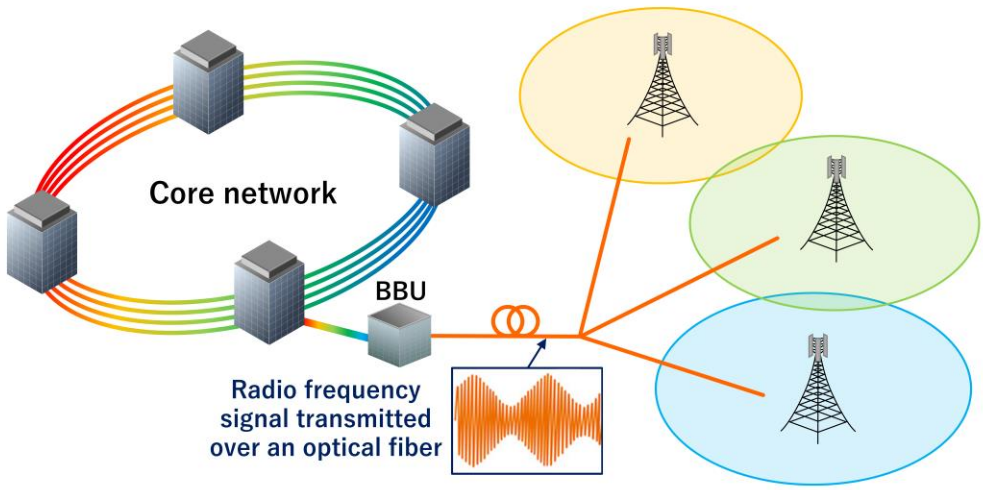

Fig. 5.34 Concept of mobile communications system with analog RoF.

wireless signals over optical fibers, allowing the original wireless signals to be retrieved simply by optical-to-electrical (O/E) conversion of the transmitted optical signals (Fig. 5.34). By applying this A-RoF, the functions of conventional wireless base stations can be separated into base station antenna and radio aggregation stations. Conventional wireless base stations have the following functions: antenna, amplifier, E/O, O/E conversion, and signal processing. By applying analog RoF and integrating signal processing functions into radio aggregation stations, it is possible to simplify the functions of the base station antenna. This is expected to improve installation and economic efficiency by reducing the size and power consumption of the base station antenna.

To realize such an A-RoF transmission system, a semiconductor laser capable of modulating at millimeter-wave band frequencies is required. General lasers cannot directly modulate at such high frequencies because their modulation bandwidth is limited by photon-carrier resonance (relaxation oscillation). Recently, photon-photon resonance (PPR) lasers have attracted attention due to their potential for modulation bandwidth extension [76]-[79]. Beyond 5G mobile communication systems use the millimeter-wave band and are allocated a wide signal bandwidth of 400 MHz for a single channel and 800 MHz by combining two channels. For A-RoF systems transmitting a single channel, ultra-

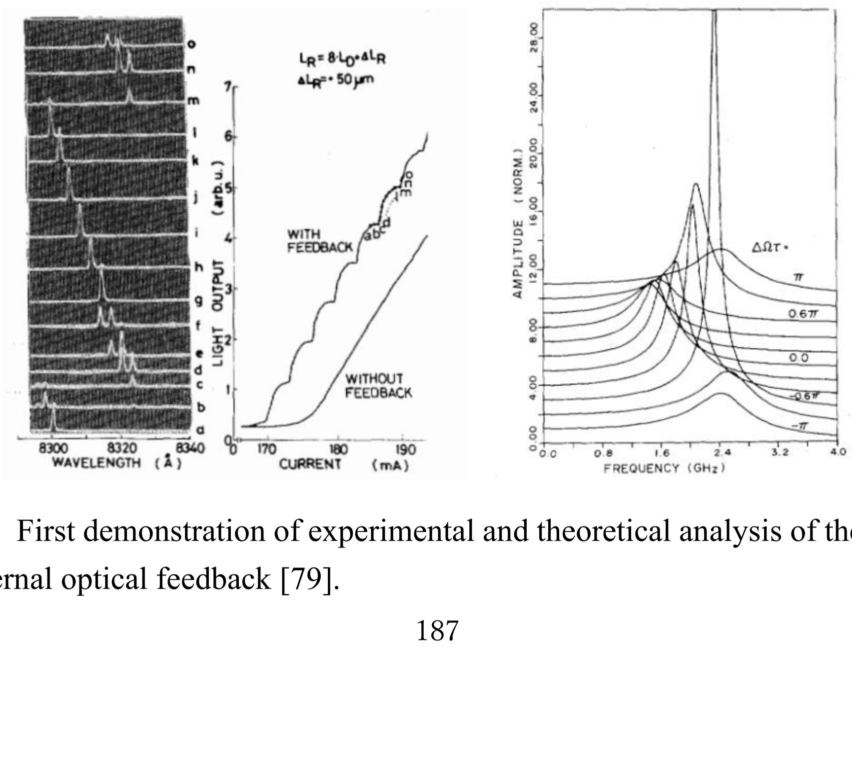

Fig. 5.35 First demonstration of experimental and theoretical analysis of the influences of the external optical feedback [79].

wide modulation bandwidths on the order of megahertz to several tens of gigahertz are essentially not necessary. As mentioned above, the bandwidth of 5G mobile signals is 400 MHz for a single channel, so high response is required within the limited bandwidth of the target frequency. Since PPR can be obtained in a specific frequency band depending on the structure, it is expected that PPR lasers can be used as a light source for A-RoF.

5.4.2 Photon-photon resonance (PPR) for high-speed modulation

One of the major themes for increasing the transmission capacity of optical communication systems is to increase the response speed of semiconductor lasers. Although semiconductor lasers can be made faster by shortening their resonators, the response speed is not fast enough. The promising technology is photon-photon resonance (PPR). By adding an external resonator, the interaction between the returned light and the oscillating light can be induced, generating a second resonance peak in the response characteristics, and expanding the bandwidth. This resonance phenomenon is an effect that has been known for a long time (Fig. 5.35), but it has been attracting significant attention in the past few years. When attempting to expand the response bandwidth of a semiconductor laser light source with an integrated external resonator by setting this

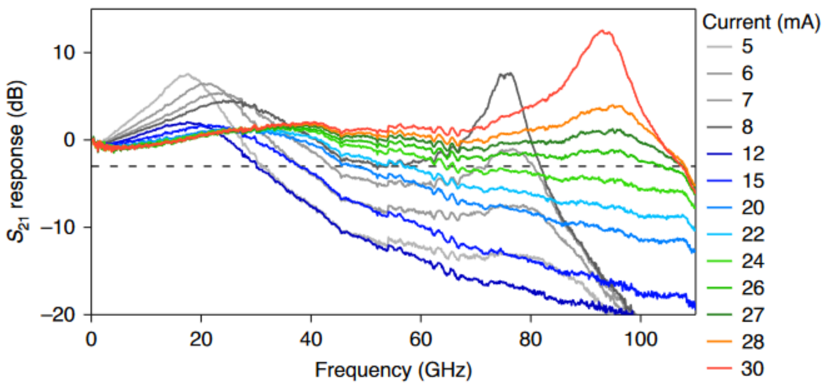

Fig. 5.36 High speed operation of 108 GHz bandwidth using membrane laser with structure for PPR [81].

second resonance peak to the high-frequency region, a problem arises with the response characteristics in the high-frequency region during direct current modulation. During direct current modulation, the response sensitivity in the high-frequency region above the relaxation oscillation frequency drops sharply in inverse proportion to the square of the modulation frequency, and if the second resonance frequency is set too high, the response sensitivity in the frequency band between the relaxation oscillation frequency and the second resonance frequency deteriorates, and a flat response characteristic cannot be obtained. Therefore, it is not possible to obtain a flat response characteristic. Therefore, the use of PPR in communication systems that require a wide bandwidth is problematic. However, for A-RoF applications, a bandwidth of about 1 GHz at a specific wavelength is sufficient, and thus PPR is expected to be applied. In recent years, PPR operation demonstrations using membrane lasers have been reported. The waveguide was formed in the front to induce reflections at the front facets, and the active region length was 50 μm. By employing the photon–photon resonance at 95 GHz due to optical feedback from an integrated output waveguide, this group achieved f_{3dB} at 108 GHz as shown in Fig. 5.36 and 256 Gbit/s four-level pulse-amplitude modulations (PAM-4) with a directly modulated membrane laser [81].

Theoretical analysis of photon-photon resonance can utilize the analytical method of external optical feedback [82]. In the model, the standard rate equations are modified to include an additional term for the τ-delayed electric field,

$$\frac{d}{dt}E(t)e^{j\omega t} = \left(j\omega_n(N) + \frac{1}{2}(g(N) - g_{th})\right)E(t)e^{j\omega t} + \kappa E(t-\tau)e^{j\omega(t-\tau)}, \quad (5.9)$$

where ω is the laser oscillation frequency, $\omega_n = n\pi c/n_{\mathrm{eq}}L_{\mathrm{D}}$, g_{th} is threshold gain (same as cavity loss) and κ is feedback coefficient. The delay of the additional term is related to the external cavity (with index n_{w}) length L as $\tau = 2Ln_{\mathrm{w}}/c$. Stationary lasing condition can be obtained from this equation by setting E to be constant. The real and imaginary parts of the equation, when they are separated, can be written as

$$g(N) - g_{th} + 2\kappa \cos(\omega\tau) = 0, \tag{5.10}$$

$$\omega_n(N) - \omega - \kappa \sin(\omega\tau) = 0. \tag{5.11}$$

Since both gain and resonance frequency are dependent on excited carrier density *N*, these equations are mutually coupled. For the analysis of dynamic states, the small signal responses are obtained by differentiating rate equations, as follows

$$d\left(\frac{dN}{dt}\right) = \frac{\eta_i}{qV_a}dI - v_g S dg - v_g g dS - dN\frac{d}{dN}\left(R_{sp} + R_{nr}\right), \tag{5.12}$$

$$d\left(\frac{dE}{dt}\right) = \left(jd\omega_n + \frac{1}{2}dg\right)E(t) + \left(j\omega_n + \frac{1}{2}(g - g_{th})\right)dE(t) + \kappa dE(t-\tau). \tag{5.13}$$

Since the photon density *S* is proportional to the square of the absolute value of the electric field, the small signal response can be obtained by solving these equations to calculate the transfer function. Solving this equation requires very complex calculations, but small-signal responses can also be obtained by calculating small changes in the numerical analysis. The carrier and photon densities at a given time *t* can be expressed as follows

Table 5.4 Parameters for laser analysis.

Parameters	Value
Internal quantum efficiency η_i	0.75
Stripe width W_s	0.8 μm
Total thickness of core d_{core}	5 × 5.4 nm
Bimolecular recombination coefficient *B*	1.6×10^{-10} cm^3/s
Auger coefficient *C*	5×10^{-29} cm^6/s
Transparent carrier density N_{tr}	1.5×10^{18} cm^{-3}
Gain coefficient g_0	1500 cm^{-1}
Differential gain *dg/dN*	7.2×10^{-16} cm^2
Feedback coefficient κ	0.2

$$N(t+\Delta t) = N(t) + \left(\frac{\eta_i}{qV_a} I(t) - \left(R_{sp} + R_{nr}\right) - v_g g(t) S(t)\right)\Delta t, \qquad (5.14)$$

$$S(t+\Delta t) = \left| E(t) + \left(j\omega_n(t) + \frac{1}{2}\left(g(t) - g_{th}\right) \right) E(t)\Delta t + \kappa E(t-\tau)\Delta t \right|^2. \qquad (5.15)$$

In this analysis, Δt is calculated as 10^{-12} s, since the frequency response is calculated on the order of 10^{10} Hz. When the injection current is sinusoidal, the carrier density and photon density also respond sinusoidally. During transients, the amplitude fluctuates greatly, and when it converges, the small signal response can be obtained by determining the amount of amplitude fluctuation. The parameters used in the analysis are listed in Table 5.4. These values are the same as those used in the calculations in Chapter 2. The figure shows the results of the analysis with the distance between the active layer edge and the reflective surface as a parameter. Fig. 5.37 shows the calculated small signal response with injection current at I_b = 3 mA. The lasing wavelength is adjusted so that the phase at that injection current satisfies the resonance state. The figure shows that as the waveguide length increases, the PPR peak shifts to the lower frequency side. If PPR is used for B5G/6G RoF applications, the PPR peak should be obtained at millimeter

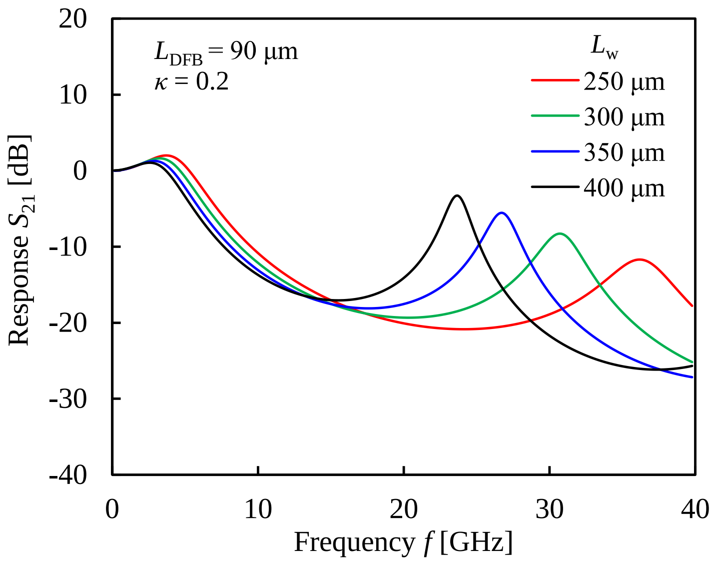

Fig. 5.37 Small signal response S_{21} calculated for various waveguide length.

wave band frequencies (~28 GHz). The analysis performed with these parameters showed that a PPR peak can be observed at 27 GHz with a waveguide length of 350 μm.

5.4.3 Characterization and future prospect

A device was fabricated to obtain PPR with a semiconductor membrane laser. A schematic diagram of the fabricated device is shown in Fig. 5.38. A cross-sectional view of the active layer section as shown in Fig. 5.39(a), and the fabricated device has the BRW structure directly bonded on a Si substrate. Fig. 5.39(b) shows a cross-section in the cavity direction. In edge-emitting lasers, the waveguide is generally formed in the front, and PPR is induced by the feedback from the cleaved facet. However, several limitations arise when PPR is induced by cleavage. The peak of the PPR is determined by the reflectivity of the reflective surface and the length of the waveguide. When a reflective surface is

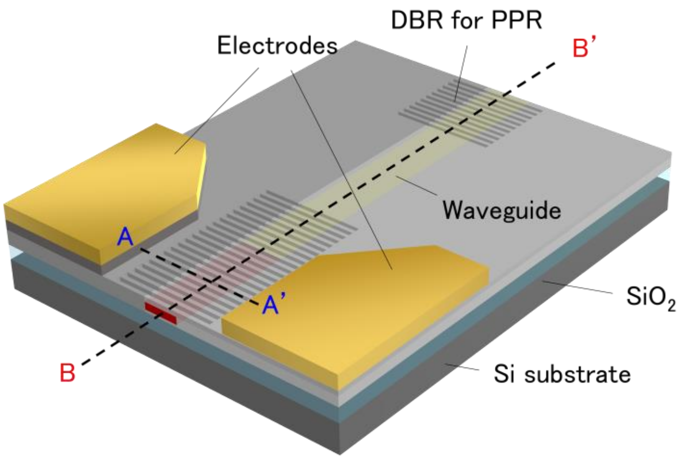

Fig. 5.38 Schematic of membrane DR laser with the structure for PPR.

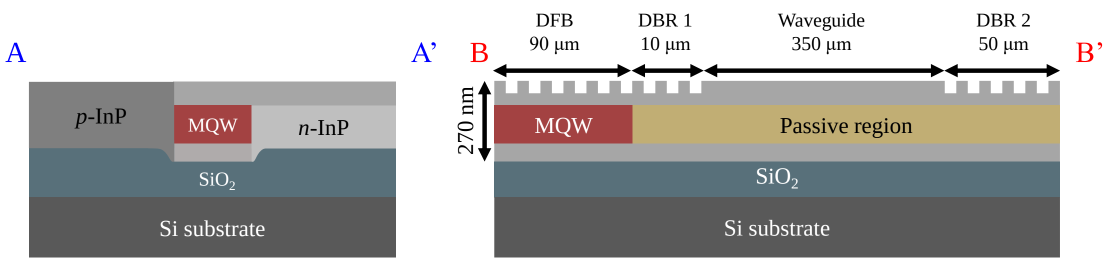

Fig. 5.39 Cross sectional view for detailed description of the grating section.

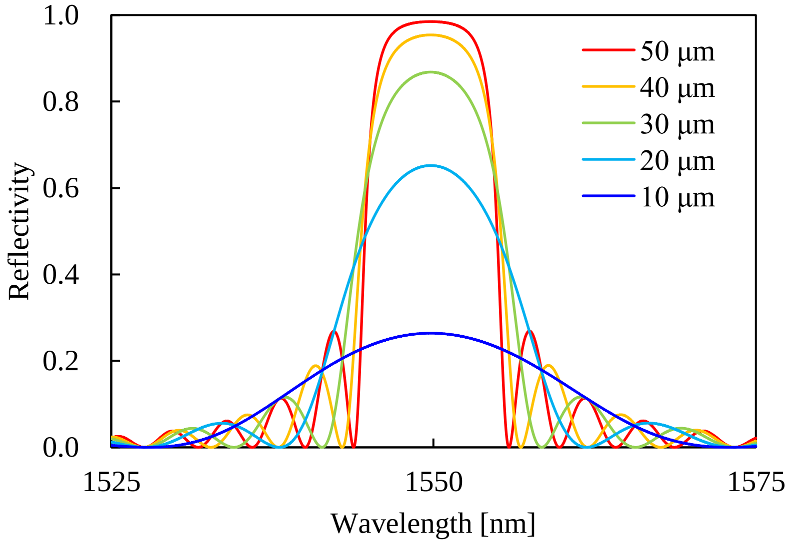

Fig. 5.40 Reflectivity with each DBR length.

formed by cleavage, the reflectivity depends on the refractive index of the material, so basically the reflectivity can be varied only within a small range. The length of the waveguide is determined by the accuracy of the cleavage, which makes it difficult to determine the length with high accuracy and may cause the PPR peak to deviate from the design. Therefore, a structure that forms a reflective surface by DBR was proposed. As shown in Fig. 5.39(b), the proposed structure consists of a waveguide and DBR behind the DR laser. This structure oscillates as a DR laser by DFB and DBR1, and the optical output is reflected by DBR2 and feedback to the active layer. DBR2 was designed for high reflectivity, which reduces backward emission and increases the efficiency of the DR laser. The amount of feedback to the active layer can be controlled by DBR1. In general, if the feedback amount is too high, it can cause instability in operation, and if it is too low, it requires a large optical output to induce PPR. Fig. 5.40 shows the relationship between DBR length and reflectance. In this calculation, the grating depth is designed to be 20 nm. In this study, DBR1 was designed to be 10 μm to account for losses in the waveguide and reflectance in DBR2. The waveguide length was designed to be 350 μm to achieve a PPR peak at 27 GHz.

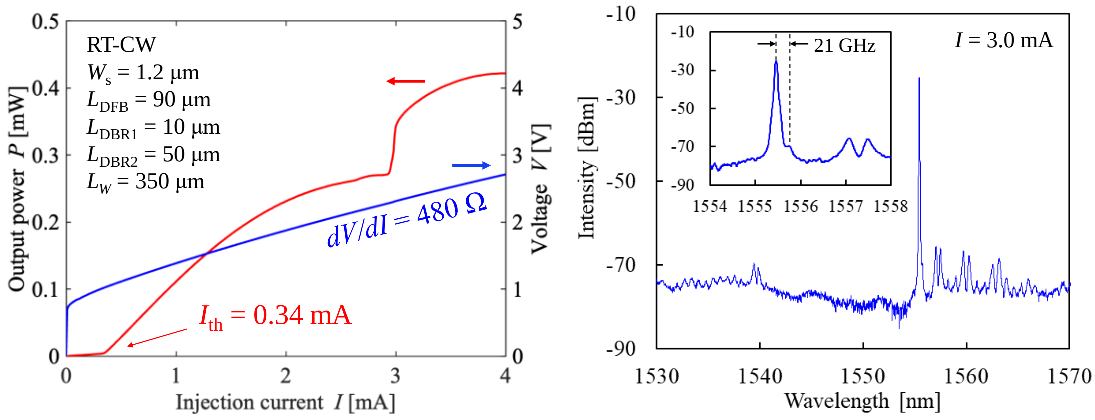

(a) (b)

Fig. 5.41 Static characteristics of the fabricated membrane laser with structure of PPR: (a) *I-L* and *I-V* characteristic and (b) Spectrum at injection current of 3.0 mA.

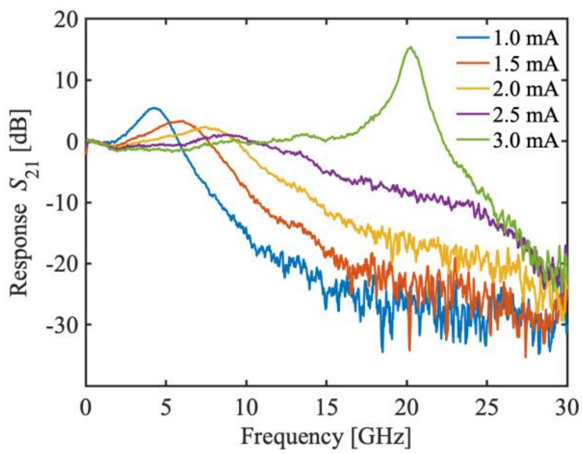

Fig. 5.42 Small signal response S_{21} measured for various bias current.

Fig. 5.41(a) shows the *I-L* and *I-V* characteristics of the fabricated device with stripe width of 1.2 μm and DFB length of 90 μm. A threshold current of 0.34 mA and an external differential quantum efficiency of 21% at low injection current were obtained, showing static characteristics almost comparable to those of DR lasers without PPR structure. As the injection current is increased, the output attenuates due to the interaction with the reflected light from DBR2, and a kink occurs at I = 3.0 mA. Fig. 5.41(b) shows the spectrum at an injection current of 3.0 mA, where the kink occurs. In addition to the DFB mode, the spectrum shows periodic peaks due to the FP mode caused by the backward reflection. The inset shows an expanded spectrum near the lasing wavelength, and a wavelength difference corresponding to 21 GHz was confirmed between the lasing mode and the side mode. The small-signal response of this device was measured at injection currents from 1 mA to 3 mA, and the results are shown in Fig. 5.42. When the injection current is less than 2 mA, the small-signal response is similar to that of a DR laser without PPR structure. As the injection current was further increased, the slope at the high frequency side became gradual, and a strong peak was observed at 20.1 GHz at injection current of 3.0 mA, where the kink was occurring. This peak shows a higher response than the response at low frequencies and the peak of the relaxation oscillation frequency at low injection currents, which is caused by PPR. The PPR peak frequency is also nearly consistent with the frequency difference observed from the spectrum. These results demonstrate that PPR can be induced by a membrane laser using the proposed structure. However, the frequency of the PPR peak was different from the design. This was because the optical path length changed due to an error in the refractive index of the waveguide, and the analysis was calculated assuming zero reflection from the front. As for the length of DBR1, the relationship between its length and modulation characteristics has not been experimentally demonstrated. A redesign is needed that takes these considerations into account.

5G mobile signal transmission experiments using membrane lasers were performed by Dr. K. Nishimura *et al*. of KDDI Research, Inc [83]. The device structure is almost the

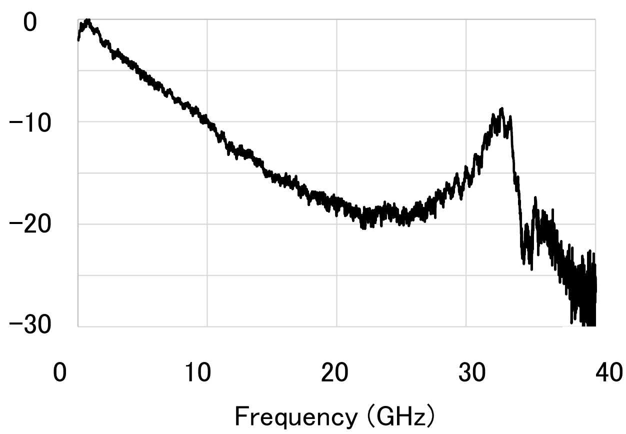

Fig. 5.43 Frequency response of PPR LD at injection current of 4.58 mA [83].

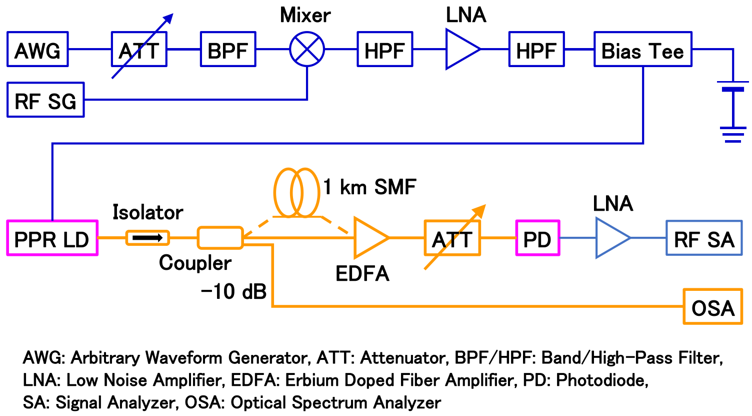

Fig. 5.44 Schematic of experimental setup [83].

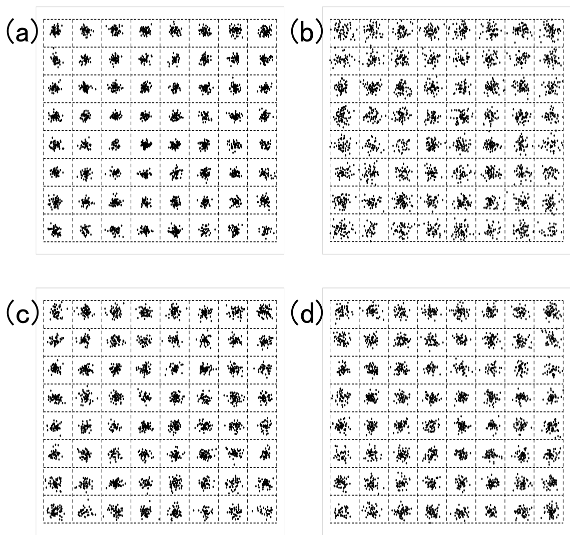

Fig. 5.45 Constellations of signals: (a) single channel modulation, (b) single channel modulation and 1-km SMF transmission, and (c) lower-band and (d) upper-band channels with dual channel modulation [83].

same as described above, with a DFB length of 90 μm, L_{DBR1} = 10 μm, and L_{DBR2} = 100 μm. The backward waveguide for feedback is slightly shorter at 250μm. As a result, the wavelength spacing of the FP mode derived from the backward waveguide broadened, and the PPR peak shifted to the high frequency side as shown in Fig. The PPR peak was observed at 32.8 GHz. Under the specified bias conditions, modulation by a 5G-compliant signal with a 64 Quadrature Amplitude Modulation (QAM) format was performed. The experimental setup, shown in Fig, facilitated the generation of input signals with a bandwidth of 400 MHz centered at 31.0 GHz or an 800 MHz bandwidth achieved by bonding two channels centered at 31.2 GHz and 31.6 GHz. These signals were produced through the upconverting 5G-compliant signals with a center frequency of 9.6 GHz. Single-channel transmission tests were performed on 1 km of single-mode fiber (SMF) under the bias conditions and signal frequencies. It is noteworthy that these conditions were meticulously selected to achieve optimal Error Vector Magnitude (EVM) values, as detailed below. Fig shows the signal constellations for the lower and upper band channels for (a) single channel modulation, (b) single channel modulation with 1 km SMF transmission, and (c) dual channel modulation. The average EVM for the single-channel case was 4.1%. For the dual-channel case, it was 5.1% for the lower-band channel and 5.4% for the upper-band channel. 1-km SMF transmission degrades to 6.7% for single-channel modulation, but this value is below the threshold value of 8.0% defined for 64QAM signals in the 3GPP specification. Experimental results confirm that membrane DR lasers with PPR structures are a promising solution for short reach A-RoF systems transmitting RF signals in the millimeter wave band. The design flexibility of the laser structure, which allows the PPR resonant frequency to be determined, opens the possibility of tuning to higher frequencies, such as the 60 GHz band allocated for 5G, or the higher frequency bands envisioned for next-generation mobile systems. This is an initial attempt, and further performance improvements are expected through optimization of various parameters in the device structure and experimental conditions.

5.5 Conclusion

In conclusion, this chapter has explored diverse applications leveraging the unique attributes of membrane lasers, specifically focusing on their low power consumption and rapid response time. The investigated applications spanned various domains, emphasizing the versatility of membrane lasers in addressing contemporary challenges in optical communication and beyond. The application of on-chip optical interconnect was discussed in Section 5.2, highlighting the significance of short-distance optical communication and the specific requirements for on-chip optical interconnect. An in-depth exploration of optical neural networks followed in Section 5.3, encompassing the utilization of photonic integrated circuits and proposing an innovative concept involving membrane lasers for an all-optical neural network. The discussion also encompassed the characterization of these applications and provided insights into their future prospects. Furthermore, Section 5.4 delved into the application of membrane lasers in the context of B5G/6G communication systems. This included examining Radio-over-Fiber (RoF) applications and exploring the potential of Photon-Photon Resonance (PPR) for high-speed modulation. The section concluded with an assessment of the applications' characteristics and offered a glimpse into their future potential. In summary, this chapter underscores the adaptability and promising prospects of membrane lasers across a spectrum of applications. The insights gained from the experimental results and discussions pave the way for further advancements and innovations in the field, contributing to the evolution of optical technologies for future communication systems.

Reference

[1] IEEE. "IEEE802.3bs-2017 – IEEE Standard for Ethernet Amendment 10: Media Access Control Parameters, Physical Layers, and Management Parameters for 200 Gb/s and 400 Gb/s Operation," Jan. 2017.

[2] L. D. Hutcheson, P. Hangen, and A. Husain, “Optical interconnects replace hardwire: Light promises to relieve bottlenecks in electric interconnections from cabinet to cabinet, board to board, IC to IC—and even within chips,” *IEEE spectrum*, vol. 24, pp. 30-35, 1987.

[3] M. Taubenblatt, “Optical interconnects for high performance computing,” in *Optical Fiber Communication Conference*, p. OThH3, 2011.

[4] A. Louri, S. Furlonge, and C. Neocleous, “Experimental demonstration of the optical multi-mesh hypercube: scaleable interconnection network for multiprocessors and multicomputers,” *Applied optics*, vol. 35, pp. 6909-6919, 1996.

[5] T. H. Szymanski and H. S. Hinton, “Reconfigurable intelligent optical backplane for parallel computing and communications,” *Applied Optics*, vol. 35, pp. 1253-1268, 1996.

[6] K. Hirabayashi, T. Yamamoto, and S. Hino, “Optical backplane with free-space optical interconnections using tunable beam deflectors and a mirror for bookshelf-assembled terabit per second class asynchronous transfer mode switch,” *Optical Engineering*, vol. 37, pp. 1332-1342, 1998.

[7] R. A. Nordin, W. R. Holland, and M. A. Shahid, “Advanced optical interconnection technology in switching equipment,” *Journal of lightwave technology*, vol. 13, pp. 987-994, 1995.

[8] A. Guha, J. Bristow, C. Sullivan, and A. Husain, “Optical interconnections for massively parallel architectures,” *Applied optics*, vol. 29, pp. 1077-1093, 1990.

[9] J. P. Bristow, C. T. Sullivan, S. D. Mukherjee, Y. Liu, and A. Husain, “Progress and status of guided-wave optical interconnection technology,” in *OE/LASE'93: Optics, Electro-Optics, & Laser Applications in Science& Engineering*, 1993, pp. 4-10.

[10] J. P. Bristow, Y. Liu, T. Marta, S. Bounnak, K. Johnson, Y.-S. Liu, *et al.*, “Cost-effective optoelectronic packaging for multichip modules and backplane level optical interconnects,” in *Photonics West'95*, 1995, pp. 61-73.

[11] J. E. Thomson, H. Levesque, E. Savov, F. Horwitz, B. L. Booth, and J. E. Marchegiano, “Optical waveguide circuit board with a surface-mounted optical

receiver array," *Optical Engineering*, vol. 33, pp. 939-945, 1994.

[12] C. Moss, "Optical interconnect for modular avionics," in *Interconnection Technology (Digest No. 1994/220)*, 1994, pp. 6/1-6/5.

[13] L. W. Shacklette, K. M. Stengel, L. A. Eldada, C. Xu, and J. T. Yardley, "Polymeric waveguides for optical backplanes," in *SPIE's 1995 Symposium on OE/Aerospace Sensing and Dual Use Photonics*, 1995, pp. 107-117.

[14] D. Israel, R. Baets, M. J. Goodwin, N. Shaw, M. D. Salik, and C. J. Groves-Kirkby, "Multimode polymeric Y junctions for star couplers in backplane optical interconnect," *Applied optics*, vol. 36, pp. 5091-5096, 1997.

[15] R. T. Chen, H. Lu, D. Robinson, Z. Sun, T. Jannson, D. Plant, *et al.*, "60 GHz board-to-board optical interconnection using polymer optical buses in conjunction with microprism couplers," *Applied physics letters*, vol. 60, pp. 536-538, 1992.

[16] J. Guttmann, H.-P. Huber, O. Krumpholz, M. Rode, R. Bogenberger, and K.-P. Kuhn, "Optical backplanes with integrated polymer waveguides," *Optical Engineering*, vol. 39, pp. 673-679, 2000.

[17] I.-K. Cho, K. B. Yoon, S. H. Ahn, M. Y. Jeong, H.-K. Sung, B. H. Lee, *et al.*, "Board-to-board optical interconnection system using optical slots," *IEEE Photonics Technology Letters*, vol. 16, pp. 1754-1756, 2004.

[18] C. Kromer, G. Sialm, C. Berger, T. Morf, M. L. Schmatz, F. Ellinger, *et al.*, "A 100-mW 4× 10 Gb/s transceiver in 80-nm CMOS for high-density optical interconnects," *IEEE Journal of Solid-State Circuits*, vol. 40, pp. 2667-2679, 2005.

[19] T. Takemoto, H. Yamashita, T. Yazaki, N. Chujo, Y. Lee, and Y. Matsuoka, "A 25-to-28 Gb/s High-Sensitivity (9.7 dBm) 65 nm CMOS Optical Receiver for Board-to-Board Interconnects," *IEEE Journal of Solid-State Circuits*, vol. 49, pp. 2259-2276, 2014.

[20] N. Bamiedakis, J. Beals, R. V. Penty, I. H. White, J. V. DeGroot, and T. V. Clapp, "Cost-effective multimode polymer waveguides for high-speed on-board optical interconnects," *IEEE Journal of Quantum Electronics*, vol. 45, pp. 415-424, 2009.

[21] T. Mikawa, M. Kinoshita, K. Hiruma, T. Ishitsuka, M. Okabe, S. Hiramatsu, *et al.*, "Implementation of active interposer for high-speed and low-cost chip level optical interconnects," *IEEE journal of selected topics in quantum electronics*, vol. 9, pp. 452-459, 2003.

[22] M. Tokunari, H.-H. Hsu, K. Toriyama, H. Noma, and S. Nakagawa, "High-bandwidth density and low-power optical MCM using waveguide-integrated organic substrate," *Journal of Lightwave Technology*, vol. 32, pp. 1207-1212, 2014.

[23] F. E. Doany, C. L. Schow, C. W. Baks, D. M. Kuchta, P. Pepeljugoski, L. Schares, *et al.*, "160 Gb/s bidirectional polymer-waveguide board-level optical interconnects using CMOS-based transceivers," *IEEE Transactions on Advanced Packaging*, vol. 32, pp. 345-359, 2009.

[24] S. Nakagawa, "High-density optical multi-chip module on waveguide-integrated carrier," in *OptoElectronics and Communications Conference and Photonics in Switching*, 2013, p. WL3

[25] R. H. Dennard, F. H. Gaensslen, V. L. Rideout, E. Bassous, and A. R. LeBlanc, "Design of ion implanted MOSFET's with very small physical dimensions," *IEEE Journal of Solid-State Circuits,* vol. 9, pp. 256-268, 1974.

[26] P. Kapur, J. P. McVittie, and K. C. Saraswat, "Technology and reliability constrained future copper interconnects. I. Resistance modeling," *IEEE Transactions on Electron Devices,* vol. 49, pp. 590-597, 2002.

[27] T. Sakurai, "Approximation of wiring delay in MOSFET LSI," *IEEE Journal of solid-state circuits,* vol. 18, pp. 418-426, 1983.

[28] A. Hokazono, S. Kawanaka, K. Tsumura, Y. Hayashi, H. Tanimoto, T. Enda, *et al.*, "Guideline for low-temperature-operation technique to extend CMOS scaling," in *Electron Devices Meeting*, IEDM'06. International, pp. 1-4, 2006.

[29] P. Morrow, C.-M. Park, S. Ramanathan, M. Kobrinsky, and M. Harmes, "Three-dimensional wafer stacking via Cu-Cu bonding integrated with 65-nm strained-Si/low-k CMOS technology," *IEEE electron device letters*, vol. 27, pp. 335-337, 2006.

[30] V. Adler and E. G. Friedman, "Repeater design to reduce delay and power in resistive interconnect," *IEEE Transactions on Circuits and Systems II: Analog and Digital Signal Processing,* vol. 45, pp. 607-616, 1998.

[31] K. Banerjee and A. Mehrotra, "A power-optimal repeater insertion methodology for global interconnects in nanometer designs," *IEEE Transactions on Electron Devices,* vol. 49, pp. 2001-2007, 2002.

[32] J. A. Burns, B. F. Aull, C. K. Chen, Chang-Lee Chen, C. L. Keast, J. M. Knecht, V. Suntharalingam, K. Warner, P. W. Wyatt and D. W. Yost "A Wafer-Scale 3-D Circuit Integration Technology", *IEEE Transactions on Electron Devices*, vol. 53, No. 10, pp. 2507-2516, 2006.

[33] V. R. Almeida, C. A. Barrios, R. R. Panepucci, and M. Lipson, "All-optical control of light on a silicon chip," *Nature,* vol. 431, pp. 1081-1084, 2004.

[34] K. Ohashi, K. Nishi, T. Shimizu, M. Nakada, J. Fujikata, J. Ushida*, et al.*, "On-chip optical interconnect," *Proceedings of the IEEE,* vol. 97, pp. 1186-1198, 2009.

[35] M. Notomi, A. Shinya, K. Nozaki, T. Tanabe, S. Matsuo, E. Kuramochi*, et al.*, "Low-power nanophotonic devices based on photonic crystals towards dense photonic network on chip," *IET circuits, devices & systems,* vol. 5, pp. 84-93, 2011.

[36] M. Binggeli and F. Li, "Scaling Optical Communication for On-Chip Interconnect," *International Conference on Electronic Packaging Technology (ICEPT)* , pp. 1178-1183, 2018.

[37] T. Ishikawa, T. Higashi, T. Uchida, T. Fujii, T. Yamamoto, H. Shoji, et al., "Evaluation of differential gain of 1.3/spl mu/m AlGaInAs/InP strained MQW lasers," in Indium Phosphide and Related Materials, 1998 International Conference on, 1998, pp. 729-732.

[38] D. A. Miller, "Device requirements for optical interconnects to silicon chips," *Proceedings of the IEEE,* vol. 97, pp. 1166-1185, 2009.

[39] W. Fang, "Study of High Temperature and High Efficiency Operation of Membrane Photonic Integrated Circuits on Si Substrate" Doctoral Thesis, Tokyo institute of technology, 2022.

[40] W. Wang, S. A. M. E. Moataz, W. Fang, N. Takahashi, Y. Oiso, T. Amemiya, N. Nishiyama, "Design of InP-based membrane waveguide on Si substrate toward low propagation loss and high-efficiency coupling with laser", Photonic Device Workshop 2020, P3, Nov. 2020.

[41] R. Xue, W. Fang, N. Takahashi, S. Katsumi, Y. Ohiso, T. Amemiya, N. Nishiyama, "Low Loss InP-Rib Waveguide on Si Substrate for Membrane Photonic Integrated Circuits", The 69nd JSAP Spring Meeting, 24p-D214-3, Mar. 2022.

[42] Y. LeCun, Y. Bengio, and G. Hinton, "Deep learning," *Nature*, vol. 521, pp. 436–444, 2015.

[43] D. Silver, A. Huang, C. J. Maddison, A. Guez, L. Sifre, G. van den Driessche, J. Schrittwieser, I. Antonoglou, V. Panneershelvam, M. Lanctot, *et al*., "Mastering the game of Go with deep neural networks and tree search," *Nature*, vol. 529, pp. 484–489, 2016.

[44] S. Hershey, S. Chaudhuri, D. P. W. Ellis, J. F. Gemmeke, A. Jansen, R. C. Moore, M. Plakal, D. Platt, R. A. Saurous, B. Seybold, M. Slaney, R. J. Weiss, and K. Wilson, "Cnn architectures for large-scale audio classification," in *Proc. IEEE Int. Conf. Acoust., Speech Signal Process. (ICASSP)*, 2017, pp. 131–135.

[45] A. Esteva, B. Kuprel, R. A. Novoa, J. Ko, S. M. Swetter, H. M. Blau, and S. Thrun, "Dermatologist-level classification of skin cancer with deep neural networks," *Nature*, vol. 542, no. 7639, pp. 115–118, 2017.

[46] G. E. Moore, "Cramming more components onto integrated circuits, Reprinted

from Electronics, volume 38, number 8, April 19, 1965, pp.114 ff.," *IEEE Solid-State Circuits Society Newsletter*, vol. 11, no. 3, pp. 33–35, 2006.

[47] G. van der Sande, D. Brunner, and M. C. Soriano, "Advances in photonic reservoir computing," *Nanophotonics*, vol. 6, no. 3, pp. 561–576, 2017.

[48] K. Kitayama, M. Notomi, M. Naruse, K. Inoue, S. Kawakami, and A. Uchida, "Novel frontier of photonics for data processing-Photonic accelerator," *APL Photonics*, vol. 4, no. 9, p. 090901, 2019.

[49] R. Hamerly, "The Future of Deep Learning Is Photonic: Reducing the energy needs of neural networks might require computing with light," *IEEE Spectr*, vol. 58, no. 7, pp. 30–47, 2021.

[50] G. Alagappan, J. Ong, Z. Yang, T. Ang, W. Zhao, Y. Jiang, W. Zhang, C. Png, "Leveraging AI in Photonics and Beyond," *Photonics*, vol. 9, no. 2, p. 75, 2022.

[51] B. J. Shastri, A. N. Trait, T. Ferreira de Lima, W. H. P. Pernice, H. Bhaskaran. C. D. Wright, P. R. Prucnal, "Photonics for artificial intelligence and neuromorphic computing," *Nat Photonics*, vol. 15, no. 2, pp. 102–114, 2021.

[52] R. Hamerly, L. Bernstein, A. Sludds, M. Soljačić, and D. Englund, "Large-Scale Optical Neural Networks Based on Photoelectric Multiplication," *Phys Rev X*, vol. 9, no. 2, p. 021032, 2019.

[53] A. R. Totovic, G. Dabos, N. Passalis, A. Tefas, and N. Pleros, "Femtojoule per MAC Neuromorphic Photonics: An Energy and Technology Roadmap," *IEEE Journal of Selected Topics in Quantum Electronics*, vol. 26, no. 5, pp. 1–15, 2020.

[54] M. A. Nahmias, T. F. de Lima, A. N. Tait, H.-T. Peng, B. J. Shastri, and P. R. Prucnal, "Photonic Multiply-Accumulate Operations for Neural Networks," *IEEE Journal of Selected Topics in Quantum Electronics*, vol. 26, no. 1, pp. 1–18, 2020.

[55] J. Cheng, H. Zhou, and J. Dong, "Photonic Matrix Computing: From Fundamentals to Applications," *Nanomaterials*, vol. 11, no. 7, p. 1683, 2021.

[56] Y. Shen, N. C. Harris, S. Skirlo, M. Prabhu, T. Baehr-Jones, M. Hochberg, X. Sun, S. Zhao, H. Larochelle, D. Englund, M. Solijacic, "Deep learning with coherent nanophotonic circuits," *Nat Photonics*, vol. 11, no. 7, pp. 441–446, 2017.

[57] R. Hamerly, "The Future of Deep Learning Is Photonic: Reducing the energy needs of neural networks might require computing with light," *IEEE Spectr*, vol. 58, no. 7, pp. 30–47, 2021.

[58] N. C. Harris, R. Braid, D. Bunandar, J. Carr, B. Dobbie, C. Dorta-Quinones, J. Elmhurst, M. Forsythe, M. Gloud, S. Gupta, S. Kannan, T. Kenney, G. Kong, T. Lazovich, S. Mckenzie, C. Ramey, C. Ravi, M. Scott, J. Sweeney, O. Yildirim, K. Zhang, "Accelerating artificial intelligence with silicon photonics," in *Optical*

Fiber Communication Conference (OFC) 2020, 2020, p. W3A.3.

[59] L. Yang, R. Ji, L. Zhang, J. Ding, and Q. Xu, "On-chip CMOS-compatible optical signal processor," *Opt Express*, vol. 20, no. 12, p. 13560, 2012.

[60] A. N. Tait, T. F. de Lima, E. Zhou, A. X. Wu, M. A. Nahmias, B. J. Shastri, P. R. Prucnal, "Neuromorphic photonic networks using silicon photonic weight banks," *Sci Rep*, vol. 7, no. 1, p. 7430, 2017.

[61] A. N. Tait, A. X. Wu, T. F. de Lima, E. Zhou, B. J. Shastri, M. A. Nahmias, P. R. Prucnal, "Microring Weight Banks," *IEEE Journal of Selected Topics in Quantum Electronics*, vol. 22, no. 6, pp. 312–325, 2016.

[62] X. Xu, M. Tan, B. Corcoran, J. Wu, A. Boes, T. G. Nguyen, S. T. Chu, B. E. Little, D. G. Hicks, R. Morandotti, A. Mitchell, D. J. Moss, "11 TOPS photonic convolutional accelerator for optical neural networks," *Nature*, vol. 589, no. 7840, pp. 44–51, 2021.

[63] S. Ohno, R. Tang, K. Toprasertpong, S. Takagi, and M. Takenaka, "Si Microring Resonator Crossbar Array for On-Chip Inference and Training of the Optical Neural Network," *ACS Photonics*, vol. 9, no. 8, pp. 2614–2622, 2022.

[64] G. Mourgias-Alexandris, A. Tsakyridis, N. Passalis, A. Tefas, K. Vyrsokinos, and N. Pleros, "Low-latency chip-to-chip optical interconnects implemented using a reconfigurable silicon photonic switch matrix," *Optics Express*, vol. 27, no. 7, pp. 9620–9630, 2019.

[65] M. M. Pour Fard, I. A. D. Williamson, M. Edwards, K. Liu, S. Pai, B. Bartlett, M. Minkov, T. W. Hughes, S. Fan, and T. A. Nguyen, "Time-Resolved Studies of Photonic Crystals Cavity Modes with Stroboscopic Scanning Optical Microscopy," *Optics Express*, vol. 28, no. 8, p. 12138, 2020.

[66] J. Crnjanski, M. Krstić, A. Totović, N. Pleros, and D. Gvozdić, "Real-time deep learning-based photonic switch fabric control for optical data center networks," *Optics Letters*, vol. 46, no. 9, pp. 2003–2006, 2021.

[67] Y. Huang, W. Wang, L. Qiao, X. Hu, and T. Chu, "Optical resonator with an embedded diode for active tuning of whispering-gallery modes," *Optics Letters*, vol. 47, pp. 1810-1813, 2022.

[68] Cheng, Z., Tsang, H. K., Wang, X., Xu, K. & Xu, J.-B, "In-plane optical absorption and free carrier absorption in graphene-on-silicon waveguides," *IEEE J. Sel. Top. Quantum Electron,* vol. 20, pp. 43–48, 2014.

[69] I. A. D. Williamson, T. W. Hughes, M. Minkov, B. Bartlett, S. Pai, and S. Fan, "Reprogrammable electro-optic nonlinear activation functions for optical neural

networks," *IEEE Journal of Selected Topics in Quantum Electronics*, vol. 26, no. 1, pp. 1-12, 2019.

[70] S. Sakai, N. Takahashi, T. Amemiya, N. Nishiyama, "全光ニューラルネットワークに向けた ReLU 関数としての GaInAsP 半導体薄膜レーザの構造検討", 第70回応用物理学会春季学術講演会, Mar. 2023.

[71] T. Bai, A. Alkhateeb, and R. W. Heath, "Coverage and capacity of millimeter-wave cellular networks," *IEEE Commun. Mag*., vol. 52, no. 9, pp. 70–77, Sep. 2014.

[72] A. I. Sulyman, A. T. Nassar, M. K. Samimi, G. R. MacCartney, Jr., T. S. Rappaport, and A. Alsanie, "Radio propagation path loss models for 5G cellular networks in the 28 GHz and 38 GHz millimeter-wave bands," *IEEE Comms. Mag*., vol. 52, no. 9, pp. 78–86, Sep. 2014.

[73] S. Ishimura, B. Kim, K. Tanaka, K. Nishimura, H. Kim, Y. C. Chung, and M. Suzuki, "Simultaneous Transmission of Aggregated Microwave and Millimeter-wave Signals over Fiber with Parallel IM/PM Transmitter for Mobile Fronthaul Links," *Proc. 43rd European Conference on Optical Communication*, Paper Tu.1.B.1, 2017.

[74] K. Ito, M. Suga, Y. Shirato, N. Kita, and T. Onizawa: "A novel centralized beamforming scheme for radio-over-fiber systems with fixed wavelength allocation," *IEICE Communications Express*, Vol.8, No.12, pp.584-589, 2019.

[75] T. Nagayama, K. Furuya, S. Akiba, J. Hirokawa, and M. Ando:"Millimeter-wave antenna beam forming by radio-over-fiber with 1.3 µm light source and variable delay line," *OECC and PGC2017*, pp. 1-2, 2017.

[76] P. Bardella and I. Montrosset, "A New Design Procedure for DBR Lasers Exploiting the Photon–Photon Resonance to Achieve Extended Modulation Bandwidth," *IEEE Journal of Selected Topics in Quantum Electronics*, vol. 19, no. 4, pp. 1502408-1502408, 2013.

[77] L. Bach, W. Kaiser, J. P. Reithmaier, A. Forchel, M. Gioannini, V. Feies, and I. Montrosset, "22-GHz modulation bandwidth of long cavity DBR laser by using a weakly laterally coupled grating fabricated by focused ion beam lithography," *IEEE Photonics Technology Letters*, vol. 16, no. 1, pp. 18-20, 2004.

[78] M. Radziunas, A. Glitzky, U. Bandelow, M. Wolfrum, U. Troppenz, J. Kreissl, and W. Rehbein, "Improving the Modulation Bandwidth in Semiconductor Lasers by Passive Feedback," *IEEE Journal of Selected Topics in Quantum Electronics*, vol. 13, no. 1, pp. 136-142, 2007.

[79] J. Kreissl, V. Vercesi, U. Troppenz, T. Gaertner, W. Wenisch, and M. Schell, "Up

to 40 Gb/s Directly Modulated Laser Operating at Low Driving Current: Buried-Heterostructure Passive Feedback Laser (BH-PFL)," *IEEE Photonics Technology Letter*s, vol. 24, no. 5, pp. 362-364, 2012.

[80] R. Lang and K. Kobayashi, "External Optical Feedback Effects on Semiconductor Injection Laser Properties," *Journal of Quantum Electronics*, vol. QE-16, no. 3, pp. 347-355, 1980.

[81] S. Yamaoka, N.-P. Diamantopoulos, H. Nishi, R. Nakao, T. Fujii, K. Takeda, T. Hiraki, T. Tsurugaya, S. Kanazawa, H. Tanobe, T. Kakitsuka, T. Tsuchizawa, F. Koyama, and S. Matsuo, "Directly modulated membrane lasers with 108 GHz bandwidth on a high-thermal-conductivity silicon carbide substrate," *Nature Photonics*, vol. 15, pp. 28-35, 2021.

[82] R. Lang and K. Kobayashi, "External optical feedback effects on semiconductor injection laser properties," *IEEE Journal of Quantum Electronics*, vol. 16, no. 3, pp. 347-355, 1980.

[83] K. Nishimura, N. Takahashi, S. Nimura, K. Tsutsui, N. Nishiyama, H. Takahashi, and M. Suzuki, "Direct Modulation of Membrane DR Laser Involving Photon-Photon Resonance by 5G Mobile Signal in Millimeter-Wave Band," *Opto-Electronics and Communications Conference (OECC)*, pp. 1-3, 2023.

Chapter 6
Conclusion

The purpose of this study was to deepen the understanding of semiconductor lasers and to pursue the ideal semiconductor laser in terms of power consumption. Semiconductor lasers range from high-power lasers used for processing materials to low-threshold and low-power lasers used for sensing, and their structures vary widely depending on the application. Even in data transmission applications, the optimum structure differs between long-range and short-range communications because of the different characteristics required of lasers. While wavelength chirp and line width are important characteristics for long-distance transmission, low power consumption and high speed are required for short-distance communication to find advantages over electricity-based communication. Thus, the required characteristics differ depending on the application. In this study, focusing on short-range optical communications, which have not yet been put into practical use, characteristics of semiconductor lasers were investigated to clarify the parameters that affect the required performance, in pursuit of the ideal semiconductor laser. In the field of short-range optical communications, energy cost, defined by optical output power and modulation speed, is an important metric. Laser characteristics, which are influenced by parameters such as cavity length and optical confinement, play a crucial role. Shorter cavity lengths can improve threshold current and modulation efficiency, but excessively short cavity lengths increase resistance, resulting in insufficient gain and affecting threshold. Optimal optical confinement, especially in the vertical direction, improves threshold current and modulation efficiency. Membrane lasers offer superior vertical optical confinement, while ridge lasers offer superior horizontal confinement. To achieve ultra-low threshold and high modulation efficiency, optical confinement in both directions must be enhanced. Photonic crystal lasers achieve this but suffer from low output power due to saturation caused by high differential resistance. Furthermore, strong confinement in the direction of light propagation reduces output power and differential quantum efficiency. Balancing these factors is complex and involves trade-offs between structural parameters and laser characteristics. A comprehensive understanding of these tradeoffs is essential to determine the ideal semiconductor laser. Therefore, based on the above circumstances, the following objectives were listed and studied in this thesis.

(1) Investigation of design of membrane laser with suitable optical confinement structure
  (a) Calculation of membrane laser characteristics for suitable laser design
  (b) Establishment of fabrication techniques
(2) Realization of low power consumption membrane laser
  (a) Characterization of static and dynamic properties of membrane DR laser
  (b) Demonstration of low power consumption membrane optical link
(3) Demonstration of membrane laser deployment in various applications

Towards achieving the objective (1), theories for understanding the relationship between fundamental laser properties and structural parameters were discussed in Chapter 2. This chapter analyzes semiconductor membrane lasers, focusing on key parameters such as threshold current, external differential quantum efficiency, and optical confinement in the transverse and cavity directions. The goal is to identify ways to analyze the fundamental characteristics and overall performance and to explore ways to optimize these lasers. Membrane lasers are a promising approach to enhance optical confinement and improve laser performance by increasing the refractive index difference in the vertical direction. In this study, we investigated structures that can further reduce power consumption by improving optical confinement in the transverse and cavity directions.

First, as a lateral optical confinement structure, we proposed and investigated an embedded ridge waveguide (BRW) structure in which the lateral cladding layer is thinner than the active layer. Focusing on the fundamental characteristics of internal loss and differential resistance, we designed the ridge depth to minimize these parameters while enhancing optical confinement and found that d = 50 nm was optimal. In addition, an experimental guideline of $W_d < 0.5$ μm was obtained by taking into account the slope near the active layer caused by the fabrication process.

Next, the introduction of asymmetric waveform pitch modulation (ACPM) as an optical confinement structure in the cavity direction was investigated: the transfer matrix method (TMM), which is commonly used in the analysis of DFB lasers, was clarified in detail, and the carrier density distribution in the cavity was also analyzed by extending the rate equation in the cavity direction. Using these methods, we have established a method to obtain an optimal design for a membrane DR laser with ACPM grating that is expected to suppress spatial hole-burning. When hole-burning occurs, the main-mode gain is reduced due to insufficient carrier supply. As a result of analyzing the gain difference between the main and side modes for each structure, it was estimated that stable operation with the lowest gain difference is obtained when the phase-arrangement region (PAR) length is 0.25 at a cavity length of 30 μm and when the phase-arrangement region (PAR) length is 0.31 at 40 μm. The introduction of these improved optical confinement structures is expected to reduce the power consumption of membrane DR lasers.

In chapter 3, focusing on the realization of the ridge buried waveguide (BRW) structure and the formation of gratings, this presentation will delve into the details of membrane laser fabrication techniques. Next, selective regrowth using organometallic vapor phase epitaxy (OMVPE) is discussed and optimal design parameters for BRW structures are scrutinized. To achieve the desired BRW structure, two matters are examined, including etching of the side cladding layer and control of the regrowth time. a detailed examination of the OMVPE conditions reveals the interaction between mask width and growth thickness, and the regrowth time to obtain a ridge depth of $d = 50$ nm at each mask width is experimentally determined. The regrowth time to obtain a ridge depth of $d = 50$nm for each mask width was experimentally determined. In addition, a study was conducted to reduce the calculated slope width (W_d) to 0.5 μm or less. The experimental results emphasize the importance of wet etching time in determining W_d, and a wet etching time of 10 minutes was found to be optimal for achieving the desired structure.

The second half of this chapter moves on to grating formation on surfaces using electron beam lithography (EBL) and outlines in detail the principles of grating design for DR lasers. The theoretical considerations are validated through experiments to determine the grating period for optimal laser performance. Challenges encountered in previous studies were remedied by revising the fabrication process. The grating formation method was rearranged and the transition from wet etching to dry etching was investigated. The results showed that the damage to the active layer caused by dry etching was negligible. This process improvement solved the problems of previous studies and enabled uniform fabrication.

Towards achieving the objective (2), we shifted our focus to the experimental characterization of semiconductor membrane lasers and sought to define the ideal semiconductor laser characteristics. The initial epi-wafer modifications and fabrication of membrane DR lasers, coupled with discussions on power consumption in various applications, were important stages of the research. The threshold current of 0.13 mA and external differential quantum efficiency from front facet of 23% were obtained. The threshold current is 40% lower than the threshold current of 0.21 mA for the flat structure and uniform grating in the previous study, due to the increase in optical confinement factor by the BRW structure and the reduction in threshold gain by the phase shift of the ACPM grating. The differential resistance was also successfully reduced to 480 Ω by bringing the distance between the electrode and the active layer to 0.8 μm. In addition, the change in active layer thickness and the improvement of thermal resistance by direct bonding resulted in an increase in saturation injection current up to 5 mA, despite the short cavity of 40 μm.

In Chapter 5, we developed a panorama of applications that take advantage of the low power consumption and fast response of semiconductor membrane lasers. From on-chip optical interconnection to deep learning to analog radio-over-fiber, each application highlighted the versatility and adaptability of membrane lasers.

In conclusion, this paper not only advances our knowledge in this area, but also opens the door for continued exploration and innovation. The journey from understanding the fundamental properties to realizing practical applications underscores the importance of semiconductor membrane lasers in shaping the landscape of optical technology.

Acknowledgment

I would like to express my gratitude to my research advisors, Prof. Nobuhiko Nishiyama and Prof. Shigehisa Arai, for providing me supervision, guidance, encouragement, and support during my studies at Tokyo Institute of Technology. I would like to thank them for giving me the opportunity to present my research in a variety of conferences. The experience and profit I obtained will be of grand importance to my further studies.

I would like to show my greatest appreciation to Assoc. Prof. Tomohiro Amemiya, Specially Appointed Associate Prof. Yoshitaka Ohiso, and Specially Appointed Prof. Tsuyoshi Horikawa. They provided their professional knowledge and patience to support my research and encouraged me to face difficulties in daily life.

I would like to thank Prof. Yasuyuki Miyamoto, Prof. Masahiro Asada, Assoc. Prof. Safumi Suzuki, Research staff Kenji Morita, Toshiaki Kitamura, and Tsukuru Katsuyama for providing research guidance and assistance in daily life.

I would like to thank Assoc. Prof. Yuya Shoji, Prof. Shigeru Nakagawa, and Specially Appointed Prof. Kensuke Ogawa for guidance and meaningful discussion in the joint seminar.

I would like to acknowledge honorable Prof. Yasuharu Suematsu, Prof. Kenichi Iga, Prof. Fumio Koyama, Prof. Hiroyuki Uenohara, Prof. Tomoyuki Miyamoto, and Assoc. Prof. Masahiro Watanabe for their encouraging and constructive discussions.

I would like to thank Senior Distinguished Researcher Shinji Matsuo of NTT device technology for fruitful discussions.

I wish to acknowledge Prof. Toshihiko Baba of Yokohama National University, Prof. Katsuyuki Utaka of Waseda University, Prof. Kazuhiko Shimomura of Sophia University, Prof. Michihiko Suhara of Tokyo Metropolitan University, Associate Prof. Takeo Maruyama, and the members of the summer seminar on optical communications for their helpful advice and fruitful discussions.

I would like to thank Dr. Zhichen Gu (Asahi KASEI Corp.), and Dr. Junichi Suzuki (Mitsubishi Electric Corp.) for sharing their experiences selflessly with me in daily research life.

I would like to thank Dr. Takehiko Kikuchi (Sumitomo Electric Industries, Ltd), Mr. Fumihito Tachibana (Toyota Motor Corporation), Mr. Yusei Goto (Accenture PLC), and Mr. Shoichi Yoshitomi (FANUC Corporation) for their help in my experiments and daily life.

I would like to thank Dr. Daisuke Inoue (Sumitomo Electric Industries, Ltd) Ms. Nagisa Nakamura (Ricoh Company, Ltd), and Mr. Takamasa Yoshida (NTT DATA Corporation) for their help in fabricating membrane laser and teaching me the theoretical acknowledgment.

I would like to thank Dr. Weicheng Fang (Huawei) for helpful discussion and help in experiments in daily life.

I would like to thank all help and support from the membrane group members, Mr. Koichi Saito (Hitachi, Ltd.), Mr. Ruihao Xue (Huawei), Ms. Weiqi Wang (Huawei), Mr. Shunto Katsumi, and Mr. Keigo Tsutsui.

I would like to thank Dr. Moataz Eissa, Dr. Hibiki Kagami, and Dr. Sho Okada for their help in EB lithography and daily life.

I would also like to thank the laboratory members, Mr. Takuya Mitarai (Sumitomo Electric Industries, Ltd), Mr. Shoichi Yoshitomi, Mr. Kensho Oguri, Dr. J. Jitcharoenchai Napat, Ms. Yuning Wang (Sony), Dr. Yuduan Wang, Ms. Yahui Wang (Huawei), Ms. Makoto Tanaka (Murata Manufacturing Co., Ltd.), Mr. Takayuki Miyazaki, Mr. Yuta Yokomura (Mitsubishi Electric Corp.), Mr. Yutaka Makihara (RT Corporation), Mr. Hiromu Onodera, Mr. Takeru Nose, Mr. Keita Yamaguchi, Mr. Itsuki Sakamoto, Mr. Ryuki Sasaki, Mr. Naohito Saito, Mr. Takuma Kitabayashi, Mr. Tatsuki Hato, Mr. Keisuke Masuda, Mr. Yoki Nishi, Mr. Shun Yoshida, Mr. Kaibin Yao, and Mr. Yuduki Maeda.

I would like to thank all of my colleagues in Prof. Arai's group, Prof. Asada's group, Prof. Miyamoto's group, Assoc. Prof. Suzuki's group, and Assoc. Prof. Watanabe's group.

I would like to thank the kindness and help of the secretaries, Ms. Emi Takada, Ms. Asoko Suzuki, Ms. Hitomi Matsumura, and Ms. Kyoko Kasukawa.

I deeply appreciate my family; their love, support, and encouragement motivated me to move on and face the most difficult challenges.

The author was especially supported by Japan Society for the Promotion of Science (JSPS) for Research Fellowship for Young Scientists (#23KJ0935) and Advanced Research Infrastructure for Materials and Nanotechnology in Japan (ARIM) (#JPMXP1222IT0026, JPMXP1223IT0006).

Publication list

Journal papers

[1] **N. Takahashi**, W. Fang, R. Xue, S. Okada, Y. Ohiso, T. Amemiya, N. Nishiyama, "Optical ReLU using membrane lasers for an all-optical neural network," *Optics Letters*, Vol. 47, No. 21, pp. 5715-5718, 2022.

[2] **N. Takahashi**, W. Fang, Y. Ohiso, T. Amemiya and N. Nishiyama, "Lateral Confinement Enhanced Membrane Laser with Buried-Ridge-Waveguide Structure", *Journal of Optical Society of America B*, Vol. 38, No. 11, pp. 3340-3345, 2021.

[3] W. Fang, **N. Takahashi**, T. Horikawa, Y. Ohiso, R. Xue, S. Katsumi, T. Amemiya, N. Nishiyama, "High-temperature and high-efficiency operation of membrane optical link with buried-ridge-waveguide bonded on Si substrate," *Optics Express*, Vol. 30, Issue 19, pp. 34420-34428, 2022.

[4] W. Fang, **N. Takahashi**, Y. Ohiso, T. Amemiya, N. Nishiyama, "Reduced thermal resistance of membrane Fabry-Perot laser bonded on Si through room-temperature, surface-activated bonding assisted by a-Si nano-film," *IEEE Journal of Quantum Electronics*, Vol. 58, No. 2, 2000208, 2022.

[5] W. Fang, **N. Takahashi**, Y. Ohiso, T. Amemiya and N. Nishiyama, "High-Quality, Room-Temperature, Surface-Activated Bonding of GaInAsP/InP Membrane Structure on Silicon", *Jpn. J. of Appl. Phys*, Vol. 59, 060905, 2020.

International conference

[1] **N. Takahashi**, Y. Wang, N. Nishiyama, K. Williams, S. Latkowski and Y. Jiao, "Compact widely-tunable laser on an InP membrane on silicon," *The 28th Opto-Electronics and Communications Conference (OECC 2023)*, OECC2023-0320-40, Jul. 2023. (Oral)

[2] **N. Takahashi**, W. Fang, R. Xue, S. Katsumi, Y. Ohiso, T. Amemiya, N. Nishiyama,

"Low threshold current operation of membrane DR laser on Si with buried-ridge waveguide and ACPM grating for On-chip Optical Interconnection," *28th International Semiconductor Laser Conference (ISLC 2022)*, WB-06, Oct. 2022. (Oral)

[3] **N. Takahashi**, W. Fang, R. Xue, S. Katsumi, Y. Ohiso, T. Amemiya, N. Nishiyama, "Proposal of ReLU activation function using III-V semiconductor membrane laser for optical neural network," *The 15th Pacific Rim Conference on Lasers and Electro-Optics (CLEO-PR 2022)*, CMP11B-02, Jul.-Aug. 2022. (Oral)

[4] **N. Takahashi**, W. Fang, Y. Ohiso, T. Amemiya and N. Nishiyama, "Lateral Optical Confinement Enhanced GaInAsP Membrane Laser on Si for On-chip Optical Interconnection", *27th International Semiconductor Laser Conference (ISLC 2021)*, Oct. 2021. (Oral)

[5] **N. Takahashi**, W. Fang, R. Xue, S. Katsumi, T. Amemiya and N. Nishiyama, " Lasing Characteristics of GaInAsP Membrane Distributed-Reflector Laser on Si with Buried Ridge Waveguide Structure," *11th International Symposium on Photonics and Electronics Convergence (ISPEC 2021)*, Dec. 2021. (Poster)

[6] **N. Takahashi**, W. Fang, W. Wang, T. Amemiya and N. Nishiyama, "Buried-Ridge-Waveguide Type GaInAsP/InP Membrane Lasers for Reduction of Differential Resistance," *10th International Symposium on Photonics and Electronics Convergence (ISPEC 2020)*, S-20, Dec. 2020. (Poster)

[7] **N. Takahashi**, N. Nakamura, T. Yoshida, W. Fang, T. Amemiya, N. Nishiyama, and S. Arai, "Buried-ridge-waveguide Type GaInAsP/InP Membrane Distributed-Reflector Lasers for Reduction of Differential Resistance," *Compound Semiconductor Week 2019*, MoP-D-11, May. 2019. (Poster)

[8] K. Nishimura, **N. Takahashi**, S. Nimura, K. Tsutsui, N. Nishiyama, H. Takahashi, and M. Suzuki, "Direct Modulation of Membrane DR Laser Involving Photon-Photon Resonance by 5G Mobile Signal in Millimeter-Wave Band," *in Optoelectronics and Communication Conference*, 2023, pp. 1-3.

[9] W. Fang, **N. Takahashi**, T. Horikawa, Y. Ohiso, R. Xue, S. Katsumi, T. Amemiya,

and N. Nishiyama, "High Temperature Operation of Membrane Photonic Integrated Circuits with Buried-Ridge-Waveguide on Si", *28th International Semiconductor Laser Conference (ISLC2022)*, accepted, Matsue, Japan, Oct. 2022.

[10] W. Fang, **N. Takahashi**, R. Xue, S. Katsumi, T. Amemiya and N. Nishiyama, "Low Thermal Resistance of Membrane Distributed Feedback Laser Fabricated by Nano-film Assisted Room-temperature Surface Activated Bonding", *11th International Symposium on Photonics and Electronics Convergence (ISPEC2021)*, Tokyo, Japan, P-25, Dec. 2021.

[11] W. Fang, **N. Takahashi**, Y. Ohiso, T. Amemiya and N. Nishiyama, "Thermal Resistance Reduction of GaInAsP/Si Membrane Laser bonded by Room Temperature Si-nano-film Assisted Surface Activated Bonding", *Compound Semiconductor week 2021 (CSW2021)*, Stockholm, Sweden, TuA2-3, May. 2021.

[12] W. Fang, **N. Takahashi**, W. Wang, T. Amemiya and N. Nishiyama, "Investigation of thermal shunt structure of semiconductor membrane laser based on BCB bonding for enhancing heat evacuation", *10th International Symposium on Photonics and Electronics Convergence (ISPEC2020)*, Tokyo, Japan, S-07, Nov. 2020.

[13] W. Wang, W. Fang, K. Saito, **N. Takahashi**, T. Amemiya, N. Nishiyama, "Design of low loss InP-based membrane optical components on Si substrate", *9th International Symposium on Photonics and Electronics Convergence (ISPEC2019)*, Tokyo, Japan, P15, Nov. 2019.

Domestic conference

[1] **高橋直樹**, 筒井慧悟, Weicheng Fang, 勝見駿斗, 大礒義孝, 雨宮智宏, 西村公佐, 高橋英憲, 鈴木正敏, 西山伸彦, "後方 DBR による光子-光子共鳴を用いた GaInAsP 半導体薄膜 DR レーザの高速直接変調動作の検討", 2023 年電子情報通信学会総合大会, Mar. 2023.

[2] 高橋直樹, 方偉成, Xue Ruiha, 勝見駿斗, 大磯義孝, 雨宮智宏, 西山伸彦, "光閉じ込め構造改善による GaInAsP 半導体薄膜分布反射型レーザの低しきい値電流動作", 2022 年電子情報通信学会ソサイエティ大会, Sep. 2022.

[3] 高橋直樹, 方偉成, 岡田祥, 大礒義孝, 雨宮智宏, 西山伸彦, "光ニューラルネットワークに向けた III-V 族半導体薄膜レーザを用いた光活性化関数(ReLU)の提案", 第 83 回応用物理学会秋季学術講演会, Sep. 2022.

[4] 高橋直樹, 方偉成, Xue Ruihao, 勝見駿斗, 大礒義孝, 雨宮智宏, 西山伸彦, "リッジ埋め込み導波路構造および ACPM 回折格子を導入した GaInAsP 半導体薄膜レーザの発振特性", 第 69 回応用物理学会春季学術講演会, 26a-E301-3, Mar. 2022.

[5] 高橋直樹, 方偉成, 大礒義孝, 雨宮智宏, 西山伸彦, "リッジ埋め込み導波路構造による強横方向光閉じ込め GaInAsP 半導体薄膜レーザの発振特性", 第 82 回秋季応用物理学会, 10p-N103-8, Sep. 2021.

[6] 高橋直樹, 方偉成, WANG Weiqi, 大礒義孝, 雨宮智宏, 西山伸彦, "「奨励講演」GaInAsP 半導体薄膜分布反射型レーザの最適な光閉じ込めに関する考察", Photonic Device Workshop 2020, Nov. 2020.

[7] 高橋直樹, 方偉成, 齋藤 孝一, 雨宮智宏, 西山伸彦, "GaInAsP 半導体薄膜 DR レーザへの ACPM 構造導入の理論検討", 2019 年電子情報通信学会ソサイエティ大会, C-3-10, Sep. 2019.

[8] 高橋直樹, 齋藤孝一, 方偉成, 雨宮智宏, 西山伸彦, "GaInAsP 半導体薄膜分布反射型レーザの最適な光閉じ込めに関する考察,"電子情報通信学会レーザ・量子エレクトロニクス研究会(LQE), IEICE Technical Report, Vol. 119, No. 231, pp. 7-10, Oct. 2019.

[9] 高橋直樹, 中村なぎさ, 吉田崇将, 方偉成, 雨宮智宏, 西山伸彦, 荒井滋久, "GaInAsP/InP リッジ埋め込み構造による半導体薄膜分布反射型レーザの微分抵抗,"第 66 回応用物理会春季学術講演会, 12a-W611-9, Mar. 2019.

[10] 雨宮智宏, 岡田祥, 高橋直樹, 佐々木龍耶, 堀川剛, 渥美裕樹, 小田悠貴, 原悠太, 野田真司, 山本宏, Thomas Uhrmann, Andrea Kneidinger, 森莉紗子, 藤井恭, 浅井隆宏, 塩田大, 西山伸彦, "UV ナノインプリントリソグラフィを用いた

大面積集積フォトニクスプロセスの開発”, 第 84 回応用物理会秋季学術講演会, Sep. 2023

[11] 吉田俊, **<u>高橋直樹</u>**, 雨宮智宏, 西山伸彦, “Si 細線導波路-InP 細線導波路層間結合に向けた結合器の設計, ”電子情報通信学会エレクトロニクスソサイエティ大会, 2023 年電子情報通信学会ソサイエティ大会, Sep. 2023.

[12] 西村公佐, **<u>高橋直樹</u>**, 二村真司, 筒井慧悟, 西山伸彦, 高橋英憲, 鈴木正敏, ” 光子-光子共鳴構造を有するメンブレン DR レーザのミリ波帯 5G モバイル信号による直接変調”, 2023 年電子情報通信学会ソサイエティ大会, Sep. 2023.

[13] 坂井駿介, **<u>高橋直樹</u>**, 雨宮智宏, 西山伸彦, “全光ニューラルネットワークに向けた ReLU 関数としての GaInAsP 半導体薄膜レーザの構造検討”, 第 70 回応用物理学会春季学術講演会, Mar. 2023.

[14] W. Fang, **<u>N. Takahashi</u>**, T. Horikawa, Y. Ohiso, R. Xue, S. Katsumi, T. Amemiya, and N. Nishiyama, “High temperature operation of membrane optical link with buried-ridge-waveguide on Si bonded by surface activated bonding”, *IEICE Society Conference*, submitted, online, Sep. 2022.

[15] W. Fang, **<u>N. Takahashi</u>**, R. Xue, S. Katsumi, Y. Ohiso T. Amemiya and N. Nishiyama, “110 ˚C high temperature operation of GaInAsP/Si membrane DFB Laser bonded by a-Si nano-film assisted surface activated bonding”, *The 69th Japan Society of Applied Physics Spring Meeting*, Sagamihara, Japan, 24p-D214-1, Mar. 2022.

[16] R. Xue, W. Fang, **<u>N. Takahashi</u>**, S. Katsumi, T. Amemiya, and N. Nishiyama, “Characterization of InP-Rib waveguide on Si substrate for membrane photonic integrated circuits”, *The 69th JSAP Spring Meeting*, 24p-D214-3, 2022.

[17] W. Fang, **<u>N. Takahashi</u>**, Y. Ohiso T. Amemiya and N. Nishiyama, “Thermal resistance reduction of membrane FP laser bonded by a-Si nano-film assisted surface activated bonding”, *The 82nd Japan Society of Applied Physics Autumn Meeting*, Nagoya, Japan, 10p-N405-2, Sep. 2021.

[18] W. Wang, S. A. M. E. Moataz, W. Fang, **<u>N. Takahashi</u>**, Y. Oiso, T. Amemiya, N.

Nishiyama, “Design of InP-based membrane waveguide on Si substrate toward low propagation loss and high-efficiency coupling with laser”, *Photonic Device Workshop 2020*, P3, Nov. 2020.

[19] W. Fang, **N. Takahashi**, W. Wang, T. Amemiya and N, Nishiyama, "Investigation of heat generation reduction effect of semiconductor membrane laser using thermal shunt structure", *IEICE Society Conference*, C-3/4-30, Sep. 2020.

[20] W. Fang, **N. Takahashi**, Y. Ohiso, T. Amemiya and N. Nishiyama, "Investigation of bonding interface and strain characteristics in surface activated bonding assisted by Si-nano film”, *The 67th JSAP Spring Meeting*, Tokyo, Japan, 15p-B508-6, Mar. 2020.

[21] W. Wang, W. Fang, K. Saito, **N. Takahashi**, T. Amemiya, N. Nishiyama, “ Analysis of Low loss InP-based membrane waveguide for optical interconnection on Si substrate”, *The 67th JSAP Spring Meeting*, 15p-B508-5, Mar. 2020.

[22] 中村なぎさ, 吉田崇将, Fang Weicheng, **高橋直樹**, 雨宮智宏, 西山伸彦, 荒井滋久,“GaInAsP/InP リッジ薄膜導波路半導体薄膜 DR レーザの高速動作化におけるエネルギーコスト”, 第 79 回応用物理学会秋季学術講演会, 18a-232-7, Sep. 2018

Award

1. **2023 年度 第 45 回光通信研究会 Best Oral Presentation 賞**
2. **2022 年度 第 31 回ソサイエティ大会エレクトロニクスソサイエティ学生奨励賞**
3. **2021 年度 秋季第 51 回応用物理学会講演奨励賞**
4. **2019 年度 電子情報通信学会 エレクトロニクスソサイエティ レーザ量子エレクトロニクス研究会奨励賞**